Characterization of an Unusual Collection of Olfactory Neurons in the Nose

Thesis by

Cambrian Yangshao Liu

In Partial Fulfillment of the Requirements for the Degree
of

Doctor of Philosophy

CALIFORNIA INSTITUTE OF TECHNOLOGY
Pasadena, California

2012

(Defended February 17, 2012)

ACKNOWLEDGMENTS

To borrow loosely from Hillary Clinton, it takes a village to educate and train a young scientist. I am indebted to so many people for their support, advice, and patience during my time here at Caltech. It is impossible to list them all; the people I will mention below are only a small subset of those who have positively impacted me during my graduate career. So much time in doing science is spent measuring things (milliliters in a tube, cells in a ganglion, years in graduate school), but the inspiration and strength lent to me by those who populate my life are immeasurable quantities, indiscrete and unbounded. Thank you to you all.

I have always assumed that the continuous financial and scientific support provided to my project by my thesis advisor, Scott Fraser, is a vote of confidence in my abilities as a young scientist. I know that it has not always been easy for him to give this support in an era of shrinking budgets and expanding time commitments. I am so appreciative and thankful for the sacrifices Scott has made for me. Scott often has good ideas. In our discussions, he is always upbeat, and he has helped me weather the inevitable scientific ups and downs that I have encountered in my time here. Scott also has a great sense of humor. One of my regrets is that I will likely leave Caltech having never pulled off a great prank on him. Oh well, there is always time. One can never get too comfortable.

I am indebted to David Koos, my partner in crime (crime: GG-ology), field general of the GG project, “the nasal fox.” A significant argument can be made that the GG should actually be referred to as the “Koos ganglion” (KG). Cosmically, the neurons would have then expressed pGC-K instead of pGC-G, which would have been either a great boon to my career (a novel guanylate cyclase isoform!) or a detriment (no antibody, no discovery). When I began my rotation in the Fraser lab in 2006, David already knew how to dissect and image the GG, a great starting advantage for me. David has helped me out in almost every imaginable way (only an exaggeration because I have a powerful imagination) in tackling a daunting project, whether it was with doing experiments

in a hands-on way, scheming the next experiments, providing encouragement at the right times, being an advocate for my career, and dealing with the paperwork and grind of working with animals. David and I have had many long conversations about the GG and other, more-personal topics. I am grateful that he and I have had a chance to walk down the same road.

Henry Lester has been extremely generous to allow me to work in his lab and use his equipment. It is hard for me to think where my project would have gone without Henry's offer that I perform electrophysiological analysis on GG neurons. Henry challenges me and teaches me in all the right ways, and he seldom gives bad advice. He has always treated me as a professional and expected me to do things in a professional way. Obviously, this has improved my experimental methodology, but it has also elevated my scientific presentations and my technical writing. The lessons he has taught me will be extremely useful as I prepare for a career in science.

All of the electrophysiology was performed on Cheng Xiao's rig. Not only did Cheng teach me how to patch clamp, he might actually be the first person in history to have obtained whole-cell recordings from GG neurons. Cheng: you are the man; I hope you still had enough time on your rig. Cheng was (and still is) kind enough to let me use his rig for many more days and much more time than either of us initially anticipated. One of these days, when I have more cash, I should probably buy him a micromanipulator. As rig captain, Cheng allowed me to worry about tissue collection and patching. I never had to spend weeks taking the rig apart to fix 60 Hz noise; Cheng would do this for me. In some ways, I regret not having true knowledge mastery of a rig, but I suppose one cannot be an expert at everything, though perhaps I am still looking to be an expert at something. Cheng also put up with more stupid questions from an electrophysiology novice (me) than he will probably hear for the rest of his life. But, somehow, he was always kind to me! Now that is a quality I would like to possess.

My other thesis committee members have provided great professional advice to me over the years. It was Paul Patterson's idea to puff GG neurons with cortisol. John Allman proofread my first paper. Paul has offered to lend me his equipment and expertise in the behavioral analysis of mice

with defective GG organs. John offered to teach me how to section large specimens and to extract RNA from small samples, with the hope that I could do cross-species comparisons of the GG and analyze the GG transcriptome. Given the time, I would have liked to have done all these experiments. It was wonderful to have so many options and directions in which to take this project. I have no regrets about patch clamping, but if it had not worked, there were many other experiments that could have been done. Knowing this reduced my stress level significantly.

The members of the Fraser and Lester labs with whom I have had the privilege of interacting: I thank you all. I have had many great conversations with many postdocs and fellow graduate students in both labs; everyone has been extremely supportive of me. Special thanks also go to Aura Keeter, Mary Flowers, Joaquin Gutierrez, Sarah Alaniz, Alyssa Douglas, Kristy Hilands, Pat Anguiano, Eloisa Imel, Purnima Deshpande, Gary Belford, and Martha Henderson for doing the grunt work of running the labs, managing mice, making DNA from tails, dealing with bureaucracy, and basically allowing me to focus solely on the "interesting" scientific aspects of the GG project. The Biochemistry and Molecular Biophysics (BMB) option secretary, Alison Ross, has always looked out for my best interests. Many colleagues that entered the BMB option with me in 2005 became my closest friends at Caltech: especially Russ Ernst, Phil Romero, Kelly Matzen, John Ngo, Fred Tan, and Peera Jaru-Ampornpan. To all my friends, at Caltech and elsewhere, who have kindly forgiven my endless forays into all-out nerddom and my passionate monologues about a little nerve at the tip of the mouse nose: I am sorry, but I am not going to change.

My parents, Nina Lam and Kam-biu Liu, besides raising and supporting me for so many years, were the first to teach me how to be a scientist. I remember my mom trying to teach me to use Quattro Pro in the 5th grade. Both of them helped me tremendously with science fair projects in middle and high school and were willing to do whatever it took so that I would succeed. They were always willing to invest money to buy books and to photocopy journal articles when I was growing up. It must have been a challenge to feed my curiosity; they finally ended up just letting me spend all day at the LSU library. In addition, they taught me that doing science takes perseverance, luck,

and a good strategy. I would also like to thank my little sister, Beringia Liu, for being supportive and not being outwardly embarrassed by her nerd brother. There are no words that can adequately express my gratitude to my family.

Most importantly, I would like to thank Lisa Hochrein. Lisa is only my wife-to-be, my best friend, my confidante, my colleague, my best reason to get up in the morning and by far my best reason to come home in the evening, my rock, my sponge, giver of meaning and happiness, the key, the song, the means and the end. I could go on and on. Let me put it this way. I am willing to run controlled experiments to learn just about anything. But I shudder at the thought of what my life would be like if Lisa were gone or had never shown up, and I have no plans to find out. Lisa, this thesis is dedicated to you.

ABSTRACT

We have used a combination of histochemical, electrophysiological, and behavioral approaches to study signal transduction, membrane biophysics, and chemosensory function in the neurons of the mouse Grueneberg ganglion (GG) olfactory subsystem. The GG is a recently appreciated collection of ~1,000 clustered primary olfactory neurons located at the anterior tip of the mammalian nasal cavity. Despite their far-forward position, GG neurons are fully trapped beneath a keratinized epithelium and are wrapped by glial cells. This raises the question of how they contribute to the sense of smell. We found that GG neurons have key components of cGMP signal transduction pathway and are molecularly similar to GC-D neurons, which project to the enigmatic necklace glomeruli in the olfactory bulb. In electrophysiological analyses, individual GG neurons spontaneously discharged action potentials in one of three distinct temporal patterns that were stable for >20 min. An auxiliary fast-inactivating Na^+ current accounted for the various discharge patterns in computer simulations of the neuronal ionic currents. Despite differences in baseline activity, the majority of GG neurons responded to specific mammalian pheromones. In behavioral experiments, we found that the weaning of adolescent mice induced GG activity; however, the effects did not depend on ambient temperature or the presence of other animals. Because GG neurons reside on a dense vascular bed, have specialized access to serum contents, and directly responded to pressure ejections of serum, their activity can likely be modulated by internally circulating hormones or proteins associated with specific physiological states such as stress. Taken together, our results demonstrate unusual molecular and functional aspects of a morphologically and anatomically atypical olfactory nerve.

TABLE OF CONTENTS

--- Chapter 1 ---

Introduction

Overview of olfaction

A sauté of garlic and onions in butter, the finishing of chocolate-chip cookies in the oven, a lover's perfume, the wretchedness of an urban public bathroom: these are examples of the powerful ways our sense of smell (olfaction) elaborates our experiences. Terrestrial mammals possess an olfactory sense that can detect theoretically between ~10,000 and ~10,000,000 airborne odors at nanomolar concentration. The detection of airborne odors begins in the posterior region of the nasal cavity. The main olfactory epithelium (MOE) houses several million olfactory sensory neurons (OSNs) that protrude into the airspace. The inhalation of odors, which are typically hydrophobic organic molecules, and their dissolution into a superficial mucus allow the odors to make contact with OSNs. The OSNs express olfactory receptor (OR) proteins (Buck and Axel 1991) that bind to the odors and begin a signal transduction process that culminates in membrane depolarization and the propagation of action potentials along axons towards the olfactory bulb (OB). Axons of OSNs converge into discrete units called glomeruli in the superficial layer of the OB (Firestein 2001). Olfactory information is received by mitral cells that synapse with the glomeruli in the OB; the information is subsequently passed to the anterior olfactory nucleus, amygdala, and piriform cortex in the deeper parts of the brain (Miyamichi et al. 2011).

The discriminatory power of the olfactory sense is related to the number of functional OR genes collectively expressed in OSNs. Rodents, which rely on olfaction for survival (Brunet et al. 1996), have ~1,000 distinct intronless OR genes. Humans possess ~200-400 functional OR genes, but have many more OR pseudogenes. In contrast, nonmammalian vertebrates have only ~1/10 the number of OR genes found in mammals (Mombaerts 1999). The platypus, one of the earliest-evolved mammals (Venditti et al. 2011), has ~300 functional OR genes and ~400 additional OR pseudogenes (Warren et al. 2008). Thus, the large OR repertoire appears to be a uniquely mammalian property. A single OSN is thought to express

a single OR gene, and the axons of OSNs expressing the same OR gene contribute to a singular set of 2 ipsilateral glomeruli (Mombaerts 2004). Hence, one can determine which ORs are activated by determining which neurons or glomeruli are activated. Individual ORs are tuned to detect several odors, and an individual odor is recognized by several ORs (Malnic et al. 1999). The combinatorial code of odor detection means that individual odors produce "maps" of activated glomeruli in the OB (Rubin and Katz 1999; Wachowiak and Cohen 2001).

The rodent OB is composed of different domains that receive and process input from specialized sets of primary olfactory neurons located in anatomically distinct regions of the nasal cavity. The largest domain is the main OB (MOB), which handles input from the aforementioned OSNs in the MOE. A subset of the glomeruli in the MOB is additionally targeted by sensory neurons whose somata reside in the septal organ of Masera (Ma 2011). In contrast, the accessory OB (AOB) is innervated by axons from vomeronasal sensory neurons (VSNs), located in the vomeronasal (Jacobson's) organ (VNO) anterior of the MOE. VSNs express G-protein coupled receptors known as pheromone receptors (VRs) (Dulac and Axel 1995) and are involved in the detection of pheromones, cues that induce innate both behavioral responses such as freezing, aggression, flight, feeding, and copulation, and physiological responses such as the accleration of reproductive development (Brennan and Zufall 2006). VSNs respond to conspecific cues such as male bedding, as well as heterospecific cues such as snake bedding (Isogai et al. 2011). Removal of VSNs in mice results in the loss of gender identity (Kimchi et al. 2007; Stowers et al. 2002) and a deficit in courtship ultrasonic vocalizations (Wysocki et al. 1982).

Though VSNs and OSNs are broadly similar in that they reside in the epithelia in the nasal cavity, protrude into the nasal airspace, and relay information to glomeruli in the OB, they possess different olfactory signal transduction mechanisms. In the protruding cilia of OSNs, odor binding by the OR activates G_{olf} protein and the adenylate cyclase ACIII, resulting in the production of cAMP (Firestein 2001). The increase in [cAMP] opens a heterotetrameric cAMP-gated cationic channel composed of 2 CNGA2, 1 CNGA4, and 1 CNGB1b subunits (Biel and Michalakis 2007; Frings et al. 1992). The influx of ions, many of which are Ca^{2+}, not only depolarizes the neuronal membrane but also activates a Ca^{2+}-

activated Cl^- channel, whose activity amplifies the underlying depolarization due to the abnormally high intracellular [Cl^-] in OSNs (Kaneko et al. 2001; Lowe and Gold 1993). The depolarization increases the frequency of spontaneous action potentials. In the protruding microvilli of VSNs, pheromone binding to the VR activates G_i/G_o proteins. The intermediate steps of signal transduction seem to involve the subsequent activation of phospholipase C and its hydrolysis of PIP_2 into IP_3 and diaglycerol (DAG) (Zufall and Munger 2001). The electrical transduction process is initiated with the opening of the DAG-gated TRPC2 cationic channel, which depolarizes the neuronal membrane (Lucas et al. 2003). VSNs respond to nanomolar concentrations of pheromones with increases in spontaneous action potential frequency (Holy et al. 2000; Leinders-Zufall et al. 2000).

Necklace glomeruli

In a specialized region of the caudal superficial rodent OB, between the glomerular fields of the MOB and AOB, there are a set of 20-50 "atypical" glomeruli that can be distinguished by their labeling with acetylcholinesterase (AChE) histochemistry (Zheng et al. 1987). These atypical glomeruli include the modified glomerular complex in the dorsomedial OB that is active in newborn mice, suggesting a role in suckling (Greer et al. 1982). Using an aromatase antibody (later found to bind to huntingtin associated protein (Fujinaga et al. 2007)), Shinoda and colleagues demonstrated that the AChE+ atypical glomeruli form a domain in which each glomerulus resembles a bead on a necklace; thus, the atypical glomeruli are also collectively referred to as the "necklace domain" of the OB. The aromatase antibody also identified a sparsely distributed set of neurons embedded with OSNs in the caudal MOE that potentially innervated the necklace glomeruli (Shinoda et al. 1993; Shinoda et al. 1989).

These neurons, interspersed throughout the caudal MOE and having a similar morphology as OSNs, were found to express key components of a cGMP signal transduction cascade. Thus, the necklace glomeruli differ from the glomeruli of the MOB and AOB in that they represent a zone of primary cGMP transduction. These neurons express a guanylate cyclase, pGC-D, a single-pass transmembrane receptor that catalyzes the production of cGMP when stimulated (Fulle et al. 1995; Juilfs et al. 1997). The

necklace olfactory system is thereby also called the GC-D system. GC-D neurons express a cGMP-stimulated phosphodiesterase (PDE2A) and a cGMP-gated heterotetrameric cationic channel composed of 2 CNGA3 and 2 CNGB3 subunits (Meyer et al. 2000). In addition, GC-D neurons express high levels of the carbonic anhydrase CAII. Functional studies have demonstrated that GC-D neurons respond to CO_2 (Hu et al. 2007), bicarbonate (Guo et al. 2009; Sun et al. 2009), and uroguanylin (Duda and Sharma 2008; Leinders-Zufall et al. 2007) with elevations in cytosolic [Ca^{2+}] and increased spontaneous firing frequency.

Grueneberg ganglion

In 1973, Hans Grüneberg reported the startling identification of clusters of neuronal cell bodies in the most anterior region of the mouse nasal cavity, where the nasal septum is cartilaginous. Possessing large spherical nuclei, these neurons were readily discerned in hematoxylin-and-eosin-treated sections of the nasal vestibule. The neuronal clusters were sparse, appearing intermittantly in transverse serial sections spanning an anterior-posterior distance of 250 μm in the nose of the newborn mouse. Because the neuronal cell bodies were more anterior than other cranial nerves and could be distinguished from the surrounding fibers of the anterior ethmoidal nerve, Grüneberg concluded that these ganglionic cell bodies belonged to the enigmatic cranial nerve zero, *nervus terminalis*, believed to have a chemosensory function but separate from the olfactory system (Bojsen-Moller 1975; Wirsig and Leonard 1986). In the other examined mammalian samples of the adult rat, adult hamster, fetal cat, fetal anteater, and 5-month-old human embryo, Grüneberg's neurons exhibited a similar clustered morphology and likewise bilaterally occupied the dorsal septal corners of the nasal vestibule (Grüneberg 1973).

Tachibana's ultrastructural study in 1990 reported ciliated cell bodies with a ganglionic arrangement in the anterior nasal cavity of the musk shrew (Tachibana et al. 1990). However, over 30 years elapsed between Grüneberg's study and the next published report that directly addressed the so-called Grueneberg ganglion (GG) in the mouse. In 2005, a series of 5 papers, beginning with the study of Koos and Fraser, independently reclassified the mouse GG as part of the primary olfactory system

(Fleischer et al. 2006a; Fuss et al. 2005; Koos and Fraser 2005; Roppolo et al. 2006; Storan and Key 2006). This conclusion was based on 2 pieces of evidence: (1) the expression in the GG of olfactory marker protein (OMP), a protein found in all mature primary olfactory neurons, including OSNs and VSNs; and (2) the final destination of GG axons in the posterior (caudal) region of the OB. With regard to the former, GG neurons exhibit a strong green fluorescence in transgenic mice expressing green fluorescent protein (GFP) from the *Omp* locus. With regard to the latter, GG axons form 8-12 glomeruli that resemble pearls on a necklace, near the previously described GC-D necklace domain in the OB. However, the GG necklace glomeruli appear to be distinct from the classic GC-D necklace (Cockerham et al. 2009); we have termed the domain formed by GG glomeruli to be the "necklace-like" domain.

Besides their far-forward location, GG neurons are anatomically distinct in several facets from OSNs and VSNs. Present at embryonic day 16 (Fuss et al. 2005; Roppolo et al. 2006), the GG organ forms a discontinuous arrowhead shape, in contrast to the continuous pseudostratified epithelial sheets found in the MOE and VNO. GG neurons, numbering 300-600 per side, are tightly packed in clusters and are ensheathed by glial cells (Grüneberg 1973). No consistent protrusions have been found to extend from subsurface GG somata through a thin keratinized epithelium into the nasal cavity (Roppolo et al. 2006). This differs from bipolar OSNs and VSNs, which each project a dendritic process that terminates as a ciliated (in OSNs) or microvillar (in VSNs) knob, at which ORs and VRs are localized, in the nasal cavity. Each GG neuron has a single axonal projection. These projections collect into a single fascicle that extends caudally and crosses the bony cribriform plate on the medial sides of the olfactory bulbs (Koos and Fraser 2005).

GG neurons are likely to have a chemosensory function. The report of GG responses to alarm pheromones by Brechbuhl and colleagues marked a major advance in the functional characterization of the neurons (Brechbuhl et al. 2008). It was demonstrated that GG neurons exhibit increases in cytosolic $[Ca^{2+}]$ when exposed to saline droplets collected from cages of recently asphyxiated mice. Curiously, the cytosolic $[Ca^{2+}]$ rise did not require extracellular Ca^{2+}. The $[Ca^{2+}]$ increase was not observed with exposures to CO_2-infused, cold, or acidified saline. No responses were observed with exposures to a

nipple wash or urine of conspecific animals. As the water-soluble characteristic of the stimulus agreed with previously described properties of mammalian alarm pheromones (Kiyokawa et al. 2005), whose exact chemical identities have not been elucidated, and the responses were observed in GG neurons in acute slice preparations of the mouse nasal vestibule, it was claimed that the GG directly detects and mediates behavioral responses to alarm pheromones. In support of this claim, surgical ablations of the GG resulted in the disappearance of animal freezing-immobility responses in behavioral assays that exposed mice to the putative alarm pheromone (Brechbuhl et al. 2008).

A nearly simultaneous report by Mamasuew and colleagues proposed a second GG stimulus modality (Mamasuew et al. 2008). It was found that a modest lowering of ambient temperature (e.g., from 25˚C to 15˚C) induced the new production of c-Fos mRNA, a marker of neuronal activity, in the GG. Neonatal mice displayed the greatest sensitivity to cold, as visible c-Fos transcription in the GG of these mice could be observed with the lowering of ambient temperature to 22˚C. In adult mice, no c-Fos transcription in the GG was evident when the ambient temperature was lowered to 15˚C. In a later study, Mamasuew and colleagues demonstrated that coolness-induced GG c-Fos transcription depended on a cyclic nucleotide-gated cationic channel subunit, CNGA3, that is primarily found in cone photoreceptor cells in the eye but is also expressed in the GG (Mamasuew et al. 2010). Schmid and colleagues supported and extended the *in vivo* work by showing *in vitro* TTX-dependent increases in cytosolic [Ca^{2+}] could be induced by exposing acute slices of the GG to cold saline (Schmid et al. 2010), with an ET_{50} of ~16˚C. Curiously, *in vitro* the GG responses to cold were unaffected by the deletion of *Cnga3*.

Outline of chapters

Due to their unusual far-anterior location, their presence at birth and throughout life, and their apparent exclusiveness to mammals, GG neurons are interesting objects of study for researchers of various specializations. The following chapters describe original contributions to the molecular, electrophysiological, and functional characterization of mouse GG neurons.

Chapter 2 reports the identification of proteins and small molecules involved in a potential odor-evoked transduction pathway in mouse GG neurons. In contrast to OSNs, GG neurons do not express ORs and lack the transduction machinery of OSNs and VSNs (Roppolo et al. 2006). GG neurons express one type of pheromone receptor, V2r83, and several trace-amine associated receptors (TAARs) that have olfactory functions, but these expression patterns are either restricted to animals younger than p21 (TAARs) or have unknown functional significance (V2r83 and TAARs) (Fleischer et al. 2006b; Fleischer et al. 2007). Chapter 2 demonstrates ciliary localization of a membrane-bound receptor guanylate cyclase and a cGMP-gated cationic channel subunit in GG neurons. These results were independently obtained and in general agreement with those simultaneously reported by Fleischer and colleagues (Fleischer et al. 2009). The molecular similarities between the GG and GC-D neurons are discussed.

Chapter 3 describes the electrophysiological characterization of voltage-dependent ionic conductances in mouse GG neurons. Similar to OSNs (Lynch and Barry 1991; Ma et al. 1999; Vargas and Lucero 1999; Weiss et al. 2011) and VSNs (Dibattista et al. 2008; Liman and Corey 1996; Ukhanov et al. 2007), GG neurons exhibit two fast-inactivating Na^+ conductances, a delayed-rectifier K^+ conductance, a non-inactivating Ca^{2+} conductance, and hyperpolarization-activated "funny" currents. This chapter focuses on the unique relationship between the two Na^+ conductances and presents a Hodgkin-Huxley computer model that predicts how the Na^+ conductances may contribute to the heterogeneity of spontaneous firing patterns in GG neurons.

Electrophysiological studies of chemosensory function in the mouse GG are presented in Chapter 4. These experiments were performed on the acute slice preparation of the mouse nasal vestibule, presented in Chapter 3, and report on the odorant modulation of spontaneous firing. Chapter 4 supports and extends previous *in vivo* work that demonstrated the CNGA3-dependent responsiveness of GG neurons to certain isoforms of dimethylpyrazine (Mamasuew et al. 2011a; Mamasuew et al. 2011b), a pheromone capable of altering reproductive cycles in mice (Jemiolo and Novotny 1994; Ma et al. 1998). The work presented here also shows excitatory responses to cGMP and inhibitory responses to general

lipophilic molecules in individual GG neurons. Moreover, it is suggested that serum and cortisol serve as biologically relevant GG stimuli.

Chapter 5 reports immunohistochemical experiments showing that specific behavioral manipulations induce the nuclear accumulation of c-Fos protein, a marker for neuronal activity, in GG neurons. These manipulations involve as their common element the separation of unweaned mice from their parents. Maternal separation is a highly anxiogenic stimulus, leading to an increase in pup ultrasonic vocalizations (Hofer and Shair 1978). This chapter discusses the potential relationship between this new work and the existing literature on the GG detection of alarm pheromones and cold.

A prevailing theme of this work centers on the mechanisms of information processing by GG neurons. These mechanisms are partially revealed, from the subcellular level to the organ level. At the end of the thesis, directions for future work are discussed.

REFERENCES

Biel M, and Michalakis S. Function and dysfunction of CNG channels: insights from channelopathies and mouse models. *Mol Neurobiol* 35: 266-277, 2007.

Bojsen-Moller F. Demonstration of terminalis, olfactory, trigeminal and perivascular nerves in the rat nasal septum. *J Comp Neurol* 159: 245-256, 1975.

Brechbuhl J, Klaey M, and Broillet MC. Grueneberg ganglion cells mediate alarm pheromone detection in mice. *Science* 321: 1092-1095, 2008.

Brennan PA, and Zufall F. Pheromonal communication in vertebrates. *Nature* 444: 308-315, 2006.

Brunet LJ, Gold GH, and Ngai J. General anosmia caused by a targeted disruption of the mouse olfactory cyclic nucleotide-gated cation channel. *Neuron* 17: 681-693, 1996.

Buck L, and Axel R. A novel multigene family may encode odorant receptors: a molecular basis for odor recognition. *Cell* 65: 175-187, 1991.

Cockerham RE, Puche AC, and Munger SD. Heterogeneous sensory innervation and extensive intrabulbar connections of olfactory necklace glomeruli. *PLoS One* 4: e4657, 2009.

Dibattista M, Mazzatenta A, Grassi F, Tirindelli R, and Menini A. Hyperpolarization-activated cyclic nucleotide-gated channels in mouse vomeronasal sensory neurons. *J Neurophysiol* 100: 576-586, 2008.

Duda T, and Sharma RK. ONE-GC membrane guanylate cyclase, a trimodal odorant signal transducer. *Biochem Biophys Res Commun* 367: 440-445, 2008.

Dulac C, and Axel R. A novel family of genes encoding putative pheromone receptors in mammals. *Cell* 83: 195-206, 1995.

Firestein S. How the olfactory system makes sense of scents. *Nature* 413: 211-218, 2001.

Fleischer J, Hass N, Schwarzenbacher K, Besser S, and Breer H. A novel population of neuronal cells expressing the olfactory marker protein (OMP) in the anterior/dorsal region of the nasal cavity. *Histochem Cell Biol* 125: 337-349, 2006a.

Fleischer J, Mamasuew K, and Breer H. Expression of cGMP signaling elements in the Grueneberg ganglion. *Histochem Cell Biol* 131: 75-88, 2009.

Fleischer J, Schwarzenbacher K, Besser S, Hass N, and Breer H. Olfactory receptors and signalling elements in the Grueneberg ganglion. *J Neurochem* 98: 543-554, 2006b.

Fleischer J, Schwarzenbacher K, and Breer H. Expression of trace amine-associated receptors in the Grueneberg ganglion. *Chem Senses* 32: 623-631, 2007.

Frings S, Lynch JW, and Lindemann B. Properties of cyclic nucleotide-gated channels mediating olfactory transduction. Activation, selectivity, and blockage. *J Gen Physiol* 100: 45-67, 1992.

Fujinaga R, Yanai A, Nakatsuka H, Yoshida K, Takeshita Y, Uozumi K, Zhao C, Hirata K, Kokubu K, Nagano M, and Shinoda K. Anti-human placental antigen complex X-P2 (hPAX-P2) anti-serum recognizes C-terminus of huntingtin-associated protein 1A common to 1B as a determinant marker for the stigmoid body. *Histochem Cell Biol* 128: 335-348, 2007.

Fulle HJ, Vassar R, Foster DC, Yang RB, Axel R, and Garbers DL. A receptor guanylyl cyclase expressed specifically in olfactory sensory neurons. *Proc Natl Acad Sci U S A* 92: 3571-3575, 1995.

Fuss SH, Omura M, and Mombaerts P. The Grueneberg ganglion of the mouse projects axons to glomeruli in the olfactory bulb. *Eur J Neurosci* 22: 2649-2654, 2005.

Greer CA, Stewart WB, Teicher MH, and Shepherd GM. Functional development of the olfactory bulb and a unique glomerular complex in the neonatal rat. *J Neurosci* 2: 1744-1759, 1982.

Grüneberg H. A ganglion probably belonging to the N. terminalis system in the nasal mucosa of the mouse. *Z Anat Entwicklungsgesch* 140: 39-52, 1973.

Guo D, Zhang JJ, and Huang XY. Stimulation of guanylyl cyclase-D by bicarbonate. *Biochemistry* 48: 4417-4422, 2009.

Hofer MA, and Shair H. Ultrasonic vocalization during social interaction and isolation in 2-weeek-old rats. *Dev Psychobiol* 11: 495-504, 1978.

Holy TE, Dulac C, and Meister M. Responses of vomeronasal neurons to natural stimuli. *Science* 289: 1569-1572, 2000.

Hu J, Zhong C, Ding C, Chi Q, Walz A, Mombaerts P, Matsunami H, and Luo M. Detection of near-atmospheric concentrations of CO2 by an olfactory subsystem in the mouse. *Science* 317: 953-957, 2007.

Isogai Y, Si S, Pont-Lezica L, Tan T, Kapoor V, Murthy VN, and Dulac C. Molecular organization of vomeronasal chemoreception. *Nature* 478: 241-245, 2011.

Jemiolo B, and Novotny M. Inhibition of sexual maturation in juvenile female and male mice by a chemosignal of female origin. *Physiol Behav* 55: 519-522, 1994.

Juilfs DM, Fulle HJ, Zhao AZ, Houslay MD, Garbers DL, and Beavo JA. A subset of olfactory neurons that selectively express cGMP-stimulated phosphodiesterase (PDE2) and guanylyl cyclase-D define a unique olfactory signal transduction pathway. *Proc Natl Acad Sci U S A* 94: 3388-3395, 1997.

Kaneko H, Nakamura T, and Lindemann B. Noninvasive measurement of chloride concentration in rat olfactory receptor cells with use of a fluorescent dye. *Am J Physiol Cell Physiol* 280: C1387-1393, 2001.

Kimchi T, Xu J, and Dulac C. A functional circuit underlying male sexual behaviour in the female mouse brain. *Nature* 448: 1009-1014, 2007.

Kiyokawa Y, Kikusui T, Takeuchi Y, and Mori Y. Alarm pheromone that aggravates stress-induced hyperthermia is soluble in water. *Chem Senses* 30: 513-519, 2005.

Koos DS, and Fraser SE. The Grueneberg ganglion projects to the olfactory bulb. *Neuroreport* 16: 1929-1932, 2005.

Leinders-Zufall T, Cockerham RE, Michalakis S, Biel M, Garbers DL, Reed RR, Zufall F, and Munger SD. Contribution of the receptor guanylyl cyclase GC-D to chemosensory function in the olfactory epithelium. *Proc Natl Acad Sci U S A* 104: 14507-14512, 2007.

Leinders-Zufall T, Lane AP, Puche AC, Ma W, Novotny MV, Shipley MT, and Zufall F. Ultrasensitive pheromone detection by mammalian vomeronasal neurons. *Nature* 405: 792-796, 2000.

Liman ER, and Corey DP. Electrophysiological characterization of chemosensory neurons from the mouse vomeronasal organ. *J Neurosci* 16: 4625-4637, 1996.

Lowe G, and Gold GH. Nonlinear amplification by calcium-dependent chloride channels in olfactory receptor cells. *Nature* 366: 283-286, 1993.

Lucas P, Ukhanov K, Leinders-Zufall T, and Zufall F. A diacylglycerol-gated cation channel in vomeronasal neuron dendrites is impaired in TRPC2 mutant mice: mechanism of pheromone transduction. *Neuron* 40: 551-561, 2003.

Lynch JW, and Barry PH. Inward rectification in rat olfactory receptor neurons. *Proc Biol Sci* 243: 149-153, 1991.

Ma M. Multiple Olfactory Subsystems Convey Various Sensory Signals. 2011.

Ma M, Chen WR, and Shepherd GM. Electrophysiological characterization of rat and mouse olfactory receptor neurons from an intact epithelial preparation. *J Neurosci Methods* 92: 31-40, 1999.

Ma W, Miao Z, and Novotny MV. Role of the adrenal gland and adrenal-mediated chemosignals in suppression of estrus in the house mouse: the lee-boot effect revisited. *Biol Reprod* 59: 1317-1320, 1998.

Malnic B, Hirono J, Sato T, and Buck LB. Combinatorial receptor codes for odors. *Cell* 96: 713-723, 1999.

Mamasuew K, Breer H, and Fleischer J. Grueneberg ganglion neurons respond to cool ambient temperatures. *Eur J Neurosci* 28: 1775-1785, 2008.

Mamasuew K, Hofmann N, Breer H, and Fleischer J. Grueneberg ganglion neurons are activated by a defined set of odorants. *Chem Senses* 36: 271-282, 2011a.

Mamasuew K, Hofmann N, Kretzschmann V, Biel M, Yang RB, Breer H, and Fleischer J. Chemo- and thermosensory responsiveness of Grueneberg ganglion neurons relies on cyclic guanosine monophosphate signaling elements. *Neurosignals* 19: 198-209, 2011b.

Mamasuew K, Michalakis S, Breer H, Biel M, and Fleischer J. The cyclic nucleotide-gated ion channel CNGA3 contributes to coolness-induced responses of Grueneberg ganglion neurons. *Cell Mol Life Sci* 67: 1859-1869, 2010.

Meyer MR, Angele A, Kremmer E, Kaupp UB, and Muller F. A cGMP-signaling pathway in a subset of olfactory sensory neurons. *Proc Natl Acad Sci U S A* 97: 10595-10600, 2000.

Miyamichi K, Amat F, Moussavi F, Wang C, Wickersham I, Wall NR, Taniguchi H, Tasic B, Huang ZJ, He Z, Callaway EM, Horowitz MA, and Luo L. Cortical representations of olfactory input by trans-synaptic tracing. *Nature* 472: 191-196, 2011.

Mombaerts P. Molecular biology of odorant receptors in vertebrates. *Annu Rev Neurosci* 22: 487-509, 1999.

Mombaerts P. Odorant receptor gene choice in olfactory sensory neurons: the one receptor-one neuron hypothesis revisited. *Curr Opin Neurobiol* 14: 31-36, 2004.

Roppolo D, Ribaud V, Jungo VP, Luscher C, and Rodriguez I. Projection of the Gruneberg ganglion to the mouse olfactory bulb. *Eur J Neurosci* 23: 2887-2894, 2006.

Rubin BD, and Katz LC. Optical imaging of odorant representations in the mammalian olfactory bulb. *Neuron* 23: 499-511, 1999.

Schmid A, Pyrski M, Biel M, Leinders-Zufall T, and Zufall F. Grueneberg ganglion neurons are finely tuned cold sensors. *J Neurosci* 30: 7563-7568, 2010.

Shinoda K, Ohtsuki T, Nagano M, and Okumura T. A possible functional necklace formed by placental antigen X-P2-immunoreactive and intensely acetylcholinesterase-reactive (PAX/IAE) glomerular complexes in the rat olfactory bulb. *Brain Res* 618: 160-166, 1993.

Shinoda K, Shiotani Y, and Osawa Y. "Necklace olfactory glomeruli" form unique components of the rat primary olfactory system. *J Comp Neurol* 284: 362-373, 1989.

Storan MJ, and Key B. Septal organ of Gruneberg is part of the olfactory system. *J Comp Neurol* 494: 834-844, 2006.

Stowers L, Holy TE, Meister M, Dulac C, and Koentges G. Loss of sex discrimination and male-male aggression in mice deficient for TRP2. *Science* 295: 1493-1500, 2002.

Sun L, Wang H, Hu J, Han J, Matsunami H, and Luo M. Guanylyl cyclase-D in the olfactory CO2 neurons is activated by bicarbonate. *Proc Natl Acad Sci U S A* 106: 2041-2046, 2009.

Tachibana T, Fujiwara N, and Nawa T. The ultrastructure of the ganglionated nerve plexus in the nasal vestibular mucosa of the musk shrew (Suncus murinus, insectivora). *Arch Histol Cytol* 53: 147-156, 1990.

Ukhanov K, Leinders-Zufall T, and Zufall F. Patch-clamp analysis of gene-targeted vomeronasal neurons expressing a defined V1r or V2r receptor: ionic mechanisms underlying persistent firing. *J Neurophysiol* 98: 2357-2369, 2007.

Vargas G, and Lucero MT. Dopamine modulates inwardly rectifying hyperpolarization-activated current (Ih) in cultured rat olfactory receptor neurons. *J Neurophysiol* 81: 149-158, 1999.

Venditti C, Meade A, and Pagel M. Multiple routes to mammalian diversity. *Nature* 479: 393-396, 2011.

Wachowiak M, and Cohen LB. Representation of odorants by receptor neuron input to the mouse olfactory bulb. *Neuron* 32: 723-735, 2001.

Warren WC, Hillier LW, Marshall Graves JA, Birney E, Ponting CP, Grutzner F, Belov K, Miller W, Clarke L, Chinwalla AT, Yang SP, Heger A, Locke DP, Miethke P, Waters PD, Veyrunes F, Fulton L, Fulton B, Graves T, Wallis J, Puente XS, Lopez-Otin C, Ordonez GR, Eichler EE, Chen L, Cheng Z, Deakin JE, Alsop A, Thompson K, Kirby P, Papenfuss AT, Wakefield MJ, Olender T, Lancet D, Huttley GA, Smit AF, Pask A, Temple-Smith P, Batzer MA, Walker JA, Konkel MK, Harris RS, Whittington CM, Wong ES, Gemmell NJ, Buschiazzo E, Vargas Jentzsch IM, Merkel A, Schmitz J, Zemann A, Churakov G, Kriegs JO, Brosius J, Murchison EP, Sachidanandam R, Smith C, Hannon GJ, Tsend-Ayush E, McMillan D, Attenborough R, Rens W, Ferguson-Smith M, Lefevre CM, Sharp JA, Nicholas KR, Ray DA, Kube M, Reinhardt R, Pringle TH, Taylor J, Jones RC, Nixon B, Dacheux JL, Niwa H, Sekita Y, Huang X, Stark A, Kheradpour P, Kellis M, Flicek P, Chen Y, Webber C, Hardison R, Nelson J, Hallsworth-Pepin K, Delehaunty K, Markovic C, Minx P, Feng Y, Kremitzki C, Mitreva M, Glasscock J, Wylie T, Wohldmann P, Thiru P, Nhan MN, Pohl CS, Smith SM, Hou S, Nefedov M, de Jong PJ, Renfree MB, Mardis ER, and Wilson RK. Genome analysis of the platypus reveals unique signatures of evolution. *Nature* 453: 175-183, 2008.

Weiss J, Pyrski M, Jacobi E, Bufe B, Willnecker V, Schick B, Zizzari P, Gossage SJ, Greer CA, Leinders-Zufall T, Woods CG, Wood JN, and Zufall F. Loss-of-function mutations in sodium channel Nav1.7 cause anosmia. *Nature* 472: 186-190, 2011.

Wirsig CR, and Leonard CM. Acetylcholinesterase and luteinizing hormone-releasing hormone distinguish separate populations of terminal nerve neurons. *Neuroscience* 19: 719-740, 1986.

Wysocki CJ, Nyby J, Whitney G, Beauchamp GK, and Katz Y. The vomeronasal organ: primary role in mouse chemosensory gender recognition. *Physiol Behav* 29: 315-327, 1982.

Zheng LM, Ravel N, and Jourdan F. Topography of centrifugal acetylcholinesterase-positive fibres in the olfactory bulb of the rat: evidence for original projections in atypical glomeruli. *Neuroscience* 23: 1083-1093, 1987.

Zufall F, and Munger SD. From odor and pheromone transduction to the organization of the sense of smell. *Trends Neurosci* 24: 191-193, 2001.

--- Chapter 2 ---

Grueneberg ganglion olfactory subsystem employs a cGMP signaling pathway

Cambrian Y. Liu, Scott E. Fraser, David S. Koos

This chapter is reproduced with minor modification from

> Liu CY, Fraser SE, and Koos DS. Grueneberg ganglion olfactory subsystem employs a cGMP signaling pathway. *J Comp Neurol* 516: 36-48, 2009.

D.S.K. collected the data and images that were used in Figure 7.

ABSTRACT

The mammalian olfactory sense employs several olfactory subsystems situated at characteristic locations in the nasal cavity to detect and report on different classes of odors. These olfactory subsystems use different neuronal signal transduction pathways, receptor expression repertoires, and axonal projection targets. The Grueneberg Ganglion (GG) is a newly appreciated olfactory subsystem with receptor neurons located just inside of the nostrils that project axons to a unique domain of interconnected glomeruli in the caudal olfactory bulb. It is not well understood how the GG relates to other olfactory subsystems in contributing to the olfactory sense. Furthermore, the range of chemoreceptors and the signal transduction cascade utilized by the GG have remained mysterious. To resolve these unknowns, we explored the molecular relationship between the GG and the GC-D neurons, another olfactory subsystem that innervates similarly interconnected glomeruli in the same bulbar region. We found that mouse GG neurons express the cGMP-associated signaling proteins phosphodiesterase 2a, cGMP-dependent kinase II, and cyclic nucleotide gated channel subunit A3 coupled to a chemoreceptor repertoire of cilia-localized particulate guanylate cyclases (pGC-G and pGC-A). The primary cGMP signaling pathway of the GG is shared with the GC-D neurons, unifying their target glomeruli as a unique center of olfactory cGMP signal transduction. However, the distinct chemoreceptor repertoire in the GG suggests that the GG is an independent olfactory subsystem. This subsystem is well suited to detect a unique set of odors and to mediate behaviors that remained intact in previous olfactory perturbations.

KEYWORDS

necklace glomeruli, interconnected glomeruli, cGMP, guanylate cyclase, cilia, nasal vestibule, sensory subsystems

INTRODUCTION

Mice and other macrosmatic mammals possess a diverse set of odor-sensing neuronal subsystems that function together to produce a powerful and nuanced sense of smell (Fig. 1A). These subsystems have characteristic locations in the nasal cavity. Each olfactory subsystem utilizes a specific type of chemoreceptor and signal transduction cascade to detect distinct classes of chemicals and ultimately to influence certain behaviors. Once activated, the primary sensory neurons of a given subsystem directly transmit olfactory information to discrete subsystem-specific domains of the first olfactory processing center in the brain, the olfactory bulb. The olfactory subsystems range from being very large and detecting a broad spectrum of chemicals (*e.g.*, volatile molecules distinguished by >1000 odorant receptors on millions of neurons in the mouse Main Olfactory System and Septal Organ) to being very small (*e.g.*, ~550 neurons in the mouse Grueneberg Ganglion) and possessing highly specialized detection functions (*e.g.*, volatile amines detected by trace-amine associated receptor-expressing neurons) (Breer et al., 2006; Munger et al., 2008).

The Main Olfactory System (MOS) is the largest olfactory subsystem and is composed of the odorant receptor-expressing olfactory sensory neurons located within the main olfactory epithelium (MOE). Binding of volatile odor ligands to odorant receptors localized to the cilia of the olfactory sensory neurons triggers the production of cAMP. These transient elevations of cAMP open a cyclic nucleotide gated channel and result in the depolarization of the neurons. The signals are then transmitted along axons to glomeruli in the main olfactory bulb. Another olfactory subsystem, the Accessory Olfactory System (AOS), located in the vomeronasal organ (VNO) in the mouse, is believed to sense pheromones and genetically encoded ligands through a separate set of receptors coupled to cAMP-independent IP_3/PLC signaling cascades. Olfactory inputs from this subsystem are transmitted to the accessory olfactory bulb (Firestein, 2001; Munger et al., 2008). The AOS is involved in behaviors linked to gender identification (Stowers et al., 2002), mating, and aggression (Halpern, 1987) in rodents.

The sensed odorants, mediated behaviors, and signal transduction mechanisms are far less known for the Grueneberg Ganglion (GG), a newly appreciated olfactory subsystem located at the rostral tip of

the rodent nose just inside of the nostrils (Fig. 1A,B). The GG olfactory subsystem consists of a clustered collection of neurons lining the dorsal medial nasal vestibule that are separated from the nasal cavity by a keratinized epithelium (Fig. 1C). This epithelium is permeable to externally applied water-soluble dyes (Brechbuhl et al., 2008), suggesting that the GG may have access to external odors. GG neurons are ensheathed by glial-like satellite cells (Fig. 1D) (Brechbuhl et al., 2008; Grüneberg, 1973; Tachibana et al., 1990). Despite its unusual location and morphology, the olfactory nature of the GG was revealed by its lifelong expression of olfactory marker protein (OMP), a protein that is expressed at varying levels in all of the known olfactory subsystems, as well as its direct innervation of a spatially distinct region of the olfactory bulb at the junction of the main and accessory olfactory bulbs (Fleischer et al., 2006a; Fuss et al., 2005; Koos and Fraser, 2005; Roppolo et al., 2006; Storan and Key, 2006). The GG axons form unusual glomeruli interconnected by axons, and thus appear like beads on a string. The GG glomeruli are very similar in location and morphology to the previously characterized necklace glomeruli (Shinoda et al., 1993; Shinoda et al., 1989), which are formed by the axons of the GC-D olfactory subsystem (Hu et al., 2007; Juilfs et al., 1997; Leinders-Zufall et al., 2007). The olfactory necklace glomeruli are marked by acetylcholinesterase activity and are labeled by an antibody raised against human placental antigen (Shinoda et al., 1993; Shinoda et al., 1989). The GG glomeruli appear immunohistochemically distinct from the necklace glomeruli. However, because of their juxtaposition and similar morphology, we term the interconnected "necklace-like" glomeruli formed by the GG the "necklace-like domain."

The GG forms before birth and persists throughout the animal's entire life (Fleischer et al., 2006a; Fuss et al., 2005; Grüneberg, 1973; Koos and Fraser, 2005; Roppolo et al., 2006; Storan and Key, 2006). Although the GG is present in most mammals (Grüneberg, 1973), its relationship to other olfactory subsystems in contributing to the mammalian olfactory sense is not well understood. As a result, the functional relevance of the GG has remained mysterious.

A recent report suggests that the GG is necessary for mediating a panic-like freezing behavior in adult mice in response to alarm pheromone, a water-soluble but unidentified odor released by animals under stress conditions (Brechbuhl et al., 2008). How the adult GG detects these important odorants is

unclear. Small subsets of GG neurons have been reported to express a variety of chemosensory receptors such as odorant receptors, pheromone receptors, and trace amine associated receptors (Fleischer et al., 2006b; Fleischer et al., 2007); however, such expressions are transient, restricted to fetal and perinatal stages of life. The significance of this transient expression remains unclear because the associated signal transduction molecules, such as G_{olf} and transient receptor potential C2 (TRPC2), canonically employed by these receptors appear not to be expressed (Roppolo et al., 2006).

The anatomical similarity of the necklace and necklace-like glomeruli, as well as the molecular differences between the GG, MOS, and AOS, prompted us to test the GG's relationship to the sensory neurons that innervate the necklace domain, the GC-D olfactory subsystem. The sensory cells in this small but specialized olfactory chemosensory subsystem express a membrane-bound guanylate cyclase (pGC-D) and employ a cGMP signal transduction pathway (Fulle et al., 1995; Juilfs et al., 1997; Leinders-Zufall et al., 2007; Meyer et al., 2000). Like the adult GG, they lack the chemosensory receptors and signal transduction molecules employed by the MOS and AOS (Juilfs et al., 1997; Meyer et al., 2000; Walz et al., 2007). In performing this comparison, we find that the GG employs a cGMP signal transduction system somewhat similar to the GC-D olfactory subsystem; however, the neurons of the GG express a different set of membrane-bound guanylate cyclases throughout the life of the animal. We propose that these receptors mediate the chemosensory function of the GG.

MATERIALS AND METHODS

Animals

Mice were maintained as per Caltech IACUC-approved protocol. Genetically modified mice strains used were 1) OMP-GFP (Potter et al., 2001), 2) GCD-iTG (Hu et al., 2007), 3) GCD-iTL (Walz et al., 2007), and 4) PLP-GFP (Fuss et al., 2000). OMP-GFP mice were generated via a knock-out/knock-in procedure in which the OMP coding region was replaced with GFP by homologous recombination at the *OMP* locus. The resulting mouse strain expresses GFP from the endogenous *OMP* promoter (Potter et al., 2001). GCD-iTG and GCD-iTL mice were generated by the targeted insertion of an internal ribosome

entry sequence (IRES) followed by the tau microtubule localization sequence fused to GFP (GCD-iTG) or LacZ (GCD-iTL) downstream of the endogenous pGC-D coding region, in the *Gucy2d* locus. As a result, transcription from the endogenous *Gucy2d* promoter results in a bicistronic mRNA which is translated into the endogenous pGC-D and a microtubule-localized reporter protein (Walz et al., 2007). PLP-GFP (proteolipid protein-GFP) mice were generated by pronuclear injection of a construct containing a modified 2.4 kb upstream promoter, exon 1, and intron 1of PLP and where subsequent exons were replaced with GFP coding sequence (Fuss et al., 2000; Wight et al., 1993). The resulting transgenic mice express endogenous PLP from the unmodified endogenous *PLP* promoter and express GFP from the randomly-inserted, modified, exogenous *PLP* promoter construct (Fuss et al., 2000).

All animals used were postnatal. Immunohistochemical experiments performed in this study to validate these transgenic lines are described in the Results section. Experiments to validate OMP-GFP mice were performed on heterozygous animals that possessed a wild-type allele of OMP.

Immunohistochemistry

Young and adult animals were euthanized with CO_2 and decapitated. Isolated nasal vestibules and other olfactory organs were immersion-fixed in 4% paraformaldehyde in phosphate buffered saline (PBS) overnight at 4˚C. Tissues were decalcified in 13% EDTA overnight. From these preparations, either cryosections (18 μm), thick agarose-embedded sections (100 μm), or whole-mount nasal epithelia were extracted.

Tissue was placed in blocking solution consisting of 0.3% Triton-X in PBS with 4% normal goat or horse serum for >4 h at room temperature. Tissue was incubated with primary antibody (with Triton-X and serum) overnight at 4˚C. For immune-adsorption studies, primary antibody was incubated with a 100-fold molar excess of antigenic blocking peptide before being added to the tissue. The next day, unbound primary antibody was rinsed away with >4 changes of PBS. Secondary antibody was applied for 2 h at room temperature or overnight at 4˚C. After washing, tertiary label (with Triton-X but no serum) was applied to tissue for 2 h at room temperature.

For antibody stainings with diaminobenzidine (DAB) chromogen development, tissue was washed with 0.3% hydrogen peroxide in PBS before the staining process was started. Signal was revealed with a Ni-enhanced DAB kit (Thermo Scientific) with a development time of 5-12 minutes in the dark. DAB-developed tissue was washed in multiple changes of PBS. Tissue was mounted in 80% glycerol, or dehydrated in ascending ethanol/water series, cleared in xylenes, mounted in Krystalon (EMD Chemicals), and coverslipped.

For fluorescently-labeled tissue, the final PBS washes included 0.2 μM Topro-3 (Invitrogen) as a nuclear stain. Tissue was mounted with Gel-Mount (Biomeda) or PBS and coverslipped.

Immunostainings in the GG were repeated on at least 4 entire ganglia with mice at different ages to verify the staining patterns (each mouse has two Grueneberg Ganglia, one per side).

Immunoblots (Western blots)

Freshly dissected tissues from the eyes, nasal vestibules, MOE, kidneys, and intestines of CO_2-euthanized adult mice were separately homogenized using a pestle in RIPA buffer (150 mM NaCl, 1% Triton-X, 0.5% sodium deoxycholate, 0.1% SDS, 50 mM Tris, pH 8.0) with an EDTA-free protease inhibitor cocktail (Roche). After 2 h of mixing at 4˚C, samples were spun at 12,000 *g*. The supernatant was reserved for immunoblots.

For Tris-glycine SDS-PAGE, protein samples were boiled in Laemmli loading buffer (60 mM Tris, 2% SDS, 10% glycerol, 5% β-mercaptoethanol, 0.01% bromophenol blue, pH 6.8) for 5 minutes before loading into the wells of a discontinuous acrylamide gel system with an 8% resolving gel. MagicMark XP protein standard (Invitrogen) was used as a ladder. Separated proteins were transferred to Amersham Hybond N+ nylon membranes (GE Healthcare) overnight at 22V at 4˚C in transfer buffer (39 mM glycine, 48 mM Tris, 0.037% SDS, 20% methanol).

Membranes were blocked in 5% nonfat dry milk in TBST (125 mM NaCl, 25 mM Tris, 0.1% Tween-20, pH 8.0) and incubated overnight at 4˚C with primary antibodies. After extensive washes in TBST, membranes were incubated for 2 h at room temperature with a horseradish peroxidase-conjugated

goat anti-rabbit secondary antibody (Jackson Immunoresearch) at 1:5,000 dilution. Bound antibodies were detected with the Amersham ECL+ enhanced chemiluminescence system (GE Healthcare). Chemiluminescent signal was captured onto X-ray film (Kodak).

Predicted molecular weights were obtained computationally from the protein sequence using the ProtParam program on the Swiss ExPASy Proteomics Server (au.expasy.org). Unless otherwise noted, chemicals were obtained from Sigma.

Antibodies

Primary antibodies used are described in Table 1. For primary antibodies raised in a rabbit, the secondary antibody was biotinylated anti-rabbit IgG, raised in goat (Vector Labs), diluted in saline with normal goat serum at 3 µg/mL working concentration for thin sections, or 0.75 µg/mL working concentration for thick sections or whole mounts. For primary antibodies raised in a goat, the secondary antibody was biotinylated anti-goat IgG, raised in horse (Vector Labs), diluted in saline with normal horse serum at the same concentration used for the anti-rabbit secondary. For fluorescent labeling, tertiary label was streptavidin-conjugated Alexa 555 dye (Invitrogen) at 2 µg/mL working concentration. For DAB-labeling, tertiary label was streptavidin-conjulated horseradish peroxidase (MP Biomedical) at 1:500 working dilution.

The goat anti-OMP antibody used in this study has been validated previously for use on immunoblots and immunohistochemical experiments. Immunoblots of HeLa cells transiently transfected with rat OMP detected a 19 kDa protein corresponding to the molecular weight of OMP and a 38 kDa band that likely represents an OMP homodimer (Koo et al., 2004). In immunostainings performed in mice, this antibody labeled glomeruli in the olfactory bulb and olfactory sensory neurons in the MOE (Cummings et al., 2000). The rabbit anti-GFAP (glial fibrillary acidic protein) antibody used in this study has been used previously in an immunohistochemical study to identify astrocytes in the developing mouse brain (Henion et al., 2003). On immunoblots with rat cerebellum homogenate, this antibody recognized a 50 kDa band corresponding to rodent GFAP and a 45 kDa GFAP-related band (manufacturer's datasheet).

The rabbit anti-PLP (proteolipid protein) antibody has been shown in previous immunohistochemical studies to label specifically myelinated nerve fibers in the mouse (Papastefanaki et al., 2007). The rabbit anti-CNGA3 antibody has been shown previously to recognize a 76 kDa protein corresponding to mouse CNGA3 on immunoblots with mouse retinal homogenate. In immunohistochemical applications, it recognized the anticipated segments on cone photoreceptor neurons. Pre-incubation of the antibody with its antigenic blocking peptide abolished staining on the immunoblots and in the immunofluorescence experiments (Matveev et al., 2008).

Previously unvalidated antibodies were validated in several ways. First, an immunoblot was performed with a lysate of tissue that is known to express the protein of interest. Second, the antibody's suitability for immunohistochemistry was evaluated by fluorescence immunostaining on thin sections of mouse positive control tissue. Third, if the antibody was found to label GG neurons, immunoadsorption studies were performed with an antigenic blocking peptide, when available. Validation experiments performed in this study are described in the Results section.

X-gal histochemistry

The development of X-gal blue precipitate in pGC-D-expressing tissues was performed as previously described (Walz et al., 2007).

Transmission electron microscopy

Mice were anesthetized with Avertin (2-2-2-tribromoethanol, Sigma) and transcardially perfused with fixative (4% paraformaldehyde, 1.25% glutaraldehyde (Ted Pella), in 0.06M phosphate buffer, pH 7.4, 37˚C). Isolated nares were trimmed of excess tissue and post-fixed (4% paraformaldehyde, 1.25% glutaraldehyde, in 0.1M NaCacodylate, pH 7.4, 4˚C). Tissue was stained for 1 h at 4˚C with 2% OsO_4 in veronal acetate + 5% sucrose, washed with 0.1M maleate buffer (pH 5), and incubated for 1 h at room temperature in 1% uranyl acetate prepared in maleate buffer. After dehydration through a graded ethanol series, tissue was embedded in ascending propylene oxide/Epon resin (Fluka) solutions until 100% Epon

resin and solidified at 60˚C. 120 nm semi-serial sections were floated onto formvar-coated copper EM grids (Ted Pella) and allowed to dry; they were then stained with uranyl acetate and lead citrate, rinsed with water, and allowed to dry completely prior to EM imaging.

Optical imaging

Samples were imaged on various Zeiss microscopes depending on the type of staining and the required resolution. Fluorescence imaging was performed on a Zeiss LSM510 upright confocal microscope system. High-magnification (40×, 1.3NA and 63×, 1.25NA oil objectives) fluorescent images were generated from z-projections of approximately 1 µm optical sections by reducing the pinhole size to 1 Airy unit. The pinhole size could be increased to optimize signal-to-noise for weaker signals. Lower-magnification (20×, 0.5NA objective) fluorescence images were assembled from approximately 6 µm optical sections. Multiphoton imaging of PLP-GFP transgenic mice (Fig. 1D) was performed on freshly isolated naris tissue using a 40× water immersion objective and a home-built multiphoton system (Potter et al., 1996). Brightfield images were obtained on a Zeiss Axiophot compound microscope.

Uniform adjustments to image brightness/contrast and noise reduction with a median filter were performed with ImageJ (National Institutes of Health, USA) and Paint Shop Pro (Corel). When comparisons were made between the GG and the MOE, the channel of comparison was imaged with the same power and gain, and subsequent brightness and contrast enhancements were made to the same level in both organs.

RESULTS

Components of the cGMP signaling pathway are expressed in the GG

Phosphodiesterases degrade cyclic nucleotides that are essential second messengers involved in neuronal activation in most olfactory subsystems. To examine phosphodiesterase expression in the GG and other mouse olfactory subsystems, we used a strain of mice (OMP-GFP) to help visualize these

olfactory subsystems in their anatomical locations. In OMP-GFP mice, the primary olfactory sensory neurons of all olfactory subsystems are highlighted by the expression GFP (Potter et al., 2001). Immunostaining these transgenic mice with an OMP-specific antibody revealed that all GFP-expressing neurons were strongly labeled by the antibody (Fig. 1E,F). Antibody labeling was observed in the GFP-positive glomerular layer of the olfactory bulb (Fig. 1G), but labeling was not found in GFP-negative cells in the nasal vestibule, MOE, or olfactory bulb (n = 4 mice). These results show that the OMP-GFP mouse strain faithfully reveals the location of the primary sensory neurons of the mouse olfactory subsystems.

The neurons of the GG do not express the cAMP-specific phosphodiesterase (PDE4A) that is found in the olfactory sensory neurons (OSNs) of the MOS. In neonatal mice, an antibody to the cAMP-selective PDE4A specifically labeled the highly OMP-expressing neurons in the MOE (n = 4; Fig. 2A), consistent with previous reports (Juilfs et al., 1997). In contrast, all OMP-expressing GG neurons were negative for PDE4A (n = 4 ganglia from the same mice as Fig. 2A; Fig. 2B), suggesting that the cAMP signaling pathway commonly used in OSNs is not employed by the GG neurons. On immunoblots with MOE lysate, this antibody recognized five bands between 60 and 100 kDa that likely represent splice variants of PDE4A (Bolger et al., 1996; Rena et al., 2001; Shakur et al., 1995).

In contrast, we find the expression in the GG of the cGMP-stimulated phosphodiesterase 2a (PDE2A) isoform (Bender and Beavo, 2006), which implicates cGMP as the predominant second messenger molecule in this olfactory subsystem, similar to the neurons of the GC-D olfactory subsystem (Juilfs et al., 1997). In the MOE, a PDE2A antibody labeled only a small subset of weakly OMP-expressing neurons in the caudal neuroepitheliary layers (Fig. 2C), corresponding to the GC-D neurons (Ring et al., 1997). The recognized protein was ~100 kDa on immunoblots, close to the predicted 105 kDa size for mouse PDE2A. In the nasal vestibule, OMP-expressing GG neurons were intensely positive for PDE2A from birth to adult-aged mice (Fig. 2D). Vascular endothelial cells were also labeled by the antibody (Sadhu et al., 1999). Pre-incubation of PDE2A antibody with its antigenic peptide, or omission of the primary antibody, abolished the staining (Fig. 2E,F).

cGMP-Dependent Kinases. Downstream signaling effects of cGMP are mediated by cGMP-dependent kinases, which exist in three isoforms, the splice-variants cGKIα and cGKIβ, and cGKII (Feil et al., 2003). A cGKII antibody labeled OMP-expressing GG neurons in the nasal vestibules of adult OMP-GFP mice (Fig. 3A). The labeling appeared to be concentrated on the membranes of GG neurons, consistent with previous descriptions of cGKII localization (Feil et al., 2003). This antibody was validated by its labeling of the brush borders of mouse intestinal villi (Fig. 3B), in accord with previous reports of cGKII protein expression (Golin-Bisello et al., 2005; Jarchau et al., 1994; Markert et al., 1995). On immunoblots with mouse intestinal lysate, this antibody recognized a ~80 kDa protein consistent with the 86 kDa cGKII protein and a ~70 kDa band that may correspond to a previously-observed 72 kDa degradation product of cGKII (El-Husseini et al., 1998; French et al., 1995). Collectively, these results suggest that the cGKII antibody faithfully labels cGKII-expressing cells and that cGKII mediates downstream signaling effects of cGMP production in the GG olfactory subsystem.

Cyclic Nucleotide Gated Channels. In order to further investigate the molecular nature of the GG neurons we explored the expression of cyclic nucleotide gated (CNG) channels that can mediate neuronal depolarization. In the neurons of the MOS, the tetrameric CNG channel composed of two CNGA2, one CNGA4, and one CNGB1b subunits depolarizes the neuron during elevation of cGMP or cAMP levels (Biel and Michalakis, 2007; Frings et al., 1992). Previous work has shown that these channel subunits are not expressed in the GG (Roppolo et al., 2006).

An antibody specific to mouse CNGA3 (Matveev et al., 2008) revealed that the neurons of the GG express CNGA3. The antibody was validated in thin sections from the mouse retina, revealing staining in cone photoreceptors (Fig. 3C), consistent with CNGA3's known role in cGMP-dependent phototransduction as a heterotetramer with CNGB3 (Kohl et al., 1998; Tanaka et al., 1989). In the nasal vestibules of OMP-GFP mice, the antibody specific to CNGA3 labeled unusual whip-like subcellular domains on the somata of OMP-expressing GG neurons (Fig. 3D). Interestingly, the same CNGA3 subunit is expressed on the ciliary receptive domains of the GC-D neurons (Leinders-Zufall et al., 2007; Meyer et al., 2000). GC-D neurons visualized in a *Gucy2d* targeted GFP transgenic mouse line, GCD-iTG

(Hu et al., 2007; Walz et al., 2007), exhibited CNGA3 antibody labeling in their dendritic knobs (Fig. 3E). Thus, CNGA3 is expressed by the neurons of the olfactory subsystems that innervate the necklace and necklace-like domains.

Particulate guanylate cyclase expression in the GG

In the GC-D olfactory subsystem, a particulate guanylate cyclase isoform (pGC-D) is thought to serve as the chemosensor, producing cGMP in response to urinary derivates (guanylin and uroguanylin) (Leinders-Zufall et al., 2007). The sensory neurons of the GC-D olfactory subsystem can be recognized in the neonatal mouse MOE by their staining with a PDE2A antibody; these same neurons were GFP-positive in the GCD-iTG mice (Fig. 4A), verifying the fidelity of GCD-iTG mice in revealing the neurons employing pGC-D. The similar innervation targets of the GG and the GC-D olfactory subsystems motivated us to search for particulate guanylate cyclase isoforms expressed in the GG that could mediate the GG's chemosensory function.

In contrast to the GC-D olfactory subsystem, GG sensory neurons (recognized with the PDE2A antibody) were not GFP-positive in GCD-iTG neonatal mice. Four ganglia were examined in their entirety, and none of the PDE2A-labeled GG neurons exhibited detectable GFP fluorescence (Fig. 4B). Identical results were obtained in adult (6 weeks old) GCD-iTG mice (n = 6 ganglia) and in a separate *Gucy2d*-targeted, LacZ-expressing transgenic mouse strain (GCD-iTL, n = 4 ganglia). Thus, the GG does not express the pGC-D receptor protein, in contrast to the neurons of the GC-D olfactory subsystem.

In addition to pGC-D, there are six known pGC isoforms in the mouse (A, B, C, E, F, G), each with distinct expression patterns throughout the body, but not yet explored in the olfactory pathway (Kuhn, 2003). A panel of affinity-purified pGC antibodies was used to survey the expression of these other mouse pGCs in the GG. The antibodies to pGC-A, B, C, E, and F were found suitable for use in immunohistochemistry because they labeled the expected cellular structures in the kidney, vasculature, intestine, and eye (pGC-E and pGC-F), respectively, in fluorescent immunostainings (Supporting Fig. 1). Immunoblots performed on the respective tissue lysates confirmed that these antibodies could detect the

proteins of appropriate molecular weights (Table 2). *A priori* control experiments with the pGC-G antibody were not possible because the tissue distribution pattern of this protein in rodents is not fully understood.

Of the six pGC isoforms tested, only antisera directed against pGC-G (Fig. 5A) and pGC-A (Fig. 5B) labeled neurons of the GG. The labeling was entirely absent when these antibodies were pre-incubated with their respective antigenic peptides (Fig. 5C-F). pGC-A is a natriuretic peptide receptor used in a variety of organ systems as a regulator of vascular tone and water retention (Kuhn, 2003). pGC-G is an orphan guanylate cyclase with unknown functions (Kuhn et al., 2004; Schulz et al., 1998). The two isoforms differed in their expression patterns: pGC-G was detected on most GG neurons (Fig. 5A) at both neonatal and adult ages (Fig. 5G,H); in contrast, pGC-A was detected in only a small subset of GG neurons scattered throughout the GG organ (Fig. 5B). In immunoblotting experiments with nasal vestibule lysate, the pGC-G antibody recognized a single ~120 kDa band, consistent with the predicted size of 123 kDa for mouse pGC-G (Fig. 5M). pGC-G expression was absent from the GC-D neurons (n = 5 mice; Fig. 5I,J).

pGC-G is localized to GG cilia

Intriguingly, pGC-G expression was restricted to unusual subcellular domains on the somata of GG neurons, very similar to the pattern of the CNGA3 staining. Thin sections imaged at high magnification revealed that the pGC-G-immunoreactive region appeared as thin fibers on the peripheries of the GG somata, with no observable directional preference. These fibers followed the contours of GG cells in a “whip-like” fashion (Fig. 5K,L). In some cases, the fibers extended from one GG neuron to touch a neighboring GG neuron. However, none of these whip-like fibers protruded from a GG neuron into the nasal cavity (n = 16 ganglia).

Immunoreactivity for pGC-G protein was not detected on the tight-fitting glial cells that ensheath the GG neurons. These ensheathing glia could be visualized in the PLP-GFP mouse line (Fuss et al., 2000), in which the proteolipid protein (PLP) promoter drives the expression of GFP. The ensheathing

glia were not labeled by an antibody raised against PLP protein; this is not surprising given that multiple protein products can be derived from PLP promoter activity (Macklin et al., 1987; Nave et al., 1987). The GFP-expressing cells in PLP-GFP mice were colabeled by an antibody to glial fibrillary acidic protein (Fig. 6A), which has been previously shown to mark the ensheathing glia of GG olfactory subsystem (Brechbuhl et al., 2008). In the PLP-GFP transgenic, GFP-positive glial cells and their processes can be seen to wrap the clusters of GG neurons (Fig. 6B), including the intensely pGC-G stained structures at the periphery of the GG somata (Fig. 6C).

Electron Microscopy. To identify the GG subcellular domains that are decorated with pGC-G, we performed an ultrastructural analysis of the ganglion using transmission electron microscopy. In semi-serial thin sections of the adult nasal vestibule, each GG neuron was observed to be decorated by a plurum of cilia whose ultrastructural morphologies are consistent with the pGC-G-labeled subcellular domains seen with light microscopy. These cilia are seen erupting out from clusters of basal bodies deep within the cell soma (Fig. 7A,B). The cilia are grouped (Fig. 7C,D) and appear as long bundles that follow the contour of the cell in a variety of orientations (Fig. 7E,F). The encasement of GG neurons by the ensheathing cells was tight enough that the ciliary bundles were observed to be partially indented into the membranes of the GG cells. Ciliary bundles were not observed to protrude through this ensheathing cell layer, nor were ganglionic processes found to project into the nasal cavity.

DISCUSSION

Particulate guanylate cyclase expression in the GG

Two different receptor guanylate cyclases (pGC-G and pGC-A), a cGMP-stimulated phosphodiesterase (PDE2A), a cGMP-dependent kinase (cGKII), and a cGMP-activated channel containing CNGA3 subunits are expressed in the GG. Together, these components, from receptor to effector, reveal a cGMP signal transduction pathway that can mediate GG chemoreception (Fig. 8). The expression of pGC-G on most neurons of the GG and its exclusion from many other tissues in the mouse (Kuhn et al., 2004) suggests that pGC-G is responsible for mediating a GG-specific chemosensory

function. Assuming that they serve as the sole receptors, the ligands for pGC-A and pGC-G dictate the range of molecules that are detected by the GG. These ligands may include natriuretic peptides or the, at-present, chemically undefined mammalian alarm pheromone. Binding of the cognate ligands to pGC-A/G triggers the production of cGMP, subsequently inducing CNGA3 channels to depolarize the GG neuron and activating cGKII kinase activity. PDE2A degrades the cyclic nucleotides, thereby resetting the system to the un-activated state.

It is possible that direct binding of ligands to pGC-G and pGC-A is not the only means of GG chemosensory transduction. There may be unidentified chemoreceptors that act in parallel or upstream of the particulate guanylate cyclases. For example, in the eye, light absorbed by photopigments results in the hydrolysis of cGMP by Pde proteins and subsequent closure of cyclic nucleotide gated channels (Bender and Beavo, 2006; Biel and Michalakis, 2007). Calcium-inhibited particulate guanylate cyclases work downstream to restore the original cGMP levels and thereby to end the hyperpolarizing signal (Sokal et al., 2003). Thus, the guanylate cyclases play a crucial role in the visual system, but they are not directly responsible for the retinal sensitivity to light. While there is ample evidence that pGC-D is the first step in chemosensory transduction in the GC-D olfactory subsystem, recent experiments have suggested a role for adjunctive proteins. Individual neurons of the GC-D olfactory subsystem differ in their responses to the pGC-D ligands uroguanylin and guanylin (Duda and Sharma, 2008; Leinders-Zufall et al., 2007). Moreover, the detection of carbon dioxide (CO_2) by this olfactory subsystem requires a carbonic anhydrase to convert CO_2 into the pGC-D-activating bicarbonate form (Sun et al., 2009). Further biochemical studies on pGC-G will help uncover its exact role in the GG olfactory subsystem.

The localization of pGC-G and pGC-A to GG neuronal cilia suggests a critical contribution of these receptor guanylate cyclases to the chemosensory function of the GG olfactory subsystem. Ciliary localization of chemosensory receptors and signal transduction components is a common feature of the olfactory subsystems. For example, odorant receptors, pheromone receptors, and signaling elements such as adenylyl cyclase, G protein, and cyclic nucleotide gated channels are preferentially localized to cilia in

the MOS or microvilli in the AOS (Firestein, 2001). Similarly, pGC-D is localized to the cilia of neurons in the GC-D olfactory subsystem (Juilfs et al., 1997).

The far-forward location of the GG, just inside of the nostrils, appears to place the GG in prime position to be the first olfactory subsystem to interrogate inhaled molecules. However, in contrast to the receptive ciliary structures of other olfactory subsystems, the GG cilia do not protrude into the nasal cavity. The ultrastructural results of this study generally agree with previous electron microscopic studies on the GG in the mouse (Brechbuhl et al., 2008) and the musk shrew (Tachibana et al., 1990). However, in our studies, no GG cilia were found to escape entrapment by the ensheathing cell population and project into the extra-ganglionic matrix, in contrast to previous reports (Brechbuhl et al., 2008). These results suggest that potential GG ligands must be able to penetrate rapidly both the keratinized epithelium and the ensheathing cell layer to access the cilia. Small gaseous or lipid-soluble molecules are thus candidates for detection by the GG. While GG cilia are decorated with chemoreceptors, their subsurface location suggests that they are not optimally positioned for direct sampling of odorants drawn in the airspace of the nasal cavity. The logic for this unusual subsurface arrangement of GG receptive structures is unclear and should be a continued topic of study.

Classification of the GG olfactory subsystem

The GG should be classified as a noncanonical olfactory subsystem because it employs a cGMP signaling pathway, distinct from the MOS. The far-rostral location, unusual morphology, and unique receptor repertoire of the GG suggest that this olfactory subsystem senses a unique set of odors. The GG shares some signal transduction components with the GC-D olfactory subsystem; however, the GG might be activated differently during various odor sampling modalities such as sniffing (Verhagen et al., 2007), normal smelling, and retronasal flow due to its position and ensheathment.

The similarities in the signal transduction pathways used by the GG and the GC-D neurons extend to their innervation of the necklace and necklace-like domains, suggesting that they form a unique pathway of olfactory information processing. Both the necklace and the necklace-like domains form

distinct sets of interconnected glomeruli (“separate necklaces”) at the junction of the main and accessory olfactory bulbs. While the exact effects of chemosensory processing in this domain on animal behavior are not known, its unique position, morphology, and signaling repertoire suggest that it effects atypical functions. This is reinforced in recent studies in which a surgical ablation of the GG abolished the animal’s freezing response to the presence of alarm pheromone (Brechbuhl et al., 2008). While the functions of the MOS and the AOS have been explored by genetic ablations (Baker et al., 1999; Stowers et al., 2002; Trinh and Storm, 2003), these ablations should not have affected the GG or GC-D olfactory subsystems. Thus, behaviors that remain intact in these knock-out strains may be transduced by the GG and/or GC-D olfactory subsystems. Genetic ablations targeting cGMP signaling components downstream of the particulate guanylate cyclases might serve as experimental animal models to elucidate functions mediated by this domain of interconnected glomeruli.

ACKNOWLEDGMENTS

We wish to thank P. Mombaerts and W.B. Macklin for generously providing us with genetically-modified mouse strains, X.-Q. Ding for kindly donating antibodies, L.A. Trinh and J. Edens for technical assistance, and J.M. Allman for suggestions on the manuscript. This work was supported by the National Institutes of Health (USA), grant RPN2-EY018241

REFERENCES

Baker H, Cummings DM, Munger SD, Margolis JW, Franzen L, Reed RR, Margolis FL. 1999. Targeted deletion of a cyclic nucleotide-gated channel subunit (OCNC1): biochemical and morphological consequences in adult mice. J Neurosci 19(21):9313-9321.

Bender AT, Beavo JA. 2006. Cyclic nucleotide phosphodiesterases: molecular regulation to clinical use. Pharmacol Rev 58(3):488-520.

Biel M, Michalakis S. 2007. Function and dysfunction of CNG channels: insights from channelopathies and mouse models. Mol Neurobiol 35(3):266-277.

Bolger GB, McPhee I, Houslay MD. 1996. Alternative splicing of cAMP-specific phosphodiesterase mRNA transcripts. Characterization of a novel tissue-specific isoform, RNPDE4A8. J Biol Chem 271(2):1065-1071.

Brechbuhl J, Klaey M, Broillet MC. 2008. Grueneberg ganglion cells mediate alarm pheromone detection in mice. Science 321(5892):1092-1095.

Breer H, Fleischer J, Strotmann J. 2006. The sense of smell: multiple olfactory subsystems. Cell Mol Life Sci 63(13):1465-1475.

Cummings DM, Emge DK, Small SL, Margolis FL. 2000. Pattern of olfactory bulb innervation returns after recovery from reversible peripheral deafferentation. J Comp Neurol 421(3):362-373.

Duda T, Sharma RK. 2008. ONE-GC membrane guanylate cyclase, a trimodal odorant signal transducer. Biochem Biophys Res Commun 367(2):440-445.

El-Husseini AE, Bladen C, Williams JA, Reiner PB, Vincent SR. 1998. Nitric oxide regulates cyclic GMP-dependent protein kinase phosphorylation in rat brain. J Neurochem 71(2):676-683.

Feil R, Lohmann SM, de Jonge H, Walter U, Hofmann F. 2003. Cyclic GMP-dependent protein kinases and the cardiovascular system: insights from genetically modified mice. Circ Res 93(10):907-916.

Firestein S. 2001. How the olfactory system makes sense of scents. Nature 413(6852):211-218.

Fleischer J, Hass N, Schwarzenbacher K, Besser S, Breer H. 2006a. A novel population of neuronal cells expressing the olfactory marker protein (OMP) in the anterior/dorsal region of the nasal cavity. Histochem Cell Biol 125(4):337-349.

Fleischer J, Schwarzenbacher K, Besser S, Hass N, Breer H. 2006b. Olfactory receptors and signalling elements in the Grueneberg ganglion. J Neurochem 98(2):543-554.

Fleischer J, Schwarzenbacher K, Breer H. 2007. Expression of trace amine-associated receptors in the Grueneberg ganglion. Chem Senses 32(6):623-631.

French PJ, Bijman J, Edixhoven M, Vaandrager AB, Scholte BJ, Lohmann SM, Nairn AC, de Jonge HR. 1995. Isotype-specific activation of cystic fibrosis transmembrane conductance regulator-chloride channels by cGMP-dependent protein kinase II. J Biol Chem 270(44):26626-26631.

Frings S, Lynch JW, Lindemann B. 1992. Properties of cyclic nucleotide-gated channels mediating olfactory transduction. Activation, selectivity, and blockage. J Gen Physiol 100(1):45-67.

Fulle HJ, Vassar R, Foster DC, Yang RB, Axel R, Garbers DL. 1995. A receptor guanylyl cyclase expressed specifically in olfactory sensory neurons. Proc Natl Acad Sci U S A 92(8):3571-3575.

Fuss B, Mallon B, Phan T, Ohlemeyer C, Kirchhoff F, Nishiyama A, Macklin WB. 2000. Purification and analysis of in vivo-differentiated oligodendrocytes expressing the green fluorescent protein. Dev Biol 218(2):259-274.

Fuss SH, Omura M, Mombaerts P. 2005. The Grueneberg ganglion of the mouse projects axons to glomeruli in the olfactory bulb. Eur J Neurosci 22(10):2649-2654.

Golin-Bisello F, Bradbury N, Ameen N. 2005. STa and cGMP stimulate CFTR translocation to the surface of villus enterocytes in rat jejunum and is regulated by protein kinase G. Am J Physiol Cell Physiol 289(3):C708-716.

Grüneberg H. 1973. A ganglion probably belonging to the N. terminalis system in the nasal mucosa of the mouse. Z Anat Entwicklungsgesch 140(1):39-52.

Halpern M. 1987. The organization and function of the vomeronasal system. Annu Rev Neurosci 10:325-362.

Henion TR, Qu Q, Smith FI. 2003. Expression of dystroglycan, fukutin and POMGnT1 during mouse cerebellar development. Brain Res Mol Brain Res 112(1-2):177-181.

Hu J, Zhong C, Ding C, Chi Q, Walz A, Mombaerts P, Matsunami H, Luo M. 2007. Detection of near-atmospheric concentrations of CO2 by an olfactory subsystem in the mouse. Science 317(5840):953-957.

Jarchau T, Hausler C, Markert T, Pohler D, Vanderkerckhove J, De Jonge HR, Lohmann SM, Walter U. 1994. Cloning, expression, and in situ localization of rat intestinal cGMP-dependent protein kinase II. Proc Natl Acad Sci U S A 91(20):9426-9430.

Juilfs DM, Fulle HJ, Zhao AZ, Houslay MD, Garbers DL, Beavo JA. 1997. A subset of olfactory neurons that selectively express cGMP-stimulated phosphodiesterase (PDE2) and guanylyl cyclase-D define a unique olfactory signal transduction pathway. Proc Natl Acad Sci U S A 94(7):3388-3395.

Kohl S, Marx T, Giddings I, Jagle H, Jacobson SG, Apfelstedt-Sylla E, Zrenner E, Sharpe LT, Wissinger B. 1998. Total colourblindness is caused by mutations in the gene encoding the alpha-subunit of the cone photoreceptor cGMP-gated cation channel. Nat Genet 19(3):257-259.

Koo JH, Gill S, Pannell LK, Menco BP, Margolis JW, Margolis FL. 2004. The interaction of Bex and OMP reveals a dimer of OMP with a short half-life. J Neurochem 90(1):102-116.

Koos DS, Fraser SE. 2005. The Grueneberg ganglion projects to the olfactory bulb. Neuroreport 16(17):1929-1932.

Kuhn M. 2003. Structure, regulation, and function of mammalian membrane guanylyl cyclase receptors, with a focus on guanylyl cyclase-A. Circ Res 93(8):700-709.

Kuhn M, Ng CK, Su YH, Kilic A, Mitko D, Bien-Ly N, Komuves LG, Yang RB. 2004. Identification of an orphan guanylate cyclase receptor selectively expressed in mouse testis. Biochem J 379(Pt 2):385-393.

Leinders-Zufall T, Cockerham RE, Michalakis S, Biel M, Garbers DL, Reed RR, Zufall F, Munger SD. 2007. Contribution of the receptor guanylyl cyclase GC-D to chemosensory function in the olfactory epithelium. Proc Natl Acad Sci U S A 104(36):14507-14512.

Macklin WB, Campagnoni CW, Deininger PL, Gardinier MV. 1987. Structure and expression of the mouse myelin proteolipid protein gene. J Neurosci Res 18(3):383-394.

Markert T, Vaandrager AB, Gambaryan S, Pohler D, Hausler C, Walter U, De Jonge HR, Jarchau T, Lohmann SM. 1995. Endogenous expression of type II cGMP-dependent protein kinase mRNA and protein in rat intestine. Implications for cystic fibrosis transmembrane conductance regulator. J Clin Invest 96(2):822-830.

Matveev AV, Quiambao AB, Browning Fitzgerald J, Ding XQ. 2008. Native cone photoreceptor cyclic nucleotide-gated channel is a heterotetrameric complex comprising both CNGA3 and CNGB3: a study using the cone-dominant retina of Nrl-/- mice. J Neurochem 106(5):2042-2055.

Meyer MR, Angele A, Kremmer E, Kaupp UB, Muller F. 2000. A cGMP-signaling pathway in a subset of olfactory sensory neurons. Proc Natl Acad Sci U S A 97(19):10595-10600.

Munger SD, Leinders-Zufall T, Zufall F. 2008. Subsystem Organization of the Mammalian Sense of Smell. Annu Rev Physiol.

Nave KA, Lai C, Bloom FE, Milner RJ. 1987. Splice site selection in the proteolipid protein (PLP) gene transcript and primary structure of the DM-20 protein of central nervous system myelin. Proc Natl Acad Sci U S A 84(16):5665-5669.

Papastefanaki F, Chen J, Lavdas AA, Thomaidou D, Schachner M, Matsas R. 2007. Grafts of Schwann cells engineered to express PSA-NCAM promote functional recovery after spinal cord injury. Brain 130(Pt 8):2159-2174.

Potter SM, Wang CM, Garrity PA, Fraser SE. 1996. Intravital imaging of green fluorescent protein using two-photon laser-scanning microscopy. Gene 173(1 Spec No):25-31.

Potter SM, Zheng C, Koos DS, Feinstein P, Fraser SE, Mombaerts P. 2001. Structure and emergence of specific olfactory glomeruli in the mouse. J Neurosci 21(24):9713-9723.

Rena G, Begg F, Ross A, MacKenzie C, McPhee I, Campbell L, Huston E, Sullivan M, Houslay MD. 2001. Molecular cloning, genomic positioning, promoter identification, and characterization of the novel cyclic amp-specific phosphodiesterase PDE4A10. Mol Pharmacol 59(5):996-1011.

Ring G, Mezza RC, Schwob JE. 1997. Immunohistochemical identification of discrete subsets of rat olfactory neurons and the glomeruli that they innervate. J Comp Neurol 388(3):415-434.

Roppolo D, Ribaud V, Jungo VP, Luscher C, Rodriguez I. 2006. Projection of the Gruneberg ganglion to the mouse olfactory bulb. Eur J Neurosci 23(11):2887-2894.

Sadhu K, Hensley K, Florio VA, Wolda SL. 1999. Differential expression of the cyclic GMP-stimulated phosphodiesterase PDE2A in human venous and capillary endothelial cells. J Histochem Cytochem 47(7):895-906.

Scheving LA, Russell WE. 1996. Guanylyl cyclase C is up-regulated by nonparenchymal cells and hepatocytes in regenerating rat liver. Cancer Res 56(22):5186-5191.

Scheving LA, Russell WE, Chong KM. 1996. Structure, glycosylation, and localization of rat intestinal guanylyl cyclase C: modulation by fasting. Am J Physiol 271(6 Pt 1):G959-968.

Schulz S, Wedel BJ, Matthews A, Garbers DL. 1998. The cloning and expression of a new guanylyl cyclase orphan receptor. J Biol Chem 273(2):1032-1037.

Shakur Y, Wilson M, Pooley L, Lobban M, Griffiths SL, Campbell AM, Beattie J, Daly C, Houslay MD. 1995. Identification and characterization of the type-IVA cyclic AMP-specific phosphodiesterase RD1 as a membrane-bound protein expressed in cerebellum. Biochem J 306 (Pt 3):801-809.

Shinoda K, Ohtsuki T, Nagano M, Okumura T. 1993. A possible functional necklace formed by placental antigen X-P2-immunoreactive and intensely acetylcholinesterase-reactive (PAX/IAE) glomerular complexes in the rat olfactory bulb. Brain Res 618(1):160-166.

Shinoda K, Shiotani Y, Osawa Y. 1989. "Necklace olfactory glomeruli" form unique components of the rat primary olfactory system. J Comp Neurol 284(3):362-373.

Sokal I, Alekseev A, Palczewski K. 2003. Photoreceptor guanylate cyclase variants: cGMP production under control. Acta Biochim Pol 50(4):1075-1095.

Storan MJ, Key B. 2006. Septal organ of Gruneberg is part of the olfactory system. J Comp Neurol 494(5):834-844.

Stowers L, Holy TE, Meister M, Dulac C, Koentges G. 2002. Loss of sex discrimination and male-male aggression in mice deficient for TRP2. Science 295(5559):1493-1500.

Sun L, Wang H, Hu J, Han J, Matsunami H, Luo M. 2009. Guanylyl cyclase-D in the olfactory CO2 neurons is activated by bicarbonate. Proc Natl Acad Sci U S A 106(6):2041-2046.

Tachibana T, Fujiwara N, Nawa T. 1990. The ultrastructure of the ganglionated nerve plexus in the nasal vestibular mucosa of the musk shrew (Suncus murinus, insectivora). Arch Histol Cytol 53(2):147-156.

Tanaka JC, Eccleston JF, Furman RE. 1989. Photoreceptor channel activation by nucleotide derivatives. Biochemistry 28(7):2776-2784.

Trinh K, Storm DR. 2003. Vomeronasal organ detects odorants in absence of signaling through main olfactory epithelium. Nat Neurosci 6(5):519-525.

Verhagen JV, Wesson DW, Netoff TI, White JA, Wachowiak M. 2007. Sniffing controls an adaptive filter of sensory input to the olfactory bulb. Nat Neurosci 10(5):631-639.

Walz A, Feinstein P, Khan M, Mombaerts P. 2007. Axonal wiring of guanylate cyclase-D-expressing olfactory neurons is dependent on neuropilin 2 and semaphorin 3F. Development 134(22):4063-4072.

Wight PA, Duchala CS, Readhead C, Macklin WB. 1993. A myelin proteolipid protein-LacZ fusion protein is developmentally regulated and targeted to the myelin membrane in transgenic mice. J Cell Biol 123(2):443-454.

TABLES

Table 1: Antibodies used in this study

Antibody	Vendor	Dilution	Immunizing Sequence	Mouse Homology
Goat anti-OMP (whole antiserum)	Wako #54-1000	1:13,000	Rat OMP (NP_036748) 1-163	163/163 (100%)
Rabbit anti-Pde2a (affinity-purified)	Fabgennix #PD2A-101AP	1:1,000	Rat Pde2a (NP_001137319) 904-921 SNNSLDFLDEEYEVPDLD	18/18 (100%)
Rabbit anti-Pde4a (affinity-purified)	Fabgennix #PD4-112AP	1:250	Rat Pde4a (NP_037233) 831-844 ISAPGRWGSGGDPA	14/14 (100%)
Rabbit anti-cGKII (whole antiserum)	Santa Cruz Biotechnology # sc-25430	1:200	Human cGKII (NP_006250) 1-120	108/120 (90%)
Rabbit anti-CNGA3 (whole antiserum)	Kindly provided by X.-Q. Ding	1:750	Mouse CNGA3 (NP_034048) 77-97 SNAQPNPGEQKPPDGGEGRKE	21/21 (100%)
Rabbit anti-pGC-A (affinity-purified)	Fabgennix #PGCA-101AP	1:250	Rat pGC-A (NP_036745) 1042-1057 VRTYWLLGERGCSTRG	16/16 (100%)
Rabbit anti-pGC-B (affinity-purified)	Fabgennix #PGCB-201AP	1:200	Rat pGC-B (NP_446290) 1029-1047 GKMRTYWLLGERKGPPGLL	18/19 (95%)
Rabbit anti-pGC-C (affinity-purified)	Fabgennix #PGCC-301AP	1:200	Rat pGC-C (NP_037302) 1048-1063 RVASYKKGFLEYMQLN	16/16 (100%)
Rabbit anti-pGC-E (affinity-purified)	Fabgennix #PGCE-501AP	1:1,000	Rat pGC-E (NP_077356) 1091-1108 PERRKKLEKARPGQFTGK	18/18 (100%)
Rabbit anti-pGC-F (affinity-purified)	Fabgennix #PGCF-601AP	1:400	Rat pGC-F (NP_446283) 1090-1108 EIAAFQRRKAERQLVRNKP	19/19 (100%)
Rabbit anti-pGC-G (affinity-purified)	Fabgennix #PGCG-701AP	1:500	Rat pGC-G (NP_620611) 1085-1100 PLPEFTEEEAKVPEIL	15/16 (94%)
Rabbit anti-GFAP (whole antiserum)	Abcam # ab7260	1:600	Human GFAP (NP_002046) 1-432	393/432 (91%)
Rabbit anti-PLP (whole antiserum)	Abcam # ab28486	1:500	Mouse myelin PLP (NP_035253) 109-128 CGKGLSATVTGGQKGRGSRG	20/20 (100%)

Described are the host animals, commercial sources, working concentrations, and immunizing sequences (with accession numbers) of the antibodies.

Table 2: Western blot characterization of pGC antibodies

Antibody	Mouse Tissue Lysate	Approximate Detected Bands (kDa)	Predicted Band (kDa)
Rabbit anti-pGC-A	Kidney	120	119
Rabbit anti-pGC-B	Kidney	120	117
Rabbit anti-pGC-C	Intestine	180, 55	120*
Rabbit anti-pGC-E	Retina	110	120
Rabbit anti-pGC-F	Retina	110	124
Rabbit anti-pGC-G	Nasal vestibule	120	123

* Observed band size for pGC-C on immunoblots is known to be variable, ranging from 50 to 240 kDa (Scheving and Russell, 1996; Scheving et al., 1996).

Described are the results of immunoblots performed with pGC antibodies on various mouse tissue sources.

FIGURE LEGENDS

Figure 1: The Grueneberg Ganglion (GG) is an unusual olfactory nerve at the rostral tip of the mouse nose. A) Schematic of the nasal cavity and septum of a mouse showing the olfactory subsystems. Both GG and GC-D subsystems (neurons as orange spots) project axons (orange lines) to a unique spatial domain containing sets of interconnected glomeruli in the caudal region of the olfactory bulb. The MOE is part of the MOS. The VNO is part of the AOS. Green lines demarcate anatomical locations in the nasal cavity; blue lines demarcate regions of the brain. B) In this medial view of a whole-mount preparation from an OMP-GFP mouse, GG neurons express olfactory marker protein (OMP, in white) and are arranged as clusters of cells comprising an arrowhead-shaped organ. C) OMP-expressing GG neurons (green) seen in thin section do not project cellular processes into the nasal cavity (n.c.). They are separated by a keratinized epithelium (KE, magenta) that is labeled with an antibody to particulate guanylate cyclase E. D) *En face* view of proteolipid protein (PLP-GFP)-expressing glial cells in the nasal vestibule that ensheathe GG neurons. In thin sections (E-G): E) GG neurons visualized in nasal vestibules of OMP-GFP mice (GFP in green) positively stain for OMP protein (magenta). F) GFP-positive OSNs (green) in the OMP-GFP mouse MOE stain positively for OMP (magenta). G) OMP-GFP mice faithfully report expression of OMP in the glomerular layer (GL) of the olfactory bulb (GFP in green, OMP immunostaining in magenta). SO = septal organ; D = dorsal; V = ventral; R = rostral; C = caudal; ONL = olfactory nerve layer; EPL = external plexiform layer. Scale bars: B) 250 μm; C) 15 μm; D) 60 μm; E-F) 30 μm; G) 60 μm.

Figure 2: The GG expresses a cGMP-stimulated phosphodiesterase. A-B) PDE4A staining in thick sections from neonatal OMP-GFP mice in the MOE (A) and the rostral nasal vestibule (B). GG neurons correspond to OMP-positive cells in the nasal vestibule. C-D) PDE2A staining in the neonatal MOE (C) and nasal vestibule (D). The PDE2A antibody labeled GG neurons and vascular endothelial cells in the nasal vestibule. E-F) Immunoadsorption study with the PDE2A antibody in whole-mount preparations. Unblocked PDE2A antibody (magenta) labeled adult GG neurons (green) in the nasal vestibules of OMP-

GFP mice (E), but there was no labeling when the antibody was blocked with the immunizing peptide (F). Scale bars: 40 μm.

Figure 3: Downstream cGMP signal transduction components are expressed in the GG. A) In OMP-GFP mice, GFP-fluorescing GG neurons (green) in the nasal vestibule express cGKII (magenta). On some neurons the cGKII antibody labels the GG neuron membrane (arrow). B) The cGKII antibody (red) labels the villus brush borders in the intestine (nuclei are in blue). C) CNGA3 antibody (red) labels photoreceptor segments (arrow) in thin sections from the mouse retina (nuclei are in blue). D) GG neurons (green) express CNGA3 (magenta) on unusual "whip-like" subcellular domains. E) Neurons of the GC-D olfactory subsystem, highlighted by GFP expression (green) in the GCD-iTG transgenic mouse, express CNGA3 (magenta) on their dendritic knobs (arrows). Scale bars: A) 20 μm B) 60 μm; C) 30 μm; D) 20 μm; E) 60 μm.

Figure 4: The GG does not express pGC-D. A) PDE2A immunolabeling in thick sections from the olfactory neuroepithelium of a transgenic GCD-iTG mouse. GFP-positive GC-D neurons (green) express PDE2A (magenta), consistent with their use of a cGMP signaling pathway. B) PDE2A-positive GG cells (magenta) in thick sections from the nasal vestibule are devoid of GFP (green) and, hence, pGC-D. Scale bars: 60 μm.

Figure 5: Particulate guanylate cyclase expression in the GG. A-B) In whole-mount preparations, all GG neurons (green) express pGC-G (A, magenta) on unusual subcellular domains. In contrast, only a small, broadly distributed subset of GG neurons (white asterisks) express pGC-A (B, magenta) on the same subcellular domains. C-D) Immunoadsorption study with the pGC-G antibody (magenta) and its antigenic blocking peptide on GG neurons (green). Labeling is observed when the antibody is unblocked (C) but is abolished when it is blocked (D). E-F) Blocking experiment with the pGC-A antibody (magenta) on GG neurons (green). Unblocked antibody labels the small GG neuron subset (E), blocked antibody does not

(F). G-H) pGC-G is expressed in GG neurons (red asterisks) at all ages, from PD2/neonatal (G) to adult (H) ages. Gray-black areas indicate staining. I-J) A comparison on pGC-G expression the GG and GC-D olfactory subsystems of GCD-iTG mice reveals that pGC-G (magenta) is expressed in GG neurons of the nasal vestibule (I) but not in the GC-D neurons (green) of the caudal MOE (J). K) High magnification view of pGC-G-expressing "whip"-like subcellular domains (black staining, red arrows) in a whole-mount preparation. L) High magnification view of pGC-G localization (magenta) on a GG neuron (green) at different optical z planes (in μm) in thin sections. Labeled subcellular domains follow the surface contours of GG neurons. M) Immunoblot with pGC-G antibody on nasal vestibule lysate. A single 120 kDa band is labeled. Lanes correspond to the relative amount of protein loaded. Scale bars: A-B) 60 μm; C-F) 10 μm; G-H) 40 μm; I-J) 30 μm; K) 15 μm; L) 5 μm.

Figure 6: pGC-G expression in relation to the GG ensheathing cells. A) In whole-mount preparations, GFP-positive fibers (green) in the nasal vestibules of PLP-GFP mice colocalize with GFAP staining (magenta). B) In thin cross sections of the nasal vestibule, GFP-positive cells (green) in PLP-GFP mice can be seen to envelop GG neurons stained with the OMP antibody (magenta). C) In thin sections, pGC-G (magenta) does not colocalize with the glial-like ensheathing cell population (green) visualized in PLP-GFP mice. Scale bars: A) 25 μm; B-C) 20 μm.

Figure 7: Ultrastructural view of GG neurons. A) Low magnification view of a single GG neuron. A cluster of ciliary basal bodies is visible in the yellow highlighted region, next to the nucleus [1]. The GG neuron is ensheathed by a glial cell [2]. B) The inset region of (A), magnified. Ciliary basal bodies [3] are in close proximity to a mitochondrion [4]. C-D) A closer view of the clusters of ciliary basal bodies [3]. These clusters are supported by a ring of actin filaments, visible in (D). E-F) Out of these basal bodies, long ciliary fibers [5] erupt and follow the membrane contour of the GG neuron. These fibers are held tight to the membrane by the glial-like ensheathing cells. Lower-right orange inset magnified areas outlined in red (F). Scale bars: A) 3 μm; B) 0.5 μm; C-D) 0.25 μm; E) 0.5 μm F) 1 μm (inset: 0.3 μm).

Figure 8: The cGMP signal transduction pathway in the GG. Binding of atrial natriuretic peptide (ANP), B-type natriuretic peptide (BNP), or other as-of-yet unidentified ligands to pGC-A or unknown ligands to pGC-G induces the conversion of GTP to cGMP by the particulate guanylate cyclases. The produced cGMP can then open CNGA3 channels to depolarize the GG neuron, induce additional signaling through cGKII, or be degraded to GMP by PDE2A.

ABBREVIATIONS

ANP	Atrial natriuretic peptide
AOS	Accessory Olfactory System
BNP	B-type natriuretic peptide
cGKII	cGMP-dependent kinase II
cGMP	Cyclic guanosine monophosphate
CNGA3	Cyclic nucleotide gated channel A3
EPL	External plexiform layer
GC-D	Particulate guanylate cyclase D
GFAP	Glial fibrillary acidic protein
GFP	Green fluorescent protein
GG	Grueneberg Ganglion
GMP	Guanosine monophosphate
GTP	Guanosine triphosphate
iTG	Internal ribosome entry site fused to tau protein fused to GFP
iTL	Internal ribosome entry site fused to tau protein fused to LacZ
MOE	Main Olfactory Epithelium
MOS	Main Olfactory System
n.c.	Nasal cavity
OMP	Olfactory marker protein
ONL	Olfactory nerve layer
OSN	Olfactory sensory neuron
PDE2A	Phosphodiesterase 2a
PDE4A	Phosphodiesterase 4a
pGC-A	Particulate guanylate cyclase A
pGC-D	Particulate guanylate cyclase D
pGC-G	Particulate guanylate cyclase G
PLP	Proteolipid protein
SO	Septal organ
TEM	Transmission electron microscopy
tg	Transgenic animal
VNO	Vomeronasal Organ

FIGURES

Figure 1:

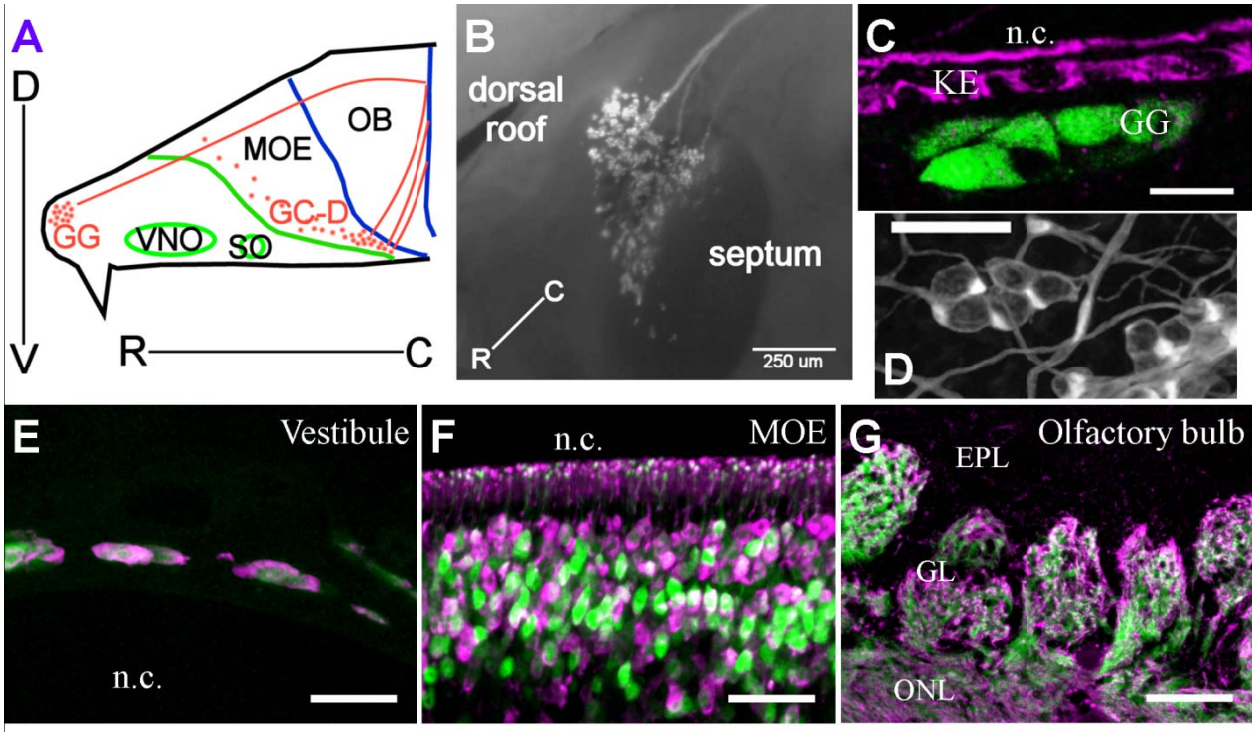

Figure 2:

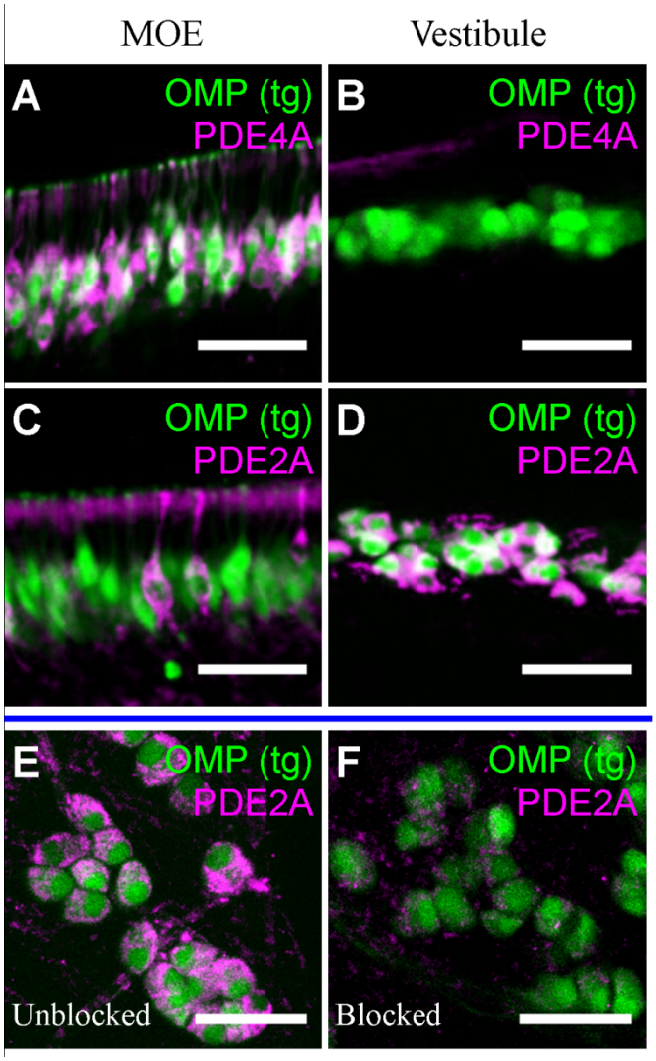
MOE
Vestibule
A
OMP (tg)
PDE4A
B
OMP (tg)
PDE4A
C
OMP (tg)
PDE2A
D
OMP (tg)
PDE2A
E
OMP (tg)
PDE2A
Unblocked
F
OMP (tg)
PDE2A
Blocked

Figure 3:

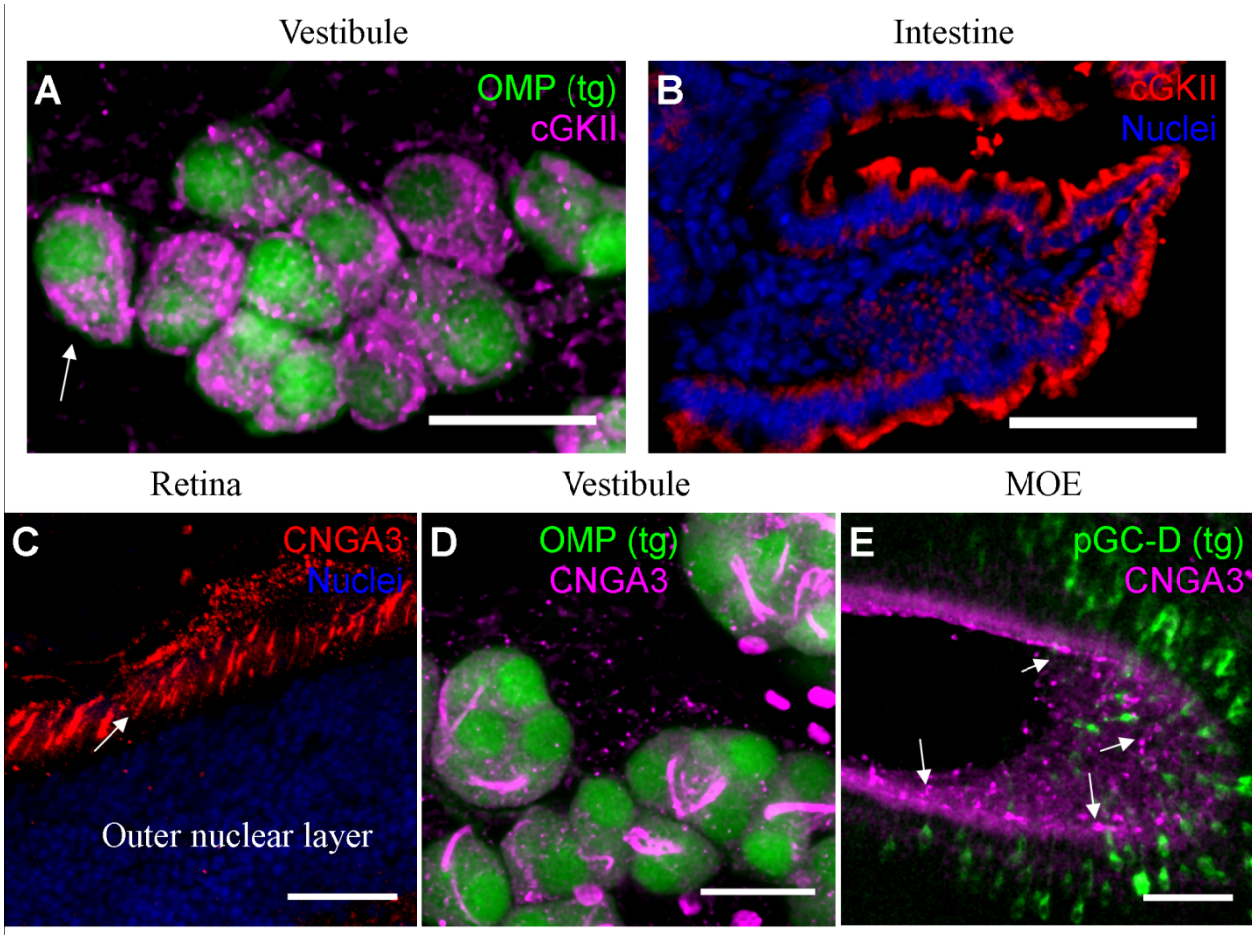
Vestibule
Intestine
A
OMP (tg)
cGKII
B
cGKII
Nuclei
Retina
Vestibule
MOE
C
CNGA3
Nuclei
Outer nuclear layer
D
OMP (tg)
CNGA3
E
pGC-D (tg)
CNGA3

Figure 4:

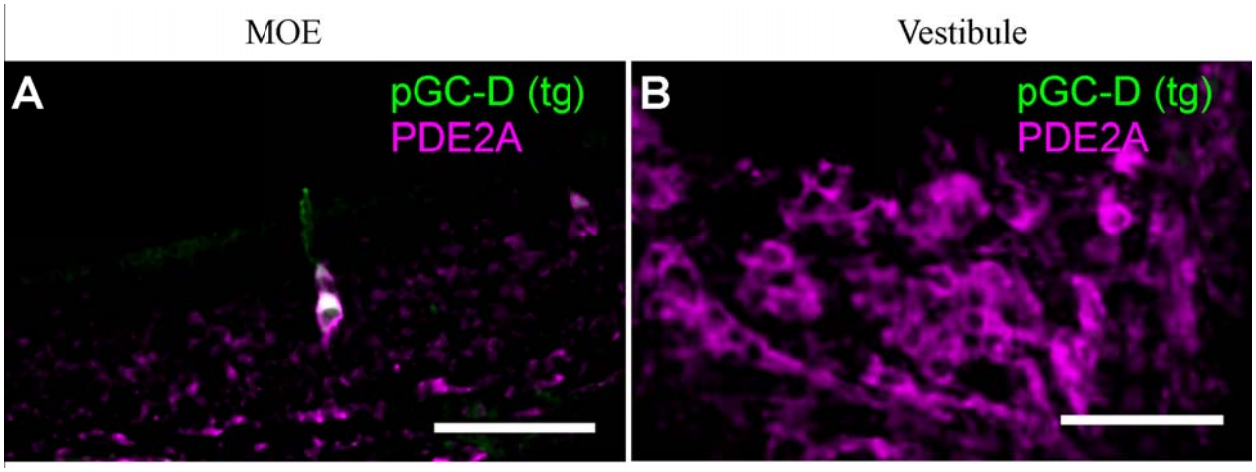

Figure 5:

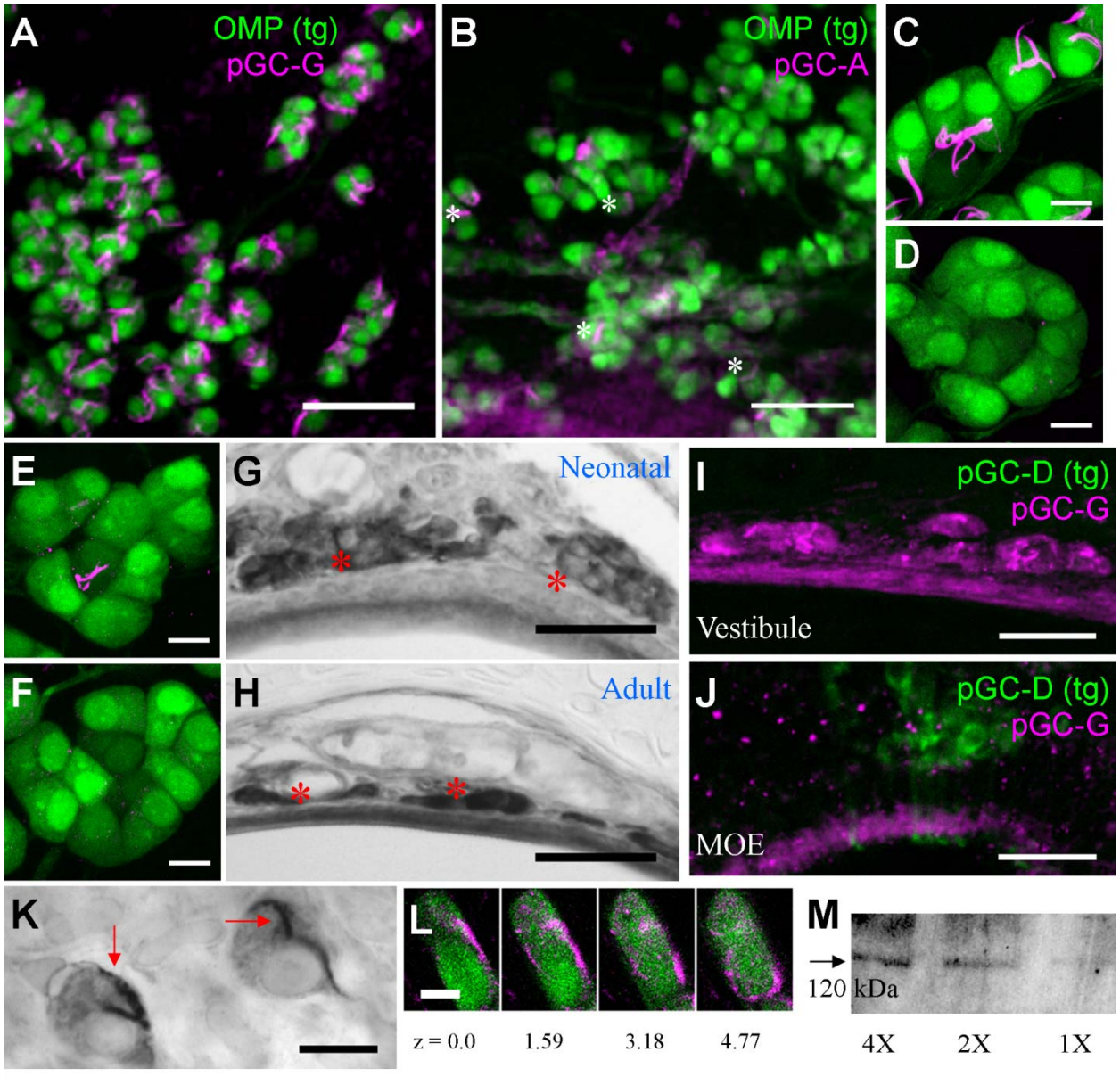
A
OMP (tg)
pGC-G
B
OMP (tg)
pGC-A
C
D
E
F
G
Neonatal
H
Adult
I
pGC-D (tg)
pGC-G
Vestibule
J
pGC-D (tg)
pGC-G
MOE
K
L
z = 0.0
1.59
3.18
4.77
M
120 kDa
4X
2X
1X

Figure 6:

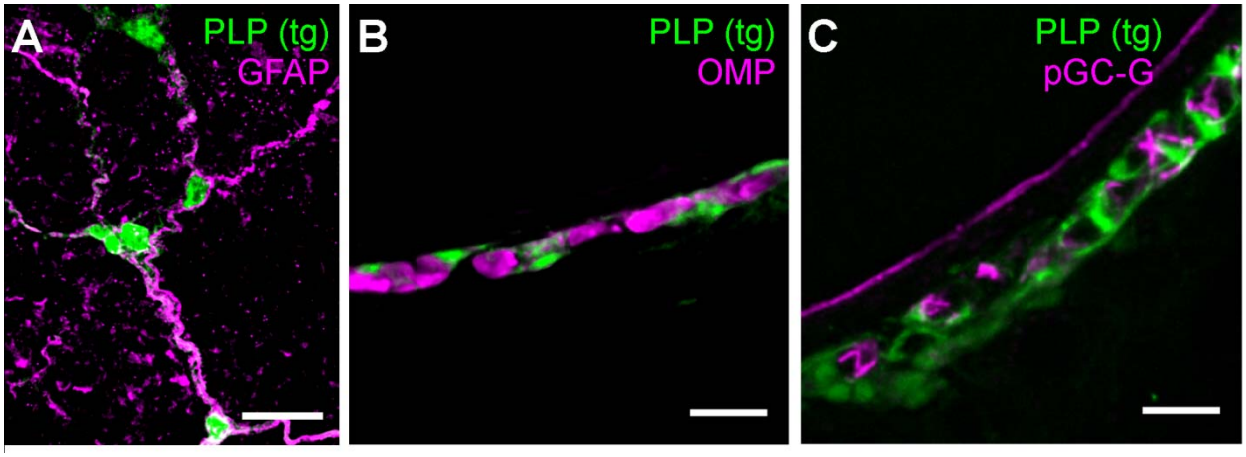

Figure 7:

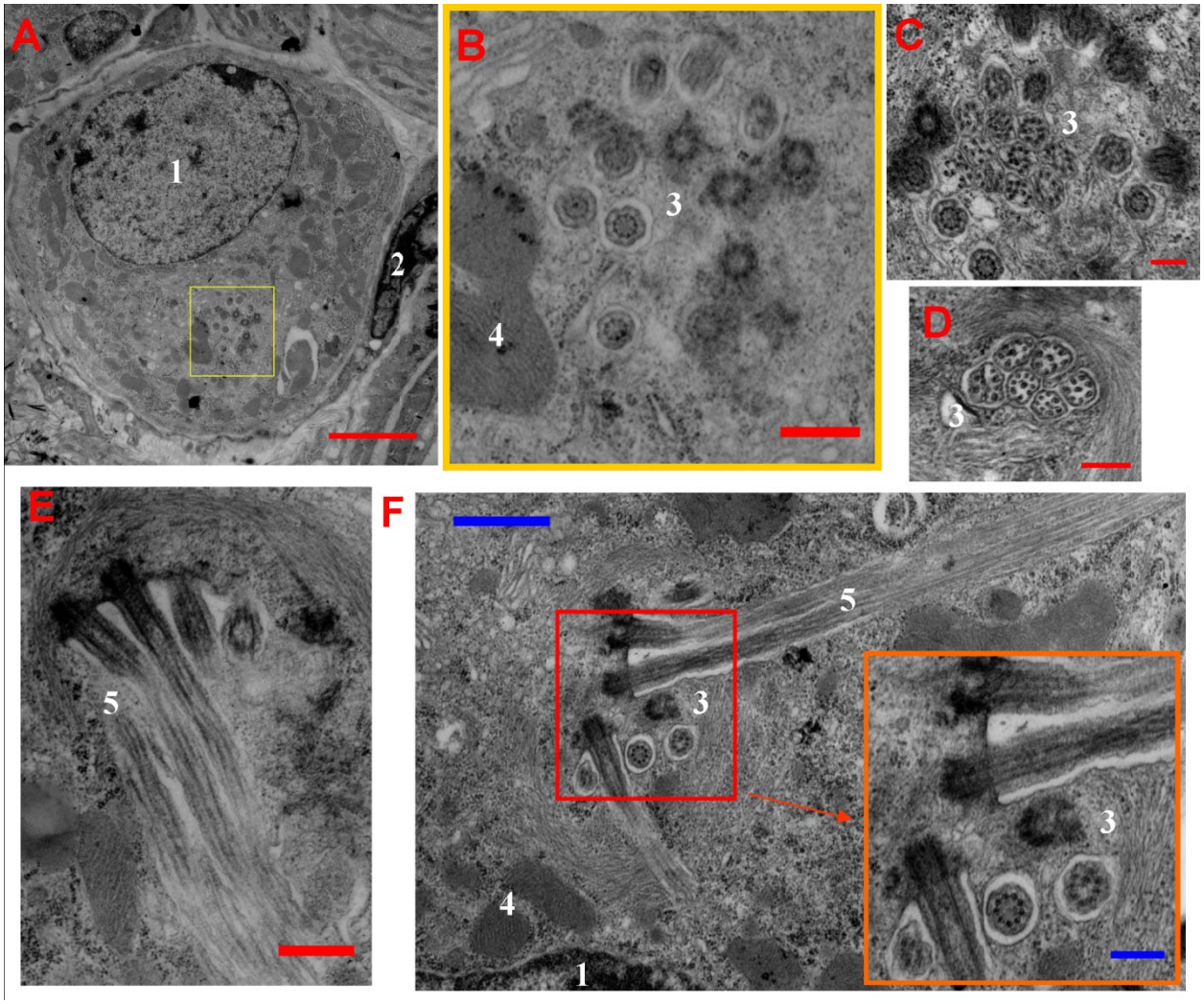

Figure 8:

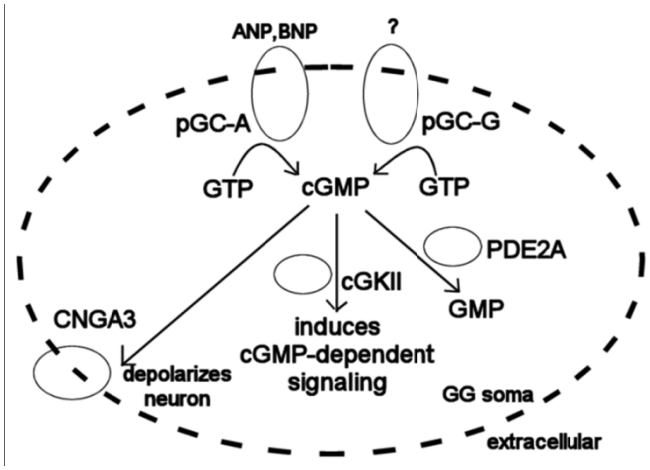
ANP,BNP
?
pGC-A
pGC-G
GTP
cGMP
GTP
PDE2A
cGKII
GMP
CNGA3
induces
cGMP-dependent
signaling
depolarizes
neuron
GG soma
extracellular

SUPPORTING FIGURES

Supporting Figure 1:

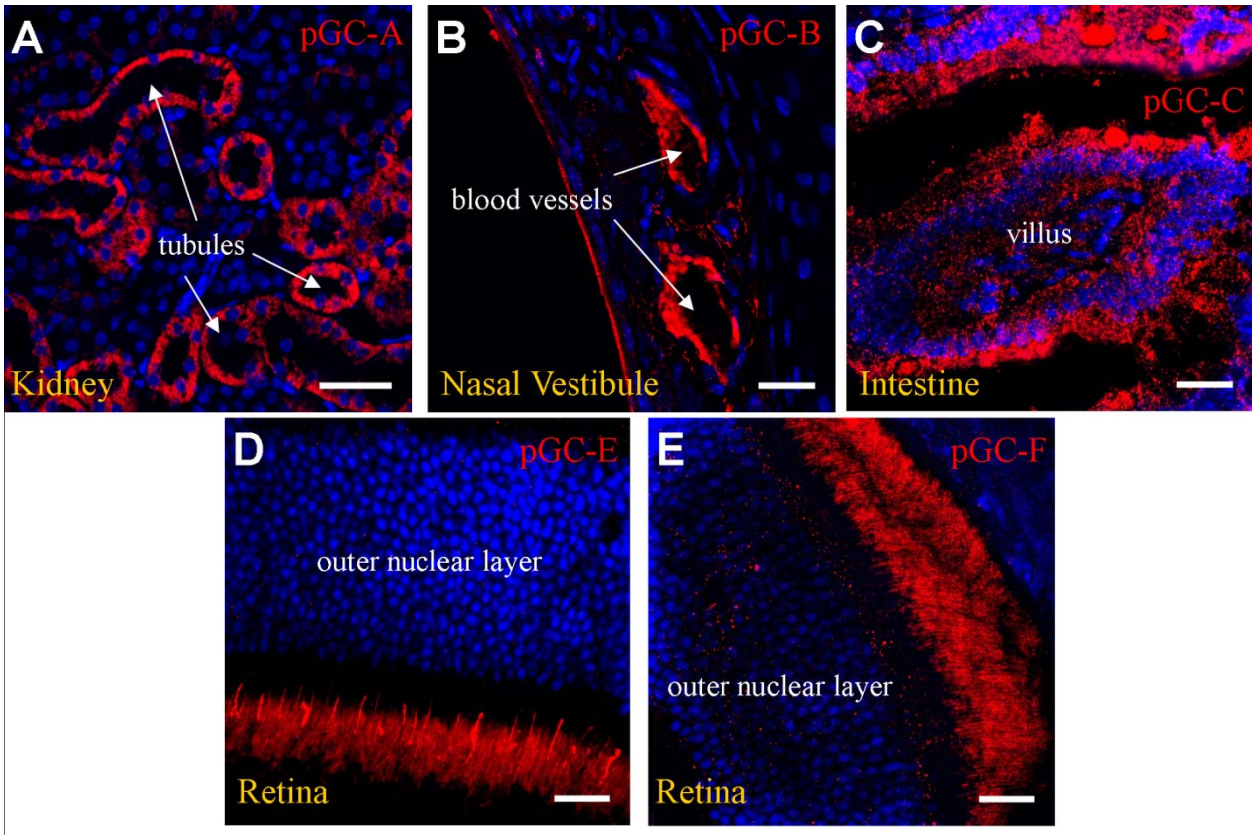

Immunohistochemical validation of pGC antibodies on different tissue types. Antibodies to pGC-A (A), pGC-B (B), pGC-C (C), pGC-E (D), and pGC-F (E) were used to stain kidney (A), nose (B), intestine (C), and retinal (D,E) tissue. Antibody signal is in red. Nuclei visualized using Topro-3 are in blue. These antibodies each exuberantly recognized proteins in their respective control tissues. Thus, they are fit for use in immunostaining experiments. Scale bars: A) 40 µm; B-E) 20 µm.

--- Chapter 3 ---

Electrophysiological characterization of Grueneberg ganglion olfactory neurons: spontaneous firing, sodium conductance, and hyperpolarization-activated currents

Cambrian Y. Liu, Cheng Xiao, Scott E. Fraser, Henry A. Lester, David S. Koos

C.X. performed initial patch clamp experiments to reveal the basic phenomena discussed in this chapter.

ABSTRACT

Mammals rely on their acute olfactory sense for their survival. The most anterior olfactory subsystem in the nose, the Grueneberg ganglion (GG), plays a role in detecting alarm pheromone, cold, and urinary compounds. GG neurons respond homogeneously to these stimuli with increases in intracellular [Ca^{2+}] or transcription of immediate-early genes. In this electrophysiological study, we used patch clamp techniques to characterize the membrane properties of GG neurons. Our results offer evidence of functional heterogeneity in the GG. GG neurons fire spontaneously and independently in several stable patterns, including phasic and repetitive single-spike modes of discharge. Whole-cell recordings demonstrated two distinct voltage-gated fast-inactivating Na^+ currents with different steady-state voltage dependencies and different sensitivities to tetrodotoxin. These Na^+ currents confer dual mechanisms of action potential generation. Alterations in the ratios of the two Na^+ conductances in Hodgkin-Huxley computer simulations resulted in different levels of repetitiveness of firing. Additionally, GG neurons exhibited hyperpolarization-activated inward currents (I_h) that modulated spontaneous firing. Thus, in GG neurons the heterogeneity of firing patterns is linked to the unusual repertoire of ionic currents. The membrane properties described here will aid the interpretation of chemosensory function in the GG.

KEYWORDS

Sodium currents, burst firing, pacemaking, hyperpolarization-activated cationic channels, patch clamp, neuronal simulations

INTRODUCTION

The Grueneberg ganglion (GG) is a specialized olfactory subsystem located at the far-anterior end of the nasal cavity in many mammals (Fleischer et al. 2006a; Fuss et al. 2005; Grüneberg 1973; Koos and Fraser 2005; Roppolo et al. 2006; Storan and Key 2006). The subsurface neuronal clusters that comprise the GG are ensheathed by glial-like satellite cells (Brechbuhl et al. 2008; Liu et al. 2009; Tachibana et al. 1990). Axons of the GG in mice form 8-12 glomeruli in the caudal, necklace-like domain in the olfactory bulb (Fuss et al. 2005; Koos and Fraser 2005; Liu et al. 2009). GG neurons express olfactory marker protein (OMP) (Fleischer et al. 2006a; Koos and Fraser 2005; Liu et al. 2009; Storan and Key 2006) and signal transduction components necessary to utilize cGMP as the primary second messenger (Fleischer et al. 2009; Liu et al. 2009).

GG neurons in mice function in a variety of contexts. Most GG neurons exhibit increases in cytosolic [Ca^{2+}] when exposed to a so-called alarm pheromone, composed of water-soluble compounds collected during the asphyxiation of mice (Brechbuhl et al. 2008). The vast majority of neurons in both *in vivo* (Mamasuew et al. 2008) and *in vitro* (Schmid et al. 2010) studies respond to cold with increased c-Fos levels and [Ca^{2+}] bursts, respectively. Thermosensitive [Ca^{2+}] bursts rely on tetrodotoxin-sensitive Na^{+} channels (Schmid et al. 2010), supporting the idea that GG neurons encode and process information by firing action potentials. It has also been shown that GG neurons respond to dimethylpyrazine and related urinary compounds *in vivo* (Mamasuew et al. 2011).

The largely homogeneous responses in the GG organ within each sensory context suggest that a single GG neuron functions multimodally. Gene expression studies indicate that GG neurons express various potential odor receptors, including the membrane-bound guanylate cyclases pGC-G and pGC-A (Liu et al. 2009), a pheromone receptor V2r83 (Fleischer et al. 2006b), and several trace amine-associated receptors (Fleischer et al. 2007). In particular, pGC-G and V2r83 are expressed on the same sets of neurons (Fleischer et al. 2009). *In vivo* studies demonstrate that both cold temperatures and dimethylpyrazine are detected by the pGC-G/V2r83 neuronal subset (Mamasuew et al. 2011; Mamasuew et al. 2010).

Previous studies on GG function have inferred neuronal activity from immediate-early gene expression (Mamasuew et al. 2008; Mamasuew et al. 2011), cytosolic [Ca^{2+}] elevations (Brechbuhl et al. 2008; Schmid et al. 2010), and alterations in animal stress behavior (Brechbuhl et al. 2008) . It is not known if the responses seen in these assays correspond to uniform electrical behaviors in GG neurons. The anatomical properties of the GG have posed severe challenges to electrophysiological recordings. The glial sheath prevents access of microelectrodes. The surrounding cartilage precludes gentle dissociation of GG neurons. Even in organotypic preparations, a thin keratinized epithelium makes microelectrode recordings quite difficult (Brechbuhl et al. 2008; Liu et al. 2009). As a result, our knowledge about the membrane properties and electrical outputs of GG neurons is limited.

Here, in acute slices of the GG, patch clamp experiments were undertaken to gain an initial understanding of electrical transduction in the GG. We found evidence of functional heterogeneity in the receptor neurons. In extracellular recordings, we detected spontaneous firing that could be categorized into three intrinsic patterns. Whole-cell recordings enabled an identification of two subtypes of fast-inactivating voltage-gated Na^+ currents with different sensitivities to tetrodotoxin (TTX), and one type of hyperpolarization-activated cationic current (I_h). These Na^+ currents confer two different modes of action potential generation based on membrane status and may underlie heterogeneous interpretations of evoked activity. We also incorporated the Na^+ currents into a Hodgkin-Huxley computer model and analyzed their potential contributions to the spontaneous discharge pattern of a simulated GG neuron.

MATERIALS AND METHODS

Animal Care

Mice were maintained as per Caltech IACUC-approved protocol. Genetically modified mice that express green fluorescent protein (GFP) in mature olfactory neurons (OMP-GFP mice) were a gift from P. Mombaerts. Their generation and characterization have been previously described (Liu et al. 2009; Potter et al. 2001). All animals used were postnatal.

Electrophysiology

Recordings were performed on acute slices of the far-anterior nasal vestibule from OMP-GFP heterozygous mice aged p4-p14. To prevent dissociation of protease-treated slices and neuronal activation artifacts resulting from CO_2 exposure (Chao et al. 2010), most recordings were performed in a bicarbonate-free extracellular solution, instead of the usual 95% O_2/5% CO_2 (carbogen)-saturated artificial cerebrospinal fluid (ACSF). Using the following protocol, we could obtain membrane seals of GΩ resistance from the somata of >10 neurons per recording session.

Mice were transported from the Caltech animal facility to the dissection station, sacrificed, and decapitated. The nasal vestibules were skinned, separated from the rest of the nasal cavity, and trimmed of excess tissue. Dissection and subsequent sectioning were performed in a cold glycerol-based saline solution (glycerol HEPES-buffered saline, or gHBS) to promote neuronal viability, containing (in mM): 272 glycerol, 2.5 KCl, 10 HEPES, 2 $CaCl_2$, 1.3 $MgCl_2$, 10 D-glucose, pH 7.4 (adjusted with KOH).

After dissection, nasal vestibules were infiltrated with 4.5% low-melt agarose (LMA) in Ringer's solution for 10 s at 37 ˚C and immediately embedded in additional 4.5% LMA. LMA-embedded noses were allowed to solidify on ice for 1 min, and were cut into 100-µm transverse slices containing GG neurons (5 - 7 slices per animal) in cold gHBS, using a Vibratome (VT-1000S, Leica).

Slices were washed with room-temperature HEPES buffered saline (HBS), containing (mM): 136 NaCl, 2.5 KCl, 10 HEPES, 2 $CaCl_2$, 1.3 $MgCl_2$, 10 D-glucose, pH 7.4 (adjusted with NaOH). They were incubated with 0.1% prewarmed type II collagenase (Invitrogen) in HBS for 10 min at 37 ˚C in a tissue culture incubator infused with 5% CO_2. Slices were rinsed with warmed HBS and recovered at 37 ˚C in HBS for 5-25 min, depending on the animal's age. Slices were stored at room temperature for 5-300 min prior to recording in HBS at room temperature (23 - 25 ˚C). Several slices were prepared with a glycerol-based artificial cerebrospinal fluid (gACSF) and recorded in artificial cerebrospinal fluid (ACSF) superfused with 95% O_2/5% CO_2 as control experiments, according to recipes described previously (Xiao et al. 2009).

GG neurons were visualized with an upright microscope (BX50WI, Olympus) and blue-light (GFP) illumination. Slices were positioned and anchored in a perfusion chamber. Cell-attached and whole-cell patch clamp techniques were used to record electrophysiological signals with a MultiClamp 700B amplifier (Axon Instruments, Molecular Devices), Digidata 1322 analog-to-digital converters (Axon Instruments), and pClamp 9.2 software (Axon Instruments). Data were sampled at 10 kHz and low-pass filtered at 2 kHz. Junction potential was nulled just before seal formation.

The patch electrodes had resistances of 3 - 8 MΩ when filled with intrapipette solutions. For characterization of Na^+ and putative Ca^{2+} currents, we used a CsCl-based intrapipette solution containing (mM): 110 CsCl, 30 TEA-Cl, 10 HEPES, 1 $CaCl_2$, 2 $MgCl_2$, 2 MgATP, 5 EGTA, pH 7.4 (adjusted with CsOH). For current clamp studies and characterization of K^+ currents, we used a KCl-based intrapipette solution containing (mM): 140 KCl, 10 HEPES, 1 $CaCl_2$, 2 $MgCl_2$, 2 KATP, 5 EGTA, pH 7.4 (adjusted with KOH). Na^+-free extracellular solution contained (mM): 136 N-methyl-D-glucamine (NMDG), 2.5 KCl, 10 HEPES, 10 D-glucose, 2 $CaCl_2$, 1.3 $MgCl_2$, pH 7.4 (adjusted with HCl). Predicted junction potentials between the patch pipette and the HBS bath solution were 2.7 mV for the CsCl-based intrapipette solution and 4.0 mV for the KCl-based intrapipette solution. Predicted junction potential for the KCl-based intrapipette solution in extracellular NMDG-based Na^+-free solution was 9.3 mV. Junction potentials were corrected offline during data analysis. Capacitance compensation was not performed unless otherwise noted; the capacitance of the patched cells was estimated offline by integration of the exponential discharge function induced by a 5 mV voltage step from the holding potential. Series resistance compensation was not performed unless otherwise noted, when it was compensated to 50 - 90% by the Multiclamp 700B amplifier. Series resistances were normally in the range of 10 - 40 MΩ. Data were discarded when series resistances exceeded 40 MΩ.

GG neurons were selected for recording based on: (1) the presence of GFP, (2) a protruding surface amenable to patch pipette approach, and (3) the absence of intracellular granularity. Spontaneous firing was recorded in cell-attached mode, prior to breakthrough of the cell membrane. Current-voltage relationships were derived from 0.1-2 s depolarizing pulses from various holding potentials (-55 mV, -70

mV, -85 mV, or -120 mV) to test potentials between the holding potential and +50 mV, at increments of 10 mV. Hyperpolarization-activated cationic currents (I_h) were evoked by 3 s hyperpolarizing pulses to test potentials between -55 mV and -135 mV with a decrement of 10 mV. Current-clamp studies were performed with 0.3-10 s current pulses.

Tetrodotoxin (50 nM - 2 μM, Calbiochem) application and ion substitutions were performed by bath perfusion. Responses to 8-br-cGMP were tested by 10 psi pressure ejection (Parker Instrumentation) from a filled patch pipette placed 20 μm from the cell soma. Unless otherwise noted, all chemicals were obtained from Sigma.

Immunohistochemistry

Immunohistochemistry was performed as previously described (Liu et al. 2009). Briefly, adult mice (>6 weeks in age) were euthanized with CO_2 and decapitated. Nasal vestibules were dissected and fixed overnight in cold 4% paraformaldehyde in phosphate-buffered saline (PBS). After cryoprotection in ascending sucrose/PBS (maximum sucrose: 30% w/v) mixtures, nasal vestibules were rapidly frozen in Tissue-Tek O.C.T. (Sakura) and cryosectioned at 12 μm thickness at -23˚C. Sections were adhered to glass slides and thawed in PBS. Slides were incubated with rabbit anti-HCN1 antibody without Triton-X (1:400, Alomone Labs, catalog #APC-056) for 18 h at 4˚C. After several washes with PBS, slides were incubated with biotinylated anti-rabbit antibodies and streptavidin-bound Alexa Fluor 555 (Invitrogen) probes. Results were imaged on a Zeiss LSM510 upright confocal microscope with laser excitation at 488 nm and 543 nm wavelengths. Optical sectioning was performed at 2 μm thickness. Images were processed and reconstructed in ImageJ (NIH).

Other antibodies used were rabbit anti-S100β (1:1000, Abcam, catalog #ab52642) and rabbit anti-GFAP (1:600, Abcam, catalog #ab7260).

RT-PCR

Adult mice (age: 2-3 months) were euthanized with CO_2 and decapitated. Nasal vestibules were dissected and trimmed of excess tissue. GG organs and surrounding epithelium were carefully separated from the cartilaginous nasal septum and collected in 600 µL Trizol reagent (Invitrogen) on ice. The solution was vigorously vortexed for 5 min or until the tissue was observed to dissociate. Chloroform (125µL) was added to separate RNA from proteins, and after centrifugation the aqueous phase was preserved for subsequent isopropanol precipitation and ethanol cleaning. RNA pellets were re-dissolved in water at 50˚C. First strand synthesis was performed with 1 µg of RNA template using oligo-dT DNA primers with the Superscript III (Invitrogen) kit. 2 µL of the first-strand cDNA library was used for gene amplification using PCR with HotStar Taq (Qiagen).

For control experiments, the RNA from a single cerebrum from an adult mouse (age: 2 months) was extracted.

Primers for gene amplification were as follows (from 5' end to 3' end): Omp – forward: ACTGGAACGTGGTTCTGGAC, reverse: CACAGAGGCCTTTAGGTTGG; Hcn1 - forward: ACCAGCTGACATGCGCCAGAA, reverse: GCTTCACGATCTGCTTCAGGATCTCGT; Hcn2 - forward: GAAGATGTTTGATGAGGACAGCAT, reverse: GCACGCCGCATCATGGGGTAT; Hcn3 - forward: GGCGCCACGTGTTATGCCATG, reverse: TCAGAGCGTTTCCGCTGCAG; Hcn4 - forward: CAGCGACCAGATCCTCCCCGA, reverse: GCGCAGAGCCCTAGCGGTTTT.

Data Analysis

Electrophysiological data were analyzed with Clampfit 9.2 and with custom-written routines in MATLAB 7.4.0. Current-voltage curves for inward Na^+ currents were obtained by measuring the peak inward current amplitude within 1 ms after the depolarization command, to exclude the activation of axonal currents. For Ca^{2+} and K^+ currents, peak currents during the depolarizing pulse were used. Data were then imported to MATLAB for offline leak current subtraction. Activation and inactivation curves for Na^+ and K^+ channels were fit to a two-state (open or closed) Boltzmann sigmoid model with a single voltage-dependent transition. Half-activated voltages ($V_{1/2}$) were derived from the Boltzmann fit in

MATLAB. Inactivation time constants (τ_h) were calculated by fitting Na^+ currents to Hodgkin-Huxley equations (Hodgkin and Huxley 1952) for Na^+ current (see below, "Simulations"). AP rise times were obtained from Clampfit. Unless otherwise indicated, the reporting of values in the format ($x \pm y$) indicates the mean value is x and the inferential standard error value is y.

Spontaneous APs were extracted from > 3 min traces using the template search feature of Clampfit 9.2. Templates were developed by visual identification of APs at the start of each trace, according to their rise time (< 1 ms). APs were automatically scanned, and erroneous identifications were removed. Calculations of instantaneous firing frequencies, binned (total) firing frequencies, and clustering of firing rates were performed in MATLAB with custom-written routines. Clustering of instantaneous firing rates used to distinguish patterns of spontaneous discharge was performed with a Gaussian mixture expectation-maximization algorithm, with two expected means. Phasic and sporadic patterns of discharge were distinguished by the overlap of the two Gaussian functions that provided the resultant density estimation.

The time-dependent activation of I_h and inactivation of K^+ currents were fitted to a two-component exponential function of the form:

$$I_h = Ae^{-\frac{t}{\tau_f}} + Be^{-\frac{t}{\tau_s}} + C$$

with t denoting time, I_h denoting current amplitude, A, B, and C indicating constants, and τ_f and τ_s representing the fast and slow time constants of activation and inactivation, respectively. Correlation coefficients were derived from fitting procedures in Clampfit 9.2.

Simulations

Currents recorded in voltage-clamp experiments were modeled with NEURON 7.1 (Hines and Carnevale 1997). Unless otherwise mentioned, we used the default settings of NEURON for modeling. The modeled currents were the TTX-R Na^+ current, TTX-S Na^+ current, a single voltage-gated K^+ current, and a nonspecific leak current. The data were fitted to Hodgkin-Huxley rate equations (Hodgkin

and Huxley 1952). Plots of fitted functions are shown in Supporting Fig. 1. Action potentials were simulated within a single somatic cylindrical compartment with a radius of 6 µm and a length of 6 µm. The effects of current injections on membrane potential were simulated with a stimulating electrode placed at the center of the soma. Table 1 describes the main topological and electrical parameters used in the construction of the model. These parameters were derived from the voltage-clamp data. All programming code was deposited to ModelDB (http://senselab.med.yale.edu/modeldb/).

Na^+ currents

Na^+ currents were modeled using the Hodgkin-Huxley formalism (Hodgkin and Huxley 1952):

$$I_{Na} = \overline{G}_{Na} m^3 h\left(V - V_{Na}\right)$$

with I_{Na} representing the Na^+ current, $\bar{G}_{Na}$ the maximal Na^+ conductance, m and h the parametric activation and inactivation gates, respectively, V the membrane potential, and V_{Na} the reversal potential of Na^+. G/G_{max} activation curves shown in Fig. 5E were set equal to m_∞^3; I/I_{max} inactivation curves in the same figure were set equal to h_∞. . Estimates for τ_h and τ_m were obtained by fitting depolarization-evoked Na^+ currents in voltage-clamp recordings to the functional form:

$$I_{Na} = A + B\left(1 - e^{-\frac{t}{\tau_m}}\right)^3 e^{-\frac{t}{\tau_h}}$$

with t representing time (ms) and values for A, B, τ_h, and τ_m determined in MATLAB. The values of the rate constants α_m, β_m, α_h, β_h could be calculated using the relations described by Hodgkin and Huxley (Hodgkin and Huxley 1952) (*e.g.*, $\alpha_m = m_\infty/\tau_m$).

Currents evoked by depolarizations from a holding potential of -70 mV, in cells patched with pipettes filled with a CsCl-based solution, were used to determine the Hodgkin-Huxley rate equations for TTX-S currents. The rates depended on membrane potential such that:

$$\alpha_m = \frac{0.5\left(-V - 33\right)}{e^{\frac{-V-33}{4}} - 1},\ \beta_m = 2.4e^{\frac{-V-65}{21}}$$

$$\alpha_h = 1.1e^{\frac{-V-65}{8}},\ \beta_h = \frac{1}{1+e^{\frac{-V-50}{4}}}$$

Currents evoked by depolarizations from a holding potential of -120 mV, in cells bathed in 0.1 μM TTX and patched with pipettes filled with a CsCl-based solution, were used to determine the rate equations for TTX-R currents. The rates were:

$$\alpha_m = \frac{0.25(-V-54)}{e^{\frac{-V-54}{2.3}}-1},\ \beta_m = 0.86e^{\frac{-V-66}{29}}$$

$$\alpha_h = 0.025e^{\frac{-V-65}{10.5}},\ \beta_h = \frac{1.6}{1+e^{\frac{-V-43}{31}}}$$

<u>K^+ currents</u>

K^+ currents were modeled using the Hodgkin-Huxley formalism (Hodgkin and Huxley 1952):

$$I_K = \overline{G}_K n^4 (V - V_K)$$

with I_K representing the K^+ current, $\bar{G}_K$ the maximal K^+ conductance, n the parametric activation gate, V the membrane potential, and V_K the reversal potential of K^+. A G/G_{max} activation curve was calculated from the sustained depolarization-activated K^+ currents observed in voltage-clamp recordings (from a holding potential of -65 mV); this activation curve was set equal to n_∞^4. Estimates for τ_n were computed by fitting K^+ currents obtained from GG neurons bathed in Na^+-free saline, patched with pipettes filled with a KCl-based solution. The fitting equation was:

$$I_K = A + \left(B - Be^{-\frac{t}{\tau_n}} \right)^4$$

Rates were described by the following relations:

$$\alpha_n = \frac{0.007(-V-66)}{e^{\frac{-V-66}{1.4}}-1},\ \beta_n = 0.37e^{\frac{-V-66}{35}}$$

Leak currents

Leak currents were represented by the following equation:

$$I_{leak} = \overline{G}_{leak}(V - V_{leak})$$

with I_{leak} representing the leak current, $\bar{G}_{leak}$ the maximal leak conductance, V the membrane potential, and V_{leak} the reversal potential of the nonspecific ions assumed to comprise the leak current. $\bar{G}_{leak}$ was calculated with V_{leak} = -60 mV such that the total ionic current equaled 0 (I_i = 0) at V = -55 mV, the average resting potential of GG neurons. This was performed by using the equation:

$$I_i = I_{Na} + I_K + I_{leak}$$

and using the steady-state values m_∞, h_∞, n_∞ for m, h, n, respectively.

Analysis of neuronal excitability

Simulations of 300 ms duration were performed inside nested loops that iterated over increasing amplitudes of depolarizing current injection (inner loop), various initial membrane potentials (middle loop), and different permutations of values for maximal membrane conductances (step size of 5%) of Na^+ channels (outer loop). Sampling frequency was 40 kHz. Maximal leak conductance and E_{leak} were continually adjusted such that: (1) the tested initial membrane potential was stable for the first 25 ms of the simulation, (2) maximal leak conductance always exceeded 0, and (3) $|V_i - V_{leak}| \leq 5$ mV, where V_i denotes the initial membrane potential. This produced a different maximal leak conductance at different membrane potentials. However, the differences in the resultant leak currents were small (<1%) compared to stimulating current amplitudes. Action potentials were collected in an unbiased manner as time points when $V > -20$ mV within 10 ms following the injection of current. Shifts in the modeled activation and inactivation curves of TTX-R currents were achieved by shifting the abscissa (V_m) in the plot of kinetic parameters α_m, β_m, α_h, β_h and repeating the fitting procedure. In individual experiments that involved

modification of maximal Na^+ conductances, either $\bar{G}_{TTX-R}$ or $\bar{G}_{TTX-S}$ was changed, but not both. Data were exported to text files and analyzed in MATLAB.

RESULTS

We investigated the membrane biophysics of mouse GG neurons by performing patch-clamp electrophysiological recordings from acute slices of the far-anterior mouse nose. These slices were prepared from young (p4 - p14) OMP-GFP mice, in which all mature olfactory neurons, including the GG collection, are highlighted by GFP expression (Potter et al. 2001). Even in these young animals, the glial ensheathing layer was evident in immunolabeling experiments with antibodies raised against S100β and GFAP (data not shown). The brief exposure of slices to diluted collagenase facilitated the access of micropipettes to GG neurons (Fig. 1A,B) but did not cause neuronal damage. GG neurons retained the ciliary localization of the membrane-bound guanylate cyclase pGC-G (Liu et al. 2009) and continued to express GFP (Fig. 1B,C).

Spontaneous firing

In extracellular loose-seal recordings, we observed that GG neurons discharged action potentials (APs) in the absence of stimulation. The temporal patterns of discharge of 89 neurons were grouped into three categories:

1) Repetitive single-spike (RSS): Found in 34 neurons (38%), this pattern was characterized by a continuous discharge of APs at regular intervals (Fig. 2A), resulting in firing frequencies of 10-25 Hz (mean ± standard error: 15.2 ± 0.9 Hz). A single mean instantaneous firing rate is visible on representative frequency vs. time plots of RSS firing (Fig. 2B).
2) Phasic: Found in 26 neurons (29%), this pattern consisted of bursts of APs followed by periods of electrical quiescence (Fig. 2C), resulting in an interburst frequency of 0.5-3 Hz (mean: 2.4 ± 0.3

Hz) and a variable intraburst frequency of 10-40 Hz (mean: 19.5 ± 0.6 Hz). Two mean firing rates whose difference is >5 Hz are evident on representative frequency vs. time plots of phasic firing, with lower-valued and higher-valued means corresponding to interburst and intraburst frequencies, respectively (Fig. 2D). The coefficients of variation of these two distributions are small, allowing unambiguous fits to the firing frequencies with Gaussian functions.

3) Sporadic: Found in 29 neurons (33%), this pattern was composed of randomly discharged APs (mean firing frequency: 4.9 ± 0.7 Hz) (Fig. 2E). There are two mean firing rates on representative frequency vs. time plots of sporadic firing (Fig. 2F). The lower-valued mean is smaller than 75% of the higher-valued mean. Due to higher variation in firing frequencies, density estimation is provided by overlapping Gaussian descriptors of the data.

In extracellular recordings of up to 20 min, we observed no instances of spontaneous transition between firing patterns in a single neuron. Examples of all three major firing patterns could be found in separate neurons within a single slice originating from a single animal. We observed that neighboring neurons within a ganglionic cluster fired in different patterns.

Intracellular recordings, obtained from the whole-cell patch clamp configuration, demonstrated the effects of current injections on the firing pattern. Though breakthrough could alter firing rate, it did not alter the spontaneous firing pattern (Supporting Fig. 2). Fig. 3 shows the electrical manipulation of distinct GG neurons that exhibited the various patterns of spontaneous discharge. From the resting potential, we injected currents of 10 s duration in serial steps of 10 pA magnitude, in the range between -30 pA and +50 pA. Fig. 3A-3C show that hyperpolarization of the resting potential inhibited repetitive firing. In contrast, injection of depolarizing current evoked a burst of APs. After burst termination, the rates and patterns of spontaneous firing could be monitored at a steady-state membrane potential.

The 3 main firing patterns observed in GG neurons represented intrinsic modes of discharge. Fig. 3A-B demonstrate the mutual stabilities of RSS and phasic firing, respectively, in that depolarization of the resting potential does not convert RSS firing to phasic firing, and vice versa. At strongly depolarized

resting potentials, the repetitive firing of RSS- and phasic-firing neurons was inhibited and could give the outward appearance of sporadic discharge. However, Fig. 3C shows that sporadic firing can also be an intrinsic state of GG neurons. Phasic or RSS firing was not observed with stronger depolarization in this neuron. A small fraction (4/28, 14%) of neurons manipulated in this manner did not exhibit spontaneous activity at any tested resting potential.

Successive injections of depolarizing current were associated with increases in firing frequency. All 3 firing patterns putatively consist of repetitive elements, whose frequencies are represented by the total firing rate, intraburst rate, and higher-valued mean in the RSS, phasic, and sporadic patterns, respectively. Fig. 3D-E depict the repetitive firing frequency relative to current injection for the depolarization-evoked burst (Fig. 3D) and for the spontaneous discharge (Fig. 3E) from the new steady-state baseline potential (n = 9). The firing frequency increased with stronger injections of depolarizing current.

Na^+ conductance

In voltage clamp experiments, transient inward currents (with an exponential decay time under 3 ms) and sustained outward currents were elicited by depolarizing pulses from a holding potential of -70 mV to test potentials positive of -50 mV (Fig. 4A). The depolarizing pulses did not elicit outward currents when we used a Cs^+-based intra-pipette solution (Fig. 4B), and did not evoke inward currents in the presence of 50 nM tetrodotoxin (TTX) (Fig. 4C) or in Na^+-free extracellular solution containing an equimolar substitution of NMDG for Na^+ (data not shown). Therefore, the inward and outward currents are mediated by voltage-gated Na^+ and K^+ channels, respectively.

To characterize Na^+ currents, we used the Cs^+-based intra-pipette solution. Surprisingly, depolarizing pulses to a test potential of -70 mV from holding potentials in the range of -120 mV to -100 mV elicited inward currents in 69% (24/35) of GG neurons (Fig. 4D). These inward currents exhibited an exponential decay time under 2 ms. They were still found in GG neurons recorded under alternate experimental conditions: without collagenase treatment, in adult mice (age: 1.5 months), with carbogen-

bubbled ACSF serving as the extracellular medium, and with capacitance and series resistance compensation up to 90%. Replacing extracellular Na^+ with NMDG abolished these currents (Fig. 4E), identifying their conducting ion as Na^+. They persisted in 0.5 μM TTX (Fig. 4F).

These results can be explained simply if the total inward Na^+ current in GG neurons is composed of two distinct components. One component is activated at membrane potentials more positive than -50 mV and likely inactivated at potentials more positive than -65 mV. This component is TTX-sensitive (TTX-S). The other component of is activated at potentials more positive than -70 mV and inactivated at potentials more positive than -90 mV. This second component exhibits moderate TTX-resistance (TTX-R). TTX-S and TTX-R currents have different steady-state voltage dependencies, such that at a holding potential of -70 mV, TTX-R currents are inactivated and depolarizing pulses selectively activate TTX-S currents. TTX-R and TTX-S currents are likely conducted through two distinct Na^+ channels with differential sensitivities to TTX. We performed experiments to examine systematically the current-voltage relationship of the Na^+ conductance in GG neurons; the results we describe below support this interpretation of the phenomena.

To characterize the activation of TTX-R currents, we included 0.1 μM TTX in the extracellular solution and applied depolarizing pulses of 100 ms duration from a holding potential of -120 mV (Fig. 5A). TTX-R currents were found in all examined GG neurons at all times. The I-V curve in Fig. 5C shows that TTX-R currents had a reversal potential near +50 mV, consistent with a current carried by Na^+. The time constants of activation (τ_m) and inactivation (τ_h) were fast (<1 ms and <2 ms, respectively) and were voltage dependent (Fig. 5D). The activation curve for TTX-R currents had a midpoint ($V_{1/2}$) of -44 ± 1.8 mV and a slope factor of 6.6 mV (n = 19) (Fig. 5E). TTX-R currents were not activated by depolarizing pulses in a higher extracellular concentration of TTX (2 μM, data not shown). To study steady-state inactivation of TTX-R currents, we depolarized TTX-perfused GG neurons to a test potential of -10 mV from various holding potentials positive of -160 mV (Fig. 5B). As illustrated in Fig. 5E, the inactivation curve of TTX-R currents had a midpoint $V_{1/2}$ of -103 ± 2.0 mV and a slope factor of -13 mV (n = 17).

To study the current-voltage relationship for TTX-S currents, we applied depolarizing pulses from a holding potential of -70 mV, at which TTX-R currents are inactivated, in TTX-free extracellular saline. The activation curve for TTX-S currents exhibited a midpoint $V_{1/2}$ of -34 ± 1.6 mV and a slope factor of 5.0 mV (n = 19) (Fig. 5E). This $V_{1/2}$ value represents a positive 10 mV shift compared to the activation $V_{1/2}$ of TTX-R currents, a statistically significant difference ($p = 0.0001$; two-sample t-test). The voltage activation midpoint of TTX-S currents was indistinguishable between its calculation either by the prepulse method or by the subtraction of TTX-R currents from total Na^+ currents at -120 mV holding potential (Supporting Fig. 3).

The activation curve derived from a holding potential of -120 mV in neurons perfused with extracellular saline exhibited a midpoint $V_{1/2}$ of -39 ± 1.6 mV (n = 43) (Fig. 5D). This value differed significantly from the activation $V_{1/2}$ of isolated TTX-R and TTX-S currents ($p = 0.0027$; two sample t-test), being more positive than the $V_{1/2}$ of TTX-R currents and more negative than the $V_{1/2}$ of TTX-S currents. The shape of the activation curve was approximated by the linear summation of the individual activation curves of TTX-R and TTX-S currents, with a ~55% contribution from the TTX-R curve and a ~45% contribution from the TTX-S curve. The inactivation curve of the TTX-S currents was calculated by subtracting the inactivation curve for TTX-R currents from the inactivation curve for the total Na^+ currents. The midpoint $V_{1/2}$ of inactivation for TTX-S currents was -65 mV, with a slope factor of -9.5 mV (Fig. 5E). These results are consistent with the dual composition of Na^+ currents in GG neurons.

On average, the TTX-R currents had more hyperpolarized activation and inactivation curves than their TTX-S counterparts. However, an examination of the activation curves of Na^+ currents in single neurons revealed that this was not always the rule. Within 5 min after breakthrough, we obtained the total activation curve of inward Na^+ currents from holding potentials of -55 mV, -70 mV, -85 mV, and -120 mV. At more-negative holding potentials, there was a greater contribution of the TTX-R current to the total activation curve. In 9/30 (30%) GG neurons examined in this manner, the activation $V_{1/2}$ values derived from all 4 holding potentials were within a range of 3 mV, suggesting that TTX-R and TTX-S currents have similar activation voltage dependencies in these neurons. In the other 21 GG neurons, the

activation $V_{1/2}$ values were successively more negative as the holding potential moved from -70 mV to -120 mV. In these neurons, the shifting of activation $V_{1/2}$ values in the negative direction likely reflected the increasing contribution of the hyperpolarized TTX-R activation curve to the total activation curve (Supporting Fig. 4).

Voltage-dependent K^+ and Ca^{2+} currents

A hyperpolarized activation threshold may be a nonspecific property of more-negative holding potentials and may be found in other ionic conductances in the GG. With this idea, we examined the activation curves of K^+ currents. GG neurons were studied in the whole-cell configuration with a K^+-containing intrapipette solution and a Na^+-free extracellular solution.

Fig. 6A shows that, from a holding potential of -90 mV, long (2 s) pulses to test potentials in the range between -50 mV and +40 mV evoked outward currents. The outward currents exhibited a reversal potential of approximately -80 mV (Fig 6B). These outward currents were sustained throughout the 2 s pulse at test potentials in the range between -60 mV and -10 mV. However, at test potentials more positive than -10 mV, a partially inactivating component of the outward current was observed (Fig. 6A). At a test potential of +20 mV, this inactivation had an exponential fast τ_f of 210 ± 77 ms and a slow τ_s of 2800 ± 710 ms (n=7). The steady-state component represented ~70% of the peak current. We previously showed that all of these outward currents were absent when Cs^+ replaced K^+ in the intrapipette solution (Fig. 4B); thus the currents are carried by K^+. The total K^+ current (I_K) in GG neurons is thus composed of sustained and inactivating components.

The inactivating component of I_K in GG neurons is dissimilar from the A-type current described by Connor and Stevens (Connor and Stevens 1971b). We measured and subtracted the peak outward currents evoked by depolarizing pulses to test potentials in the range between -60 mV and +40 mV from 2 different holding potentials, -65 mV ($I_{K,-65}$) and -130 mV ($I_{K,-130}$). Consistent with qualitative observations, the inactivating component of I_K was only activated at potentials more positive than -10 mV, well positive of the activation threshold of the sustained component of I_K (approximately -50 mV) (Fig. 6C-D). We

next applied depolarizing 2.5 s pulses to a test potential of +20 mV from prepulses in the range between -170 mV and +20 mV. Fig. 6D shows full inactivation of the inactivating component of I_K only at membrane potentials more positive than 0 mV, well positive of resting potential. The K^+ currents in GG neurons have the same activation threshold across different holding potentials (Fig. 6C). We did not explore pharmacological perturbations of the outward current.

In contrast to K^+ currents and similar to Na^+ currents, putative Ca^{2+} currents in the GG possess an inactivating low-threshold component. We examined the residual inward current, putatively the total Ca^{2+} current (I_{Ca}), using an intrapipette solution containing Cs^+ and an extracellular solution containing 2 μM TTX. From a holding potential of -120 mV, 100 ms depolarizing pulses to test potentials in the range between -70 mV and +50 evoked inward currents. As shown in the I-V curve in Fig. 6E, the inward current magnitude exhibited 2 distinct components (n = 4). One component was activated near resting potential, and the other was activated positive of the resting potential. The time dependency of these currents could be observed when 25 mM $BaCl_2$ was added to the extracellular solution, which enhanced the currents. The low-threshold component of I_{Ca} exhibited a gradual inactivation during a 100 ms depolarizing pulse (Fig. 6F); in contrast, the high voltage-activated component did not inactivate during a 100 ms depolarizing pulse to a test potential of +10 mV from a holding potential of -50 mV. The maximum magnitude of the observed inward I_{Ca} in physiological recording conditions was ~70 pA, nearly ~10-fold smaller than the tail currents observed in Fig. 4D.

Hyperpolarization-activated currents

In voltage-clamp experiments, hyperpolarizing pulses of 1.5 s duration from a holding potential of -55 mV revealed sustained inward currents (I_h) in most (26/30, 87%) GG neurons (Fig. 7A), suggesting the existence of hyperpolarization-activated cationic channels. I_h time-dependent activation could be described by a two-component exponential function (fast: $\tau_f = 232 \pm 27$ ms; slow: $\tau_s = 1120 \pm 690$ ms, corr. = 0.98). The rate of onset (τ_f) was faster with larger currents (data not shown), consistent with previous descriptions of I_h (Lynch and Barry 1991). Similar to I_h in olfactory sensory neurons (Vargas and

Lucero 1999), the currents in GG neurons were blocked by adding 5 mM CsCl to the extracellular solution (Fig. 7B). The I-V curve in Fig. 7C shows that the currents had a peak density of approximately -19 pA/pF at a test potential of –135 mV with an extracellular [K^+] of 2.5 mM. The activation curve in Fig. 7D demonstrates an activation $V_{1/2}$ of -105 mV and a slope factor of -9.3 mV. In intracellular current-clamp experiments, we observed that injections of hyperpolarizing current induced voltage sags in GG neurons (Fig. 3A-C), consistent with predicted effect of I_h.

Since hyperpolarization- and cyclic nucleotide-activated channels (HCN) mediate I_h (Biel et al. 2009), to test which channels mediated I_h currents, we performed RT-PCR in the nasal vestibule, where GG neurons reside, with cerebral tissue as a positive control (Fig. 9E). Only *Hcn1* mRNA was detected in the nasal vestibule. To confirm the expression of HCN1 protein in GG neurons, immunofluorescence analyses were performed using an HCN1 antibody (Fig. 9F). HCN1 was detected in most GFP+ GG neurons. These results show that I_h in GG neurons was likely mediated by HCN1 channels.

Predictions and measurements of excitability

In whole-cell recordings obtained with a K^+ intrapipette solution, the mean resting potential (V_m) was -54 ± 2.4 mV (n = 31). At resting potential, the input resistance was 2.3 ± 0.5 GΩ. Because both TTX-R and TTX-S currents represent fast-inactivating Na^+ conductance, they each can support APs. However, spontaneous APs were entirely absent when GG neurons were bathed with 0.1 μM TTX, suggesting that spontaneous APs were primarily mediated by TTX-S Na^+ currents. This observation is consistent with the voltage-clamp data of Fig. 5E, showing the near-full inactivation of TTX-R currents at resting potential.

In the presence of 0.1 μM TTX, APs could be evoked from a resting potential of -90 mV but not from -60 mV (Fig. 8A). This result agrees with the voltage-clamp data, showing the de-inactivation of TTX-R currents at negative potentials (Fig. 5E). In current-clamp recordings, we compared the APs supported by TTX-R currents only, TTX-S currents only, and both TTX-R and TTX-S currents by

injecting 10 pA depolarizing current from baseline potentials of -120 mV in 0.1 μM TTX, -60 mV in saline, and -120 mV in saline, respectively. The 3 types of APs have similar shapes, with half-widths under 2 ms. However, APs solely supported by TTX-R currents were not always followed by an AHP (Fig. 8B).

What is the function of TTX-R Na^+ currents that are mostly inactivated near resting potential? To address this question, we developed a Hodgkin-Huxley model of the GG neuron *in silico* and included a second Na^+ current with the steady-state properties of the TTX-R current. Table 1 lists the parameters, including $\bar{G}_{TTX-R}$ (maximum TTX-R conductance), that were derived from the voltage-clamp data. In computer simulations, the injection of 0.1 nA current of 10 ms duration from a resting potential of -55 mV triggered a single AP. Setting both $\bar{G}_{TTX-R}$ and $\bar{G}_{TTX-S}$ equal to 0 resulted in the removal of the AP. Selective restoration of $\bar{G}_{TTX-S}$ resulted in the recovery of the AP (data not shown). Thus, the computer model replicates the experimental observation that APs elicited from a resting potential of -55 mV are dominantly supported by TTX-S currents.

Repetitive firing from a resting potential of -55 mV could be evoked with a 10 ms current injection of 1 pA amplitude by increasing $\bar{G}_{TTX-R}$ and $\bar{G}_{TTX-S}$ to levels that were 30 times (scale: 30) their Table 1 values. $\bar{G}_K$ was not changed in these simulations. Fig. 8C demonstrates the effect on repetitive firing that resulted from modifying the ratio of TTX-R and TTX-S Na^+ conductance. At a conductance ratio (r_G, the value obtained from $\bar{G}_{TTX-R}/\bar{G}_{TTX-S}$) of 1.0, the transient injection of depolarizing current evoked a long-running train of APs. However, at an r_G value of 1.3, obtained by modifying $\bar{G}_{TTX-R}$, the current injection evoked a self-limiting burst of APs. The decreasing AP amplitudes observed with successive spikes in the burst *in silico* were consistent with observations *in vitro*. At r_G values exceeding 1.7, the current injection resulted in a single AP. The bursts of APs evoked at r_G values less than 0.9 led to a depolarized steady-state resting potential that was not observed *in vitro*. Similar results (Fig. 8D) were obtained when modifying $1/r_G$ (by changing $\bar{G}_{TTX-S}$).

In the computer model, we tested the effects of shifting both the activation and inactivation curves of the TTX-R current. Fig. 8E demonstrates that shifting both curves by +10 mV abrogated the repetitive firing from -55 mV. A -10 mV shift in the steady-state curves of the TTX-R current resulted in a similar cessation of repetitive firing. Repetitive firing could be initiated with these positively or negatively shifted curves at more positive and negative resting potentials, respectively. The most suitable membrane potentials could be predicted by calculating the approximate rheobase at various potentials (Supporting Fig. 5). We were unable to obtain the burst firing seen in Fig. 8C-D by changing r_G at these more-suitable membrane potentials.

Finally, we tested the effect of a TTX-R "knockout" by setting $\bar{G}_{TTX-R}$ equal to 0. Repetitive firing could be achieved with a 10 ms injection of 1 pA depolarizing current from a resting potential of -49 mV (Fig. 8F). No burst activity was evoked at various tested values of $\bar{G}_{TTX-S}$. Thus, TTX-R current is predicted to promote burst firing. Overall, this computer model of the "average" GG neuron suggests that the ratio and specific voltage dependencies of TTX-R and TTX-S conductances determine the repetitiveness of firing.

Pharmacological modulation of spontaneous firing

To test the role of Na^+ conductance on the degree of repetitive firing, we perfused 0.1 μM TTX onto GG neurons in extracellular recordings. The gradual increase in [TTX] should increase the ratio of TTX-R conductance to TTX-S conductance (r_G). Fig. 9A demonstrates a neuron that initially fired in the RSS pattern (trace 1). At an intermediate exposure to TTX (trace 2), the firing converted to the less-repetitive phasic pattern. At full exposure to 0.1 μM TTX, the firing was abolished (trace 3). Washout of TTX resulted in the recovery of the phasic pattern at an intermediate stage and, finally, restoration of the original RSS pattern (trace 4). Phasic-firing neurons converted to the least-repetitive sporadic firing pattern at intermediate stages of the perfusion (Fig. 9B). None of the 9 tested neurons exhibited an increase in the repetitiveness of firing at intermediate [TTX].

We next tested the contribution of I_h to spontaneous firing in GG neurons. In extracellular recordings, perfusion of 5 mM Cs^+, which abolished I_h, reduced the rate of spontaneous AP discharge in 6/17 (35%) GG neurons. The Cs^+-mediated inhibition was found in neurons representing each of the 3 identified spontaneous firing patterns. In RSS-firing and sporadically-firing neurons, Cs^+ reduced the total frequency of spontaneous discharge (Fig. 9C-D). In GG neurons that fired in the phasic pattern, Cs^+ reduced the intraburst firing frequency (Fig. 9E). Untreated GG neurons exhibited a stable firing pattern but could show small (<10%) and temporary changes in firing rate (Supporting Fig. 6). These temporary changes could be readily distinguished from Cs^+-induced changes on the basis of their different time dependencies. In whole-cell recordings, 5 mM CsCl resulted in the acute, reversible hyperpolarization of resting membrane potentials in 3/5 neurons (mean hyperpolarization: -6.0 ± 2.0 mV).

DISCUSSION

GG neurons in nasal vestibule slices

The electrophysiological characterization of GG neurons has been challenging, because the stiff surrounding tissue vitiates the access of recording electrodes to the neurons. We seldom obtained recordings from untreated slices. We demonstrate that gentle collagenase treatment of transverse slices of the mouse nasal vestibule enables patch clamp recordings from GG neurons. There are several reasons collagenase treatment helps. In electron micrographs of the mouse nasal vestibule, collagen fibrils appear to support adhesion of glial cells to neurons within clusters of GG cells (Brechbuhl et al. 2008; Liu et al. 2009). Digestion of these fibrils reduces the tension on the glial cell membranes and enables the glial cells to retract. Clusters of GG neurons, normally embedded within the tough extracellular matrix (ECM) of the slice, protrude after collagenase treatment. The reduction in ECM stiffness increases the compliance of the neuronal membrane to suction. The patch pipette also moves more readily through a softened ECM to the surfaces of the neurons. We observed no obvious differences in spontaneous firing patterns and Na^+ currents in GG neurons between collagenase-treated and untreated slices (data not shown). These data

suggest that protease digestion does not change the intrinsic properties of GG neurons. However, the treatment likely disrupted the interactions of GG neurons with other neurons or glial cells.

Voltage-dependent ionic currents

In whole-cell recordings from GG neurons, we activated distinct sets of fast-inactivating inward Na^+ currents by depolarizing the membrane from either more (-120 mV) or less (-70 mV) hyperpolarized holding potentials. The former protocol induced the TTX-R Na^+ currents that exhibited hyperpolarized shifts in both activation and inactivation curves relative to the TTX-S currents evoked by the latter protocol. Since hyperpolarization does not decrease TTX sensitivity of Na^+ channels (Roy and Narahashi 1992), we suppose that TTX-R and TTX-S currents are mediated by different Na^+ channels.

Three groups of voltage-gated Na^+ channels are reported according to their high (IC_{50}: 10 nM), moderate (IC_{50}: 1 μM), or low (IC_{50}: 50 uM) TTX sensitivity (Catterall 2000; Goldin et al. 2000). Both TTX-sensitive and TTX-resistant Na^+ currents are found in small dorsal root ganglion neurons (Akopian et al. 1996; Cummins et al. 1999; Roy and Narahashi 1992). The TTX-sensitive Na^+ currents there exhibit more hyperpolarized activation and inactivation voltages than TTX-resistant ones. However, TTX-resistant Na^+ currents in nociceptive neurons decay with a time constant ~5 ms, more slowly than the fast-inactivating TTX-R currents found in this study. TTX-sensitive and TTX-insensitive fast inactivating Na^+ currents are also reported in vomeronasal sensory neurons (Liman and Corey 1996). The TTX-insensitive Na^+ currents have hyperpolarized inactivation relations, but similar activation relations, in comparison with TTX-sensitive currents. The two subtypes of Na^+ currents in GG neurons might operate differently from those expressed in both dorsal root ganglion neurons and vomeronasal sensory neurons.

GG neurons exhibit outward K^+ currents that have sustained and inactivating components. The activation of the inactivating component was predominantly at membrane potentials more positive than -10 mV. GG neurons show graded firing rates vs. current injection and fire at lower rates than predicted by the Hodgkin-Huxley model, which are functional hallmarks the inactivating A-type K^+ current. However, the activation and inactivation curves of the inactivating K^+ current in GG neurons do not

resemble the properties of A-type current originally reported by Connor and Stevens (Connor and Stevens 1971b). Instead, the properties reported here are generally consistent with a partially inactivating delayed outward rectifier (Aldrich et al. 1979; Connor and Stevens 1971a; Ehrenstein and Gilbert 1966)). As the K^+ current may require longer times to recover from inactivation (Aldrich et al. 1979), the inactivating K^+ current may contribute to the early termination of repetitive firing by gradually reducing the AHP magnitude.

We detected I_h in most GG neurons in both voltage- (Fig. 7) and current-clamp experiments (Fig. 3). I_h contributes to pacemaker firing in several types of neurons in the CNS (Biel et al. 2009; Overton and Clark 1997; Wilson 2005) (Neuhoff et al. 2002) (Heida et al. 2008), but not in others (Raman and Bean 1999; 1997). Blocking I_h inhibited only 33% of GG neurons, with no bias in firing pattern. In the responsive cells, I_h likely helped to maintain a depolarized resting potential. This is consistent with the observed Cs^+-induced hyperpolarization. The activation curve presented in Fig. 7D predicts a small amount of activated I_h near the resting potential. In the unresponsive cells, the input resistance at rest may have been too high to reveal I_h contributions, or the resting potential may have been more depolarized than the mean value reported here. As I_h is temperature sensitive (Vargas and Lucero 1999), a greater contribution may have been observed had the experiments been performed at 37˚C.

Biophysical basis for spontaneous firing

We observed that most GG neurons spontaneously fired in either a repetitive single-spike (RSS), phasic, or sporadic pattern, as reported in CNS neurons (Grace and Bunney 1984; Swensen and Bean 2003; Wilson 2005). The RSS pattern usually exhibited a firing frequency of >10 Hz, while the phasic pattern showed long (0.3–2 s) interburst intervals and high intraburst frequency (>10 Hz). Given that both firing rate and firing pattern modulate neurotransmitter release (Aosaki et al. 1994; Overton and Clark 1997), we assume that the neurons with different firing patterns might play different roles in chemosensory information encoding.

We were not able to interconvert between RSS and phasic firing patterns in GG neurons by simple injections of depolarizing current (Fig. 3), demonstrating that firing pattern is an intrinsic property of a GG neuron. The phasic discharge pattern cannot be solely mediated by the activity of an inactivating "T-type" voltage-gated Ca^{2+} channel (Llinas and Jahnsen 1982), as bursting behavior was observed at a resting membrane potential of -55 mV, at which T-type currents are inactivated (Huguenard 1996). The actions of Ca^{2+}-activated K^+ conductances are also insufficient to explain the bursting behavior, because the break hyperpolarizations indicative of their activity, seen in other bursting systems (Goldberg and Wilson 2005), were not observed in GG neurons (Fig. 3B).

We believe the finely tuned interaction of Na^+ and K^+ channels explains the 3 spontaneous firing patterns in GG neurons. This explanation requires a short (<10 ms) initiating current that triggers the first AP. The ionic basis of this proposed initiating current is presently unknown. As demonstrated in computer simulations, the ratio of the two main components of the total Na^+ conductance, acting in concert with the K^+ conductance, is sufficient to specify the degree of repetitive firing that follows the initial AP. Sporadic firing would result from infrequent spike initiation combined with low repetitiveness. Phasic firing would arise from infrequent spike initiation combined with moderate repetitiveness. RSS firing would stem either from infrequent spike initiation with high repetitiveness, or from relatively frequent spike initiation with moderate repetitiveness. However, due to the complex relationship between absolute Na^+ half-activation values, K^+ activation, and membrane potential, we were unable to correlate experimentally these parameters with firing pattern in single neurons.

The TTX-induced alterations in firing pattern lend confidence to the computer model. As TTX acts primarily on the TTX-S current, perfusion of TTX should lead to a decrease in the maximal TTX-S conductance, effectively increasing the conductance ratio r_G. In extracellular recordings of RSS and phasic-firing neurons, the spontaneous discharge pattern transitioned to phasic and sporadic patterns, respectively. This confirms the categorization of the 3 different firing patterns as variations of a repetitive firing tendency and suggests that the firing patterns have the same fundamental ionic basis whose components are differently tuned. Other assumptions and predictions of the model will require additional

study. The firing frequency of repetitive spikes observed in the computer model is between 40 Hz and 90 Hz, which is 3-6 times higher than the frequencies observed in patch clamp experiments. The elucidation of different ionic currents, including Ca^{2+}-activated currents, and the elaboration of inactivating K^+ (Aldrich 1981) and voltage-dependent Ca^{2+} currents (Wang et al. 1991) into the model may be helpful in later versions. Because I_h only affected spontaneous firing in ~35% of GG neurons, we excluded it from the model to focus on the contributions of the TTX-R current.

To achieve the repetitive firing patterns in the computer model, the maximal Na^+ conductance had to be increased to 30 times the value obtained from voltage clamp experiments. Recent studies of the axon initial segment (AIS), where APs originate, in other neuronal systems show a Na^+ channel density in the AIS that can be 50 times the density found in the soma (Kole et al. 2008). In the voltage clamp experiments here, the observed Na^+ conductance is thus likely to be spatially nonuninform. The 30-fold increase in the Na^+ conductance resulted in a value that approximated the Na^+ conductance in the squid giant axon (0.14 S/cm^2 in this study vs. 0.12 S/cm^2 in the squid giant axon) (Hodgkin and Huxley 1952).

The experiments presented here demonstrate that 2 distinct Na^+ currents can generate heterogeneous patterns of firing, including a pulsatile pattern. Molecular identification of the TTX-R Na^+ channel in GG neurons will be critical. The computer model predicts that a genetic ablation of the TTX-R channel in GG neurons should reduce the proportion of neurons in the phasic firing state (see Fig. 8F). Future experimentation should also focus on potential ways in which an individual GG neuron can modulate or switch firing patterns. Our experiments suggest that endogenous modification of the Na^+ conductance, in particular the TTX-R conductance, may drive pattern selection. Potential modifiers include mechanical stretch (Beyder et al. 2010), calmodulin (Young and Caldwell 2005), corticosteroids (Filatov and Rich 2004), protein kinase C activity (Watson and Gold 1997), and polyunsaturated fatty acids (Vreugdenhil et al. 1996). β-subunits of Na^+ channels also play important modulatory roles in steady-state Na^+ channel properties (Patino and Isom 2010; Qu et al. 2001). Developmental or activity-induced changes in the expression of Na^+ channels can affect the relative Na^+ conductances and the pattern of spontaneous discharge.

Perspectives on chemosensory function

While most GG neurons exhibit Ca^{2+} responses to alarm pheromone and cold, this study shows that the actual electrical outputs of GG neurons are diverse. GG neurons segregate into three equally represented classes by their basal firing pattern. Thus, alarm pheromone and cold likely elicit changes in all three types of neurons.

GG neurons exhibit two mechanisms for AP generation that is explained by the presence of two fast-inactivating Na^{+} currents. Beyond its proposed function in determining spontaneous firing pattern, the TTX-R current may be responsible for a different interpretation of evoked APs at more-negative potentials. For example, APs evoked from a hyperpolarized baseline may activate Ca^{2+} influx through an inactivating voltage-gated Ca^{2+} channel. Thus, in GG neurons, hyperpolarizing stimuli may have a distinct signature beyond a mere reduction in firing rate. A recent report has shown that, in olfactory sensory neurons of the main olfactory epithelium, a second fast-inactivating Na^{+} channel is essential for the transduction of odor information to the olfactory bulb (Weiss et al. 2011). In GG neurons, spontaneous firing from a hyperpolarized resting potential may represent a distinct mode of odor transduction, due to the mobilization of TTX-R currents. Within a single neuron, multimodal detection can possibly be supported by the depolarization of the resting potential by some odors and its hyperpolarization by others.

In an earlier study, we demonstrated that GG neurons express a membrane-bound guanylate cyclase and downstream cGMP signaling components (Liu et al. 2009), similar to the GC-D olfactory subsystem, whose neurons are located in the caudal recesses of the nasal cavity (Juilfs et al. 1997) and respond to multimodal stimuli (Hu et al. 2007; Leinders-Zufall et al. 2007; Munger et al. 2010). Contrary to early observations on the electrical function of the GC-D subsystem (Leinders-Zufall et al. 2007; Munger et al. 2010), GG neurons appear to have diverse electrical outputs that can be potentially explained by an unusual set of underlying ionic conductances. This study shows that the GG has a variety of biophysical mechanisms that can potentially interact to produce complex and heterogeneous behaviors.

For example, the cyclic nucleotides that are essential for olfactory signal transduction (Zufall and Munger 2001) could also modulate I_h in GG neurons (Biel et al. 2009). The GG should serve as a model experimental system to explore how a small number of neurons performs multiple sensory functions.

ACKNOWLEDGMENTS

We thank J. Gutierrez, A.R. Douglas, and S.M.M. Alaniz for animal care and husbandry. This project was supported by grants from the U.S. National Institutes of Health and the U.S. National Science Foundation.

CONTRIBUTIONS

C.Y.L., C.X., H.A.L., S.E.F., and D.S.K. designed experiments. C.X. and H.A.L. contributed equipment. C.Y.L., C.X., and D.S.K. performed the experiments. C.Y.L. wrote the manuscript.

REFERENCES

Akopian AN, Sivilotti L, and Wood JN. A tetrodotoxin-resistant voltage-gated sodium channel expressed by sensory neurons. *Nature* 379: 257-262, 1996.

Aldrich RW. Inactivation of voltage-gated delayed potassium current in molluscan neurons. A kinetic model. *Biophys J* 36: 519-532, 1981.

Aldrich RW, Jr., Getting PA, and Thompson SH. Inactivation of delayed outward current in molluscan neurone somata. *J Physiol* 291: 507-530, 1979.

Aosaki T, Tsubokawa H, Ishida A, Watanabe K, Graybiel AM, and Kimura M. Responses of tonically active neurons in the primate's striatum undergo systematic changes during behavioral sensorimotor conditioning. *J Neurosci* 14: 3969-3984, 1994.

Beyder A, Rae JL, Bernard C, Strege PR, Sachs F, and Farrugia G. Mechanosensitivity of Nav1.5, a voltage-sensitive sodium channel. *J Physiol* 588: 4969-4985, 2010.

Biel M, Wahl-Schott C, Michalakis S, and Zong X. Hyperpolarization-activated cation channels: from genes to function. *Physiol Rev* 89: 847-885, 2009.

Brechbuhl J, Klaey M, and Broillet MC. Grueneberg ganglion cells mediate alarm pheromone detection in mice. *Science* 321: 1092-1095, 2008.

Catterall WA. From ionic currents to molecular mechanisms: the structure and function of voltage-gated sodium channels. *Neuron* 26: 13-25, 2000.

Chao YC, Cheng CJ, Hsieh HT, Lin CC, Chen CC, and Yang RB. Guanylate cyclase-G, expressed in the Grueneberg ganglion olfactory subsystem, is activated by bicarbonate. *Biochem J* 432: 267-273, 2010.

Connor JA, and Stevens CF. Inward and delayed outward membrane currents in isolated neural somata under voltage clamp. *J Physiol* 213: 1-19, 1971a.

Connor JA, and Stevens CF. Voltage clamp studies of a transient outward membrane current in gastropod neural somata. *J Physiol* 213: 21-30, 1971b.

Cummins TR, Dib-Hajj SD, Black JA, Akopian AN, Wood JN, and Waxman SG. A novel persistent tetrodotoxin-resistant sodium current in SNS-null and wild-type small primary sensory neurons. *J Neurosci* 19: RC43, 1999.

Ehrenstein G, and Gilbert DL. Slow changes of potassium permeability in the squid giant axon. *Biophys J* 6: 553-566, 1966.

Filatov GN, and Rich MM. Hyperpolarized shifts in the voltage dependence of fast inactivation of Nav1.4 and Nav1.5 in a rat model of critical illness myopathy. *J Physiol* 559: 813-820, 2004.

Fleischer J, Hass N, Schwarzenbacher K, Besser S, and Breer H. A novel population of neuronal cells expressing the olfactory marker protein (OMP) in the anterior/dorsal region of the nasal cavity. *Histochem Cell Biol* 125: 337-349, 2006a.

Fleischer J, Mamasuew K, and Breer H. Expression of cGMP signaling elements in the Grueneberg ganglion. *Histochem Cell Biol* 131: 75-88, 2009.

Fleischer J, Schwarzenbacher K, Besser S, Hass N, and Breer H. Olfactory receptors and signalling elements in the Grueneberg ganglion. *J Neurochem* 98: 543-554, 2006b.

Fleischer J, Schwarzenbacher K, and Breer H. Expression of trace amine-associated receptors in the Grueneberg ganglion. *Chem Senses* 32: 623-631, 2007.

Fuss SH, Omura M, and Mombaerts P. The Grueneberg ganglion of the mouse projects axons to glomeruli in the olfactory bulb. *Eur J Neurosci* 22: 2649-2654, 2005.

Goldberg JA, and Wilson CJ. Control of spontaneous firing patterns by the selective coupling of calcium currents to calcium-activated potassium currents in striatal cholinergic interneurons. *J Neurosci* 25: 10230-10238, 2005.

Goldin AL, Barchi RL, Caldwell JH, Hofmann F, Howe JR, Hunter JC, Kallen RG, Mandel G, Meisler MH, Netter YB, Noda M, Tamkun MM, Waxman SG, Wood JN, and Catterall WA. Nomenclature of voltage-gated sodium channels. *Neuron* 28: 365-368, 2000.

Grace AA, and Bunney BS. The control of firing pattern in nigral dopamine neurons: burst firing. *J Neurosci* 4: 2877-2890, 1984.

Grüneberg H. A ganglion probably belonging to the N. terminalis system in the nasal mucosa of the mouse. *Z Anat Entwicklungsgesch* 140: 39-52, 1973.

Heida T, Marani E, and Usunoff KG. The subthalamic nucleus part II: modelling and simulation of activity. *Adv Anat Embryol Cell Biol* 199: 1-85,vii, 2008.

Hines ML, and Carnevale NT. The NEURON simulation environment. *Neural Comput* 9: 1179-1209, 1997.

Hodgkin AL, and Huxley AF. A quantitative description of membrane current and its application to conduction and excitation in nerve. *J Physiol* 117: 500-544, 1952.

Hu J, Zhong C, Ding C, Chi Q, Walz A, Mombaerts P, Matsunami H, and Luo M. Detection of near-atmospheric concentrations of CO2 by an olfactory subsystem in the mouse. *Science* 317: 953-957, 2007.

Huguenard JR. Low-threshold calcium currents in central nervous system neurons. *Annu Rev Physiol* 58: 329-348, 1996.

Juilfs DM, Fulle HJ, Zhao AZ, Houslay MD, Garbers DL, and Beavo JA. A subset of olfactory neurons that selectively express cGMP-stimulated phosphodiesterase (PDE2) and guanylyl cyclase-D define a unique olfactory signal transduction pathway. *Proc Natl Acad Sci U S A* 94: 3388-3395, 1997.

Kole MH, Ilschner SU, Kampa BM, Williams SR, Ruben PC, and Stuart GJ. Action potential generation requires a high sodium channel density in the axon initial segment. *Nat Neurosci* 11: 178-186, 2008.

Koos DS, and Fraser SE. The Grueneberg ganglion projects to the olfactory bulb. *Neuroreport* 16: 1929-1932, 2005.

Leinders-Zufall T, Cockerham RE, Michalakis S, Biel M, Garbers DL, Reed RR, Zufall F, and Munger SD. Contribution of the receptor guanylyl cyclase GC-D to chemosensory function in the olfactory epithelium. *Proc Natl Acad Sci U S A* 104: 14507-14512, 2007.

Liman ER, and Corey DP. Electrophysiological characterization of chemosensory neurons from the mouse vomeronasal organ. *J Neurosci* 16: 4625-4637, 1996.

Liu CY, Fraser SE, and Koos DS. Grueneberg ganglion olfactory subsystem employs a cGMP signaling pathway. *J Comp Neurol* 516: 36-48, 2009.

Llinas R, and Jahnsen H. Electrophysiology of mammalian thalamic neurones in vitro. *Nature* 297: 406-408, 1982.

Lynch JW, and Barry PH. Inward rectification in rat olfactory receptor neurons. *Proc Biol Sci* 243: 149-153, 1991.

Mamasuew K, Breer H, and Fleischer J. Grueneberg ganglion neurons respond to cool ambient temperatures. *Eur J Neurosci* 28: 1775-1785, 2008.

Mamasuew K, Hofmann N, Breer H, and Fleischer J. Grueneberg ganglion neurons are activated by a defined set of odorants. *Chem Senses* 36: 271-282, 2011.

Mamasuew K, Michalakis S, Breer H, Biel M, and Fleischer J. The cyclic nucleotide-gated ion channel CNGA3 contributes to coolness-induced responses of Grueneberg ganglion neurons. *Cell Mol Life Sci* 67: 1859-1869, 2010.

Munger SD, Leinders-Zufall T, McDougall LM, Cockerham RE, Schmid A, Wandernoth P, Wennemuth G, Biel M, Zufall F, and Kelliher KR. An olfactory subsystem that detects carbon disulfide and mediates food-related social learning. *Curr Biol* 20: 1438-1444, 2010.

Neuhoff H, Neu A, Liss B, and Roeper J. I(h) channels contribute to the different functional properties of identified dopaminergic subpopulations in the midbrain. *J Neurosci* 22: 1290-1302, 2002.

Overton PG, and Clark D. Burst firing in midbrain dopaminergic neurons. *Brain Res Brain Res Rev* 25: 312-334, 1997.

Patino GA, and Isom LL. Electrophysiology and beyond: multiple roles of Na+ channel beta subunits in development and disease. *Neurosci Lett* 486: 53-59, 2010.

Potter SM, Zheng C, Koos DS, Feinstein P, Fraser SE, and Mombaerts P. Structure and emergence of specific olfactory glomeruli in the mouse. *J Neurosci* 21: 9713-9723, 2001.

Qu Y, Curtis R, Lawson D, Gilbride K, Ge P, DiStefano PS, Silos-Santiago I, Catterall WA, and Scheuer T. Differential modulation of sodium channel gating and persistent sodium currents by the beta1, beta2, and beta3 subunits. *Mol Cell Neurosci* 18: 570-580, 2001.

Raman IM, and Bean BP. Ionic currents underlying spontaneous action potentials in isolated cerebellar Purkinje neurons. *J Neurosci* 19: 1663-1674, 1999.

Raman IM, and Bean BP. Resurgent sodium current and action potential formation in dissociated cerebellar Purkinje neurons. *J Neurosci* 17: 4517-4526, 1997.

Roppolo D, Ribaud V, Jungo VP, Luscher C, and Rodriguez I. Projection of the Gruneberg ganglion to the mouse olfactory bulb. *Eur J Neurosci* 23: 2887-2894, 2006.

Roy ML, and Narahashi T. Differential properties of tetrodotoxin-sensitive and tetrodotoxin-resistant sodium channels in rat dorsal root ganglion neurons. *J Neurosci* 12: 2104-2111, 1992.

Schmid A, Pyrski M, Biel M, Leinders-Zufall T, and Zufall F. Grueneberg ganglion neurons are finely tuned cold sensors. *J Neurosci* 30: 7563-7568, 2010.

Storan MJ, and Key B. Septal organ of Gruneberg is part of the olfactory system. *J Comp Neurol* 494: 834-844, 2006.

Swensen AM, and Bean BP. Ionic mechanisms of burst firing in dissociated Purkinje neurons. *J Neurosci* 23: 9650-9663, 2003.

Tachibana T, Fujiwara N, and Nawa T. The ultrastructure of the ganglionated nerve plexus in the nasal vestibular mucosa of the musk shrew (Suncus murinus, insectivora). *Arch Histol Cytol* 53: 147-156, 1990.

Vargas G, and Lucero MT. Dopamine modulates inwardly rectifying hyperpolarization-activated current (Ih) in cultured rat olfactory receptor neurons. *J Neurophysiol* 81: 149-158, 1999.

Vreugdenhil M, Bruehl C, Voskuyl RA, Kang JX, Leaf A, and Wadman WJ. Polyunsaturated fatty acids modulate sodium and calcium currents in CA1 neurons. *Proc Natl Acad Sci U S A* 93: 12559-12563, 1996.

Wang XJ, Rinzel J, and Rogawski MA. A model of the T-type calcium current and the low-threshold spike in thalamic neurons. *J Neurophysiol* 66: 839-850, 1991.

Watson CL, and Gold MR. Modulation of Na+ current inactivation by stimulation of protein kinase C in cardiac cells. *Circ Res* 81: 380-386, 1997.

Weiss J, Pyrski M, Jacobi E, Bufe B, Willnecker V, Schick B, Zizzari P, Gossage SJ, Greer CA, Leinders-Zufall T, Woods CG, Wood JN, and Zufall F. Loss-of-function mutations in sodium channel Nav1.7 cause anosmia. *Nature* 472: 186-190, 2011.

Wilson CJ. The mechanism of intrinsic amplification of hyperpolarizations and spontaneous bursting in striatal cholinergic interneurons. *Neuron* 45: 575-585, 2005.

Xiao C, Nashmi R, McKinney S, Cai H, McIntosh JM, and Lester HA. Chronic nicotine selectively enhances alpha4beta2* nicotinic acetylcholine receptors in the nigrostriatal dopamine pathway. *J Neurosci* 29: 12428-12439, 2009.

Young KA, and Caldwell JH. Modulation of skeletal and cardiac voltage-gated sodium channels by calmodulin. *J Physiol* 565: 349-370, 2005.

Zufall F, and Munger SD. From odor and pheromone transduction to the organization of the sense of smell. *Trends Neurosci* 24: 191-193, 2001.

TABLES

Table 1: Constants used in NEURON simulations of GG neurons

Constant	**Value chosen**	**Estimation method**
C_M (μF/cm^2)	1.0	(Hodgkin and Huxley 1952)
r (spherical radius, μm)	6.0	Capacitance measurements in whole-cell mode, 5 mV test pulse
V_{Na} (mV)	+50	Voltage-clamp data, depolarization protocols
V_K (mV)	-80	Voltage-clamp data, tail currents
V_{leak} (mV)	-60	Chosen so that ionic current is 0 at V = -55 mV
$\bar{G}_{TTX-S}$ (S/cm^2)	0.00244	Voltage-clamp data, depolarization protocols from a holding potential of -70 mV, divided by h_∞ at -70 mV
$\bar{G}_{TTX-R}$ (S/cm^2)	0.00244	Fractional shift of activation curve (G/G$_{max}$) from -120 mV holding potential, with and without TTX
$\bar{G}_K$ (S/cm^2)	0.00455	Voltage-clamp data, depolarization protocols from -70 mV holding potential
$\bar{G}_{leak}$ (S/cm^2)	8.98×10^{-6}	Chosen so that ionic current is 0 at V = -55 mV

FIGURE LEGENDS

Figure 1: GG neurons in acute slices. Transverse slices of the young mouse nasal vestibule were treated with collagenase. Protruding surfaces of GG neurons were visible with brightfield optics (A), and their identity could be verified with GFP expression in OMP-GFP mice (B). GG neurons retained expression of pGC-G on cilia (C). Scale bar: 40 μm.

Figure 2: Spontaneous firing in GG neurons. Extracellular recordings revealed that GG neurons spontaneously discharge action potentials in repetitive single-spike (A-B), phasic (C-D), or sporadic (E-F) patterns. Left panels (A,C,E) show 5 s typical traces. Right panels (B,D,F) show representative frequency vs. time plots of each firing pattern over 5 min. Insets within frequency vs. time plots show Gaussian density estimates of instantaneous frequencies with annotated means. The Inset in (C) shows typical AP waveform.

Figure 3: The pattern of spontaneous discharge is an intrinsic property of a GG neuron. In intracellular current-clamp recordings, 10 s serial hyperpolarizing and depolarizing currents (10 pA per step) were injected from the resting membrane potential (defined as 0 pA, ~-55 mV). The effects of current injections were observed on (A) RSS firing, (B) phasic firing, and (C) sporadic firing. Numbers on the right of panel (C) indicate the total number of spikes evoked from the steady-state membrane potential. Note anode-break excitation. The stimulus waveform is shown as the bottom of panel (C). The relationship of depolarizing current injection to firing rate is shown for (D) evoked firing and (E) spontaneous firing from the new membrane potential baseline. The dotted line shown in (E) is a linear fit to the data.

Figure 4: Whole-cell voltage-dependent currents in GG neurons. (A-C) Depolarization to test potentials in the range of -50 mV to +50 mV from a holding potential of -70 mV (lower panel in C) induced membrane

conductances in GG neurons. (A) Depolarization pulses evoked transient inward currents and sustained outward currents. (B) Outward currents were absent when patch pipettes were filled with 110 mM Cs^+ and 30 mM tetraethylammonium. (C) Bath application of 50 nM TTX abolishes most inward currents. (D-F) Repolarization back to -70 mV from hyperpolarized test potentials in the range of -120 mV to -100 mV (lower panel in F) elicited transient inward currents (D). These inward currents were eliminated by removal of extracellular Na^+ (E) but remained in the presence of 0.5 μM TTX (F). Traces shown are from different neurons but are representative.

Figure 5: Activation and steady-state inactivation properties of Na^+ currents in GG neurons. (A) Selective activation of fast-inactivating TTX-R Na^+ currents (upper panel) was achieved with depolarizing pulses from a holding potential of -120 mV (lower panel) in 0.1 μM TTX. (B) Steady-state inactivation of TTX-R currents (upper panel) was characterized by depolarizing pulses to a test potential of -10 mV from various prepulse potentials (lower panel) in 0.1 μM TTX. (C) The I-V relationship for TTX-R currents demonstrates their reversal potential near +50 mV. (D) Hodgkin-Huxley activation (τ_m) and inactivation (τ_h) time constants for TTX-R currents were fast and voltage dependent. (E) Activation and steady-state inactivation curves of TTX-R and TTX-S currents. Fits are reported in text. Activation properties of TTX-S currents were characterized by test depolarizations from holding potentials (h.p.) positive of -70 mV; steady-state inactivation properties were calculated by subtraction of TTX-R currents from total Na^+ currents. (F) The total activation curve of Na^+ currents, derived from depolarizing pulses from a holding potential of -120 mV in saline, shows contributions from activation curves of isolated TTX-R (-120 mV, TTX) and TTX-S (-70 mV) currents. Error bars in (C) and (D) represent standard error.

Figure 6: Properties of K^+ and Ca^{2+} currents in the GG. (A) 2 s depolarizing pulses from a holding potential of -90 mV evoked outward currents. Compare the inactivating current at more positive potentials to the steady-state current at less positive potentials (arrows). (B) The I-V curve for the K^+ tail currents (from a test potential of -20 mV) demonstrates a reversal potential near -80 mV. (C) The I-V

curves for K^+ current activation from two different holding potentials (-65 mV and -135 mV) can be subtracted to isolate the I-V relationship for the inactivating component of I_K. (D) Shown are approximate steady-state curves for the steady-state (s.s.) and inactivating components of I_K. Fits were: s.s. activation – $V_{1/2}$ = -12 mV, slope = 14 mV (Boltzmann); inactivation – $V_{1/2}$ = -61 mV, slope = -22 mV (Boltzmann); activation of inactivating component – rise = 22 mV (exponential). (E) The I-V curve of putative Ca^{2+} currents shows that a component is activated at resting potential (arrow). (F) Exposure of GG neurons to extracellular 25 mM $BaCl_2$ reveals that I_{Ca} consists of both inactivating (test potential of -30 mV) and persistent (test potential of +10 mV) components. Data were collected from a holding potential of -85 mV.

Figure 7: Hyperpolarization-activated currents (I_h) in GG neurons. (A) Hyperpolarizing pulses to test potentials in the range of -55 mV to -115 mV from a holding potential of -55 mV induced inward currents that developed over several hundred ms. (B) I_h was blocked by extracellular 5 mM Cs^+. (C) The I-V relationship for membrane hyperpolarization shows inward rectification at membrane potentials more negative than -90 mV. (D) The activation curve of I_h has a midpoint of -105 mV and a slope factor of -9.3 (fit is shown by the dashed line). (E) RT-PCR was used to detect mRNA of HCN subtypes in the mouse nasal vestibule ("V"). Total RNA from a single mouse cerebrum ("C") was used as a positive control for subtype cDNA amplification. '+' and '-' respectively denote reverse transcription reactions with and without reverse transcriptase. (F) HCN1 antibody (red) labeled most GFP+ GG neurons (green) in OMP-GFP mice. The staining appears localized to the cell membrane. Scale bar: 30 μm.

Figure 8: Experimental and computational measurements of excitability. (A) In whole-cell current-clamp recordings obtained in 0.1 μM TTX, an AP could be elicited by current injection from -90 mV but not from -60 mV. (B) Superimposition of AP waveforms that use both TTX-R and TTX-S currents (black), TTX-S currents only (blue), and TTX-R currents only (red, measured in 0.1 μM TTX). Baseline V_m

differed between samples and was more negative in traces to elicit firing mediated by TTX-R currents. Computer simulations are shown in panels (C-E). Arrows indicate the injection of a 10 ms, 1 pA depolarizing current. V_m indicates the initial membrane potential of the simulation; "Scale" denotes the multiplication factor of the total Na^+ conductance over the values reported in Table 1. (C) Varying the maximal conductance of TTX-R current ($\bar{G}_{TTX-R}$), with $\bar{G}_{TTX-S} = 0.073\ \mathrm{S/cm^2}$, generates graded repetitiveness of AP discharge. Numbers at the start of the traces denote r_G, the ratio of $\bar{G}_{TTX-R}$ to $\bar{G}_{TTX-S}$. (D) Depicted is a similar experiment as in (C), except that $\bar{G}_{TTX-S}$ was varied with $\bar{G}_{TTX-R} = 0.073\ \mathrm{S/cm^2}$. Numbers at the start of the traces indicate $1/r_G$. (E) With $r_G = 1$, shifting the inactivation and activation curves of the TTX-R current by +10 mV (in the depolarizing direction, V(0.5)+10) or by -10 mV (in the hyperpolarizing direction, V(0.5)-10) removes repetitive firing. V(0.5) indicates that the activation and inactivation curves reflect the average values shown in Fig. 5E. Repetitive firing could be restored in V(0.5)+10 and V(0.5)-10 conditions by changing the initial V_m and the scale factor. (F) Burst firing is eliminated with removal of TTX-R current. $\bar{G}_{TTX-S}$ was varied, and the numbers *n* on the traces indicate $\bar{G}_{TTX-S} = n \times 0.037\ \mathrm{S/cm^2}$.

Figure 9: Pharmacological modulation of spontaneous firing. (A) RSS-firing GG neuron was slowly perfused with 0.1 μM TTX. Traces show firing pattern at different time points in the perfusion: "1" – initial firing pattern, "2" – intermediate [TTX], "3" – full effect of TTX, "4" – recovery. (B) In a similar experiment as in (A), a phasic-firing GG neuron exhibits reduced repetitiveness of firing before being fully inhibited. (C-E) Shown are frequency vs. time plots of spontaneous firing in different GG neurons perfused with 5 mM CsCl to inhibit I_h. I_h influences firing rate of (C) RSS, (D) sporadic, and (E) phasic firing patterns.

FIGURES

Figure 1

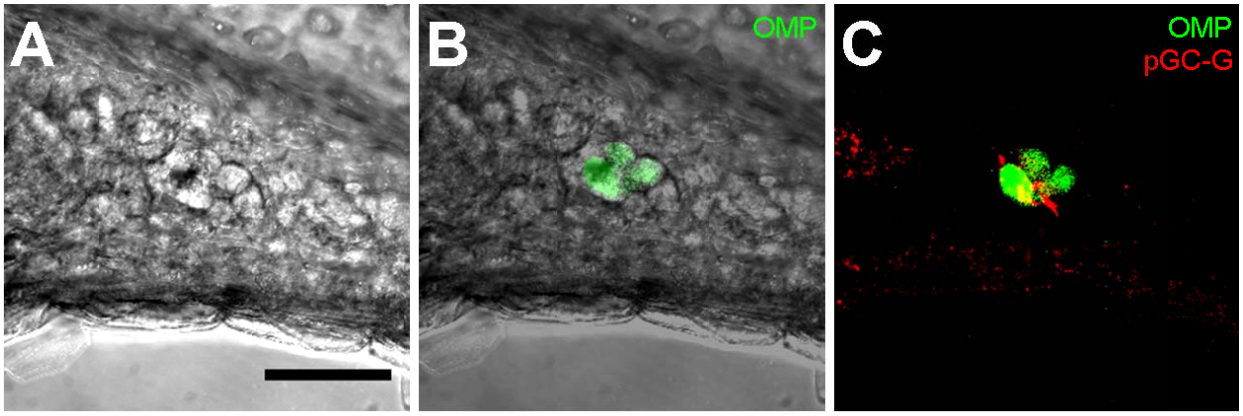

Figure 2

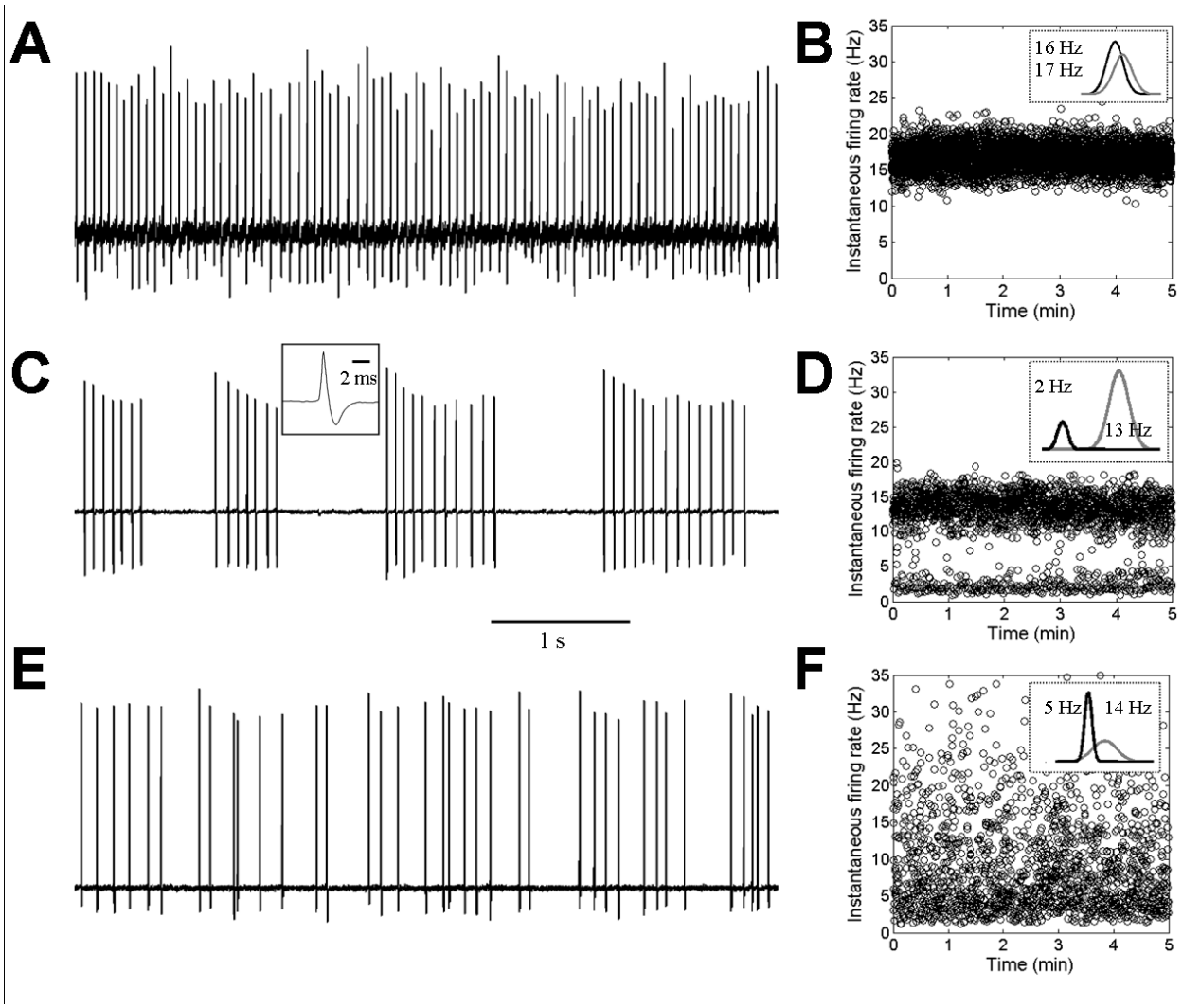
A
B
16 Hz
17 Hz
Instantaneous firing rate (Hz)
Time (min)
C
2 ms
1 s
D
2 Hz
13 Hz
Instantaneous firing rate (Hz)
Time (min)
E
F
5 Hz
14 Hz
Instantaneous firing rate (Hz)
Time (min)

Figure 3:

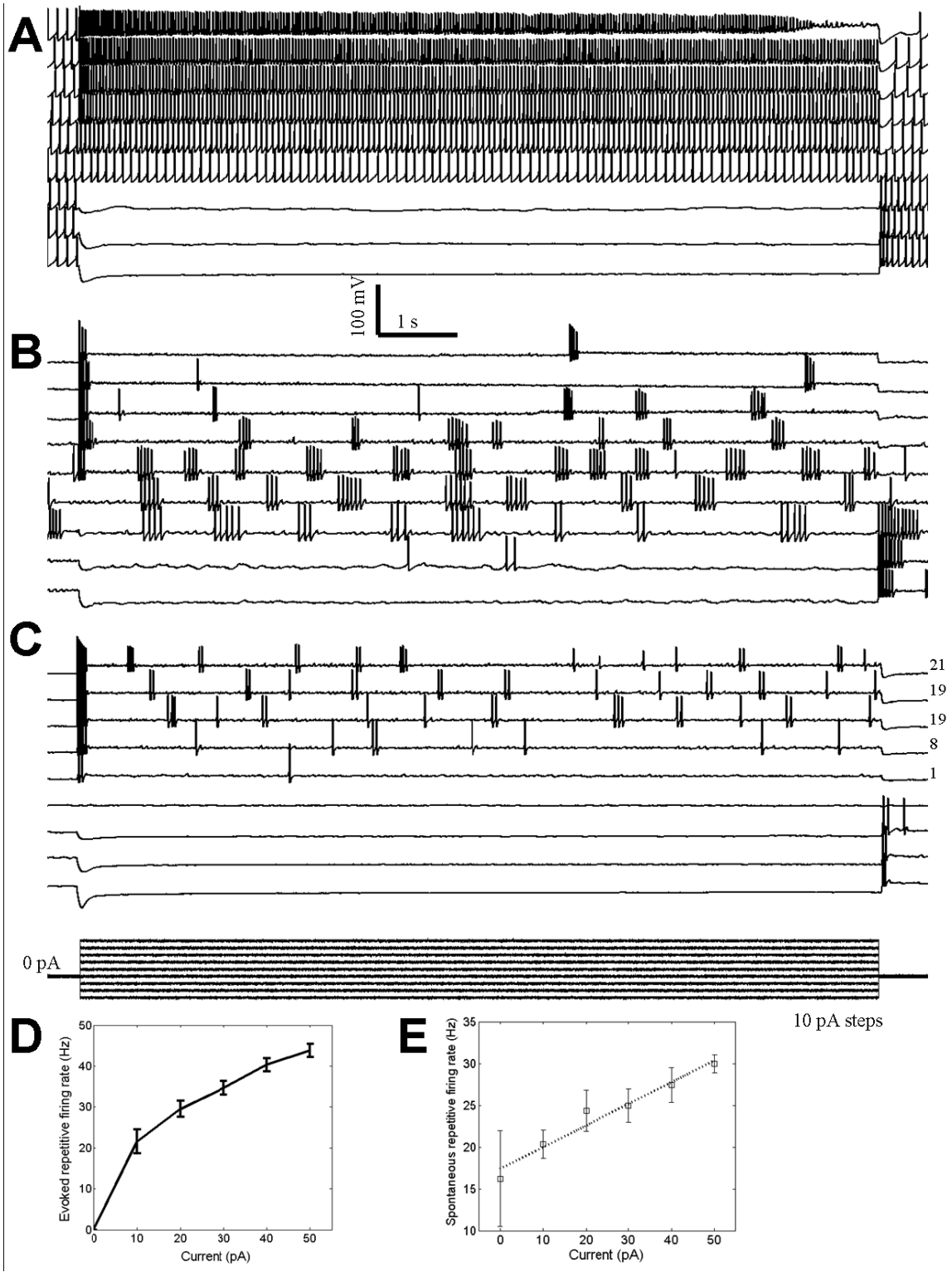
A
100 mV
1 s
B
C
21
19
19
8
1
0 pA
10 pA steps
D
Evoked repetitive firing rate (Hz)
Current (pA)
E
Spontaneous repetitive firing rate (Hz)
Current (pA)

Figure 4:

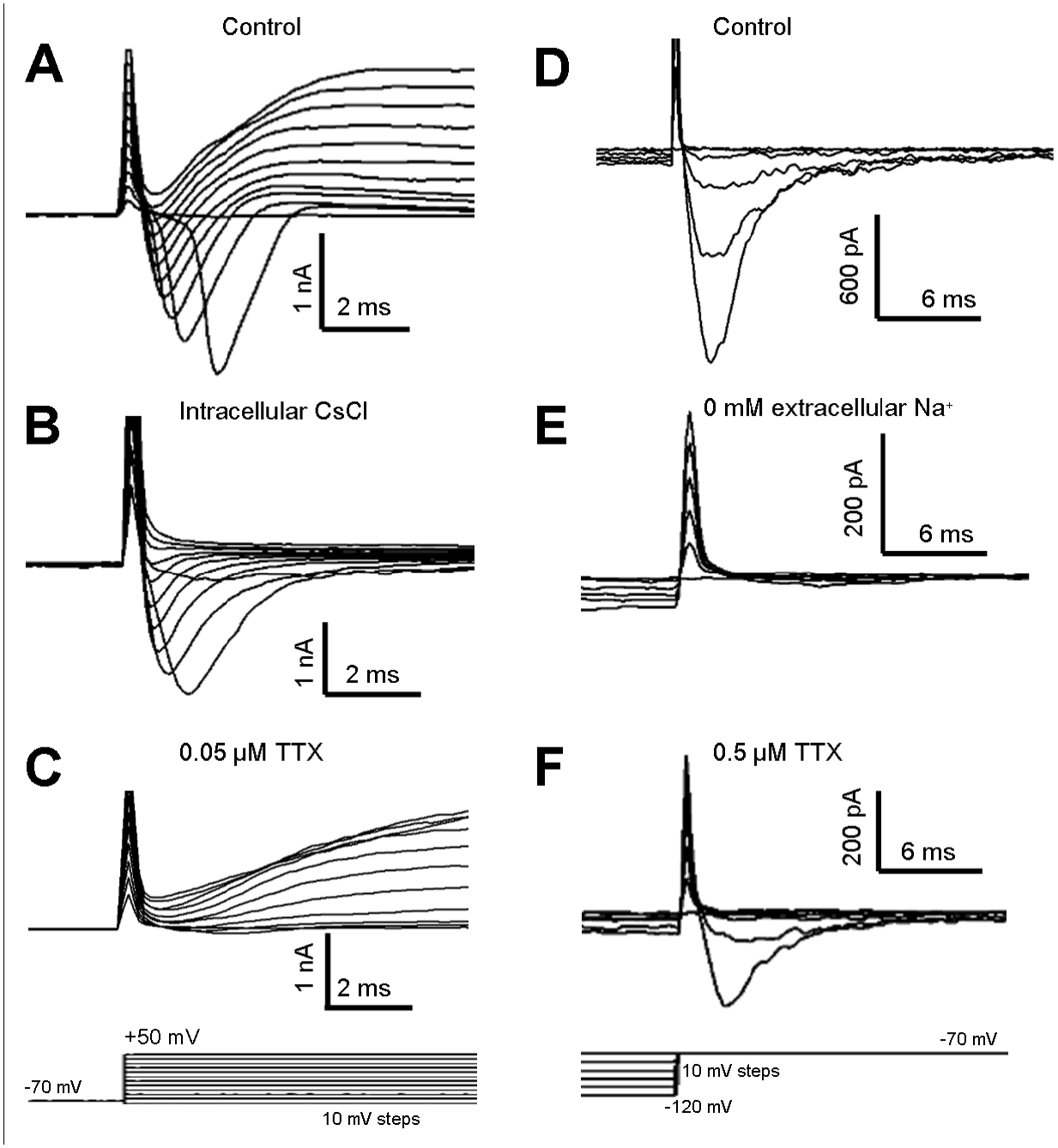
A
Control
1 nA
2 ms
B
Intracellular CsCl
1 nA
2 ms
C
0.05 µM TTX
1 nA
2 ms
+50 mV
-70 mV
10 mV steps
D
Control
600 pA
6 ms
E
0 mM extracellular Na+
200 pA
6 ms
F
0.5 µM TTX
200 pA
6 ms
-70 mV
10 mV steps
-120 mV

Figure 5:

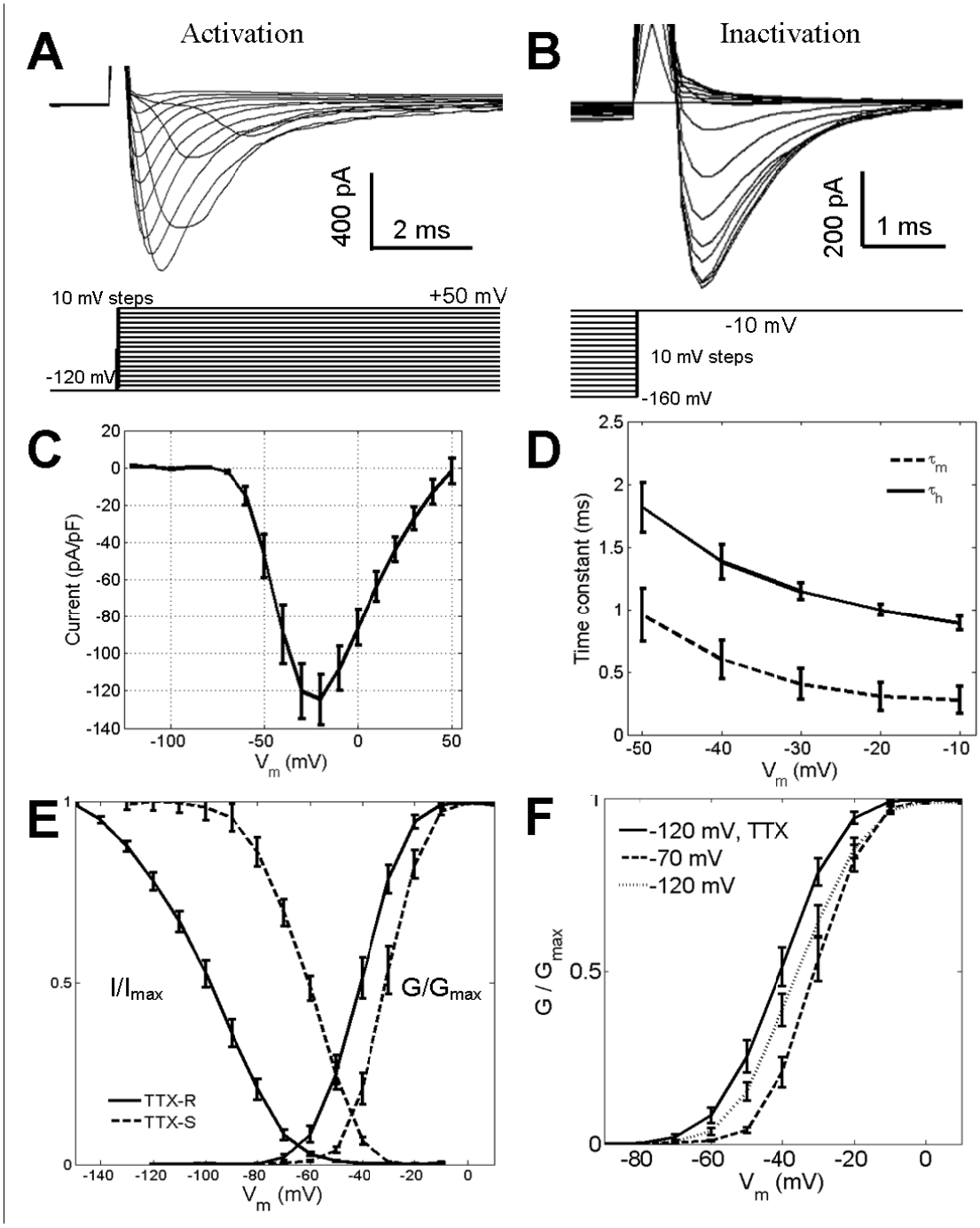
A
Activation
400 pA
2 ms
10 mV steps
+50 mV
-120 mV
B
Inactivation
200 pA
1 ms
-10 mV
10 mV steps
-160 mV
C
Current (pA/pF)
V_m (mV)
D
Time constant (ms)
τ_m
τ_h
V_m (mV)
E
I/I_max
G/G_max
TTX-R
TTX-S
V_m (mV)
F
G / G_max
-120 mV, TTX
-70 mV
-120 mV
V_m (mV)

Figure 6:

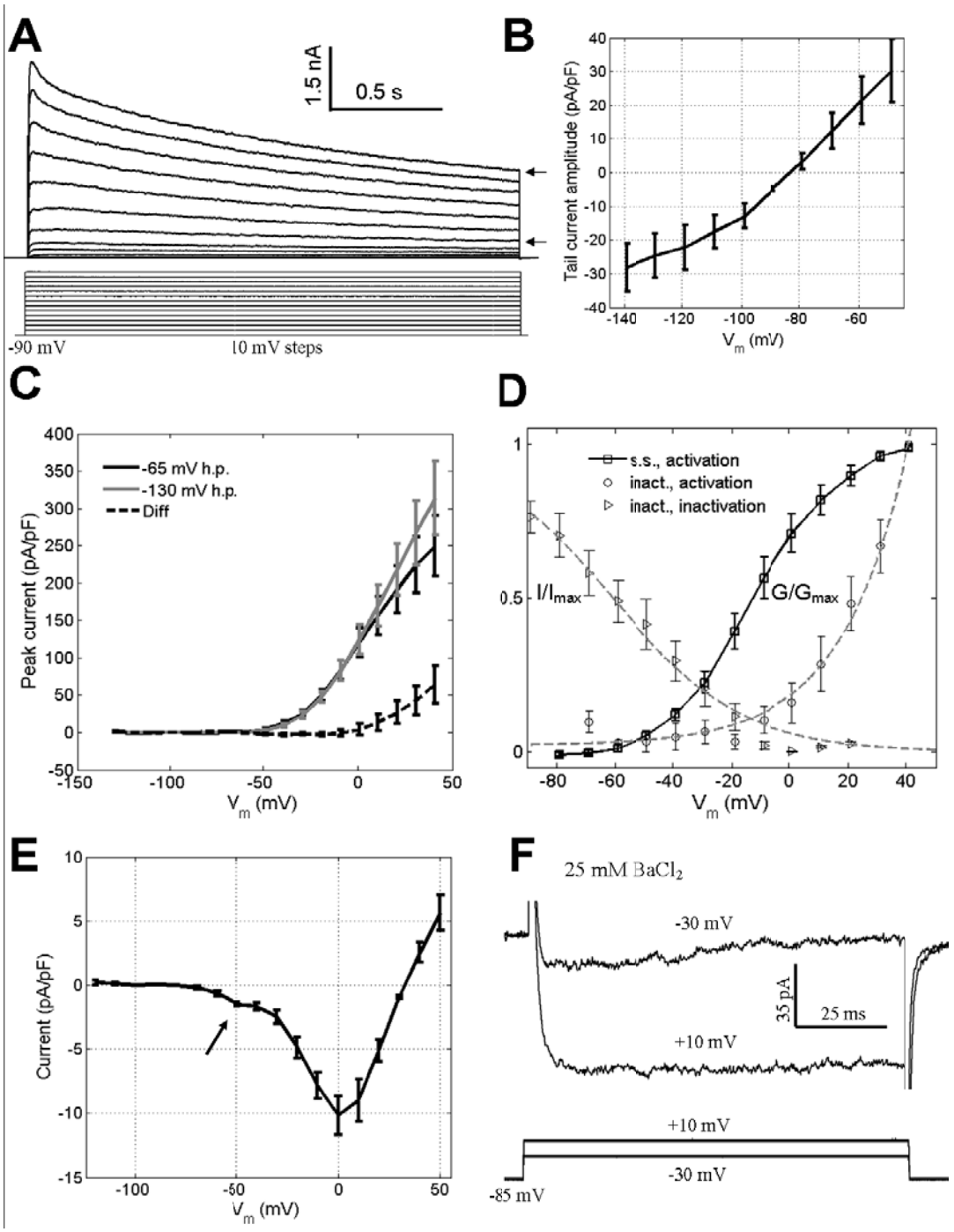
A
1.5 nA
0.5 s
-90 mV
10 mV steps
B
Tail current amplitude (pA/pF)
V_m (mV)
C
-65 mV h.p.
-130 mV h.p.
Diff
Peak current (pA/pF)
V_m (mV)
D
s.s., activation
inact., activation
inact., inactivation
I/I_{max}
G/G_{max}
V_m (mV)
E
Current (pA/pF)
V_m (mV)
F
25 mM $BaCl_2$
-30 mV
35 pA
25 ms
+10 mV
+10 mV
-30 mV
-85 mV

Figure 7:

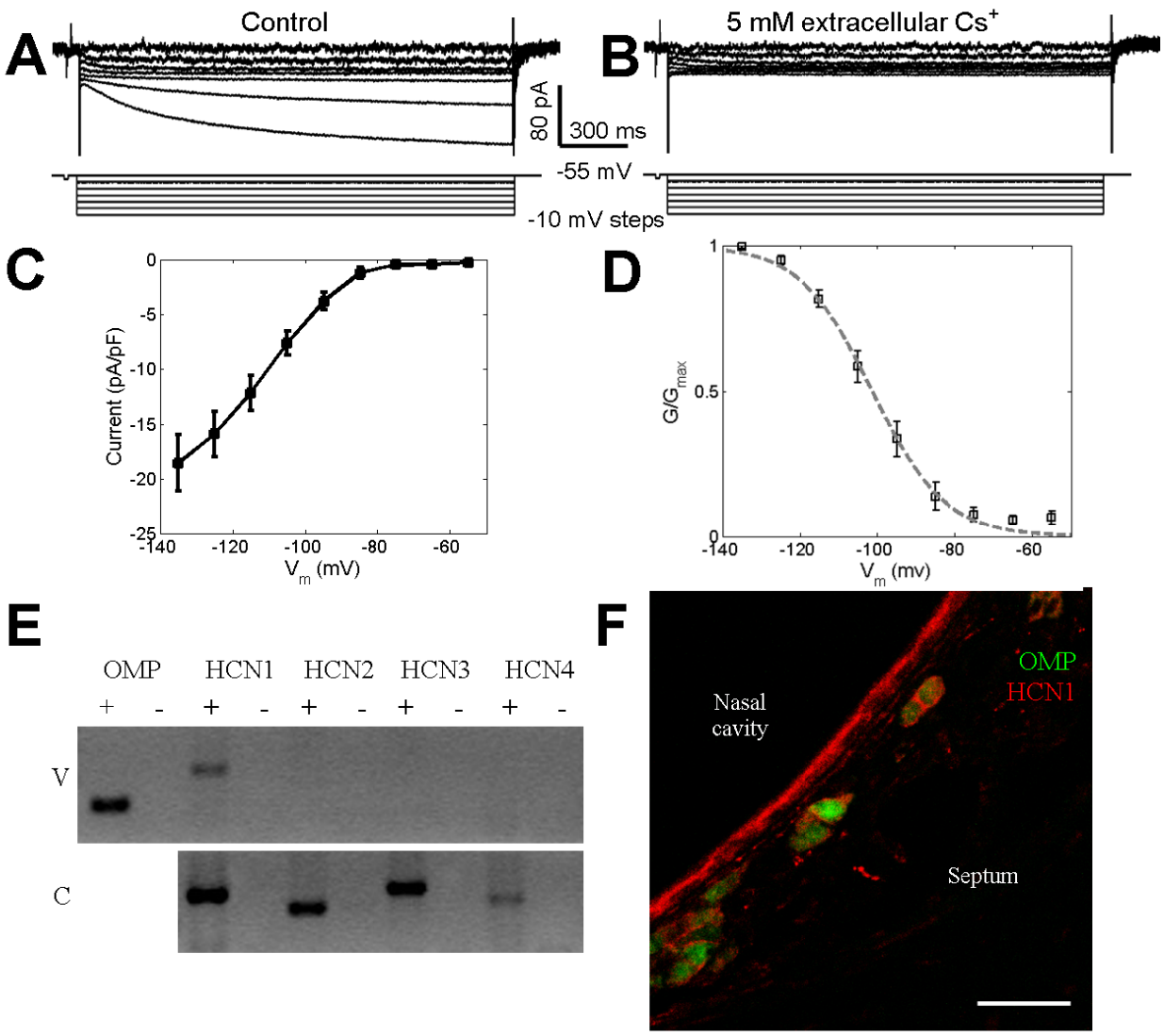
A
Control
80 pA
300 ms
-55 mV
-10 mV steps
B
5 mM extracellular Cs+
C
Current (pA/pF)
0
-5
-10
-15
-20
-25
-140
-120
-100
-80
-60
Vm (mV)
D
G/Gmax
1
0.5
0
-140
-120
-100
-80
-60
Vm (mv)
E
OMP
HCN1
HCN2
HCN3
HCN4
+ - + - + - + - + -
V
C
F
Nasal cavity
OMP
HCN1
Septum

Figure 8:

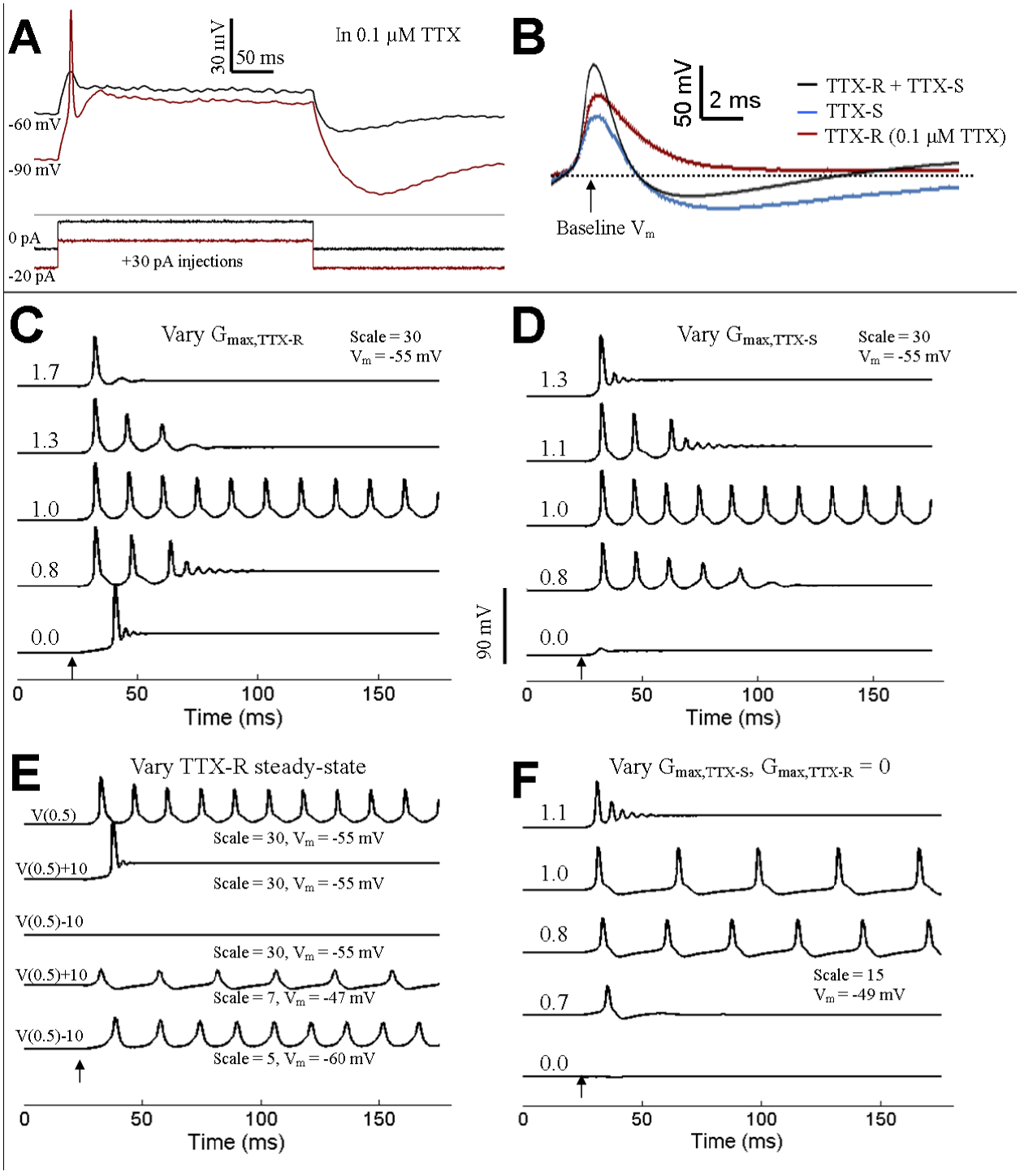
A
In 0.1 µM TTX
30 mV
50 ms
-60 mV
-90 mV
0 pA
-20 pA
+30 pA injections
B
50 mV
2 ms
TTX-R + TTX-S
TTX-S
TTX-R (0.1 µM TTX)
Baseline Vm
C
Vary Gmax,TTX-R
Scale = 30
Vm = -55 mV
1.7
1.3
1.0
0.8
0.0
0
50
100
150
Time (ms)
D
Vary Gmax,TTX-S
Scale = 30
Vm = -55 mV
1.3
1.1
1.0
0.8
0.0
90 mV
0
50
100
150
Time (ms)
E
Vary TTX-R steady-state
V(0.5)
Scale = 30, Vm = -55 mV
V(0.5)+10
Scale = 30, Vm = -55 mV
V(0.5)-10
Scale = 30, Vm = -55 mV
V(0.5)+10
Scale = 7, Vm = -47 mV
V(0.5)-10
Scale = 5, Vm = -60 mV
0
50
100
150
Time (ms)
F
Vary Gmax,TTX-S, Gmax,TTX-R = 0
1.1
1.0
0.8
Scale = 15
Vm = -49 mV
0.7
0.0
0
50
100
150
Time (ms)

Figure 9:

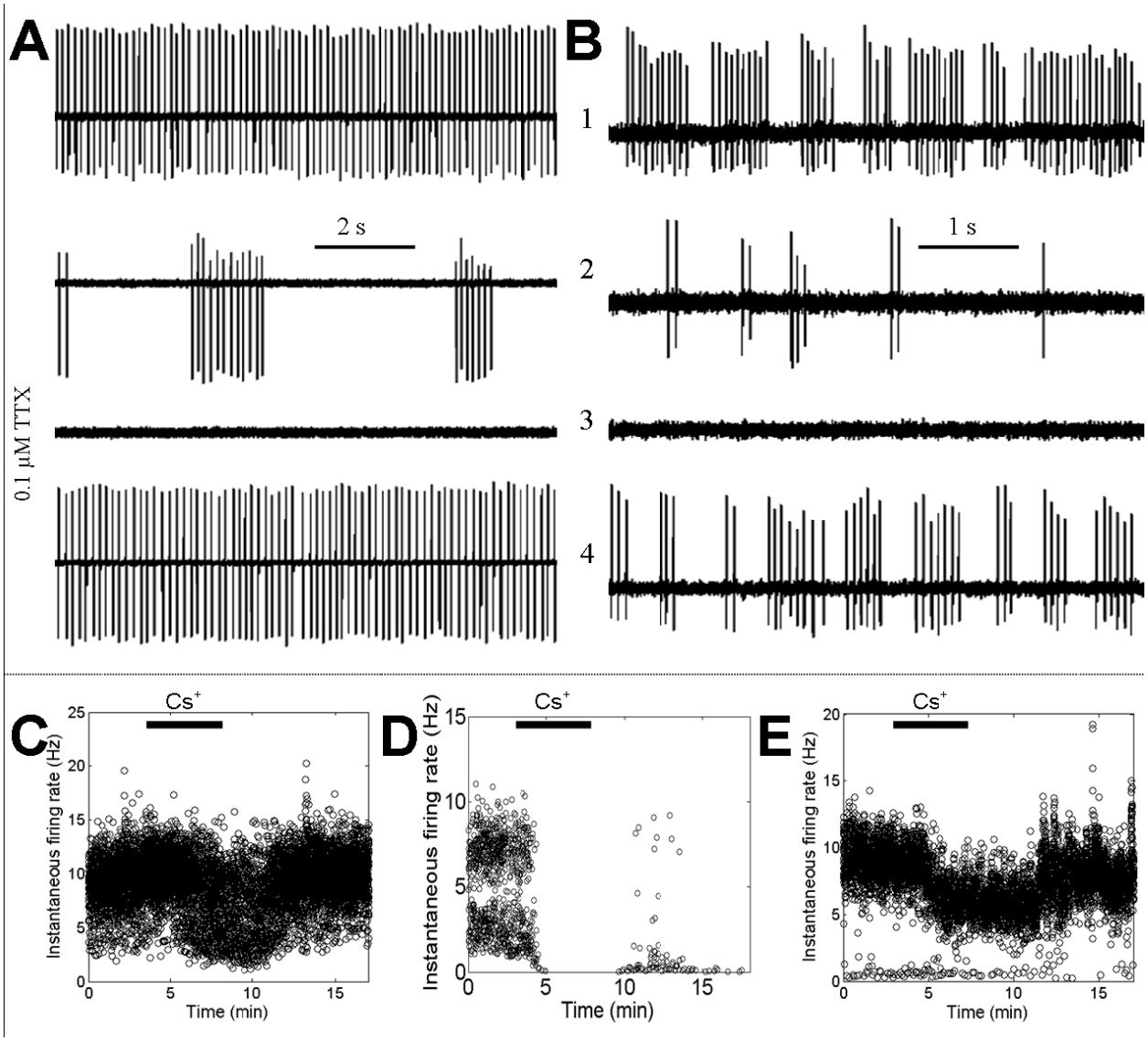
A
B
1
2
3
4
2 s
1 s
0.1 µM TTX
C
D
E
Cs+
Instantaneous firing rate (Hz)
Time (min)

Supporting Figure 1: Plots of Hodgkin-Huxley steady-state parameters

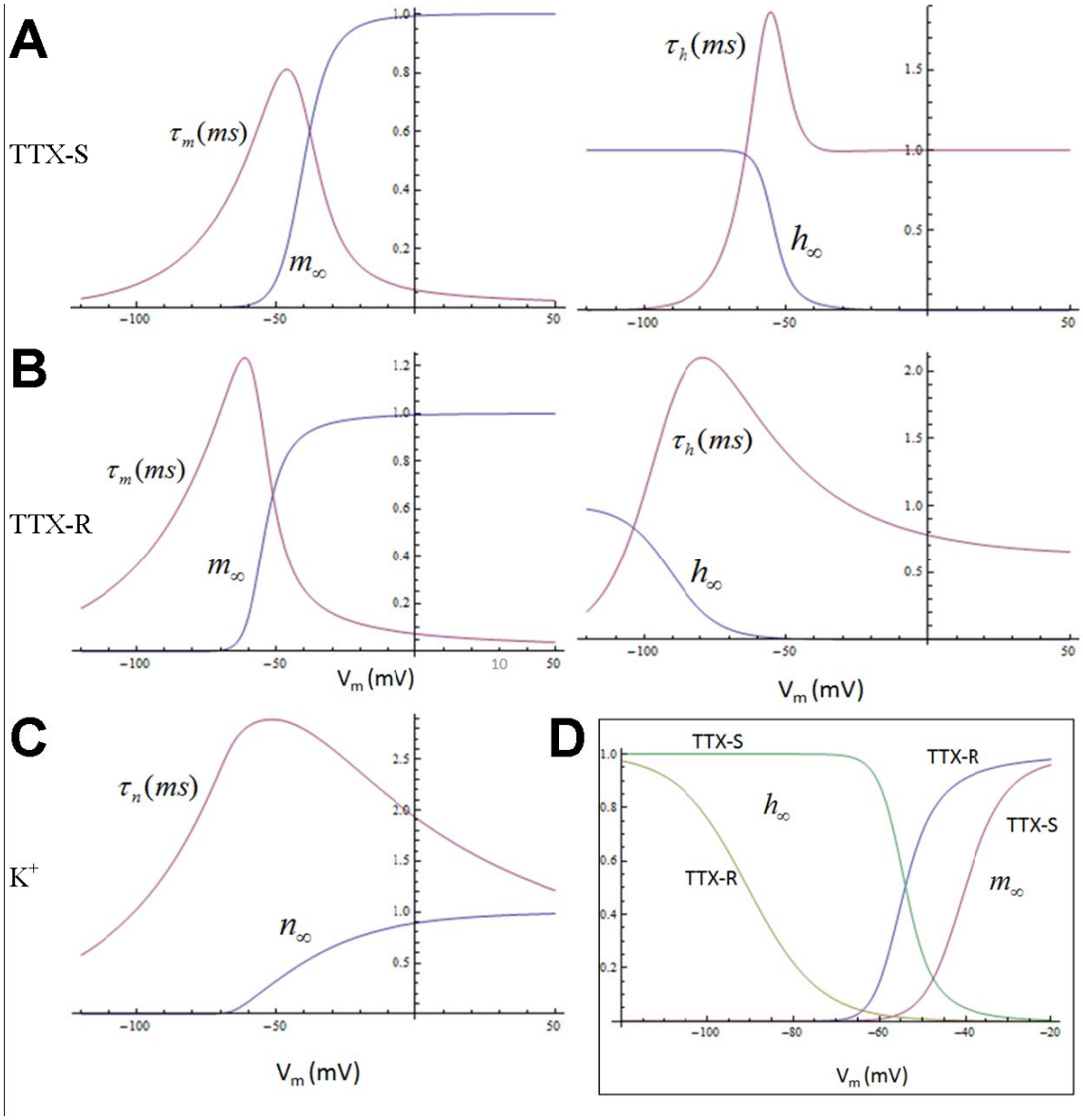

(A) Activation (m) and inactivation (h) variables as a function of voltage (V_m) for TTX-S Na^+ current. (B) m and h variables for the TTX-R Na^+ current in GG neurons. (C) Activation (n) variable for I_K in GG neurons. (D) This plot shows the off-set inactivation and activation curves for TTX-R and TTX-S conductances in GG neurons.

Supporting Figure 2: Spontaneous firing before and after breakthrough

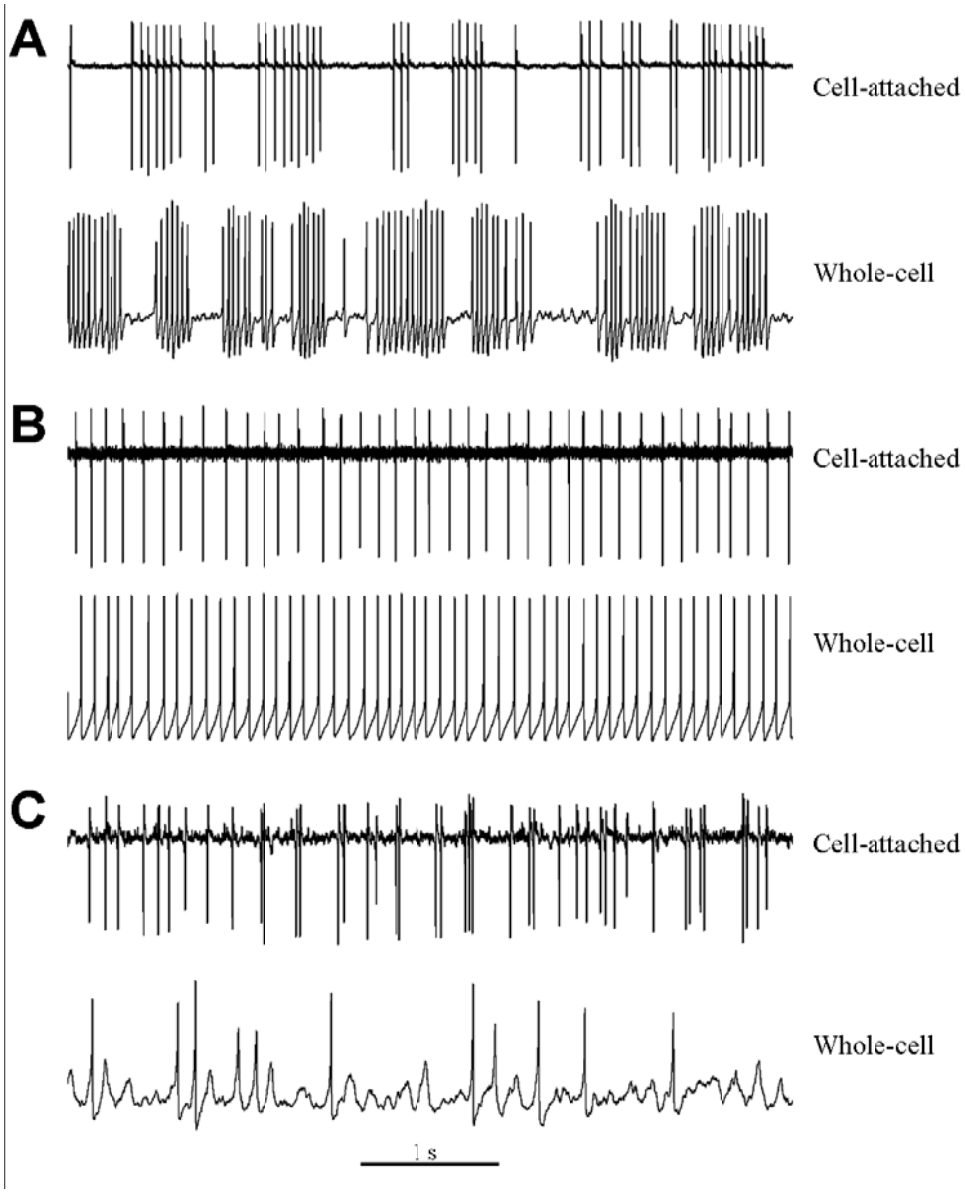

5 s traces. Breakthrough into the whole-cell configuration altered spontaneous firing rate but not the intrinsic pattern. Firing patterns: (A) phasic, (B) repetitive single-spike, (C) sporadic. Each panel represents a single cell.

Supporting Figure 3: Invariance of TTX-S activation curve over two different estimation approaches

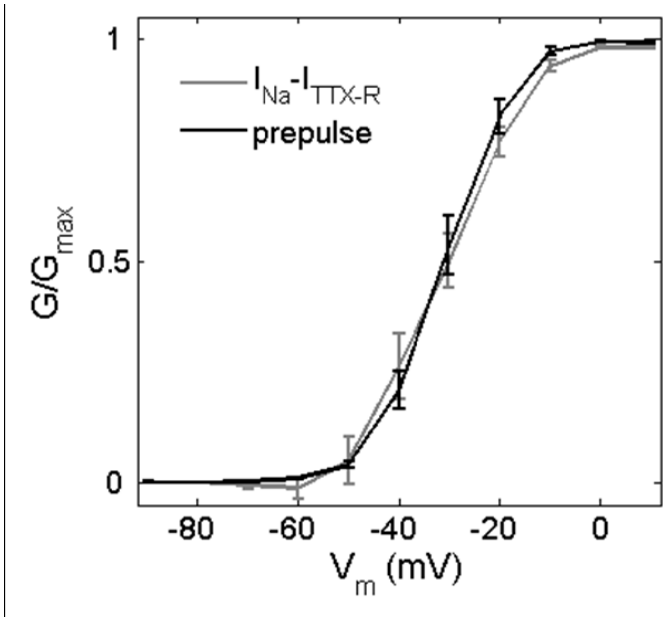

Approach #1: Subtracted TTX-R currents from total Na^+ currents (-120 mV holding potential). Approach #2: Pre-pulse method of using holding potentials more positive than -70 mV to inactivate selectively the TTX-R currents.

Supporting Figure 4: Single-cell Na^+ activation curves

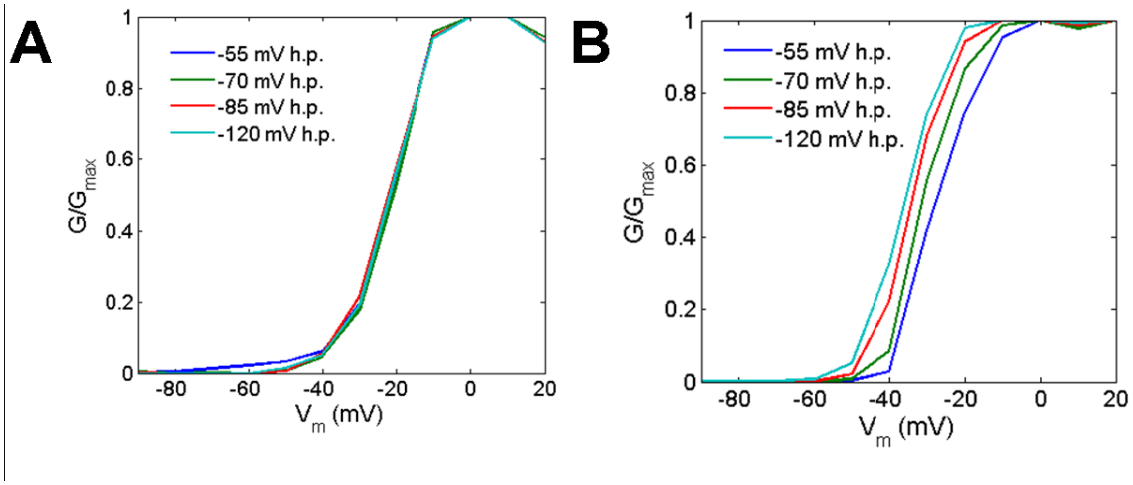

(A) In this cell, the TTX-R current has the same activation threshold as the TTX-S current. (B) In a second cell, activation curves obtained from different holding potentials show hyperpolarized voltage dependence of TTX-R currents.

Supporting Figure 5: Rheobase derived from computer simulations

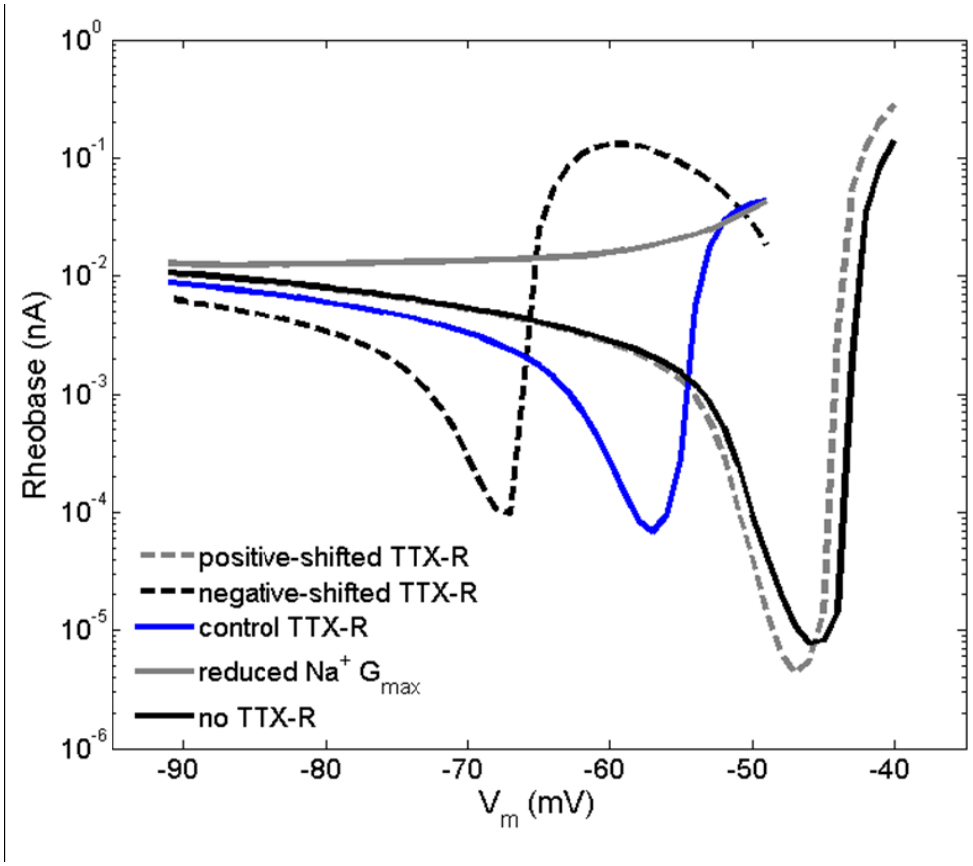

Positive- and negative-shifting of the TTX-R activation and inactivation curves changes the membrane potential that gives the absolute minimum rheobase. Increasing total Na^+ conductance lowers the rheobase. TTX-R currents appear to lower the rheobase at more negative (<-55 mV) potentials.

Supporting Figure 6: Spontaneous firing over 15 min.

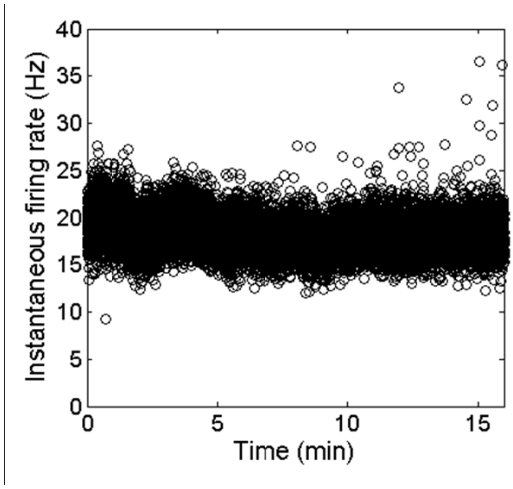

This frequency vs. time plot demonstrates small (< 10%) changes in the firing rate over 15 min. These changes would not be confused with the time-locked Cs^+-induced changes shown in the main paper.

--- Chapter 4 ---

Electrophysiological characterization of Grueneberg ganglion olfactory neurons: chemosensory responses

Cambrian Y. Liu, Cheng Xiao, Scott E. Fraser, Henry A. Lester, David S. Koos

D.S.K. assisted in the generation of the data and images shown in Figure 9.

ABSTRACT

This study provides an electrophysiological characterization of chemosensory function in Grueneberg ganglion (GG) olfactory neurons in an acute slice preparation of the mouse nasal vestibule. In patch clamp recordings, two established rodent pheromones, 2,5-dimethylpyrazine (2,5-DMP) and 2-heptanone, had excitatory and inhibitory effects, respectively, on the spontaneous firing of GG neurons. The pheromones affected all 3 patterns of spontaneous discharge. GG neurons were excited by 8-br-cGMP and the phosphodiesterase inhibitor IBMX. While responses to 8-br-cGMP and IBMX depended on the expression of the cyclic nucleotide gated cationic channel subunit CNGA3, responses to 2,5-DMP were still present in *Cnga3*$^{-/-}$ mice. Immunohistochemical and extravasation experiments demonstrated that GG neurons reside near a vascular bed. The spontaneous firing rate of GG neurons was reduced by exposure to serum and cortisol. These results indicate that GG neurons encode chemosensory information as bidirectional changes in firing rate and suggest a role for serum modulation of olfactory activity.

KEYWORDS

Patch clamp, 2,5-dimethylpyrazine, 2-heptanone, CNGA3, cGMP, odorant inhibition, pheromones, vasculature, Evans blue, extravasation, serum, cortisol

INTRODUCTION

The Grueneberg ganglion (GG) is a primary mammalian olfactory subsystem that is composed of ~1,000 glial-wrapped neuronal cell bodies located on both sides of the cartilaginous septum in the far-rostral nasal vestibule. Whereas olfactory sensory neurons (OSNs) in the main olfactory epithelium (MOE) are arranged to form a pseudostratified epithelium, GG neurons form discrete clusters that collectively occupy an arrowhead-shaped domain in the nasal vestibule. Mouse GG neurons express olfactory marker protein (OMP), a specific marker of mature primary OSNs, and possess axons that collect to form 8-12 glomeruli in the necklace-like domain of the olfactory bulb (Fleischer et al. 2006; Fuss et al. 2005; Grüneberg 1973; Koos and Fraser 2005; Roppolo et al. 2006; Storan and Key 2006).

Functionally, GG neurons *in vivo* homogeneously exhibit increased c-Fos expresion when exposed to the pheromones 2,5-dimethylpyrazine (2,5-DMP) and 2,3-dimethylpyrazine (2,3-DMP), but not to 2-heptanone (Mamasuew et al. 2011a). Both 2,5-DMP and 2-heptanone have been shown to perturb the reproductive physiology of rodents and are secreted in urine in an adrenal-mediated manner (Novotny et al. 1986). These pheromones stimulated OSNs and necklace glomeruli, in the absence of the main olfactory cAMP-gated channel subunit CNGA2 (Lin et al. 2004), as well as vomeronasal sensory neurons (VSNs) of the vomeronasal organ (VNO) (Leinders-Zufall et al. 2000; Riviere et al. 2009). In the GG, the c-Fos response to DMP compounds *in vivo* depended on the cGMP-gated cationic channel subunit CNGA3 and the membrane-bound receptor guanylate cyclase pGC-G (Mamasuew et al. 2011b), both critical components of a unique cGMP transduction pathway in the GG (Fleischer et al. 2009; Liu et al. 2009).

A second chemosensory modality for the GG involves the detection of putative alarm pheromones. Mouse GG neurons homogeneously exhibit cytosolic [Ca^{2+}] bursts in direct response to an unknown water-soluble compound collected during the asphyxiation of mice. Moreover, this compound induced freezing behavior in mice that was abolished by axotomy of the GG (Brechbuhl et al. 2008).

GG neurons act as finely-tuned cold sensors. Decreasing the ambient temperature from 25˚ C to 15˚ C resulted in increased c-Fos expression in the GG neurons of neonatal mice, an effect that was

CNGA3-dependent (Mamasuew et al. 2008; Mamasuew et al. 2010). GG neurons homogeneously exhibit [Ca^{2+}] bursts in response to cold in a temperature-dependent manner, with an ET_{50} of ~16˚ C. However, *in vitro* thermosensitivity of the GG was not reliant on CNGA3 (Schmid et al. 2010).

We recently reported an acute slice preparation that enabled patch clamp recordings of the GG (Chapter 3). GG neurons are functionally heterogeneous in that different neurons spontaneously discharge in different patterns that do not readily interconvert. These patterns could be broadly characterized as repetitive single-spike (RSS), phasic, or sporadic. Here, we describe the electrophysiological responses of GG neurons to 2,5-DMP, 2-heptanone, general odorants, and mouse serum.

MATERIALS AND METHODS

Animals

Mice were maintained as per Caltech-approved protocol. The characterization of OMP-GFP mice has been described previously (Potter et al. 2001). *Cnga3*$^{-/-}$ mice were a gift from B. Chang. These mice were maintained in the Jackson Laboratory in the Eye Mutant Resource as the cone photoreceptor function loss (cpfl5) mouse line. Genetic analysis of these mice showed that they carried a naturally-occurring point mutation in position 492 (A→G) in exon 5 of the *Cnga3* cDNA. This resulted in a T164A missense mutation in the CNGA3 protein product. Cpfl5 mice did not exhibit any cone electroretinography function (B. Chang, personal correspondence).

OMP-GFP mice were on a BL/6/129 background. *Cnga3*$^{-/-}$ and *Cnga3*$^{+/-}$ mice were on RHJ/LeJ (JR 5415) background. All animals used were postnatal.

Genotyping

The point mutation in *Cnga3*$^{-/-}$ mice was detected in genotyping assays from tail genomic DNA prepared using the PureGene kit (Qiagen). A segment of the *Cnga3* gene was amplified with PCR using HotStar Taq (Qiagen) with the following primer sequences (5’ to 3’): CTTGGACTAGTCTGCAGATG (forward) and TGGACCAGTCAAGTCCGTGG (reverse). Because the point mutation in *Cnga3* created a

restriction site, PCR products were digested with the restriction enzyme SmaI. Digestion products were resolved on a 4.5% NuSieve 3-1 agarose (Lonza) gel prepared in Tris/borate/EDTA (TBE) buffer. Tails from *Cnga3*$^{+/+}$ mice analyzed in this manner would yield one band of 90 bp; from *Cnga*$^{-/-}$ mice, 2 bands of 53 and 37 bp; from *Cnga3*$^{+/-}$ mice, 3 bands of 90, 53, and 37 bp.

Electrophysiology

Using the previously described protocol (Chapter 3), electrophysiological recordings were performed using acute nasal vestibule slices that were prepared from OMP-GFP$^{+/-}$ (mixed C57BL/6 x 129 background) or *Cnga3*$^{+/-}$ / *Cnga3*$^{-/-}$ mice in the age range of p0 to p13. Briefly, mice were euthanized and decapitated. The nasal vestibule was removed and sliced, while immersed in ice-cold modified glycerol HEPES-buffered saline (gHBS), in the transverse plane to a thickness of 100 µm with a vibratome (VT-1000S, Leica). Nasal vestibule slices were washed with HEPES-buffered saline (HBS) at room temperature and incubated with 0.1% type-II collagenase (Invitrogen)-HBS at 37˚C for 10 min. Slices were twice washed with warmed HBS. For cell-attached recordings, nasal vestibule slices were recovered in HBS at 37˚C for 5 min; for whole-cell recordings, the slices were recovered in the same manner, but for 25 min. Tissue was returned to room temperature for >30 min prior to recording. Recipe for gHBS was (in mM): 272 glycerol, 2.5 KCl, 10 HEPES, 10 D-glucose, 2 $CaCl_2$, 1.3 $MgCl_2$, pH 7.4. Recipe for HBS was (in mM): 142 NaCl, 2.5 KCl, 10 HEPES, 10 D-glucose, 2 $CaCl_2$, 1.3 $MgCl_2$, pH 7.4, osmolarity 280-290 mOsm/kg. Recipe for nominal Ca^{2+}-free HBS used in some experiments was (in mM): 142 NaCl, 2.5 KCl, 10 HEPES, 10 D-glucose, 3.3 $MgCl_2$, 0.5 EGTA, pH 7.4, osmolarity 280-290 mOsm/kg.

Neurons were visualized on an upright microscope (BX50WI, Olympus) with brightfield and fluorescent illumination. Tissue slices were kept under HBS delivered from a continuous gravity-based perfusion system. GG neurons could be identified in OMP-GFP mice by their GFP fluorescence. For recordings from nonfluorescing GG neurons (*i.e.*, *Cnga3*-mutant mice and wild-type mice), the neurons were identified by their large diameter, protrusion at the surface of the tissue slice, clustered arrangement, stereotyped location relative to blood vessels and nonsensory epithelium, and exhibition of spontaneous

firing and/or fast-inactivating voltage-gated Na^+ channels. Electrical activity was recorded with MultiClamp 700B amplifiers (Axon Instruments, Molecular Devices), Digidata 1200 analog-to-digital converters (Axon Instruments), and pCLAMP 9.2 software (Axon Instruments). Data were sampled at 10 kHz and filtered at 2 kHz. The junction potential between patch pipette and bath solution was nulled immediately before applying suction to the cell membrane.

For extracellular cell-attached recordings, the patch pipettes were filled with the bath solution (usually HBS or HBS supplemented with diluent (*e.g.*, DMSO)). For whole-cell recordings, to characterize intrinsic membrane properties such as resting membrane potential (V_m), Na^+ current activation, and I_h, the patch pipettes were filled with a high-Cl^-, K^+-based intrapipette solution containing (in mM): 140 KCl, 10 HEPES, 1 $CaCl_2$, 2 $MgCl_2$, 2 K_2ATP, 5 EGTA, pH 7.4, osmolarity 290 mOsm/kg. The predicted junction potential for this intrapipette solution with the HBS bath was 4.1 mV. To study odorant-evoked and pharmacologically modified currents, patch piettes were filled with a high-Cl^-, low Ca^{2+} intrapipette solution containing (in mM): 90 KCl, 50 K-gluconate, 10 HEPES, 5 $MgCl_2$, 5 K_2ATP, 1 Na_3GTP, 0.1 EGTA, pH 7.4, osmolarity 290 mOsm/kg. Predicted junction potential for this intra-pipette solution with the HBS bath was 8.5 mV. Junction potentials were corrected offline. Patch pipettes used for cell-attached recordings had resistances of 2-5 MΩ; those used for whole-cell recordings had resistances of 4-8 MΩ.

In cell-attached recordings, spontaneous firing of GG neurons was recorded in current-clamp mode with 0 pA holding current, to minimize artifacts resulting from holding current over the patch. In whole-cell recordings, we periodically monitored the membrane capacitance and the series resistance over the recording; otherwise, we neither cancelled the capacitive transients nor compensated the series resistance. Data were discarded if the series resistance exceeded 30 MΩ.

Working solutions of odorants and pharmacological compounds-of-interest were freshly prepared on the day of the experiment. Unless otherwise indicated, all chemicals were purchased from Sigma. Liquids were normally diluted 1:1,000, 1:5,000, 1:10,000, etc. to give the reported concentrations. Thapsigargin was purchased from Tocris Bioscience and diluted to a stock concentration of 20 mM in

DMSO. IBMX was diluted to a stock concentration of 0.5 M in DMSO. Cortisol was diluted to a stock concentration of 100 mM in DMSO. Responses were tested by filling a glass pipette with a 2 μm diameter tip with the compound of interest diluted in the bath solution (usually HBS). This "puff" pipette was mounted on a piezoelectric manipulator and connected to a controlled pressure source (Parker Instrumentation). The puff pipette was placed 5-20 μm from the cell soma. Odorants and compounds of interest were applied to the cell by computer-controlled pressure pulses (10 psi, variable durations). We did not test compounds at concentrations of >15 mM due to the potential for nonspecific artifacts relating to sudden changes in osmolarity.

Immunohistochemistry

Immunohistochemistry was performed as described previously (Liu et al. 2009). Primary antibodies used were rat anti-CD31 (1:100, BD Biosciences, cat# 557355), rabbit anti-LYVE1 (1:500, Abcam, cat# ab14917), rabbit anti-vWF (1:800, Abcam, cat# ab6994), rabbit anti-αSMA (1:500, Abcam, cat# ab5694), rabbit anti-DβH (1:500, Abcam, cat# ab43868) and rat anti-PV-1 (1:40, MECA-32 clone, BD Biosciences, cat# 550563). Secondary antibodies used were biotinylated mouse-adsorbed rabbit anti-rat IgG (3 μg/mL, Vector Labs), biotinylated goat anti-rabbit IgG (3 μg/mL, Vector Labs), and Alexa Fluor 555-conjugated donkey anti-rabbit IgG (4 μg/mL, Invitrogen). Tertiary labels used were peroxidase-streptavidin (2.5 μg/mL, MP Bio), Alexa Fluor 555-conjugated steptavidin (2 μg/mL, Invitrogen), and Alexa Fluor 633-conjugated streptavidin (2 μg/mL, Invitrogen).

For PV-1 staining, freshly dissected nasal vestibules were embedded in Tissue-Tek O.C.T. (Sakura) and flash-frozen in liquid nitrogen. Sections of 12 μm thickness were prepared on a freezing microtome and mounted onto Superfrost Plus (Fisherbrand) slides. Slides were immersed in acetone at -20˚C for 15 min. Sections were washed with phosphate-buffered saline (PBS) and incubated with the PV-1 antibody in PBS. Stain was developed with a heavy-metal enhanced diaminobenzidine-peroxide kit (Thermo Scientific), as performed previously (Liu et al. 2009).

All other antibodies were applied to 12-18 μm cryosections that had been prepared from tissue fixed in 4% (w/v) paraformaldehyde-PBS. Triton-X was omitted from some of the staining solutions to optimize membrane labelin; otherwise, it was used at 0.3%. All slides were mounted with Fluoro-Gel (Electron Microscopy Sciences) and coverslipped prior to imaging.

Extravasation assays

Intraperitoneal injections of 500 μL 2% Evans blue (EB)/PBS were performed on adult mice (ages: 1.5-2 months). After 60 min, mice were anesthetized with intraperitoneal injections of 0.5-0.7 mL of 20 mg/mL 2,2,2-tribromoethanol/PBS. Mice were transcardially exsanguinated with 1 U/mL heparin/PBS and then fixed with 4% w/v paraformaldehyde/PBS. Perfusion solutions were delivered with a variable-flow peristaltic pump through an aortic puncture. The nasal cavities and olfactory bulbs of transcardially perfused mice were isolated and immersed in 4% paraformaldehyde overnight at 4˚C.

Nasal cavities and brains were bisected for gross examination on widefield light microscopes. The MOE and VNO were decalcified overnight in 14% w/v EDTA/water. Tissues were cryoprotected in an ascending sucrose/PBS series (10%, 20%, 30%), embedded in Tissue-Tek O.C.T. (Sakura), and sectioned to 18 μm thickness on a freezing microtome. Sections were immediately adhered to slides, defrosted, and imaged (without coverslipping) on confocal microscopes.

To verify EB-labeling of olfactory subsystems, we directly applied EB to the nasal cavity. Adult mice (age: 1.5-2 months) were anesthetized with intraperitoneal injections of 20 mg/mL 2,2,2-tribromoethanol/PBS. A narrow gel-loading tip containing 5 uL of 2% EB/PBS solution was partially inserted into the left nasal cavity. After ejection of dye, the tip was removed. Mice remained anesthetized for 30 min prior to euthanasia and cardiac perfusion as described above. To remove excess dye, nasal cavities were washed with several changes of PBS before overnight immersion in cold 4% paraformaldehyde/PBS. Histological examination of specimens was performed as described above.

Isolation of serum

To isolate mouse serum, 3 wild-type BL/6/129 mice (p10) were separated from the litter and moved in a cardboard box to a separate dissection station away from the animal housing facility. Mice were immediately euthanized and decapitated over a 60-mm Petri dish containing 2 mL HBS. Blood was drained from the head and body cavities into the dish, with care to avoid contamination with urine and fecal matter. An additional 4 mL of HBS was added to the dish. Dish contents were triturated prior to centrifugation at 10,000 rpm at room temperature for 3 min. The supernatant was immediately frozen and stored at -80˚C. Serum isolate and electrophysiological bath solutions were matched in osmolarity by adjusting [NaCl]. Prior to testing, serum was passed through a 0.22-µm filter.

Imaging

Fluorescent images were obtained from a Zeiss LSM510 upright confocal microscope with laser excitation wavelengths of 488 nm, 543 nm, and 633 nm. The pinhole diameter was varied to obtain optical sections of various thicknesses. Image stacks were projected at maximum intensity. For the analysis of Evans blue (EB) extravasation, we took advantage of the far-red fluorescence of EB (Saria and Lundberg 1983) and excited tissue samples with the 633-nm laser. The images of the nasal vestibule, MOE, VNO, and olfactory bulb were obtained in succession and at the same laser power and photomultiplier gain. Brightfield photomicrographs were snapped on a Zeiss upright Axioplan microscope.

Data analysis

Electrophysiological recordings were analyzed in Clampfit 9.2 and in MATLAB 7.4.0 with custom-written routines. Recordings contained precise information about the onset and duration of the pressure puff. Action potentials (APs) were collection using the template search feature in Clampfit. The time-of-peak values of neighboring APs were used to calculate plots of instantaneous frequency vs. time. Desensitizing excitatory responses were fit over the duration of the puff to the following functional form:

$$f(t) = A\left(1 - e^{-t/\tau_a}\right)e^{-t/\tau_{ds}} + C$$

where *f(t)* represents the instantaneous frequency *f* (in Hz) as a function of time *t* (in s), τ_a and τ_{ds} represent the exponential time constants of activation and desensitization, respectively, and *A* and *C* are constants. The value of C was affixed to the average initial firing frequency (measured over 5-60 s) in RSS-firing and sporadic-firing neurons; in phasic-firing neurons, it was affixed to the average initial intraburst frequency. For excitatory responses, the fits were applied to the instantaneous intraburst frequencies in phasic-firing neurons, the total instantaneous frequency in RSS-firing neurons, and a 1-2 s bin of the total firing frequency in sporadic-firing neurons. The maximum value of *f(t)*, divided by *C*, provided an estimate of the response magnitude. Values of τ_a, τ_{ds}, and A were provided by fitting functions in MATLAB. Non-desensitizing excitatory activating responses during the puff were fit to the form:

$$f(t) = A\left(1 - e^{-t/\tau_a}\right) + C$$

where the variables have their usual meanings and constraints. The decay of the excitatory response after puff termination was fit to the function:

$$f(t) = Ae^{-t/\tau_{de}} + C$$

where τ_{de} represents the exponential time constant of decay. *C* was affixed to be the average instantaneous frequency in a time window (1-5 s) prior to puff termination. These functions were also applied to the analysis of ligand-induced inward and outward currents in whole-cell recordings, when appropriate (*i.e.*, when they provided good fits to the data).

Small inhibitory responses (change in firing rate $\Delta f < 25\%$) could be fit to the described functions. However, larger inhibitory responses were associated with the loss of spikes (*i.e.*, sampling resolution); these responses were quantified by comparing the total spike frequency during the puff to the spike frequency in the 5-60 s before the puff. A total lack of spikes during the puff was considered 100% inhibition ($\Delta f = -100\%$). A doubling of the firing rate was considered $\Delta f = +100\%$. For both excitatory and inhibitory responses, irreversible changes were considered a sign of cell death or seal loss. Data from

these neurons were not included in the analyses. In the reporting of effects, the given error is the inferential or standard error of the mean; the age range of the tested mice is also included.

Data were pooled from multiple neurons to derive dose-response relationships. In the analysis of responses to 2,5-DMP and 2,3-DMP, the responses did not exhibit a Gaussian distribution due to a significant fraction of non-responders. Population response magnitudes for 2,5-DMP and 2,3-DMP were thus calculated as probabilistic expected responses:

$$E(r_i) = n_i \bar{r}_i$$

where $\bar{r}_i$ indicates the average response magnitude among responding neurons at concentration *i*, n_i is the fraction of the tested neurons that responded at concentration *i*, and $E(r_i)$ represents the expected response magnitude for the population. The collection of $E(r_i)$ were used to calculate the dose-response relationship. In the analysis of 2-heptanone, the average inhibitory response over all tested neurons at a given concentration was used to compute the dose-response curve. This curve was fit to a Hill equation:

$$r(i) = \frac{i^a}{i^a + i_{50}}$$

where $r(i)$ is the response at concentration *i*, *a* is the Hill coefficient, and i_{50} is the half-inhibitory concentration (IC_{50}).

Fluorescent images were analyzed in ImageJ (NIH). All adjustments to image contrast and brightness were uniform and linear.

RESULTS

GG neurons in acute slices of the mouse nasal vestibule were exposed to 10 psi pressure ejections of various durations ("puffs"). The puffs were delivered from a micropipette that was placed ~20 µm from the cell soma (Fig. 1A). The micropipette contained the odorants/drugs that were diluted in the extracellular solution to the reported concentrations. The effect of the puff on the spontaneous firing of the neuron was recorded in the extracellular loose-seal configuration. The frequency vs. time plot in Fig. 1B demonstrates the effect of a 10 s puff of odorant-free saline on the spontaneous firing of one neuron.

Overall, these puffs induced no change (Δf: -0.3 ± 1.4%, n=8, p7) in the firing rate or pattern of the neurons.

Responses to 2,5-DMP and 2,3-DMP

We examined the effects of 20 s puffs of 2,5-DMP on the spontaneous firing of GG neurons. Excitatory responses to 9.3 mM 2,5-DMP were found in 33/45 (73%) neurons. Fig. 2 shows the effects of 2,5-DMP on the intrinsic patterns of spontaneous discharge. In phasic-firing neurons, the responses appeared as transient elevations in the intraburst frequency (Fig. 2A). In RSS-firing neurons (Fig. 2B), the total firing rate was transiently elevated by 2,5-DMP. In sporadic-firing neurons, the frequency vs. time plot in Fig. 2C indicates a transient burst of high-frequency spikes.

Fig. 3A shows the composite time dependence of the changes in instantaneous firing frequency induced by 20 s puffs of 1.9-9.3 mM 2,5-DMP. There was no visible latency to the responses at a maximum sampling frequency of 25 Hz. The responses were >90% desensitized by the end of the 20 s puff. The time dependence of the responses could be fit by an inactivating exponential function, which yielded a median activation time constant (τ_a) of 0.89 s and a median desensitization time constant (τ_{ds}) of 4.4 s (n=39).

GG responses to 2,5-DMP were dose- and age-dependent. Fig. 3B shows the response magnitude at 3 different concentrations (9.3, 4.6, 1.9 mM) of 2,5-DMP. The responses decreased with decreasing concentration of 2,5-DMP. Fig. 4B indicates that when GG neurons from p0-p5 mice were puffed with 9.3 mM 2,5-DMP, the responses tended to be most robust at p0-p1, when 20/21 neurons were vigorously excited. In contrast, in p3-p4 mice, only 7/15 GG neurons were excited by 2,5-DMP, and these neurons were weakly affected.

Similar to 2,5-DMP, 20 s puffs of 9.3 mM 2,3-DMP induced elevations in repetitive firing rate in 5/5 GG neurons from p1 mice (Supplementary Fig. 1). Responses to 1.9-9.3 mM 2,3-DMP had no latency, with median τ_a equal to 0.66 s and median τ_{ds} equal to 8.3 s (n=14). These parameters did not differ significantly between 2,5-DMP and 2,3-DMP (p values: τ_a= 0.27, τ_{ds} = 0.25, t-test). The effects of

2,3-DMP were dose-dependent (Fig. 3D) and declined with age (Δf, p7 = 11 ± 1%, n=5; Δf, p2 = 77 ± 20%, n=5).

We tested the effect of a related molecule, pyrazine, on GG neurons. 20 s puffs of 10 mM pyrazine excited 0/10 GG neurons from a p2 mouse. In the same mouse, 6/9 GG neurons were excited by 20 s puffs of 9.3 mM 2,5-DMP. Thus, GG neurons selectively detect 2,5-DMP and 2,3-DMP.

Responses to general odorant exposure

We tested whether 2-heptanone, a known activator of the necklace glomeruli (Lin et al. 2004), could alter spontaneous activity in the GG. In extracellular loose-seal recordings, pressure ejections (5-20 s duration) of 1.4-14 mM 2-heptanone resulted in the reversible reduction of the total spontaneous firing rate in 26/26 GG neurons from p0-p4 mice. Fig. 4A shows the inhibition of firing induced by a 5 s puff of 3.6 mM 2-heptanone. This inhibitory response is evident in the frequency vs. time plot of Fig. 4B. The inhibitory effect of 2-heptanone was dose dependent, exhibiting an IC_{50} of ~2 mM and a Hill coefficient of ~1.5 (Fig. 4C). When 7.2 mM 2-heptanone was superfused onto GG neurons, the inhibitory effect persisted for the duration (~5 min) of the exposure (n=5). Responses to 2-heptanone were still present when neurons were pretreated with 20 μM thapsigargin for 30 min (n=5) (Supplementary Fig. 2).

In whole-cell recordings, 20 s puffs of 7.2 mM 2-heptanone elicited an outward current from a holding potential of -64 mV in 5/5 examined GG neurons. These currents had peak amplitudes of 2.2 ± 0.6 pA/pF and an exponential rise time of 7.2 ± 1.9 s. There was no visible desensitization of currents during 20 s puffs. Fig. 4D shows that the currents increased in magnitude at more-positive holding potentials. In current-clamp recordings, 7.2 mM 2-heptanone induced a reversible hyperpolarization of the resting potential (Fig. 4E).

The inhibition of spontaneous firing was not specific to 2-heptanone. We tested, with 20 s puffs, the effects of 2-heptanol (alcohol), ethanol (alcohol), eucalyptol (ether), isovaleric acid (carboxylic acid), citral (aldehyde), and dimethylsulfoxide (sulfur) in the range of 5-10 mM. Table 1 lists the inhibitory responses induced by each of these tested odorants. There were some differences in the sensitivity of GG

neurons to these various substances. For example, at 150 μM, outside of the detection range for 2-heptanone, GG neurons responded to 2-heptanol with a 26 ± 13% reduction in total firing rate (n=3). In contrast, at 8.6 mM, at which GG neurons exhibit >85% inhibition due to 2-heptanone and 2-heptanol, ethanol inhibited only an 18 ± 9% inhibition. In whole-cell recordings, the effects of eucalyptol on membrane currents were similar to those observed with 2-heptanone (Supplementary Fig. 4).

Re-examining the puffs of 2,5-DMP, 2,3-DMP, and pyrazine, we found that the excitatory responses could be accompanied by inhibitory ones in the same cell. For example, at the tail of the response shown in Fig. 2B, when the excitatory response was fully desensitized, an underlying inhibitory response is apparent. Thus, the specific excitatory responses to DMP isoforms can occur against a background of nonspecific odorant-elicited inhibition. The inhibitory responses were not due to sudden changes in osmolarity, as puffs of 10 mM D-glucose altered neither firing rate nor pattern.

Function of the cGMP signaling pathway

GG neurons are proposed to employ a unique cGMP transduction pathway for chemosensory and thermosensory function (Mamasuew et al. 2011b; Mamasuew et al. 2010). Consistent with this proposal, GG neurons are excited by exposure to 8-br-cGMP, a membrane-permeant cGMP analog. 20 s puffs of 1.3 mM 8-br-cGMP excited 11/12 GG neurons (Δf: 130 ± 41%, p4-p6) (Fig. 5A). In RSS-firing and sporadic-firing neurons, the responses appeared as increases in the total firing frequency (Fig. 5B). In phasic-firing neurons, the responses were characterized by an increase in the intraburst firing frequency. The firing rates rose with a single-exponential τ_a equal to 10 ± 3.4 s during a 20 s puff and decayed with τ_{de} equal to 63 ± 9.3 s following puff termination.

We compared the responses to 8-br-cGMP with those elicited by 20 s puffs of 3-isobutyl-1-methylxanthine (IBMX), an inhibitor of phosphodiesterase proteins. In total, 20/20 GG neurons from p2-p6 mice responded to 100 μM IBMX. In 11/20 neurons, IBMX increased the total firing frequency during the puff (Fig. 5C). In the other 9 responsive neurons, the total firing frequency was decreased. As Fig. 5D illustrates, in these neurons, puff onset resulted in a burst of high-frequency, small-magnitude spikes,

followed by the sustained inhibition. These observations suggest that IBMX causes a strong depolarization of the membrane potential, which can inhibit repetitive firing in some neurons (Chapter 3). The decay time constant (τ_{de}: 6.7 ± 2.0 s, n=14) was smaller for IBMX responses (p = 0.0003) than for 8-br-cGMP responses.

In whole-cell recordings, at a holding potential of -64 mV, a 20 s puff of 100 μM IBMX elicited inward currents in 13/14 (93%) GG neurons. Fig. 6A illustrates that these currents peaked at 2.5 ± 0.6 s and had a peak amplitude -4.3 ± 0.5 pA/pF. The current magnitude declined after the peak to a steady-state level during the puff and decayed upon puff termination. Nominal removal of extracellular Ca^{2+} enhanced ~10-fold the IBMX-induced currents (peak amplitude: -41 ± 3.3 pA/pF, n=3) (Fig. 6B). Fig. 6C shows that IBMX reversibly depolarized the resting potential. Fig. 6D demonstrates that the currents were inward at negative holding potentials and outward at positive holding potentials. The estimated reversal potential of ~0 mV is consistent with a current supported by a cationic mixture.

CNGA3-dependent and -independent responses

We examined whether GG odorant responses persisted in *Cnga3*$^{-/-}$ mice. Histochemical experiments demonstrated a lack of ciliary immunoreactivity with a CNGA3-specific antibody in *Cnga3*$^{-/-}$ mice (Supplementary Fig. 5). GG neurons isolated from *Cnga3*$^{+/-}$ and *Cnga3*$^{-/-}$ littermates have similar intrinsic electrophysiological properties. GG neurons of *Cnga3*$^{-/-}$ mice exhibited all 3 spontaneous firing patterns (data not shown). In whole-cell recordings, GG neurons from *Cnga3*$^{-/-}$ mice exhibited the previously-reported (Chapter 3) extra-low voltage inactivating Na^+ current. Moreover, there were no significant differences in Na^+ current activation thresholds, I_h currents, or resting potentials between *Cnga3*$^{+/-}$ and *Cnga3*$^{-/-}$ mice (Supplementary Fig. 6). In extracellular recordings, neuronal exaltations were entirely absent with 20 s puffs of 1.3 mM 8-br-cGMP (n=17) (Fig. 7A,B) or 100 μM IBMX (n=12) (Fig. 7C,D) in *Cnga3*$^{-/-}$ mice. Thus, the depolarizing effects of increases in cyclic nucleotide concentration are fully mediated by CNGA3 channels.

Fig. 7E and 7F show examples of individual neurons from p0 *Cnga3*$^{+/-}$ and *Cnga3*$^{-/-}$ mice, respectively, in which 20 s puffs of 9.3 mM 2,5-DMP induced high-frequency bursts. This suggests that CNGA3 is not required for responses to 2,5-DMP in GG neurons. Overall, only 5/22 (23%) neurons responded in *Cnga3*$^{+/-}$ mice, and 2/17 (12%) responded in *Cnga3*$^{-/-}$ mice, within sampling error. As the *Cnga3*-mutant mouse line was in a RHJ/LeJ background (instead of BL/6/129), these results indicate some genetic background specificity in GG responses to 2,5-DMP. Inhibitory responses to 7.2 mM 2-heptanone were observed in the GG neurons of *Cnga3*$^{-/-}$ mice (Supplementary Fig. 2).

Responses to serum

We searched for other examples of biologically relevant GG stimuli. In routine histological examination of the nasal vestibule, we noticed that GG neurons were in proximity to a network of blood vessels (Fig. 8A). Fig. 8B shows that clusters of GG neurons could be within 5 μm of blood vessel walls that were positively stained for von Willebrand factor. The endothelial lining of the vasculature expressed PV-1 (Fig. 8C), a marker of the fenestrae that mediate vessel permeability in endocrine organs but not in the brain (Hallmann et al. 1995; Shue et al. 2008; Stan et al. 1999). Fig. 8D shows that a subset of the vessels was positively stained for the lymphatic marker LYVE1 (Banerji et al. 1999), suggesting that the vascular network in the nasal vestibule contains both lymphatic and blood vessels. The subsurface epithelium of the nasal vestibule is enriched with smooth muscle cells (Fig. 8E) that are likely innervated by sympathetic nerve varicosities that were positively stained for synaptophysin (Fig. 8F) and dopamine β-hydroxylase (Supplementary Fig. 7). Consistent with this idea, in electrophysiological slice recordings, we observed phasic and tonic vasoconstrictive movements in the vestibule when perfusing high K^+ and norepinephrine solutions, respectively (data not shown).

Compared to other olfactory subsystems, the GG has specialized vascular access. Fig. 9 shows the distribution of Evans blue (EB) dye in the nasal vestibule, MOE, and VNO across different methods of administration. Intraperitoneal injection of EB, which binds to serum albumin (Saria and Lundberg 1983), is a standard test of vascular permeability. In the microscopic examination of i.p.-injected animals

(Fig. 9A), the GG was strongly labeled with EB, whereas longer light exposures were needed to reveal EB in the epithelial sheets of the MOE and VNO (n=5). No dye was observed in the brain. In contrast, nasal irrigation of EB resulted in strong labeling of the MOE and the surface VNO, but lesser labeling of the nasal vestibule (n=4) (Fig. 9B). Untreated animals did not exhibit any appreciable signal (Fig. 9C).

Fig. 10A shows a mouse GG neuron that responded to a 20 s puff of diluted mouse serum with a decrease in firing rate. Overall, 17/24 (71%) neurons were inhibited by puffs of serum (Δf: -25 ± 6%, p3-p13). The effects had an exponential onset time constant of 3.3 ± 1.0 s and a decay time constant of 3.9 ± 1.0 s. All 3 spontaneous firing patterns were susceptible to alterations by serum. 20 s puffs of a high K^+ saline (osmotically balanced 30 mM KCl) showed that the serum effects were not due to ion imbalance, whose impacts have a faster time of onset (Supplementary Fig. 8). To determine what individual components of serum might be active, we considered that *in vivo* GG neurons are active in cold- (Mamasuew et al. 2008) and alarm-sensing (Brechbuhl et al. 2008) modalities, both situations of stress. Stress activates the hypothalamic-pituitary-adrenal axis to induce the adrenal-mediated secretion of cortisol or corticosterone into the blood. Fig. 10B demonstrates the inhibitory response of a GG neuron to a 20 s puff of 10 μM cortisol. A total of 7/15 (47%) neurons responded to 10 μM cortisol (Δf: -18 ± 2.3%, p5). In contrast, 20 s puffs of 150 μM norepinephrine did not affect spontaneous firing (n=5) (Fig. 10C-E).

DISCUSSION

Responses to odors and pheromones

In GG neurons, we demonstrated excitatory responses to 2,5-DMP and inhibitory responses to 2-heptanone and other general odorants. In general, these results support and extend *in vivo* experiments (Mamasuew et al. 2011a) that demonstrated c-Fos expression in GG neurons exposed to 2,5-DMP but not 2-heptanone. As c-Fos expression in neurons is not usually associated with reductions in firing rate, this assay would not be expected to detect odorant inhibition. Separately, we found that the pharmacological opening of a cGMP-gated cationic channel subunit CNGA3 mediates an excitatory effect. The increases

in firing rate likely underlie the Ca^{2+} bursts observed by Schmid and colleagues (Schmid et al. 2010). The electrophysiological properties of the IBMX-induced inward current, which is supported by CNGA3, include its inhibition by extracellular Ca^{2+} and a reversal potential near ~0 mV. These properties are consistent with previous descriptions of CNG channels in other systems (Frings et al. 1995).

The observed effects of 2,5-DMP on spontaneous firing across the 3 intrinsic discharge patterns are consistent with depolarization of the resting potential (Chapter 3). Future characterization of the size, time-dependence, and reversal potential of the membrane current will be necessary to understand its origin. Using the reported intra-pipette solutions, we were unable to obtain 2,5-DMP-induced currents in whole-cell recordings from GG neurons of p0 mice. A likely explanation is the fast dialysis of essential cellular components. Perforated patch recordings, used to study odor transduction in OSNs (Grosmaitre et al. 2006), will be beneficial.

As openings of CNGA3 channels increase firing rate in GG neurons, the channels are candidate proteins in an excitatory mechanism to explain the observed responses to 2,5-DMP. This is supported by *in vivo* studies with *Cnga3*$^{-/-}$ mice (Mamasuew et al. 2011b). However, in contrast to the *in vivo* data, we found that a minority of GG neurons in *Cnga3*$^{-/-}$ mice still exhibited transient elevations in firing rate when puffed with 2,5-DMP. Previous work has shown that OSNs can also detect 2,5-DMP in the absence of their cAMP-gated cationic channel subunit CNGA2 (Lin et al. 2004). An excitatory mechanism independent of cyclic nucleotide activity may exist in many different kinds of primary olfactory neurons and could commonly mediate detection of 2,5-DMP. In support of this, OSNs exhibit reduced responsiveness to 2,5-DMP in the presence of pharmacological inhibitors of phospholipase C (Lin et al. 2004).

The dose-response relationship of GG neurons to 2,5-DMP and 2,3-DMP is in the millimolar range. Collagenase treatment of nasal vestibule slices may have affected some surface odor recognition proteins. The millimolar dose-response curve contrasts with the observed curve in VSNs, which can detect 2,5-DMP at nanomolar concentrations (Leinders-Zufall et al. 2000), and is at least 3 orders of magnitude higher than the estimated concentration of individual pheromones in female urine (Novotny et

al. 2007). Moreover, the responses in the GG are strongest in neonatal mice, which are not sexually mature. Thus, even though 2,5-DMP can impact the reproductive cycles of rodents, the role played by the GG in this process is presently unclear. One possibility is that the activity of only several GG neurons is sufficient to trigger downstream effects in the adult. On a cellular level, a small subset of GG neurons may exhibit exceptional sensitivity to 2,5-DMP; individual VSNs have heterogeneous dose-response relationships to 2,5-DMP that vary over 4 orders of magnitude (He et al. 2010). A second possibility is that the detection of 2,5-DMP has physiological importance throughout (and possibly before) life, but that the function of the GG is only needed at neonatal ages. A third possibility is that GG neurons in neonates retain the broad chemoresponsive profile of a "common" OSN or OSN precursor, but that developmental changes toward specialization in the first several days of life remove an artifactual sensitivity to 2,5-DMP.

In order for an odorant to excite a GG neuron, its excitatory driving force must be greater than its relatively non-selective inhibitory driving force. The inhibitory effects of 2-heptanone and a few other odorants are intriguing due to the presence of a distinct Na^+ channel that is activated at hyperpolarized potentials in GG neurons (Chapter 3). Spontaneous APs at moderate concentrations of these odorants would be expected to mobilize a greater fraction of this unusual Na^+ current. In OSNs, conductance through a second Na^+ channel is required for odor transduction along axons to the olfactory bulb (Weiss et al. 2011). Alternatively, as many GG neurons exhibit high (>10 Hz) rates of spontaneous firing, inhibitory signals may have greater salience than desensitizing excitatory ones.

It is possible that 2-heptanone and other tested odorants are recognized by a broadly tuned odorant receptor (Duchamp-Viret et al. 1999). This receptor may be coupled to signal transduction elements whose final output is to induce membrane hyperpolarization. The inhibitory effects of single odorants observed in this study may be an extension of a general odorant-inhibition phenomenon. Odorant-induced hyperpolarization is also a feature of mammalian OSNs and is dependent on CNGA2 (Delay and Restrepo 2004). In our experiments on the GG, the inhibition by 2-heptanone was retained

even with removal of CNGA3. Most GG neurons do not express CNGA2 (Roppolo et al. 2006). Thus, odorant-induced hyperpolarization in the GG is likely mediated by a distinct mechanism.

The currents induced by 2-heptanone have a reversal potential of approximately -85 mV. As demonstrated in Fig. 4D, at positive holding potentials the currents could be as large as 400 pA, suggesting the movement of ions with a large electrochemical gradient. Thus, in GG neurons 2-heptanone likely increases the conductance of a K^+ channel. Because K^+ channels have multiple routes for modulation (Dilly et al. 2011), one explanation for these results is that the tested odorants either directly or indirectly (through a nonspecific chemical or physical property) interact with the K^+ channel. The odorant-induced inhibition was not a result of osmolarity or pH changes. It is also unlikely to be due to vapor pressure, as ethanol, which has a higher vapor pressure than 2-heptanone, induced only a modest inhibitory response at ~9 mM. Because odorants are often hydrophobic, lipophilicity may represent a key factor in the observed sensitivity of the inhibitory response.

Responses to serum

With the exception of 2-heptanol, whose inhibitory effects could be discerned at 150 μM, millimolar concentrations of odorants were required to observe responses in the GG. This raises the question of whether the inhibitory responses have any physiological relevance. We therefore searched for examples of biologically relevant compounds at near-physiological concentrations that could affect spontaneous activity in the GG. To this end, we found that GG neurons reside in a dense bed of blood and lymphatic vessels and are highly susceptible to vasoactive movements of autonomic origin. Injections of Evans blue dye revealed strong labeling of the nasal vestibule epithelium and weaker labeling of the MOE and VNO. These experiments suggest that neuronal activity in the GG is vulnerable to modulation by serum contents, in contrast to OSNs and vomeronasal sensory neurons.

Consistent with this hypothesis, serum reduced firing rate in the majority of GG neurons, even in neurons from a p13 mouse. We do not know if the sum of all the components in serum caused the inhibitory response and thus represents a more-native measure of spontaneous activity in the GG, or if the

serum contained one or several components of exceptional relevance, which were triggered by the presumptive animal stress during the serum isolation procedure. Nonetheless, the results suggest that inhibitory responses in the GG can be elicited by chemicals at biologically relevant concentrations.

This is not to suggest that GG neurons exclusively sample internally circulating molecules. Pheromones and hormones are found in both serum and urine (Nodari et al. 2008; Novotny et al. 2007). The far-anterior location of the ganglion should indicate that the neurons are well positioned to be the first olfactory subsystem to interrogate inhaled odorants. However, an intriguing possibility is that specific molecules in serum, by inhibiting GG neurons, may be able to nullify the responses induced by the simultaneous inhalation of excitatory odorants. The GG may therefore have the capability to calibrate autonomously its sensory sensitivity with the internal physiological status of the animal.

A potential physiological state that can modulate GG activity is stress, as previous studies have indicated a role for the GG in mediating alarm behavior (Brechbuhl et al. 2008). Stress-responsiveness in GG neurons would be conferred by a different mechanism. We found that 10 μM cortisol inhibited spontaneous firing nearly half of the tested neurons, whereas 150 μM norepinephrine had no effect. Cortisol has short-term effects on neuronal firing in other systems (Avanzino et al. 1987; Avanzino et al. 1984; Filaretov 1976; Kasai et al. 1988; Zaki and Barrett-Jolley 2002). Membrane-permeable glucocorticoids are well suited to be endogenous modulators of GG activity. Because GG neurons are ensheathed by glial cells, modulators of GG activity are likely to be gaseous or lipid-soluble. During periods of extreme stress in rodents, levels of free glucocorticoids in serum can be as high as 3 μM (Bassett et al. 1978). Other factors in serum, such as binding proteins, may increase the sensitivity of GG neurons to glucocorticoids. Previous *in vivo* work on the GG may have inadvertently revealed on the detection of stress-related compounds in the bloodstream, as naris occlusions did not eliminate the neuronal activity (Brechbuhl et al. 2008; Mamasuew et al. 2008). Triggers such as alarm pheromones and cold may be primarily detected by other sensory systems and invoke GG activity as a secondary consequence. Future studies should be directed at evaluating whether serum modulation of GG activity has any significance *in vivo*.

ACKNOWLEDGMENTS

We thank B. Chang for *Cnga3*$^{-/-}$ mice. We thank J. Gutierrez for animal husbandry. This project was supported by grants from the U.S. National Institutes of Health and the U.S. National Science Foundation.

CONTRIBUTIONS

C.Y.L. and D.S.K. performed experiments. D.S.K., C.X., H.A.L., and S.E.F. contributed equipment and guided experiments. C.Y.L. wrote the paper.

REFERENCES

Avanzino GL, Ermirio R, Cogo CE, Ruggeri P, and Molinari C. Effects of corticosterone on neurones of the locus coeruleus, in the rat. *Neurosci Lett* 80: 85-88, 1987.

Avanzino GL, Ermirio R, Ruggeri P, and Cogo CE. Effect of microelectrophoretically applied corticosterone on raphe neurones in the rat. *Neurosci Lett* 50: 307-311, 1984.

Banerji S, Ni J, Wang SX, Clasper S, Su J, Tammi R, Jones M, and Jackson DG. LYVE-1, a new homologue of the CD44 glycoprotein, is a lymph-specific receptor for hyaluronan. *J Cell Biol* 144: 789-801, 1999.

Bassett JR, Strand FL, and Cairncross KD. Glucocorticoids, adrenocorticotropichormone and related polypeptides on myocardial sensitivity to noradrenaline. *Eur J Pharmacol* 49: 243-249, 1978.

Brechbuhl J, Klaey M, and Broillet MC. Grueneberg ganglion cells mediate alarm pheromone detection in mice. *Science* 321: 1092-1095, 2008.

Delay R, and Restrepo D. Odorant responses of dual polarity are mediated by cAMP in mouse olfactory sensory neurons. *J Neurophysiol* 92: 1312-1319, 2004.

Dilly S, Lamy C, Marrion NV, Liegeois JF, and Seutin V. Ion-channel modulators: more diversity than previously thought. *Chembiochem* 12: 1808-1812, 2011.

Duchamp-Viret P, Chaput MA, and Duchamp A. Odor response properties of rat olfactory receptor neurons. *Science* 284: 2171-2174, 1999.

Filaretov AA. The afferent input and functional organization of the hypothalamus in reactions regulating pituitary-adreno-cortical activity. *Brain Res* 107: 39-54, 1976.

Fleischer J, Hass N, Schwarzenbacher K, Besser S, and Breer H. A novel population of neuronal cells expressing the olfactory marker protein (OMP) in the anterior/dorsal region of the nasal cavity. *Histochem Cell Biol* 125: 337-349, 2006.

Fleischer J, Mamasuew K, and Breer H. Expression of cGMP signaling elements in the Grueneberg ganglion. *Histochem Cell Biol* 131: 75-88, 2009.

Frings S, Seifert R, Godde M, and Kaupp UB. Profoundly different calcium permeation and blockage determine the specific function of distinct cyclic nucleotide-gated channels. *Neuron* 15: 169-179, 1995.

Fuss SH, Omura M, and Mombaerts P. The Grueneberg ganglion of the mouse projects axons to glomeruli in the olfactory bulb. *Eur J Neurosci* 22: 2649-2654, 2005.

Grosmaitre X, Vassalli A, Mombaerts P, Shepherd GM, and Ma M. Odorant responses of olfactory sensory neurons expressing the odorant receptor MOR23: a patch clamp analysis in gene-targeted mice. *Proc Natl Acad Sci U S A* 103: 1970-1975, 2006.

Grüneberg H. A ganglion probably belonging to the N. terminalis system in the nasal mucosa of the mouse. *Z Anat Entwicklungsgesch* 140: 39-52, 1973.

Hallmann R, Mayer DN, Berg EL, Broermann R, and Butcher EC. Novel mouse endothelial cell surface marker is suppressed during differentiation of the blood brain barrier. *Dev Dyn* 202: 325-332, 1995.

He J, Ma L, Kim S, Schwartz J, Santilli M, Wood C, Durnin MH, and Yu CR. Distinct signals conveyed by pheromone concentrations to the mouse vomeronasal organ. *J Neurosci* 30: 7473-7483, 2010.

Kasai M, Kannan H, Ueta Y, Osaka T, Inenaga K, and Yamashita H. Effects of iontophoretically applied cortisol on tuberoinfundibular neurons in hypothalamic paraventricular nucleus of anesthetized rats. *Neurosci Lett* 87: 35-40, 1988.

Koos DS, and Fraser SE. The Grueneberg ganglion projects to the olfactory bulb. *Neuroreport* 16: 1929-1932, 2005.

Leinders-Zufall T, Lane AP, Puche AC, Ma W, Novotny MV, Shipley MT, and Zufall F. Ultrasensitive pheromone detection by mammalian vomeronasal neurons. *Nature* 405: 792-796, 2000.

Lin W, Arellano J, Slotnick B, and Restrepo D. Odors detected by mice deficient in cyclic nucleotide-gated channel subunit A2 stimulate the main olfactory system. *J Neurosci* 24: 3703-3710, 2004.

Liu CY, Fraser SE, and Koos DS. Grueneberg ganglion olfactory subsystem employs a cGMP signaling pathway. *J Comp Neurol* 516: 36-48, 2009.

Mamasuew K, Breer H, and Fleischer J. Grueneberg ganglion neurons respond to cool ambient temperatures. *Eur J Neurosci* 28: 1775-1785, 2008.

Mamasuew K, Hofmann N, Breer H, and Fleischer J. Grueneberg ganglion neurons are activated by a defined set of odorants. *Chem Senses* 36: 271-282, 2011a.

Mamasuew K, Hofmann N, Kretzschmann V, Biel M, Yang RB, Breer H, and Fleischer J. Chemo- and thermosensory responsiveness of Grueneberg ganglion neurons relies on cyclic guanosine monophosphate signaling elements. *Neurosignals* 19: 198-209, 2011b.

Mamasuew K, Michalakis S, Breer H, Biel M, and Fleischer J. The cyclic nucleotide-gated ion channel CNGA3 contributes to coolness-induced responses of Grueneberg ganglion neurons. *Cell Mol Life Sci* 67: 1859-1869, 2010.

Nodari F, Hsu FF, Fu X, Holekamp TF, Kao LF, Turk J, and Holy TE. Sulfated steroids as natural ligands of mouse pheromone-sensing neurons. *J Neurosci* 28: 6407-6418, 2008.

Novotny M, Jemiolo B, Harvey S, Wiesler D, and Marchlewska-Koj A. Adrenal-mediated endogenous metabolites inhibit puberty in female mice. *Science* 231: 722-725, 1986.

Novotny MV, Soini HA, Koyama S, Wiesler D, Bruce KE, and Penn DJ. Chemical identification of MHC-influenced volatile compounds in mouse urine. I: Quantitative Proportions of Major Chemosignals. *J Chem Ecol* 33: 417-434, 2007.

Potter SM, Zheng C, Koos DS, Feinstein P, Fraser SE, and Mombaerts P. Structure and emergence of specific olfactory glomeruli in the mouse. *J Neurosci* 21: 9713-9723, 2001.

Riviere S, Challet L, Fluegge D, Spehr M, and Rodriguez I. Formyl peptide receptor-like proteins are a novel family of vomeronasal chemosensors. *Nature* 459: 574-577, 2009.

Roppolo D, Ribaud V, Jungo VP, Luscher C, and Rodriguez I. Projection of the Gruneberg ganglion to the mouse olfactory bulb. *Eur J Neurosci* 23: 2887-2894, 2006.

Saria A, and Lundberg JM. Evans blue fluorescence: quantitative and morphological evaluation of vascular permeability in animal tissues. *J Neurosci Methods* 8: 41-49, 1983.

Schmid A, Pyrski M, Biel M, Leinders-Zufall T, and Zufall F. Grueneberg ganglion neurons are finely tuned cold sensors. *J Neurosci* 30: 7563-7568, 2010.

Shue EH, Carson-Walter EB, Liu Y, Winans BN, Ali ZS, Chen J, and Walter KA. Plasmalemmal vesicle associated protein-1 (PV-1) is a marker of blood-brain barrier disruption in rodent models. *BMC Neurosci* 9: 29, 2008.

Stan RV, Kubitza M, and Palade GE. PV-1 is a component of the fenestral and stomatal diaphragms in fenestrated endothelia. *Proc Natl Acad Sci U S A* 96: 13203-13207, 1999.

Storan MJ, and Key B. Septal organ of Gruneberg is part of the olfactory system. *J Comp Neurol* 494: 834-844, 2006.

Weiss J, Pyrski M, Jacobi E, Bufe B, Willnecker V, Schick B, Zizzari P, Gossage SJ, Greer CA, Leinders-Zufall T, Woods CG, Wood JN, and Zufall F. Loss-of-function mutations in sodium channel Nav1.7 cause anosmia. *Nature* 472: 186-190, 2011.

Zaki A, and Barrett-Jolley R. Rapid neuromodulation by cortisol in the rat paraventricular nucleus: an in vitro study. *Br J Pharmacol* 137: 87-97, 2002.

TABLES

Table 1: GG inhibitory responses elicited by puffs of 5-10 mM odorants in p2-p5 mice.

Chemical	mM (*n*)	Δ*f*, %
2-heptanol	7.1 (2)	-99 ± 1.1
citral	5.8 (4)	-98 ± 0.9
2-heptanone	7.2 (5)	-85 ± 14
eucalyptol	6.0 (5)	-77 ± 11
pyrazine	10 (10)	-59 ± 12
isovaleric acid	1.0 (5)*	-25 ± 19
ethanol	8.6 (7)	-18 ± 9.2
DMSO	7.0 (9)	+4.8 ± 3.8
D-glucose	10 (3)	+0.6 ± 4.9

* Higher concentrations of isovaleric acid induced acidity-related artifacts (Supplementary Fig. 3).

FIGURE LEGENDS

Figure 1: GG neurons in an acute slice preparation. The chemosensory capabilities of mouse Grueneberg ganglion (GG) neurons were investigated with pressure ejections ("puffs") of odorants. A) GG neurons could be identified by their green fluorescence in OMP-GFP$^{+/-}$ mice. The pipette on the left is the patch pipette. The pipette on the right is the puff pipette that delivered the chemicals of interest. B) Frequency vs. time plot of the spontaneous firing in a GG neuron. The horizontal black line on the top of the graph indicates the onset and duration of a puff of saline. The spontaneous firing of GG neurons is not altered by puffs of saline. Scale bar: 50 μm.

Figure 2: GG neurons from neonatal mice respond to 9.3 mM 2,5-DMP. A) The spontaneous discharge of a phasic-firing GG neuron (top panel) is composed of bursts of action potential (AP) spikes. During a puff of 2,5-DMP (region 1), the firing frequency within a burst increases (lower left panel), compared to the frequency before (region 1) and after (region 3) the puff. In this same neuron, a frequency vs. time plot (lower right panel) clearly marks the reversible increase in the intraburst frequency induced by 2,5-DMP. B) 2,5-DMP in a RSS-firing neuron increases the total firing rate. The instantaneous firing rate is fit to a two-exponential functional form (inset) to account for desensitization during a 20 s puff. C) In a sporadic-firing neuron, 2,5-DMP caused a transient set of high-frequency spikes. Horizontal black lines indicate puff onset and duration.

Figure 3: Population parameters of responsive neonatal GG neurons to 2,5-DMP. A) Depicted is the median time course (black line) of the response during a 20 s puff. A desensitization of >90% is observed during the puff. Individual responses are shown in the gray dotted lines. B) GG neurons from p0 mice were puffed with various concentrations (1.9, 4.6, 9.3 mM) of 2,5-DMP, revealing the dose dependence of their responses. C) p0-p4 mice were puffed with 9.3 mM 2,5-DMP. The responses declined with increasing age. The dotted line shows an exponential decay fit to the data.

D) GG neurons responded to 2,3-DMP with dose-dependent excitations.

Figure 4: GG neurons exhibit inhibitory responses to 3.6 mM 2-heptanone. A-C) on-cell recordings. D-E) whole-cell recordings. A) 5 s puffs (horizontal black line) of 2-heptanone induce abrupt and reversible decreases in the frequency of spontaneous charge in an RSS-firing neuron. B) The frequency vs. time plot of the neuron shown in (A) supports the aforementioned inhibition. C) The effects of 2-heptanone were dose dependent and had an IC_{50} of ~2 mM. D) Depicted are 5 s puffs of 7.2 mM 2-heptanone on a neuron clamped at different holding potentials. Associated with the puff is an outward current that increases in magnitude at more positive holding potentials. E) A 20 s puff of 2-heptanone induced a reversible hyperpolarization of the resting potential in a GG neuron.

Figure 5: Small-molecule modulators of the cGMP pathway induce excitatory responses in GG neurons. A) 20 s puffs (horizontal black lines) of 1.3 mM membrane-permeant 8-br-cGMP cause neuronal exaltations. B) A frequency vs. time plot of an RSS-firing neuron shows the rise and decay of the 8-br-cGMP-induced effect. The insets show exponential fits to the rise and decay, used to derive the time constants described in the text. C) Puffs of 100 μM IBMX elicited excitatory responses in some GG neurons. D) In other neurons, IBMX caused a transient burst of high-frequency spikes followed by a decrease in the overall firing rate. The burst is shown in the left panel; the right panel depicts the frequency vs. time plot for this neuron.

Figure 6: The cyclic nucleotide pathway can elicit membrane currents and alter resting potential. A) A 20 s puff of IBMX from a holding potential of -64 mV elicits inward currents. The currents exhibited both transient and sustained components. B) Nominal removal of Ca^{2+} enlarges IBMX-induced currents ~10-fold. C) Inward currents correlate with a depolarization of the resting potential. D) IBMX was puffed onto a GG neuron that successively clamped at more-positive holding potentials. The inset shows the I-V relationship of the elicited currents and indicates a reversal potential of ~0 mV.

Figure 7: CNGA3 is essential for neuronal responses induced by cyclic nucleotides. Shown are representative frequency vs. time plots of puffs of 1.3 mM 8-br-cGMP (A,B), 100 μM IBMX (C,D), and 9.3 mM 2,5-DMP (E,F) in *Cnga3*$^{+/-}$ (A,C,E) and *Cnga3*$^{-/-}$ (B,D,F) littermates. Horizontal blank lines indicate puff onset and duration. Responses to 8-br-cGMP and IBMX were completely absent in *Cnga3*$^{-/-}$ mice.

Figure 8: GG neurons reside near a vascular bed. A) Brightfield image (red) overlaid with green fluorescent signal shows that GG neurons reside at the anterior terminus of a nasal vascular plexus. B-D) Stainings on thin sections of the nasal vestibule for B) von Willebrand factor (vWF), C) plasmalemmal vesicular associated protein (PV-1), D) lymphatic LYVE1 and CD31/PECAM-1, and E) smooth muscle actin (αSMA). F) Whole-mount staining for synaptophysin (Syp) demonstrates axon varicosities of likely-sympathetic origin in the nasal vestibule. Scale bars: A) 400 μm, B) 50 μm, C) 60 μm, D) 100 μm, E) 50 μm, F) 40 μm.

Figure 9: GG neurons have preferential vascular access. A) Intraperitoneal (i.p.) injections of Evans blue (EB) dye resulted in preferential labeling of the nasal vestibule but not the epithelial layer of the MOE and VNO olfactory organs. Inset shows sagittal view of bisected nasal cavity under white light with rightmost portion representing the olfactory bulb and leftmost portion representing the respiratory epithelium. EB signal in fluorescent microscopic images is false-colored white. GFP signal of OMP-GFP mice is in green. A large amount of EB could inhibit the local GFP signal. B) Nasal irrigation of EB preferentially labels the MOE and VNO. C) There was minimal autofluorescence in the nasal vestibule, MOE, and VNO of un-manipulated mice. Scale bars: 200 μm, 2 mm (inset).

Figure 10: Potential compounds in serum alter GG activity. 20 s puffs of A) mouse serum and B) 10 μM cortisol reduce overall firing rate in GG neurons. C-E) Frequency vs. time plots of firing in GG neurons

puffed with C) serum, D) 10 μM cortisol, and E) 150 μM norepinephrine. Horizontal black bars indicate puff onset and duration.

FIGURES

Figure 1:

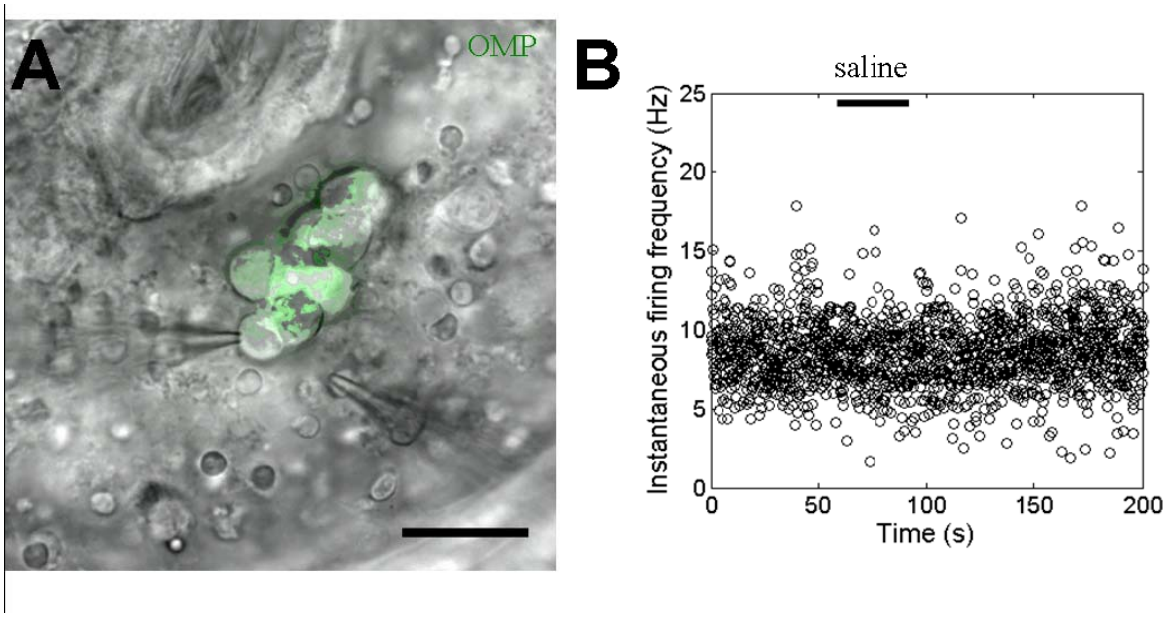

Figure 2:

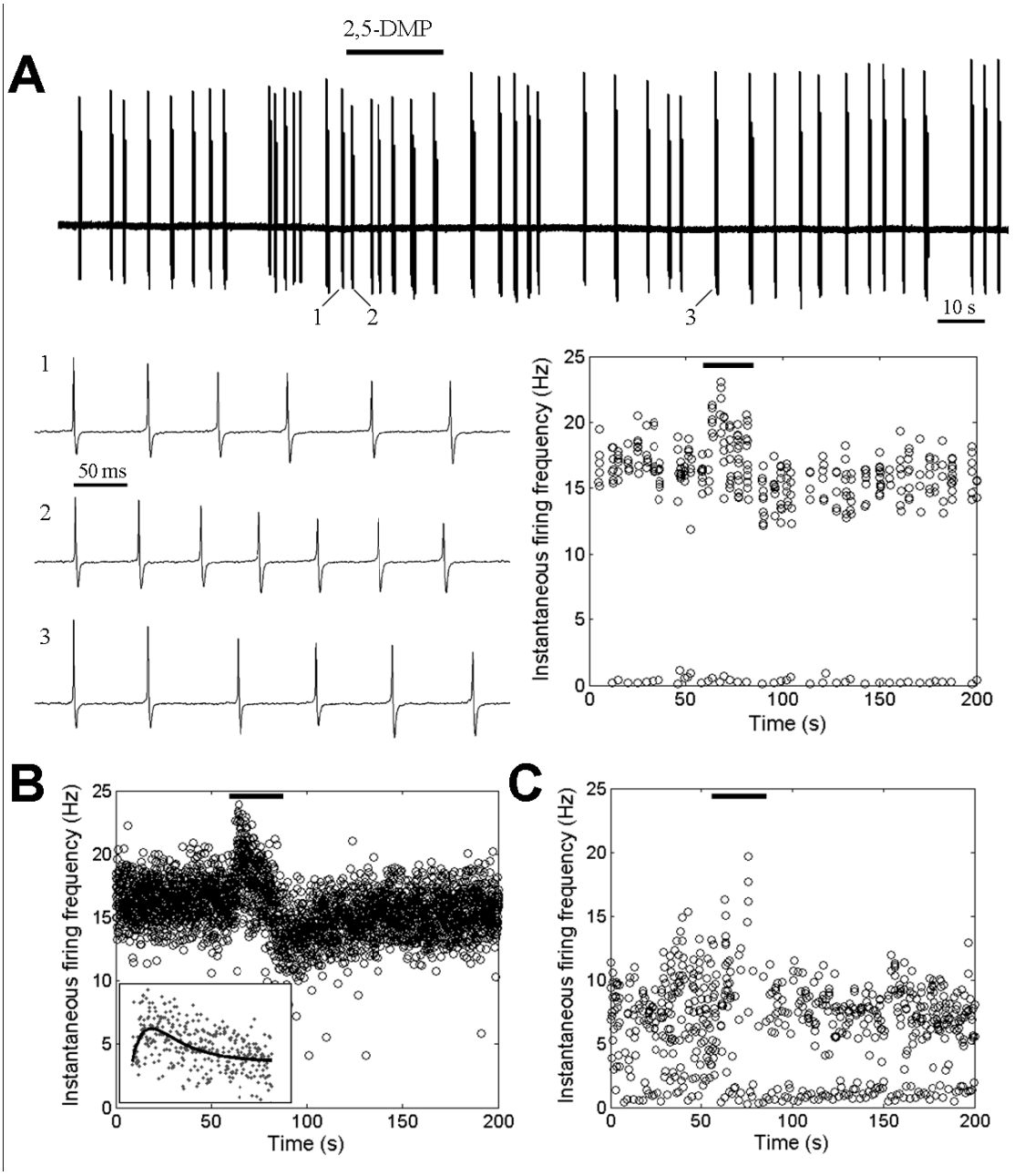
A
2,5-DMP
1
2
3
10 s
1
50 ms
2
3
Instantaneous firing frequency (Hz)
Time (s)
B
C
Instantaneous firing frequency (Hz)
Time (s)
Instantaneous firing frequency (Hz)
Time (s)

Figure 3:

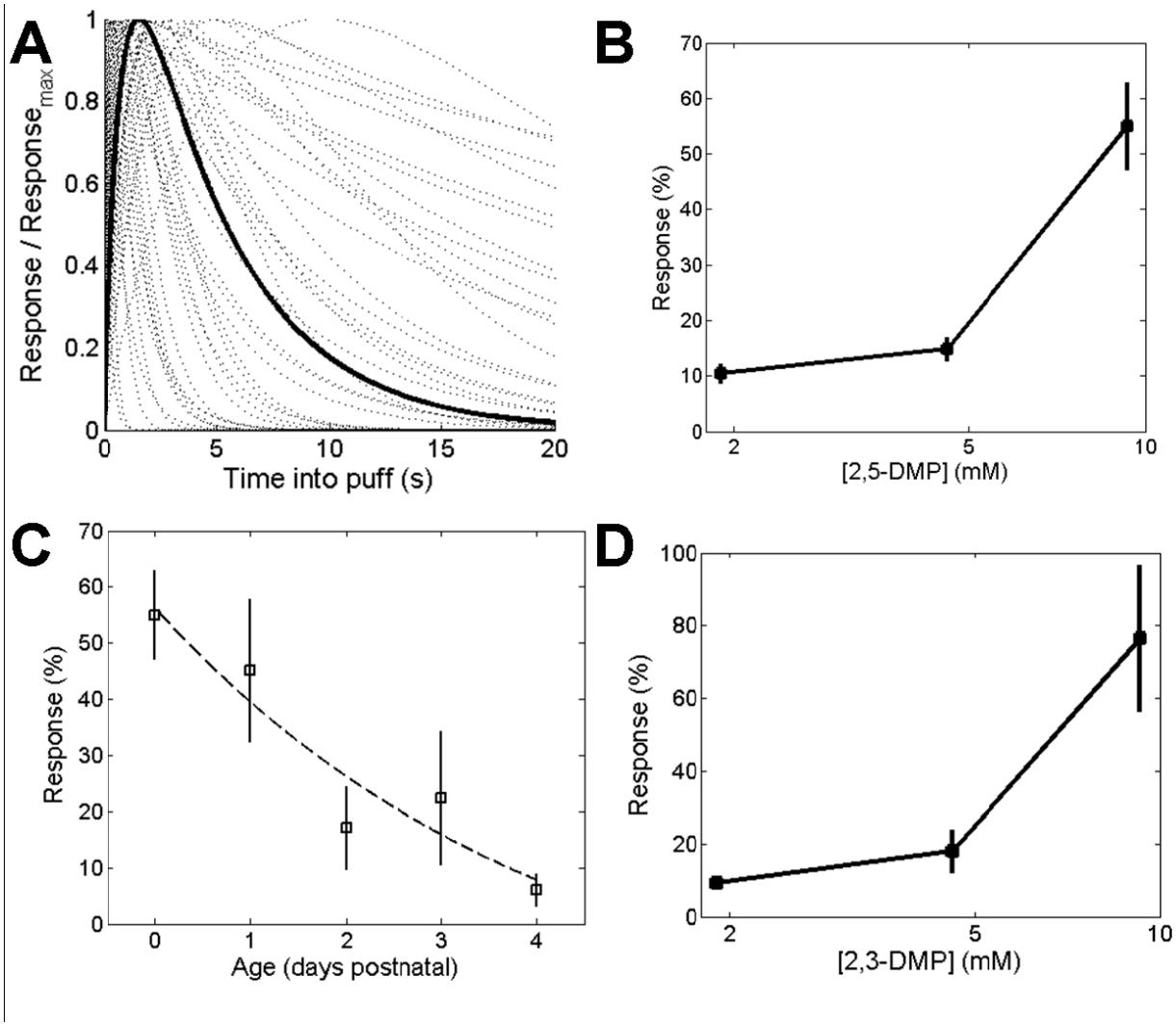
A
Response / Response$_{max}$
Time into puff (s)
B
Response (%)
[2,5-DMP] (mM)
C
Response (%)
Age (days postnatal)
D
Response (%)
[2,3-DMP] (mM)

Figure 4:

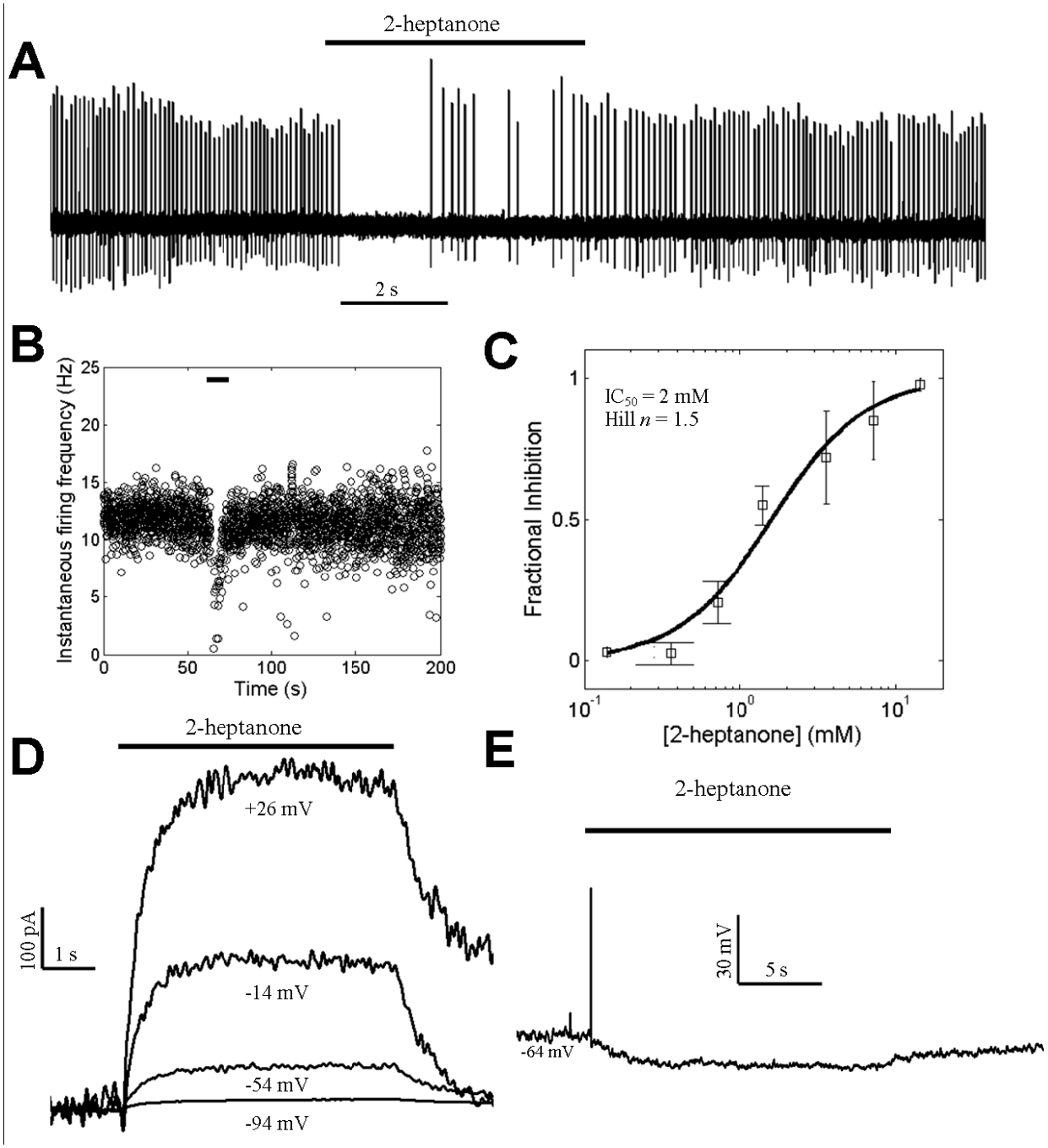
A
2-heptanone
2 s
B
Instantaneous firing frequency (Hz)
Time (s)
C
Fractional Inhibition
IC50 = 2 mM
Hill n = 1.5
[2-heptanone] (mM)
D
2-heptanone
+26 mV
-14 mV
-54 mV
-94 mV
100 pA
1 s
E
2-heptanone
30 mV
5 s
-64 mV

Figure 5:

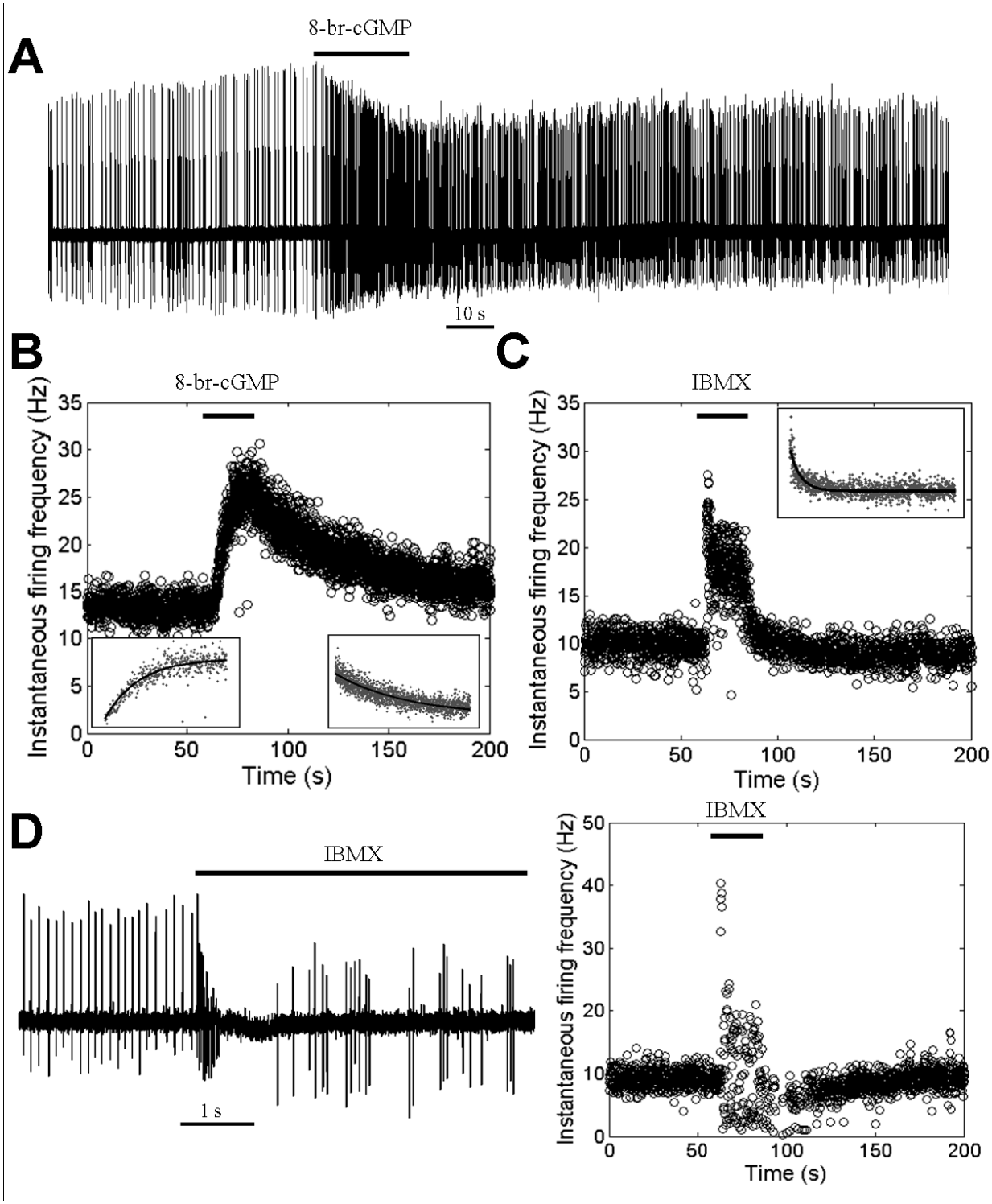
A
8-br-cGMP
10 s
B
8-br-cGMP
Instantaneous firing frequency (Hz)
Time (s)
C
IBMX
Instantaneous firing frequency (Hz)
Time (s)
D
IBMX
1 s
IBMX
Instantaneous firing frequency (Hz)
Time (s)

Figure 6:

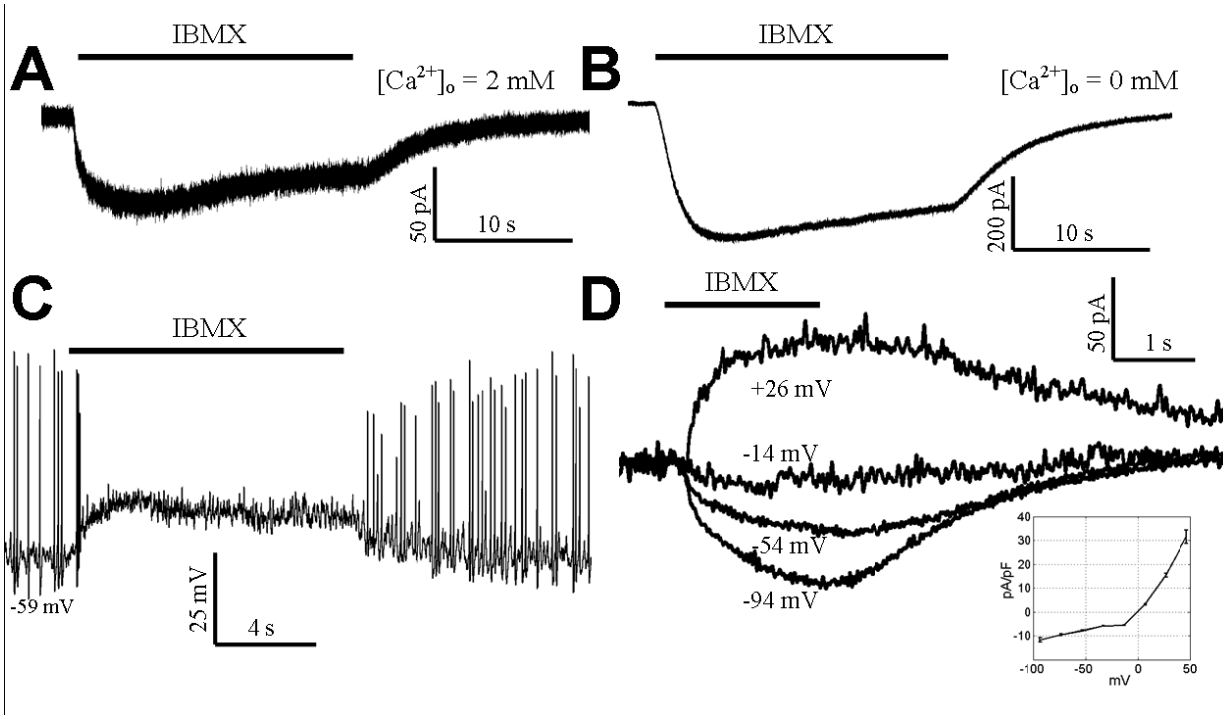
A
IBMX
[Ca2+]o = 2 mM
50 pA
10 s
B
IBMX
[Ca2+]o = 0 mM
200 pA
10 s
C
IBMX
-59 mV
25 mV
4 s
D
IBMX
50 pA
1 s
+26 mV
-14 mV
-54 mV
-94 mV
pA/pF
mV

Figure 7:

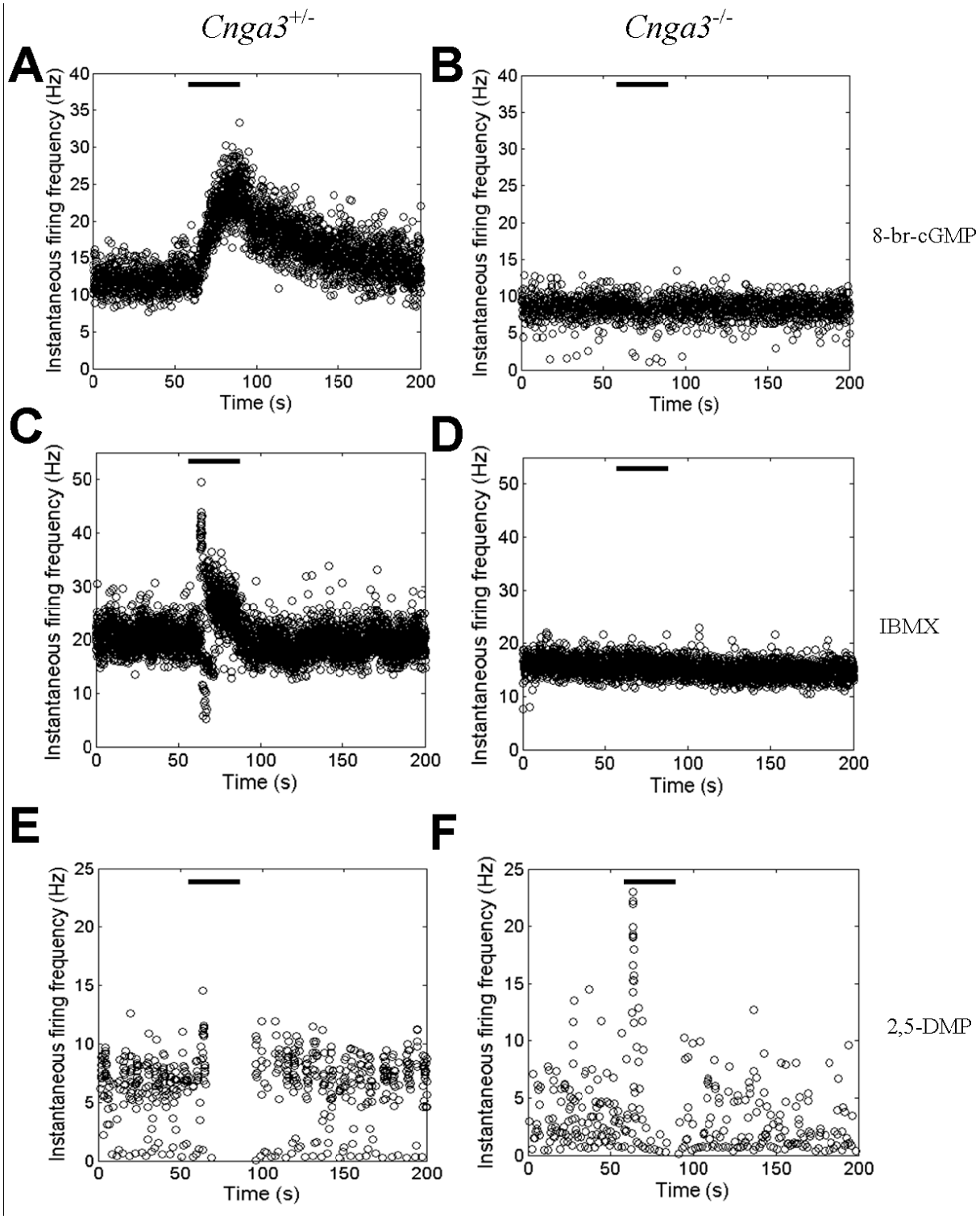
Cnga3+/-
Cnga3-/-
A
B
C
D
E
F
Instantaneous firing frequency (Hz)
Time (s)
8-br-cGMP
IBMX
2,5-DMP

Figure 8:

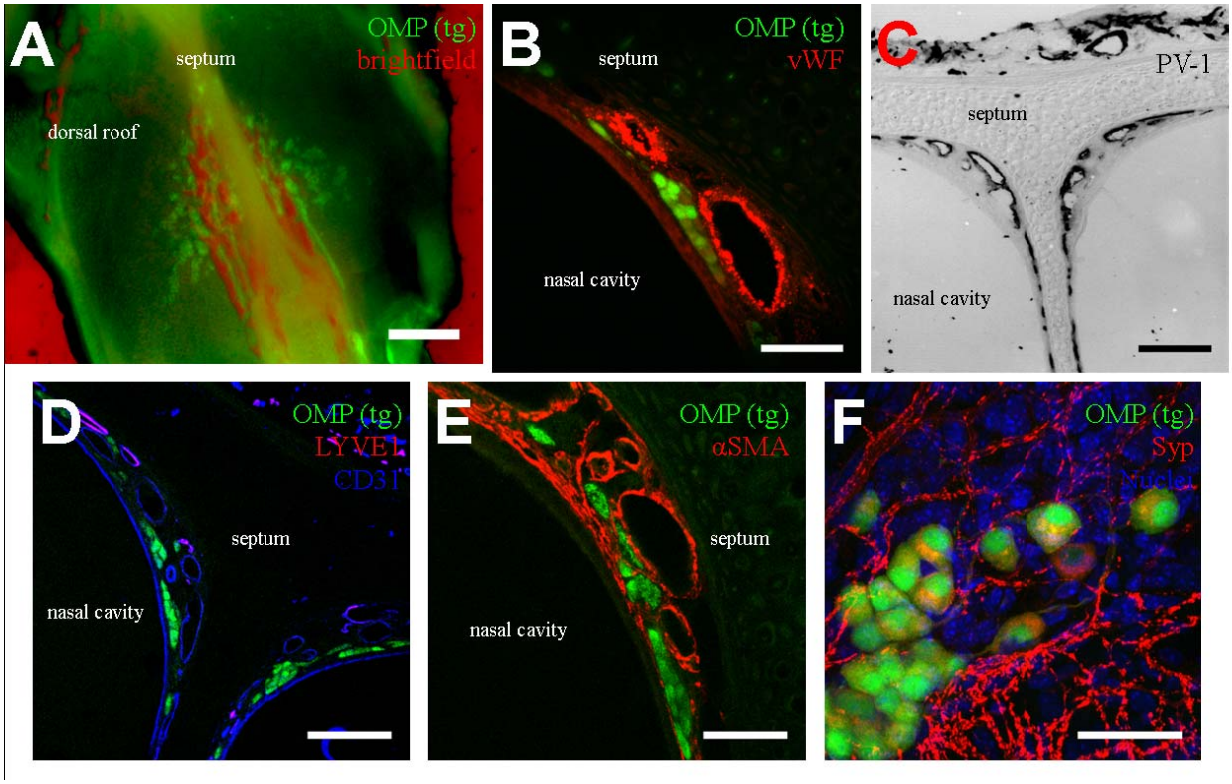
A
OMP (tg)
brightfield
septum
dorsal roof
B
OMP (tg)
vWF
septum
nasal cavity
C
PV-1
septum
nasal cavity
D
OMP (tg)
LYVE1
CD31
septum
nasal cavity
E
OMP (tg)
αSMA
septum
nasal cavity
F
OMP (tg)
Syp
Nuclei

Figure 9:

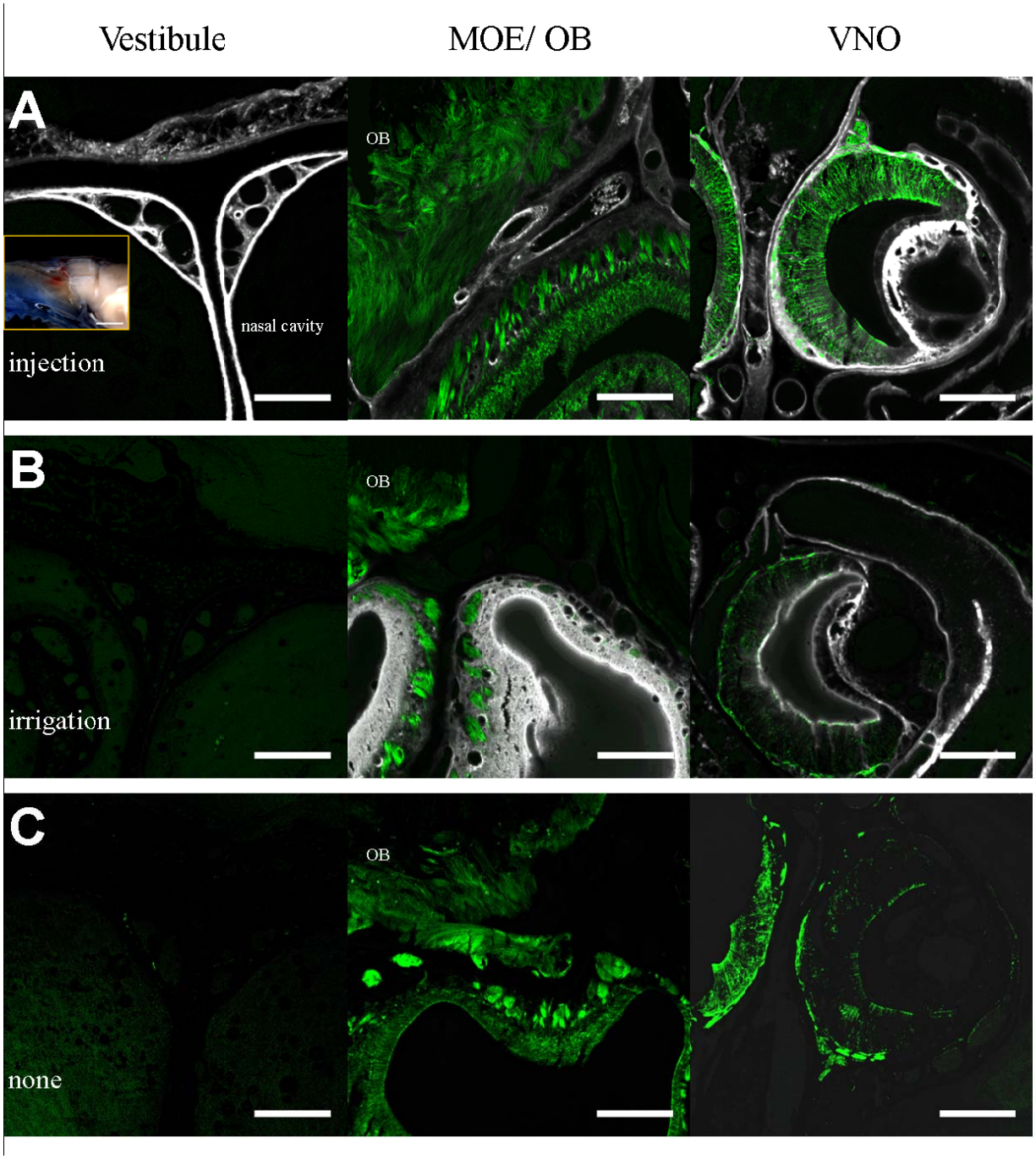
Vestibule
MOE/ OB
VNO
A
OB
nasal cavity
injection
B
OB
irrigation
C
OB
none

Figure 10:

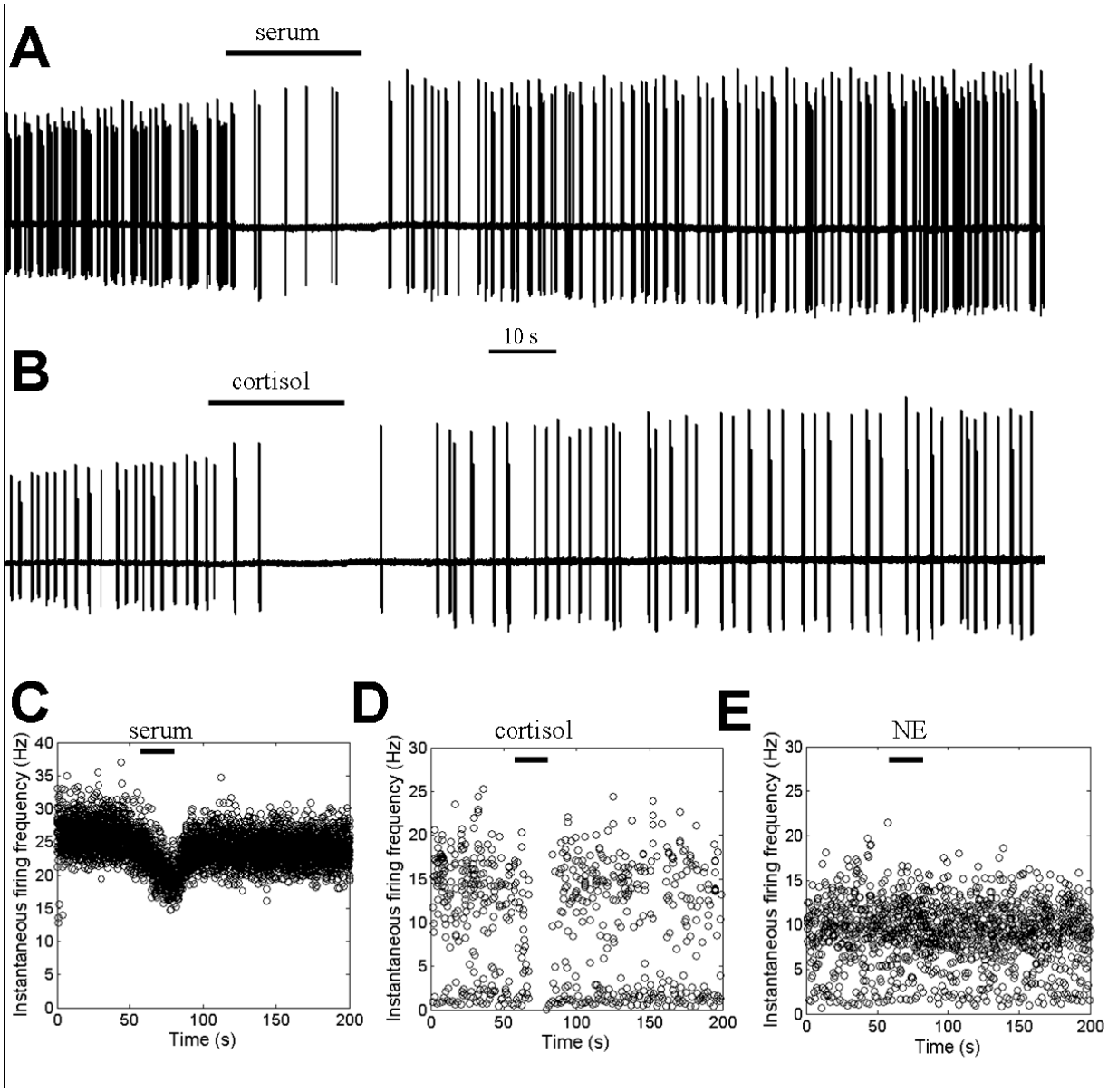
A
serum
10 s
B
cortisol
C
serum
D
cortisol
E
NE
Instantaneous firing frequency (Hz)
Time (s)

SUPPLEMENTARY FIGURES

Supplementary Figure 1:

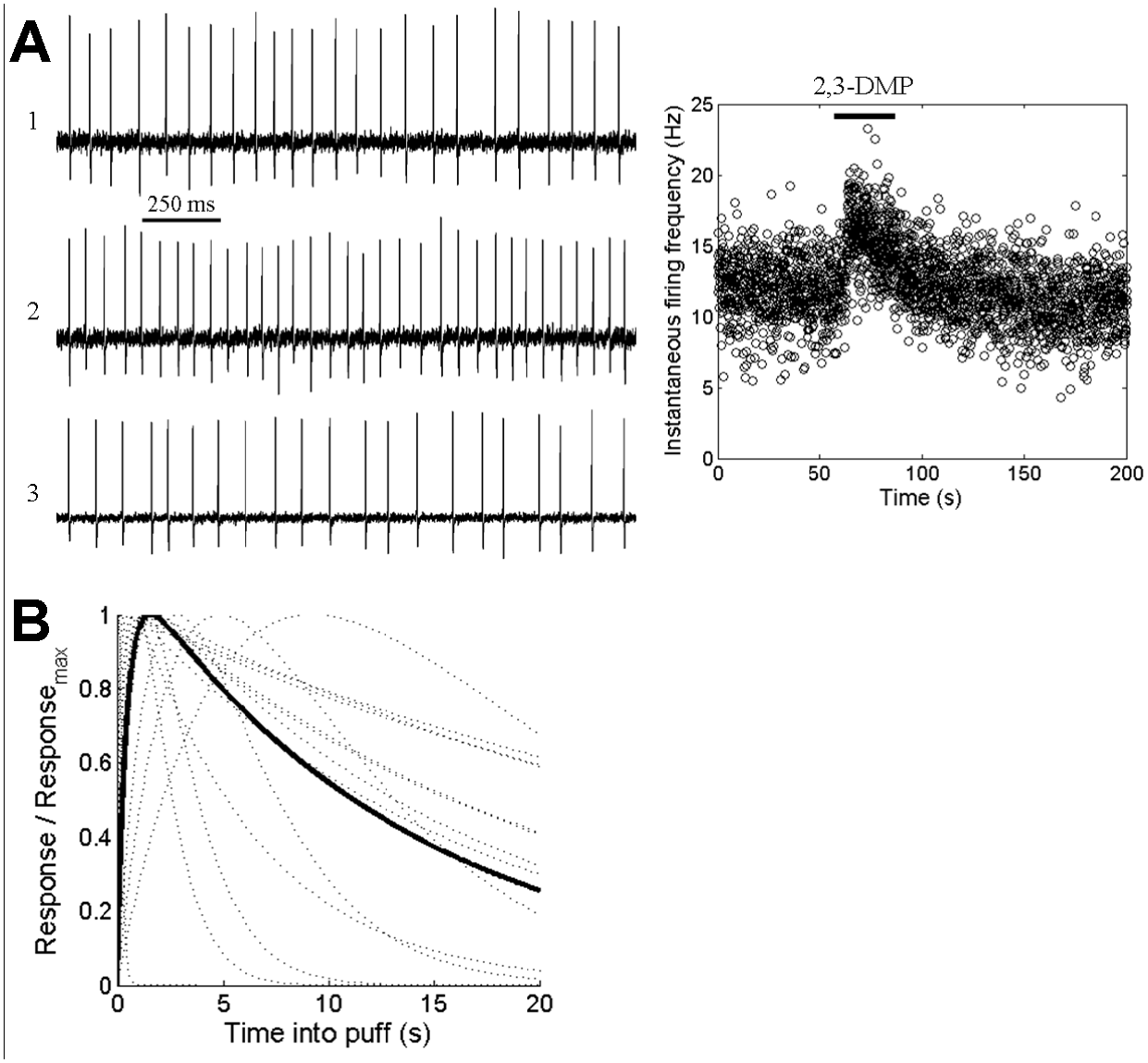

GG neurons in neonatal mice detect 2,3-DMP. A) An RSS-firing GG neuron (left panel) puffed with 9.3 2,3-DMP exhibits an increase in firing rate during (region 2) the puff, relative to before (region 1) and after (region 3) the puff. The frequency vs. time plot (right panel) demonstrates the reversible increase in firing rate. B) Responses to 2,3-DMP exhibited desensitization during a 20 s puff. The median line is shown in black; individual responses over the tested population are dotted gray.

Supplementary Figure 2:

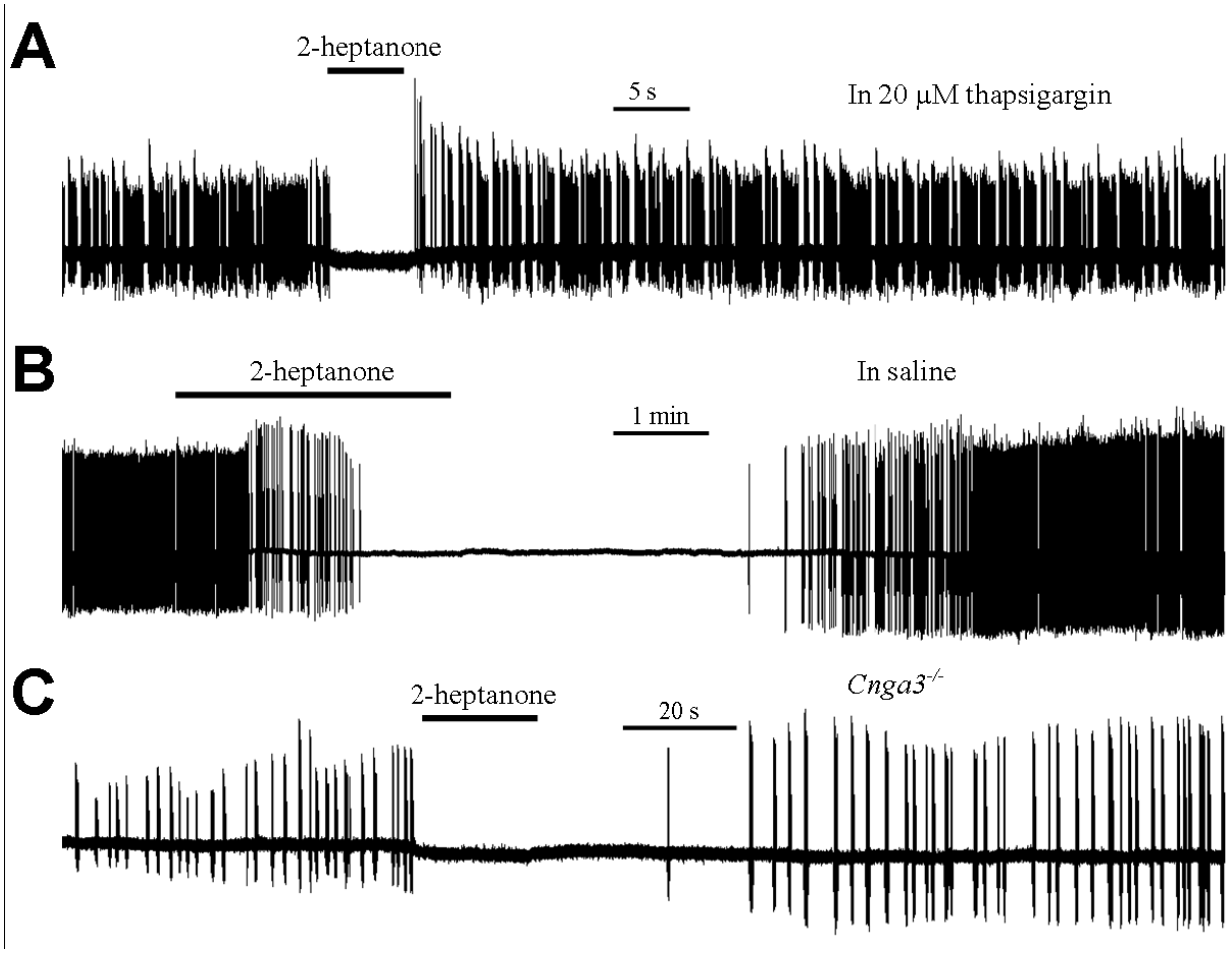

Transduction properties of 2-heptanone. A) Inhibitory responses to 7.2 mM 2-heptanone persisted when GG neurons were pretreated with 20 μM thapsigargin for 30 min. B) Superfusion of 7.2 mM 2-heptanone resulted a sustained inhibition of firing over 5 min. C) Silencing of a GG neuron by 7.2 mM 2-heptanone in a *Cnga3*$^{-/-}$ mouse. Horizontal black bars indicate onset and duration of puffs.

Supplementary Figure 3:

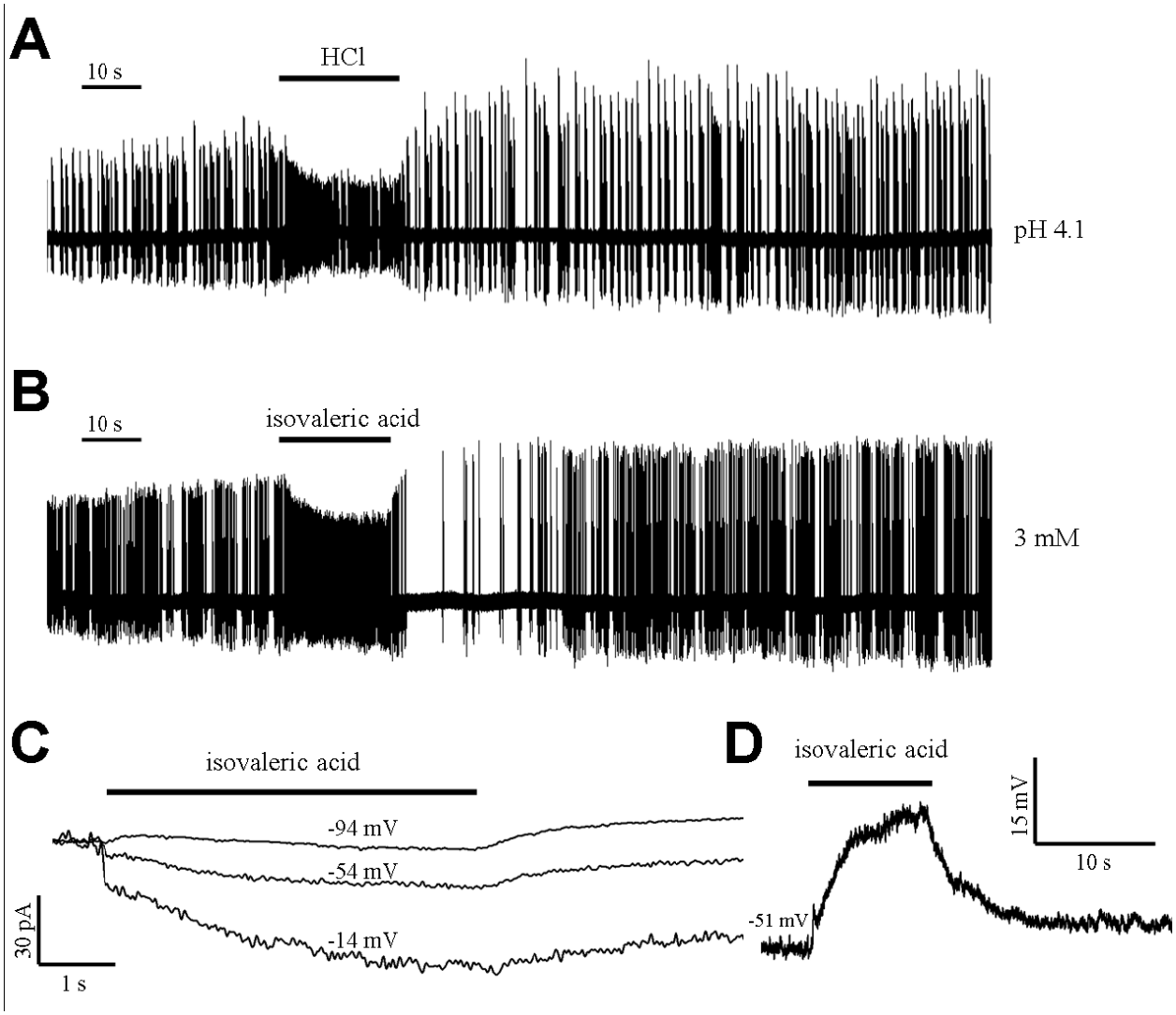

Acidified HBS evokes responses in GG neurons. A) 20 s puff of acidified HBS (pH 4.1 with HCl) excited GG neuron. B) 3 mM isovaleric acid, which acidified HBS to pH 4 also induced neuronal exaltation. C) In whole-cell recordings, puffs of 9.1 mM isovaleric acid at different holding potentials produced an unusual I-V relationship in which inward currents reversed near -80 mV. This is likely due to the shunting of a K^+ conductance. Currents are shown on the same baseline. D) Puffs of 9.1 mM isovaleric acid reversibly depolarized the resting potential of GG neurons.

Supplementary Figure 4:

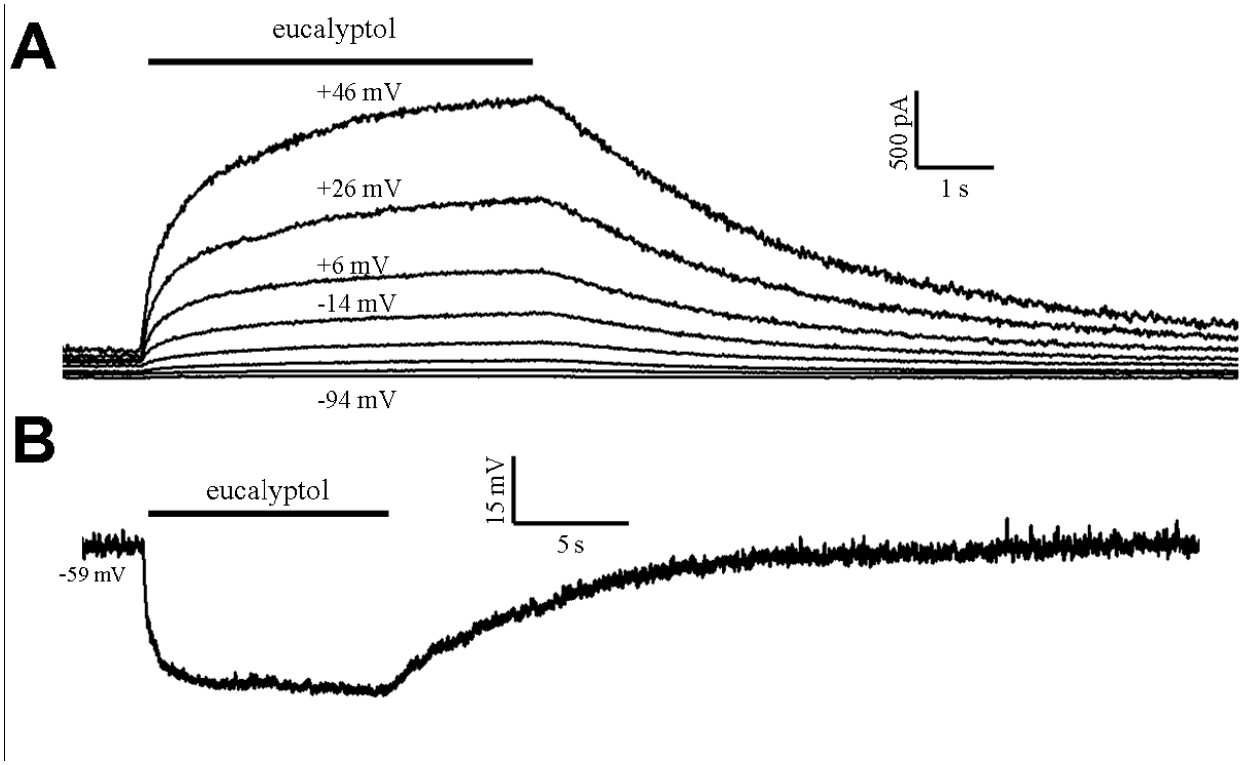

Membrane currents induced by eucalyptol. A) In whole-cell recordings, puffs of 6 mM eucalyptol at various holding potentials induced outward currents similar to those elicited by 2-heptanone. B) Inhibitory effect of eucalyptol is explained by a hyperpolarization of membrane potential. Horizontal black bars indicate time of puff onset and duration.

Supplementary Figure 5:

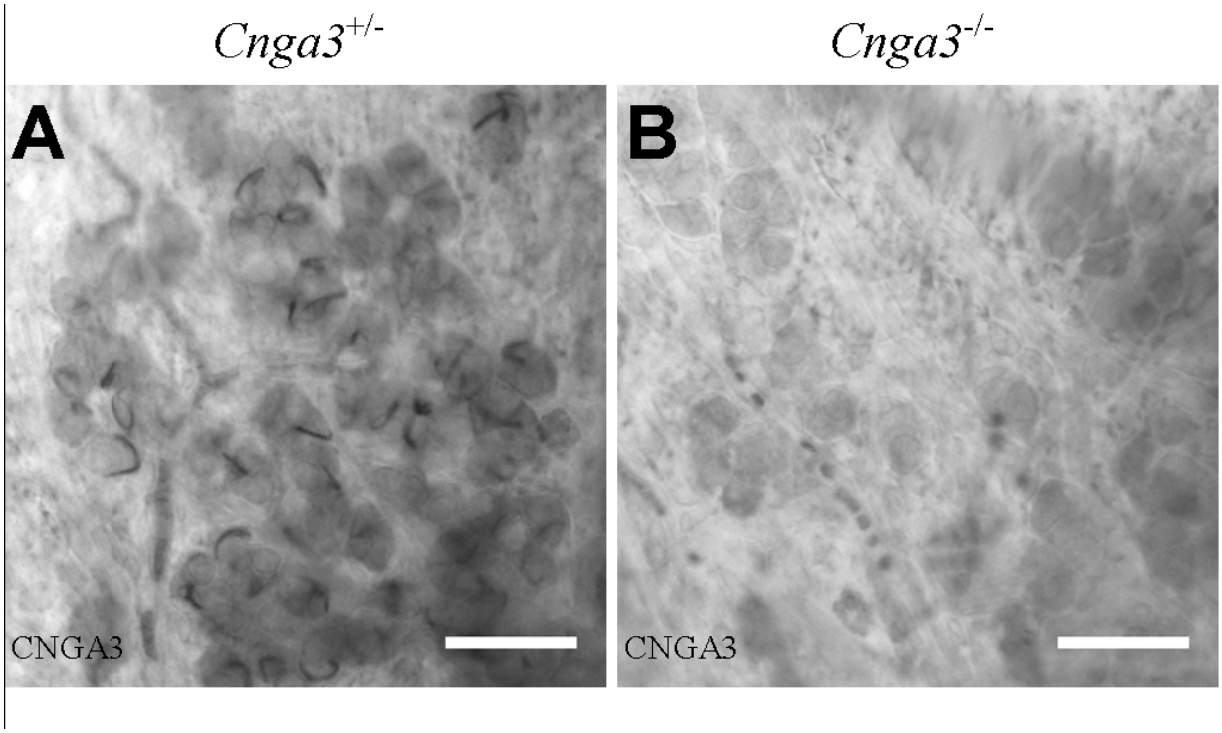

Nominal *Cnga3*$^{-/-}$ mice do not express CNGA3. A specific antibody to CNGA3 labels whip-like subcellular structures on GG neurons of *Cnga3*$^{+/-}$ mice. The labeling is absent in *Cnga3*$^{-/-}$ mice. Scale bars: 40 μm.

Supplementary Figure 6:

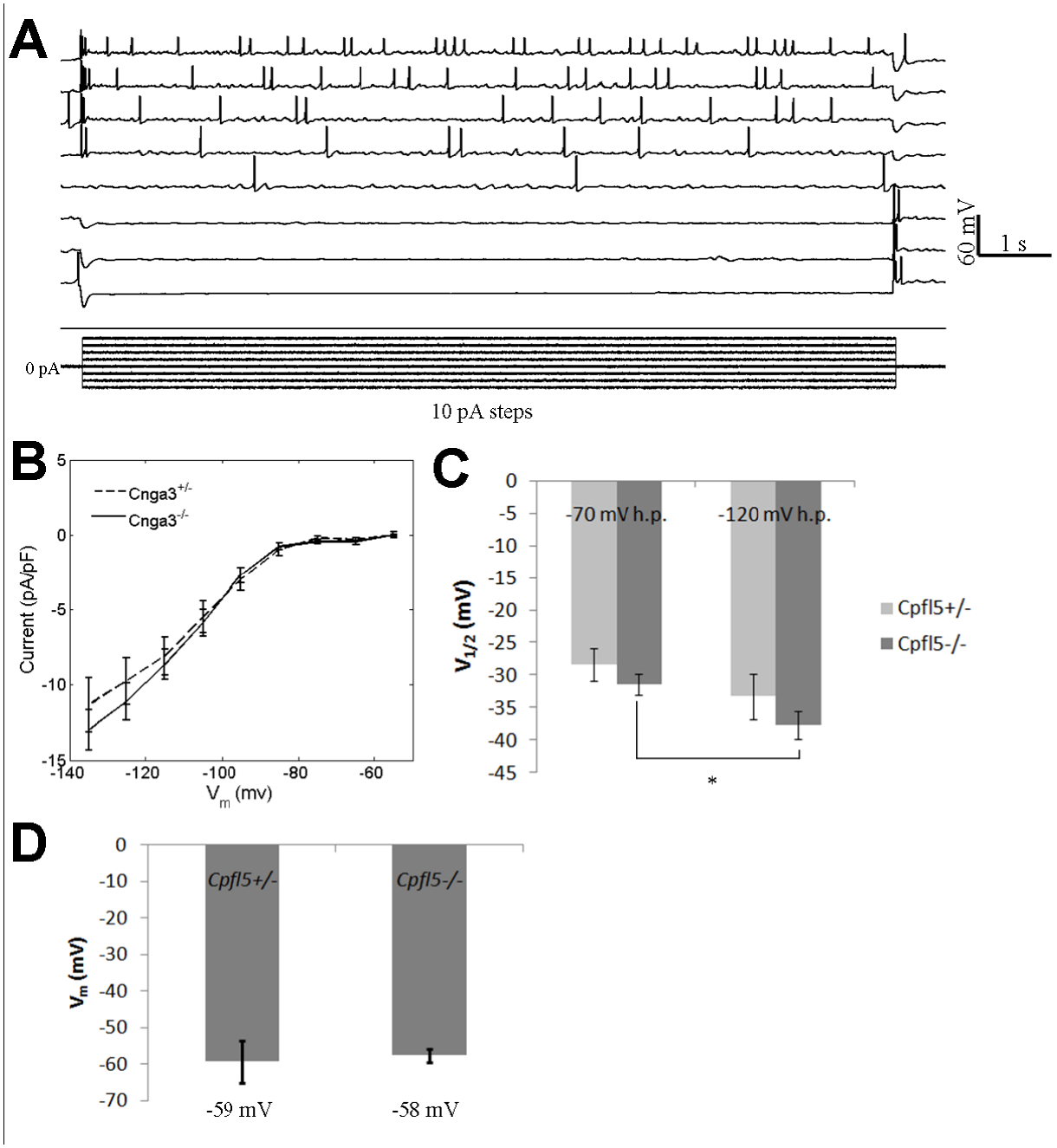

Cnga3$^{+/-}$ and *Cnga3*$^{-/-}$ mice have similar intrinsic membrane properties. A) Shown are data from a *Cnga3*$^{-/-}$ mouse. In whole-cell recordings, 10 s injections of depolarizing current in 10 pA steps from resting potential revealed increase in total spontaneous firing frequency associated with successively larger current magnitudes. Injections of hyperpolarizing current induced sags in membrane potential. These sags are indicative of I_h. Anode-break excitation is also observed. B-D) There was no difference in steady-state

properties of B) I_h, C) Na^+ current activation $V_{1/2}$ values evaluated by voltage jumps from -70 mV and -120 mV holding potentials (h.p.), or D) resting potentials in *Cnga3*$^{+/-}$ vs. *Cnga3*$^{-/-}$ mice. Asterisk (*) indicates statistical significance at $p < 0.05$ (two-sample t-test).

Supplementary Figure 7:

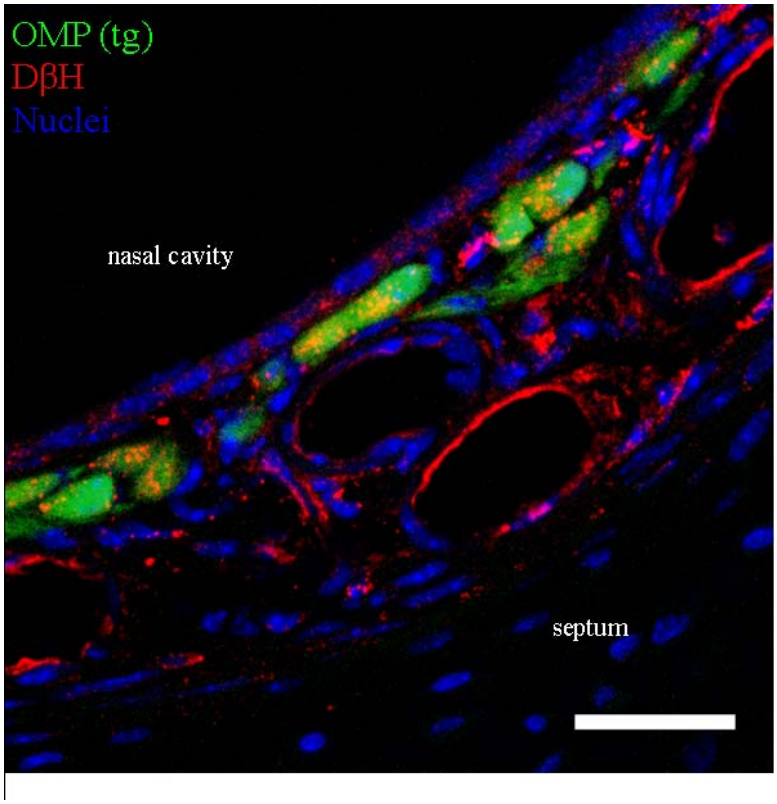

Localization of dopamine β-hydroxylase (DβH) in the nasal vestibule. Shown is the distribution of immunoreactivity for DβH in GG neurons (green) and blood vessel walls. DβH is essential for production of norepinephrine and is a marker of sympathetic nerve varicosities. Scale bar: 30 µm.

Supplementary Figure 8:

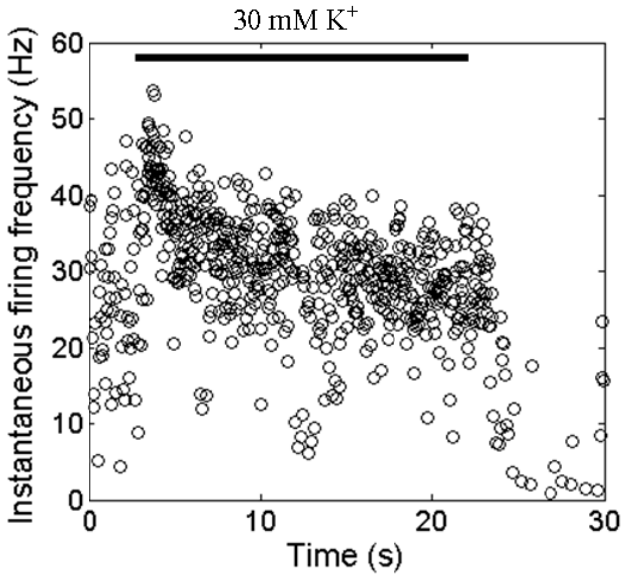

Effect of puffing a hyperkalemic solution. In contrast to responses induced by serum, which were gradually activating, responses induced by a 20 s puff of 30 mM KCl reached maximum within 2 s. Shown is a frequency vs. time plot, with horizontal black bar indicating puff onset and duration.

--- Chapter 5 ---

Weaning induces neuronal activity in the Grueneberg ganglion olfactory subsystem

Cambrian Y. Liu, Scott E. Fraser, David S. Koos

ABSTRACT

The Grueneberg ganglion (GG) is a primary olfactory subsystem bilaterally located in the far-anterior nasal vestibule of many mammals. Its ~1,000 constituent neurons are believed to serve multimodal functions in the detection of low ambient temperatures and alarm and urinary pheromones. *In vivo* studies have supported the specialization of mouse GG function to these various sensory modalities at different ages of the animal. Here, we examined behavioral manipulations that induced nuclear accumulation of c-Fos protein in the GG. As c-Fos immunoreactivity (c-Fos-IR) in the nucleus is an established marker of neuronal activation in the primary olfactory system, these experiments should provide information about the function of the GG. In mice younger than weaning age (<p20), manipulations that involved parental separation induced nuclear c-Fos-IR in GG neurons. A greater number of GG neurons were active in mice older than p5. GG responses were independent of the presence of conspecifics but dependent on the expression of the cGMP-gated cationic channel CNGA3. Several aspects of the experiments and results are inconsistent with known modalities of GG function; thus, GG neurons may have additional sensory functions during weaning.

KEYWORDS

c-Fos, nuclear accumulation, immunohistochemistry, maternal separation, weaning, stress

INTRODUCTION

In mice and many other mammals, the detection and discrimination of odors and pheromones is initiated by collections of primary olfactory neurons at several anatomically-distinct locations in the nasal cavity. At its far-anterior end, where the septum is cartilaginous, there are ~1,000 clustered neurons in the mouse that are present throughout life and that project axons forming 8-12 glomeruli in the necklace-like domain of the olfactory bulb (Fleischer et al. 2006a; Fuss et al. 2005; Grüneberg 1973; Koos and Fraser 2005; Roppolo et al. 2006; Storan and Key 2006). On the basis of their expression of olfactory marker protein (OMP), a pheromone receptor and trace-amine associated receptors at birth (Fleischer et al. 2006b; Fleischer et al. 2007), and key components of a cGMP signaling pathway that can mediate odor transduction (Fleischer et al. 2009; Liu et al. 2009), the neurons of this so-called Grueneberg ganglion (GG) have been proposed to have a primary olfactory function.

GG neurons appear to function in multiple sensory contexts. Firstly, i*n vivo* studies measuring the transcription of the c-Fos immediate-early gene in mice have demonstrated that these neurons respond to low ambient temperature primarily at neonatal ages, when mice exhibit poor auto-regulation of body temperature (Mamasuew et al. 2008). These *in vivo* neuronal responses depended on the cGMP-gated cationic channel CNGA3 (Mamasuew et al. 2010). *In vitro* studies support the function of GG neurons as finely tuned temperature sensors. GG neurons exhibited increases in cytosolic [Ca^{2+}] to cold. These increases were independent of changes in intracellular Ca^{2+} and the presence of CNGA3, but dependent on fast-inactivating Na^{+} conductance (Schmid et al. 2010). Secondly, GG neurons are also proposed to detect an alarm pheromone. They exhibited cytosolic [Ca^{2+}] bursts when exposed to an unknown water-soluble compound collected during the asphyxiation of mice. This compound induced freezing behavioral responses in adult mice (Brechbuhl et al. 2008). Thirdly, GG neurons respond to exposure to 2,5-dimethylpyrazine (Mamasuew et al. 2011a), a known rodent pheromone (Ma et al. 1998), with increases in spontaneous firing rate (Chapter 4). Certain other odorants and pheromones, such as 2-heptanone, are capable of decreasing the spontaneous firing rates in the neurons (Chapter 4).

We have examined patterns of activity in mouse GG neurons by measuring their activity-dependent nuclear accumulation of c-Fos protein. This assay has previously been used to analyze neuronal activity in olfactory neurons of the vomeronasal organ (VNO) (Kimoto and Touhara 2005). We found that parental separation reliably induced nuclear c-Fos immunoreactivity (c-Fos-IR) in GG neurons. In contrast to previous reports (Mamasuew et al. 2008), the activity levels were highest in adolescent mice and were significantly lower in neonates. GG neurons seem primed for activity during adolescent ages and may serve specialized functions during weaning. The results are discussed with attention to a recent report (Chapter 4) suggesting the modulation of GG activity by blood-borne stress hormones.

MATERIALS AND METHODS

Animal Care

Mice were maintained according to Caltech-approved protocol. Mice were housed in 6000 cm^3 plastic cages, provided with food (LabDiet 5001), and attached to an automated water delivery system equipped with quick disconnect manifold mounted drinking valves (A-160). Cages were assembled onto racks and were provided HEPA-filtered air (Enviro-gard). Ambient room temperature was kept constant at 22˚ C.

Once per week, mice were moved from soiled cages to clean cages, as part of normal maintenance procedure. Once per month, sullied water valves were replaced with clean ones. We found that experiments performed within 12 h of a regularly scheduled cage change would yield unreliable results; hence, we avoided this scenario in the experiments discussed below.

Animals were housed with an equal-phase 24 h light-dark cycle. We began and finished all experiments in the range between 1600 and 1900 h, fully within the light cycle. At these times, there was no interference from the quotidian activities of animal facility staff or other researchers. No other mice were handled by the investigators before or during the experiments on the days of the experiments. Control groups and experimental groups were formed from littermates. All mice used were of the

BL/6/129 background, except for *Cnga3*$^{-/-}$ and *Cnga3*$^{+/-}$ mice, which were of the RHJ/LeJ (JR 5415) background. *Cnga3*-mutant mice were described and characterized previously (Chapter 4).

Transport Stimulus

This stimulus produced the c-Fos staining patterns shown in Fig. 1. The cage containing the mouse dam, sire, and litter was moved to a sterile hood within the animal facility. Offspring were separated from parental mice and placed into an enclosed 1,800 cm^3 cardboard box. The cardboard box (containing mice) was then carried by the investigators out of the animal facility to a dissection station in a separate building. Mice were left in the cardboard box in the dissection station, without food or water, for 5-150 min prior to euthanasia by CO_2. Collected tissue was processed for immunohistochemistry.

Cage Change Stimulus

Sterilized cages containing clean woodchip bedding, food, and water were prepared. Parents and offspring of a single litter were moved to a sterile hood within the animal housing room. Offspring were separated and moved to the clean cage as a group (2-5 per group). The clean cage (containing the new mice) was brought to a different cubicle on the original housing rack. Mice were euthanized by CO_2 at a sterile dissection station within the housing room. Mice of a given experiment were euthanized as a group 5-150 min after the cage change. The dissection of nasal vestibules took ~3 min per mouse. Tissue was processed for immunohistochemistry.

In some experiments, the clean cage containing newly weaned mice was transported to a dissection station in a separate building (Fig. 3A). These mice were euthanized by CO_2 and processed for immunohistochemistry at this distally-located station.

The effects of human contact on GG activity (Fig. 3A) were evaluated by moving the cage (parents and offspring) to a sterile hood. Offspring mice were picked up and dropped back down into the original cage. The cage was returned to its original cubicle on the housing rack. Tissue was collected 75-120 min after these manipulations.

To evaluate the necessity of conspecific animals (Fig. 3D), clean cages were prepared in a sterile hood. Unweaned mice were moved into these clean cages such that some cages housed >2 mice and other cages housed only 1 mouse. Cages were returned to separate cubicles on the original housing rack. Mice were sacrificed after 75-120 min.

Weaning Stimulus

To discriminate between the contributions of parental separation and environmental novelty (*i.e.*, a clean cage) (Fig. 3A), mouse litters with the dam and sire were placed in a sterile hood. The dam and sire were moved to a clean cage. The cage containing the offspring was returned to its original cubicle on the animal housing rack. After 75-120 min, the offspring mice were sacrificed.

Ex vivo culture

p10 mice were transported using the described "Transport Stimulus" procedure. The animals were euthanized by cervical dislocation and decapitated. Heads were skinned. Excess bone and tissue were removed to expose the brain, olfactory bulbs, and nasopalatine duct. Remaining tissue was placed into excess pre-warmed (37˚C), pre-equilibrated (5% CO_2) Neurobasal-A media (Invitrogen), supplemented with 1X B-27 (Invitrogen), 200 mM L-glutamine, and 50 U/mL penicillin-streptomycin. Tissue was gently shaken at 37˚C for 2-6 h. Nasal vestibules were removed and fixed in cold 4% paraformaldehyde overnight and processed for immunohistochemistry.

Immunohistochemistry

Immunohistochemistry was performed as previously described (Liu et al. 2009), but with an extended incubation time (~60 h) of anti-c-Fos antibody to optimize nuclear labeling. Briefly, nasal vestibules were dissected from mice and fixed overnight in cold 4% paraformaldehyde prepared in phosphate buffered saline (PBS). After cryoprotection in buffered 30% sucrose (w/v), vestibules were embedded in Tissue-Tek O.C.T. (Sakura) and sectioned to 14 µm thickness on a freezing microtome at

-23˚C. Tissue was adhered to slides. For fluorescence staining, slides were sequentially incubated with rabbit anti-c-Fos primary antibody (EMD Chemicals, 1:10,000, cat# PC38), biotinylated goat anti-rabbit secondary antibody (Vector Labs, 3 µg/mL), and tertiary streptavidin-Alexa Fluor 555 label (Invitrogen, 2 µg/mL), with 4 changes of PBS between each incubation. PBS-buffered 0.3% Triton-X was used to promote infiltration during antibody incubations. Final PBS washes included 0.2 µM Topro-3 (Invitrogen) as a nuclear stain.

For diaminobenzidine (DAB)-based revelation of staining on thin sections, slides with adherent tissue was exposed to buffered 0.3% (v/v) hydrogen peroxide solution for 10 min prior to incubation with the primary antibody. A tertiary label of peroxidase-streptavidin (2.5 µg/mL, MP Bio) was used following the incubation of biotinylated secondary antibodies. Labeling was revealed with a Ni-enhanced DAB kit (Thermo Scientific) with a development time of 5-12 minutes in the dark. Thin sections of the VNO were processed in the same manner.

In whole-mount stainings, the superficial epithelium of the nasal vestibule (containing the GG) was peeled apart from the septum in fixed specimens. For DAB staining, the tissue was exposed to buffered 0.3% (v/v) hydrogen peroxide solution for 30 min prior to incubation with the primary antibody. After staining, tissue was adhered to a slide, in preparation for microscopic examination.

Imaging

For fluorescent imaging, slides were mounted with Fluoro-Gel (Electron Microscopy Sciences). Imaging was performed on an LSM 510 upright confocal microscope (Zeiss) with excitation laser wavelengths of 488 nm, 543 nm, and 633 nm. Optical sections of various thicknesses could be generated by varying the pinhole diameter. With a 40X/0.75 Plan-NeoFluar (Zeiss) objective, we obtained optical slices of ~4 µm thickness by using a pinhole diameter of 260 µm.

For brightfield imaging, slides were mounted with polyvinylpyrrolidone (PVP) mounting medium, containing: 2.5 g PVP 40K, 0.5 g PVP 360K, 1 mL glycerol, 50 mg n-propyl gallate, 1 crystal

thymol, 25 mL Tris buffer (pH 7.4). Brightfield images of DAB deposition were obtained on a Zeiss Axiophot compound microscope.

Data Analysis

The degree of neuronal activation in the GG organ was assessed by counting the number of GG nuclei that exhibited c-Fos accumulation in DAB-developed nasal vestibule sections. GG neurons could be recognized by their larger size, their clustering, and their faint cytosolic labeling by the antibody. Using a hand-tally counter, we performed the counting during analysis of tissue by light microscopy. Repeated counting of the same sample yielded scores within 10%. Data from several different experiments were pooled. Effect sizes were measured by comparing the nuclei counts for the experimental group versus littermate controls in the same experiment. The mean control effects across different experiments were then normalized to 1 to account for variability in baseline activity. The normalized values correspond to a dimensionless "activity index." Error bars indicate standard error. Statistical significance between groups was evaluated using the two-sample t-test with the assumption of unequal variances and a significance level of 0.05. Data analysis was performed in MATLAB 7.4.0 with custom-written routines. Images were prepared in ImageJ (NIH).

RESULTS

We found, fortuitously, that transport of unweaned mice from a housing facility to a separate euthanasia/dissection facility was sufficient to induce the nuclear c-Fos-IR in GG neurons. This was a robust stimulus resulting in >10 active neurons per animal in 25/25 mice younger than p20. The intensely stained GG nuclei were readily discerned in thin sections (Fig. 1A) and whole-mount preparations (Fig. 1B) of the mouse nasal vestibule. Fluorescent stainings with OMP-GFP mice (Potter et al. 2001) revealed a colocalization of c-Fos protein, nuclear dye, and OMP in thin sections from the anterior nasal vestibule in transported mice, confirming the c-Fos-IR to be in GG nuclei. No GG nuclear c-Fos-IR was evident in mice sacrificed within 5 min of transport and whose noses were immediately fixed (Fig. 1C). However,

the GG neurons of animals sacrificed in the range between 45 and 150 min after transport unambiguously exhibited nuclear c-Fos-IR (Fig. 1D). Transport was sufficient to elicit activity, because nuclear c-Fos-IR was still observed in GG neurons of mice that were sacrificed immediately after transport, but whose noses were cultured *ex vivo* for 2 h prior to fixation and processing (Fig. 1E). After 6 h of *ex vivo* culture, c-Fos protein in GG neurons was diffusely distributed throughout the cell (Fig. 1F), similar to transported animals sacrificed after 5 min.

Transport is a heterogeneous stimulus, with components such as temperature changes, stress, and new external chemosensory, audible, and tactile cues that would be expected to trigger activity in sensory systems. We sought to narrow the GG stimulus. To this end, we tested the effect of a cage change on GG activity ("cage change stimulus"). In these experiments, unweaned mouse pups, as a group, were moved from the company of the dam, sire, and littermates to a clean cage, located in proximity to the original cage. Mice older than p13 (but younger than p20) immediately exhibited exploratory locomotor activity in the new cage, consistent with previous observations in adult mice (Drenan et al. 2008). These pups were sacrificed 60 to 90 min after movement. At the time of sacrifice, the mice were usually found huddled together.

The cage change stimulus induced nuclear c-Fos-IR in GG neurons in 53/58 (91%) mouse pups. Fig. 2A shows the number of c-Fos-IR GG nuclei per animal in relation to the age of the animal. On average, a higher number of GG neurons were activated in animals in the age range of p6 to p21 (176 ± 18 nuclei, n=42), compared to animals in the age range of p0 to p4 (46 ± 8 nuclei, n=16, $p < 0.001$) (Fig. 2B). The highest number of observed c-Fos+ nuclei was 531 in a p13 mouse. Mice that were sacrificed at the start of the experiment exhibited almost no nuclear c-Fos-IR in the GG (5 ± 1 nuclei, n=33). A 10 min exposure to the clean cage, with subsequent return to the dam and sire, was sufficient to induce nuclear c-Fos-IR in the GG neurons of p20 mouse pups (349 ± 53 nuclei, n=3).

We found that modifications to the cage change stimulus could increase or decrease the number of active GG neurons. In p3-p7 mice, transport of the clean cage to a separate dissection station resulted in a 64 ± 10% increase (n=5, p=0.0016) in the number of active GG neurons (Fig. 3A, '1+2+3+4'). In

p16-p17 mice, we simulated weaning, in the absence of a cage change, by removing the parental mice from the cage 90 min prior to sacrifice. This was sufficient to induce nuclear c-Fos-IR in the GG of 8/9 (89%) pups, but at a significantly lower level (22 ± 5% of the activity level in cage-changed mice, $p < 0.001$) (Fig. 3A, '1+2'). These results have several implications. First, our manipulations induced nuclear c-Fos-IR in only a subset of the total number of GG neurons that are capable of responding. Second, the magnitude of the organ-level response in the GG is graded. Third, parental separation alone is sufficient to trigger activity in the GG.

We tested whether c-Fos nuclear accumulation in the GG could be due to pheromonal communication. In particular, weaning may induce new pheromonal secretion events that are detected by conspecifics. In p12 mice, the cage change stimulus did not result in nuclear c-Fos-IR in the neurons of the vomeronasal organ (VNO) (Fig. 3B-C), though the GG organs exhibited nuclear c-Fos-IR (n=3). We next examined whether GG activity required the presence of conspecifics. In these experiments, p15 mice were individually weaned to clean cages. We found no significant differences in the number of GG neurons exhibiting nuclear c-Fos-IR between mice weaned individually or as a group ($p=0.61$, n=3 per group) (Fig. 3D). Thus, the observed GG responses were not due to pheromonal exchange.

It has been suggested that odor transduction in the GG relies in cGMP signaling components (Fleischer et al. 2009; Liu et al. 2009). GG neurons express candidate odor receptors in the form of membrane-bound guanylate cyclases and the cGMP-gated cationic channel CNGA3 on their cilia (Liu et al. 2009). The cilia represent putative sites of primary odor transduction in olfactory sensory neurons (Firestein 2001). We examined the role of CNGA3 in GG activity by measuring nuclear c-Fos-IR in GG neurons of *Cnga3*$^{-/-}$ mice. In these experiments, a mixed litter of p16 *Cnga3*$^{-/-}$ and *Cnga3*$^{+/-}$ mice was randomly divided into groups no larger than 4 and weaned into clean cages. In *Cnga3*$^{-/-}$ mice subjected to this protocol, the mean number of active neurons was 24 ± 5 (n=8), a statistically-significant decrease compared to their subjected *Cnga3*$^{+/-}$ siblings (91 ± 6 nuclei, n=5, $p < 0.001$) (Fig. 3E). These results suggest that the behavioral manipulations applied to the mice in this study evoked CNGA3-dependent responses in the GG.

Though a robust stimulus, weaning was not essential for nuclear c-Fos-IR in GG neurons. Though light handling of mouse pups, absent of weaning, generally did not induce nuclear c-Fos-IR, extensive handling could produce clearly stained nuclei (data not shown). In weanlings and adults (1-3 months old), transferring the mice to a clean cage induced GG nuclear c-Fos-IR in 3/5 (60%) mice. Overall, the responses in adults were not as robust; the average number of c-Fos+ nuclei in responding animals was 78 ± 27 (unhandled adult mice had an average score of 8 ± 2 active neurons per animal, n=10).

DISCUSSION

We have demonstrated that parental separation is sufficient to induce nuclear c-Fos-IR, an established marker of neuronal activity, in the GG. The manipulations performed in this study evoked activity in a fraction (at most ~50%) of the ~1,000 GG neurons (Koos and Fraser 2005) in an animal. Weaning of mouse pups to a clean cage ("cage change stimulus") constituted a robust stimulus of GG neurons. GG responses to the cage change stimulus were more pronounced in p6-p20 mice. The induced nuclear c-Fos-IR in this age range depended on the expression of CNGA3, a cGMP-gated cationic channel. It is likely that the c-Fos protein translocation events monitored in this study correspond to cGMP-initiated electrical transduction in the GG.

Previous *in vivo* studies have shown that low ambient temperatures (Mamasuew et al. 2008) and exposure to isoforms of DMP (Mamasuew et al. 2011a) induce CNGA3-dependent (Mamasuew et al. 2011b; Mamasuew et al. 2010) transcription of the c-Fos gene. However, these previously-observed effects were most pronounced at neonatal ages (p0-p7). In this study, nuclear c-Fos-IR was reduced at neonatal ages. Stronger responses were observed at adolescent ages (>p6), when mice are better able to regulate their own body temperatures. In our cage change stimulus, the ambient temperature was constant at 22˚C; thus, at most the weaned mice experienced a temperature change of 37˚C to 22˚C. Temperature changes in this range do not alter activity in GG neurons in mice ~p14 and older (Mamasuew et al. 2008; Schmid et al. 2010). Thus, the neuronal activity inducing nuclear c-Fos-IR in the GG is unlikely to be

solely attributable to ambient temperature changes. The effects we have analyzed in this study differ from those examined in earlier studies.

GG neurons have been proposed to detect alarm pheromones (Brechbuhl et al. 2008). Because the chemical identities of the alarm pheromones remain elusive, we have not been able to verify their collection and effects in our own experiments. Nevertheless, we tested whether the GG c-Fos protein translocations seen in this study required the presence of other animals. By definition, this is a necessary condition for pheromonal communication. We found that conspecifics were not required for the cage change-induced GG activity and that removal of conspecifics had no effects on the number of activated GG neurons. It is therefore unlikely that the GG activity we observed is due to detection of an alarm pheromone.

What are possible sensory contexts that account for the GG activity patterns observed in this study? Weaned mice all experienced a loss of parental odors and cues that are indicative of an inhabited cage, such as feces and urine. GG neurons may directly respond to the absence of habitation cues or pheromones, especially those that indicate a parental presence. In electrophysiological studies, GG neurons are excited by the removal of odorants (Chapter 4). However, this mechanism cannot solely account for graded organ-level encodings of GG activity in mice that underwent post-weaning manipulations of incrementing complexity (Fig. 3A).

We favor a model in which GG neurons sample cues that relate to an internal physiological state that is induced by weaning. This physiological state has different gradations of intensity, whose levels determine the concentrations or frequency of cues. At a low intensity, such as that elicited by parental separation alone, the physiological state induced only small changes in the baseline activities of GG neurons. As a result, only a few neurons exceeded the detection threshold of our c-Fos protein assay. At a high intensity, such as that elicited by transporting newly weaned mouse pups, this physiological state induces large changes in the activities of GG neurons and incurs nuclear c-Fos-IR throughout the ganglion. Of note, the results described here are consistent with previous findings of c-Fos transcription,

stemming from maternal separation, in the GG. Interestingly, those c-Fos signals were still present with naris occlusion (Mamasuew et al. 2008).

We conjecture that the relevant physiological state induced by the weaning of pups is stress. In guinea pigs, experimental manipulations similar to those performed here induce graded levels of glucocorticoids in the bloodstream (Hennessy and Moorman 1989). Cortisol can directly reduce the spontaneous firing rate of GG neurons (Chapter 4); as c-Fos assays usually report excitatory responses, the recovery period after hormone exposure may underlie the c-Fos responses seen in this study. We do not know if the nuclear c-Fos-IR observed in this study might stem from direct interactions between GG neurons and cortisol, or if serum cortisol might simply indicate the presence of other chemicals that are detected by the GG. Nevertheless, a prediction of this model is that any experimental manipulation that induces extreme stress in an animal should alter GG activity. Consistent with this prediction, we observed GG nuclear c-Fos-IR with some experimental manipulations that did not include weaning. Exposures of mice to alarm pheromones or cold may similarly induce secondary stress states that affect GG neurons.

GG neurons appear most primed for activity in adolescent mice. In mammals, this stage of life is characterized by the natural separation of offspring from their parents. While the caudal glomeruli near the necklace-like glomeruli in the olfactory bulb exhibit increased metabolic activity during suckling (Greer et al. 1982), this role has not yet been substantiated for the GG. Our results show that GG neurons participate in suckling's juxtaposed and necessary condition, weaning. This is a critical time in a mammal's life, in which the ability to recognize and adjust to new situations and environments is a matter of life or death. The special readiness and deployment of GG neurons at this stage of life suggests a critical role for this unusual primary olfactory subsystem in a mammal's adaptation to a life on its own.

ACKNOWLEDGMENTS

We thank B. Chang for kindly providing *Cnga3*$^{-/-}$ mice. We thank J. Gutierrez, S.M.M. Alaniz, and A.R. Douglas for animal care and husbandry. This project was supported by grants from the U.S. National Institutes of Health and the U.S. National Science Foundation.

CONTRIBUTIONS

C.Y.L., D.S.K., and S.E.F. planned experiments. C.Y.L. and D.S.K. performed experiments. C.Y.L. wrote the paper.

REFERENCES

Brechbuhl J, Klaey M, and Broillet MC. Grueneberg ganglion cells mediate alarm pheromone detection in mice. *Science* 321: 1092-1095, 2008.

Drenan RM, Grady SR, Whiteaker P, McClure-Begley T, McKinney S, Miwa JM, Bupp S, Heintz N, McIntosh JM, Bencherif M, Marks MJ, and Lester HA. In vivo activation of midbrain dopamine neurons via sensitized, high-affinity alpha 6 nicotinic acetylcholine receptors. *Neuron* 60: 123-136, 2008.

Firestein S. How the olfactory system makes sense of scents. *Nature* 413: 211-218, 2001.

Fleischer J, Hass N, Schwarzenbacher K, Besser S, and Breer H. A novel population of neuronal cells expressing the olfactory marker protein (OMP) in the anterior/dorsal region of the nasal cavity. *Histochem Cell Biol* 125: 337-349, 2006a.

Fleischer J, Mamasuew K, and Breer H. Expression of cGMP signaling elements in the Grueneberg ganglion. *Histochem Cell Biol* 131: 75-88, 2009.

Fleischer J, Schwarzenbacher K, Besser S, Hass N, and Breer H. Olfactory receptors and signalling elements in the Grueneberg ganglion. *J Neurochem* 98: 543-554, 2006b.

Fleischer J, Schwarzenbacher K, and Breer H. Expression of trace amine-associated receptors in the Grueneberg ganglion. *Chem Senses* 32: 623-631, 2007.

Fuss SH, Omura M, and Mombaerts P. The Grueneberg ganglion of the mouse projects axons to glomeruli in the olfactory bulb. *Eur J Neurosci* 22: 2649-2654, 2005.

Greer CA, Stewart WB, Teicher MH, and Shepherd GM. Functional development of the olfactory bulb and a unique glomerular complex in the neonatal rat. *J Neurosci* 2: 1744-1759, 1982.

Grüneberg H. A ganglion probably belonging to the N. terminalis system in the nasal mucosa of the mouse. *Z Anat Entwicklungsgesch* 140: 39-52, 1973.

Hennessy MB, and Moorman L. Factors influencing cortisol and behavioral responses to maternal separation in guinea pigs. *Behav Neurosci* 103: 378-385, 1989.

Kimoto H, and Touhara K. Induction of c-Fos expression in mouse vomeronasal neurons by sex-specific non-volatile pheromone(s). *Chem Senses* 30 Suppl 1: i146-147, 2005.

Koos DS, and Fraser SE. The Grueneberg ganglion projects to the olfactory bulb. *Neuroreport* 16: 1929-1932, 2005.

Liu CY, Fraser SE, and Koos DS. Grueneberg ganglion olfactory subsystem employs a cGMP signaling pathway. *J Comp Neurol* 516: 36-48, 2009.

Ma W, Miao Z, and Novotny MV. Role of the adrenal gland and adrenal-mediated chemosignals in suppression of estrus in the house mouse: the lee-boot effect revisited. *Biol Reprod* 59: 1317-1320, 1998.

Mamasuew K, Breer H, and Fleischer J. Grueneberg ganglion neurons respond to cool ambient temperatures. *Eur J Neurosci* 28: 1775-1785, 2008.

Mamasuew K, Hofmann N, Breer H, and Fleischer J. Grueneberg ganglion neurons are activated by a defined set of odorants. *Chem Senses* 36: 271-282, 2011a.

Mamasuew K, Hofmann N, Kretzschmann V, Biel M, Yang RB, Breer H, and Fleischer J. Chemo- and thermosensory responsiveness of Grueneberg ganglion neurons relies on cyclic guanosine monophosphate signaling elements. *Neurosignals* 19: 198-209, 2011b.

Mamasuew K, Michalakis S, Breer H, Biel M, and Fleischer J. The cyclic nucleotide-gated ion channel CNGA3 contributes to coolness-induced responses of Grueneberg ganglion neurons. *Cell Mol Life Sci* 67: 1859-1869, 2010.

Potter SM, Zheng C, Koos DS, Feinstein P, Fraser SE, and Mombaerts P. Structure and emergence of specific olfactory glomeruli in the mouse. *J Neurosci* 21: 9713-9723, 2001.

Roppolo D, Ribaud V, Jungo VP, Luscher C, and Rodriguez I. Projection of the Gruneberg ganglion to the mouse olfactory bulb. *Eur J Neurosci* 23: 2887-2894, 2006.

Schmid A, Pyrski M, Biel M, Leinders-Zufall T, and Zufall F. Grueneberg ganglion neurons are finely tuned cold sensors. *J Neurosci* 30: 7563-7568, 2010.

Storan MJ, and Key B. Septal organ of Gruneberg is part of the olfactory system. *J Comp Neurol* 494: 834-844, 2006.

FIGURE LEGENDS

Figure 1: Transport induces nuclear c-Fos-IR in mouse pups. A) Thin section of the mouse nasal vestibule stained with c-Fos antibody shows nuclear accumulation of c-Fos protein (black) in GG neurons. B) Whole-mount view of the c-Fos-stained nasal vestibule demonstrates labeled clusters of GG nuclei. Arrows in panels A and B point to clusters of GG neurons. C-D) Transported mice were sacrificed at C) 5 min or D) 90 min and stained for c-Fos. Shown are fluorescent photomicrographs of the nasal vestibule. GG cells have green fluorescence in OMP-GFP mice. Many but not all GG neurons show nuclear c-Fos-IR at 90 min (D). E-F) *Ex vivo* culture of nasal vestibules from mice sacrificed immediately after transport. E) Noses were processed after 2 h of culturing. F) Noses processed after 6 h of culturing no longer exhibited GG nuclear c-Fos-IR (compare E and F). Arrows point to clusters of GG cells. Scale bars: A) 60 μm, B) 100 μm, C-D) 30 μm, E-F) 60 μm.

Figure 2: Weaning mouse pups to a clean age constitutes a robust stimulus of the GG. A) Plot of the number of GG nuclei demonstrating c-Fos-IR per animal as a function of the age of the pup. The 'no change' data points represent c-Fos-IR in un-manipulated mice. B) Mice older than p6 had significantly ($p < 0.001$) higher numbers of c-Fos-IR nuclei in the GG.

Figure 3: Experimental permutations of weaning alter nuclear c-Fos-IR in the GG. All effects shown are statistically significant ($p < 0.05$) unless otherwise indicated by 'ns.' Activity index was calculated by normalizing effect sizes of experimental groups to the control effect of the cage change stimulus in littermates. Normalized values from different experiments were pooled together. A) Activity index as a function of different forms of weaning. '0': untouched mice. '1': touched/handled mice. '2': weaned mice (separated from dam and sire). '3': exposure to clean cage. '4': transport. For example, '1+2+3' indicates the mice were handled, separated from the dam and sire, and moved to a clean cage. '1+2+3+4' indicates that the weaned pups in the clean were transported to a separate dissection station. B-C) The cage change stimulus did not alter activity in the VNO. Shown are photomicrographs c-Fos-stained thin sections of the

VNO of B) untouched mice and C) mice weaned to a clean cage. D) The absence of conspecific animals did not change GG nuclear c-Fos-IR under the cage change stimulus. E) *Cnga3*$^{-/-}$ mice had significantly reduced numbers of active GG neurons under the cage change stimulus. Scale bars: 80 μm.

FIGURES

Figure 1

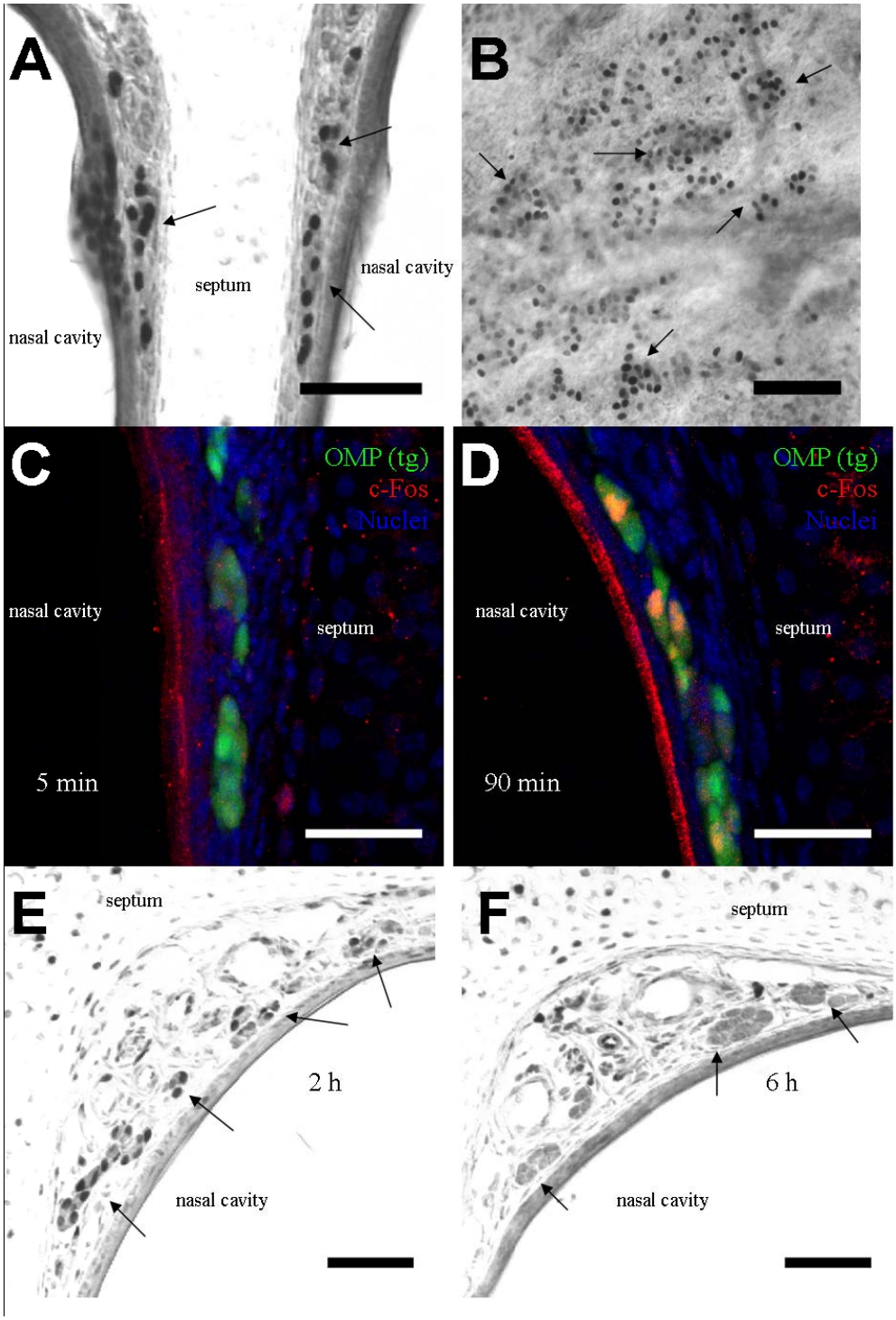

Figure 2

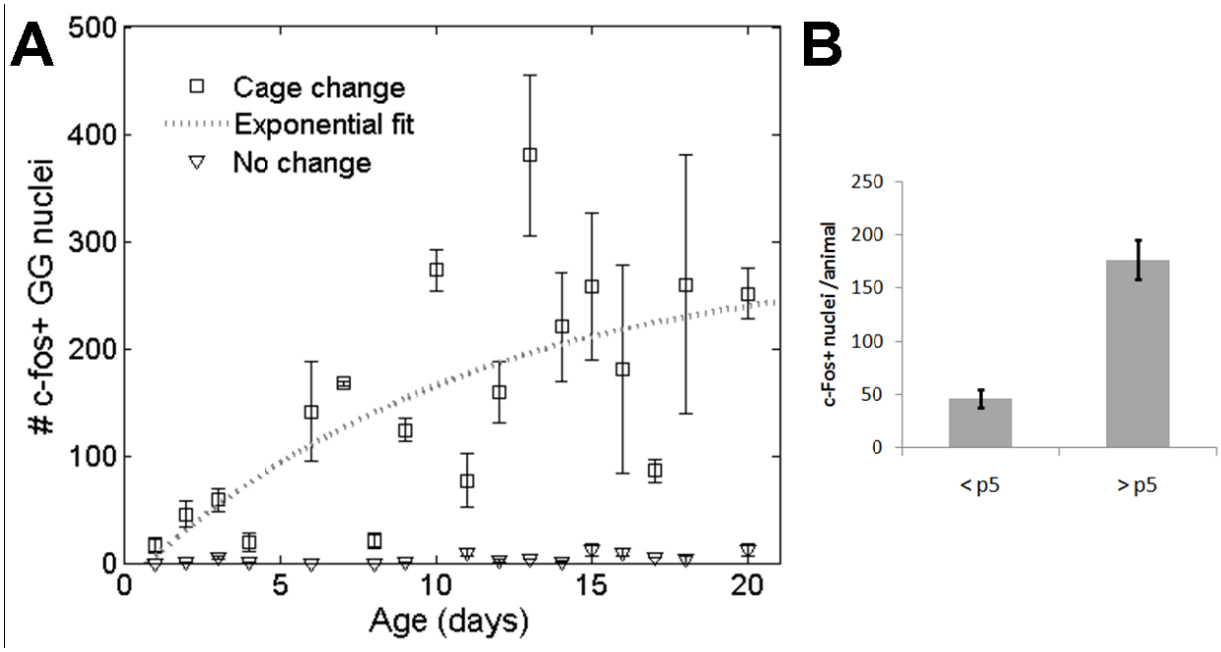
A
c-fos+ GG nuclei
Cage change
Exponential fit
No change
Age (days)
B
c-Fos+ nuclei /animal
< p5
> p5

Figure 3

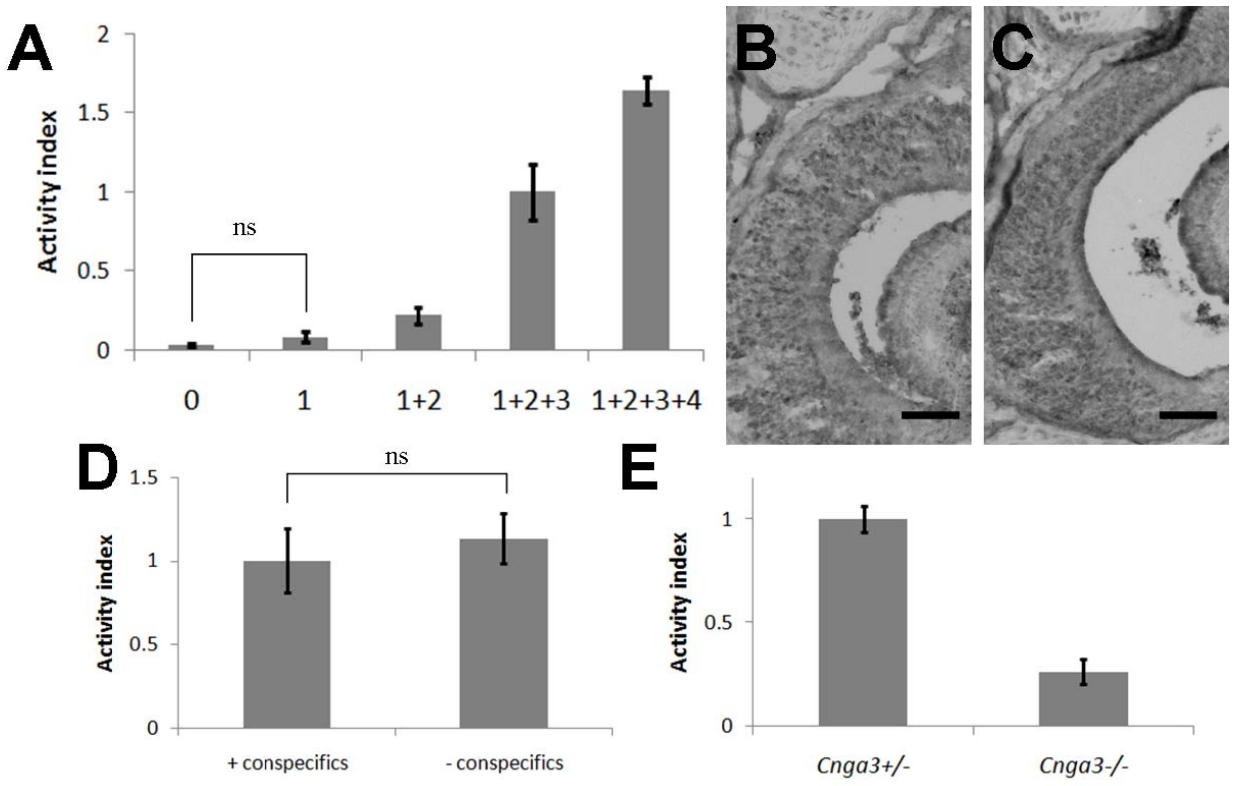
A
Activity index
2
1.5
1
0.5
0
ns
0
1
1+2
1+2+3
1+2+3+4
B
C
D
Activity index
1.5
1
0.5
0
ns
+ conspecifics
- conspecifics
E
Activity index
1
0.5
0
Cnga3+/-
Cnga3-/-

--- Chapter 6 ---

Future directions

Taken together, the presented results demonstrate multimodal functions for GG neurons. GG neurons detect cues associated with parental separation in young mice in a CNGA3-dependent manner. These cues may be sourced from serum. Other operating modalities for the GG include the CNGA3-independent excitatory detection of DMP pheromones and the inhibitory detection of a broad set of odorants. These various chemosensory modalities complement previously-identified responses of GG neurons to alarm pheromone and cold. Understanding how these different functions are integrated with one another into the molecular, electrophysiological, and behavioral characteristics of the GG will be one of many continuing challenges.

Further experimentation will be needed to build on the circumstantial evidence that supports the "internal sensing" hypothesis. It is not known if the electrophysiological responses to serum and cortisol are affected by the loss of CNGA3. CNGA3-dependent responses would suggest that the serum used in patch clamp experiments contains the compounds that might have altered GG activity *in vivo*. It will be necessary to characterize the electrophysiological responses (if any) of the GG to serum from mice exposed to the full complement of the behavioral manipulations described in Chapter 5. Column purification with mass spectrometry may help identify the serum components that trigger the electrophysiological responses. Finally, it will be important to determine if removal of adrenal glands or the functions of other sensory systems (*i.e.*, through naris occlusion) impacts GG activity.

A second direction points to the outputs of the GG. GG neurons mediate freezing behavior in adult mice exposed to a putative alarm pheromone. This shows that the GG plays an important role in how animals respond to stress. Yet nothing is known about the mechanisms by which the necklace-like

glomeruli and their downstream innervation targets generate the fear behaviors. While acetylcholinesterase positivity in the necklace glomeruli suggests integration into brain cholinergic systems, we also found that dopamine β-hydoxylase (DβH) was expressed in the GG (Chapter 4). This result confounds a simple classification of the GG as an exclusive part of any one brain system. Previous work also supports noradrenergic innervation of the necklace-like glomeruli (Brinon et al. 2001).

Despite exhibiting uniform responses to their defined chemical and thermal stimuli, GG neurons project to form 8-12 glomeruli, suggesting a heterogeneous mapping of outputs to higher-order brain systems. The molecular and functional basis for the formation of multiple glomeruli has not been elucidated. Chemical detection by pGC-G and pGC-A on a background of heterogeneous spontaneous firing patterns may account for some of the apparent output heterogeneity. This model can account for 2 types of responses on 3 spontaneous firing patterns, giving a maximum of 12 glomeruli if each unique output permutation is represented by 2 glomeruli. An attractive alternate hypothesis is that the glomeruli serve as representative targets of a topographic organization of the GG organ. For example, each glomerulus may be the destination of axons projected from a specific cluster or set of clusters of GG neurons. Injections of tract-tracing fluorescent dyes (Kobbert et al. 2000), selective photoconversion of fluorescent proteins (Chudakov et al. 2007), and trans-synaptic tracing with viral (Miyamichi et al. 2011) or plant (Baker and Spencer 1986) proteins will help to evaluate these possibilities.

Because the necklace glomeruli are situated between the glomeruli of the MOB and AOB, the GG might modulate the outputs of the other primary olfactory subsystems. For example, GG activity may alter the sensitivity or acuity of the olfactory sense. This may be important for specific situations of stress, weaning, and exposure to cold or odorant-rich/odorant-poor environments, when an increase or decrease of odor discrimination faculties would be beneficial for survival. Studies of olfactory function with genetic and surgical ablations of the GG should begin to address this hypothesis.

On a cellular level, it would be good to know the ligands of the pGC-G orphan receptor guanylate cyclase. Discovering these ligands should be part of a larger effort to understand the signaling and transduction mechanisms of GG neurons. A goal is to replicate the heterogeneous patterns of

spontaneous firing in the GG using *in silico* models of their ionic conductances. To arrive at these models, molecular identification of the conductances will be important, so that transgenesis techniques can be used to isolate the individual ionic contributions. This research in the complex-systems aspects of the GG may yield novel approaches to modify patterns and rates of neuronal activity. Furthermore, due to its far-forward location, the ganglion should be amenable to the application of exogenous small molecules. Studies of the GG may ultimately reveal new approaches to alter physiology and behavior in mammalian species.

REFERENCES

Baker H, and Spencer RF. Transneuronal transport of peroxidase-conjugated wheat germ agglutinin (WGA-HRP) from the olfactory epithelium to the brain of the adult rat. *Exp Brain Res* 63: 461-473, 1986.

Brinon JG, Crespo C, Weruaga E, Martinez-Guijarro FJ, Aijon J, and Alonso JR. Bilateral olfactory deprivation reveals a selective noradrenergic regulatory input to the olfactory bulb. *Neuroscience* 102: 1-10, 2001.

Chudakov DM, Lukyanov S, and Lukyanov KA. Tracking intracellular protein movements using photoswitchable fluorescent proteins PS-CFP2 and Dendra2. *Nat Protoc* 2: 2024-2032, 2007.

Kobbert C, Apps R, Bechmann I, Lanciego JL, Mey J, and Thanos S. Current concepts in neuroanatomical tracing. *Prog Neurobiol* 62: 327-351, 2000.

Miyamichi K, Amat F, Moussavi F, Wang C, Wickersham I, Wall NR, Taniguchi H, Tasic B, Huang ZJ, He Z, Callaway EM, Horowitz MA, and Luo L. Cortical representations of olfactory input by trans-synaptic tracing. *Nature* 472: 191-196, 2011.